Accommodating ~9 m of dextral slip on the Kekerengu Fault through ground deformation during the M_w 7.8 Kaikōura Earthquake, November 2016

by

Philippa Morris

A thesis

Submitted to Victoria University of Wellington

in partial fulfilment of the requirements for the degree of Master of Science in Geology

1897

TE HERENGA WAKA

WELLINGTON

VICTORIA UNIVERSITY OF WELLINGTON

Frontispiece: *Trace of the fault rupture along an eastern section of the Kekerengu Fault, showing one of the (undeformed) paleoseismic trenches on the right (from Little et al., 2018). Photograph taken by Julian Anderson, 20/11/2016 (using a remotely piloted aircraft).*

Abstract

The M_w 7.8 Kaikōura earthquake of November 14th 2016 provided unprecedented opportunities to understand how the ground deforms during large magnitude strike-slip earthquakes. The re-excavation and extension of both halves of a displaced paleoseismic trench following this earthquake provided an opportunity to test, refine, and extend back in time the known late Holocene chronology of surface rupturing earthquakes on the Kekerengu Fault. As part of this thesis, 28 organic-bearing samples were collected from a suite of new paleoseismic trenches. Six of these samples were added to the preferred age model from Little et al. (2018); this updated age model is now based on 16 total samples. Including the 2016 earthquake, six surface rupturing earthquakes since ~2000 cal. B.P. are now identified and dated on the Kekerengu Fault. Based on the latest five events (E0 to E4), this analysis yields an updated mean recurrence interval estimate for the Kekerengu Fault of 375 ± 32 yrs (1σ) since ~1650 cal. B.P. The older, sixth event (E5) is not included in the preferred model, as it may not have directly preceded E4; however, if this additional event is incorporated into an alternative age model that embraces all six identified events, the mean recurrence interval estimate (considered a maximum) calculated is 433 ± 22 yrs (1σ) since ~2000 cal. B.P.

Comparison of structures on an identical trench wall logged both before and after the 2016 earthquake, and analysis of pre- and post-earthquake high resolution imagery and Digital Surface Models (DSMs), has allowed me to quantify where and how ~9 m of dextral-oblique slip was accommodated at this site during the earthquake. In addition to this, I analyse the coseismic structure of the adjoining segment of the 2016 ground rupture using detailed post-earthquake aerial orthophotography, to further investigate how geological surface structures (bulged-up moletrack structures) accommodated slip in the rupture zone. These combined analyses allowed me to identify two primary deformation mechanisms that accommodated the large coseismic slip of this earthquake, and the incremental effect of that slip on the structural geology of the rupture zone. These processes include: a) discrete slip along strike-slip faults that bound a narrow, highly deformed inner rupture zone; and b), distributed deformation within this inner rupture zone. The latter includes coseismic clockwise rotation of cohesive rafts of turf, soil and near-surface clay-rich sediment. During this process, these "turf rafts" detach from the underlying soil at a mean depth of ~0.7 m, shorten by ~2.5 m (in

addition to shortening introduced by any local contractional heave), bulge upwards by <1 m, and rotate clockwise by ~19° - while also separating from one another along fissures bounded by former (now rotated) synthetic Riedel faults. This rotational deformation accommodated ~3 m of dextral strike-slip (of a total of ~9 m), after which this rotation apparently ceased, regardless of the total slip or the local kinematics (degree of transpression) at any site. The remaining slip was transferred onto later forming, throughgoing faults as discrete displacement. Analysis of the morphology and amplitude of these moletracks suggests that an increase in the degree of transpression (value of contractional heave) at a site increases the magnitude of shortening and the finite longitudinal strain absorbed by the rotated turf rafts, but does not necessarily contribute to an increase in height (generally 0.33-0.53 m on all parts of the fault). Rather, the comparison of these moletracks with those described by other authors suggests that a more controlling factor on their height is the clay content and cohesion of material deformed into the moletracks.

Finally, comparison of the before and after cross-sections of the displaced paleoseismic trench has provided, for the first time, insight into how large magnitude strike-slip ruptures are expressed in the fault-orthogonal view typical of paleoseismic trenches. Although this rupture involved ~9 m of dextral strike-slip, the cross-sectional view of the re-excavated trenches was dominated by the much lesser component of fault-perpendicular contractional heave (~1.3 m) that occurred in 2016, which did not occur in previous paleoearthquakes at the same site (these were, by contrast, transtensional). This heave was expressed as up to ~2 m of fault-transverse shortening in the inner rupture zone of the trenches, while the ~9 m of strike-slip only created cm-scale offsets across faults. Previous earthquakes at the site were expressed as cm-dm scale, mostly normal dip-separations of sub-horizontal stratigraphic units across faults, suggesting that a change in local kinematics (of ~8°) must have occurred in 2016. Such a small kinematic change may drastically impact the overall ground expression of strike-slip earthquakes - producing also complicated structures including overprinting fault strands in the rupture zone (to a few metres depth). This information poses challenges for structural geologists and paleoseismologists when interpreting (the significance of) structures in future trench walls.

Acknowledgements

First and foremost, I would like to thank my primary supervisor Tim Little, for his ongoing support and consistent input into my studies. Your dedication to the quality of science throughout my work has been phenomenal. To my co-supervisors – Matthew Hill, thank you for giving up your time on countless occasions to help me with anything I needed, and providing me with so much of the data I used throughout my work; Russ Van Dissen and Lynda Petherick, thank you for your input into various aspects of my work. To Jesse Kearse, thank you for helping me get started and answering all my silly questions about the most basic things. To the trenching team- thank you for your contributions to my work, and for providing such a supportive field work environment. To the various Victoria University staff, thank you for your words of encouragement and advice. To the office crew, thanks for all the coffee runs, crosswords, and card games – it wouldn't have been the same without you all. I also acknowledge the Earthquake Commission, who funded this project.

And finally, thank you to my family and friends, for both the numerous proofreads of my work, and for supporting me throughout all my years of study.

Table of Contents

1. Chapter One: Introduction 1

1.1 Research motivation and aims 1

1.2 The Kaikōura earthquake in a seismic hazard context 1

1.3 Research opportunities provided by the Kaikōura earthquake 2

1.4 Thesis structure 4

1.4.1 Chapter Two 5

1.4.2 Chapter Three 6

1.4.3 Chapter Four 7

1.4.4 Conclusions 7

2. Chapter Two: A revised paleoseismological record of the late Holocene ruptures on the Kekerengu Fault 9

2.1 Introduction 9

2.1.1 Background 11

2.1.2 Pre-earthquake stratigraphy and cross-cutting relationships (2016) 14

2.2 Methods of excavation, sampling and age modelling (2018) 16

2.2.1 Excavation 16

2.2.2 Sampling 18

2.2.3 Age modelling (see Appendix B.2.7 for OxCal code) 20

2.3 Results 21

2.3.1 Post-earthquake stratigraphy and cross-cutting relationships (2018) 21

2.3.2 Age Modelling and Chronology (2018) 28

2.4 Discussion 32

2.4.1 Comparison of the paleoseismic record of the Kekerengu Fault to paleoseismic data for other faults in the Marlborough Fault System (MFS) 32

2.4.2 Implications for future paleoseismic studies 35

2.6 Conclusion 36

3. Chapter Three: Formation and evolution of moletrack structures during a M_w 7.8 strike-slip earthquake 39

3.1 Introduction 39

3.2 Background and previous work 41

3.2.1 The Coulomb failure criterion and Riedel fracture zones 41

3.2.2 Laboratory deformation experiments—effect of material properties on fault zone structure 43

3.2.3 Laboratory deformation experiments—effect of boundary conditions on fault zone structure 44

3.2.4 Relevance of laboratory structures to natural earthquake rupture zones ... 45

3.3 Geomorphology and structural geology of an eastern part of the 2016 rupture on the Kekerengu Fault 49

3.3.1 Structure, geologic setting, and 2016 event displacement along the near-coastal Kekerengu Fault 49

3.3.2 Field description of the eastern Kekerengu Fault rupture and its moletracks 51

3.3.3 Description of ground deformation along the Napoleon segment 57

3.3.4 Reconstructing ground deformation along the Tirohanga segment of the Kekerengu Fault 67

3.4 Discussion 75

3.4.1 Are the Kaikōura earthquake moletracks different from previously described ones? 75

3.4.2 Evolution of moletrack structures 78

3.4.3 Detachment depth of turf rafts 84

3.4.4 Is there a change in moletrack characteristics or morphology as a result of an increasing displacement angle (i.e., α = increasingly positive/transpressional)? .. 90

3.5 Conclusion 92

4. Chapter Four: 3D analysis of incremental ground deformation as a result of ~9 m of strike-slip: Comparison of “before” and “after” logs of a displaced paleoseismic trench 95

4.1 Introduction 95

4.2 Background and previous work 98

4.2.1 Pre-earthquake stratigraphy and cross-cutting relationships (refer to Figure 4.4) 98

4.2.2 Contrast in ground deformation style between the previously recognised paleoearthquakes and the 2016 earthquake 101

4.3 General approach to evaluating how and where slip was accommodated at the trench site during the 2016 earthquake 101

4.4 Analysis of how and where displacement was partitioned during the 2016 earthquake, through comparison of pre- and post-earthquake datasets........ 102

4.4.1 Revised coseismic displacement vector at the trench site 102

4.4.2 Post-earthquake trench stratigraphy and cross cutting relationships (2018) 105

4.4.3 Structural interpretation of 2016 coseismic deformation across the rupture zone of the Kekerengu Fault at the trench site 113

4.5 Discussion 130

4.5.1 How and where ~9 m of dextral slip was accommodated at the paleoseismic trench site 130

4.5.2 Contrast in deformation style at the trench site between the last paleoearthquake and the 2016 earthquake 132

4.5.3 Expression of large magnitude strike-slip rupture in a fault perpendicular plane of view 133

4.7 Conclusions 135

Summary of Conclusions.... 137

References....141

Appendices....145

Appendix A – 2016 stratigraphy and samples 145

Appendix B – 2018 stratigraphy, samples and age modelling 147

Appendix C – Datasets used in moletrack analysis 153

Appendix D – Additional trench site data....161

List of Figures

Figure 1.1: *Map of surface fault ruptures associated with the Kaikōura earthquake…….3*

Figure 2.1: *Tectonic map of the Cook Strait………………………………………………………….11*
Figure 2.2: *Map of fault traces near the three paleoseismic trenches excavated in 2016……………………………………………………………………………………………………….13*
Figure 2.3: *Pre-earthquake log of southwest (SW) wall of Trench 1 (2016)…………………15*
Figure 2.4: *Structural map of the trench site………………………………………………………17*
Figure 2.5: *Paleofissure that re-opened during the 2016 earthquake…………………………19*
Figure 2.6: *Post-earthuake log of the southwest (SW) wall of TS1……………………………24*
Figure 2.7: *Post-earthquake log of the NE wall of TS1…………………………………………25*
Figure 2.8: *Post-earthquake log of the SW wall of TN1…………………………………………26*
Figure 2.9: *Post-earthquake log of SW wall of T4………………………………………………27*
Figure 2.10: *Age modelling results for paleoseismic choronology of the Kekerengu Fault………………………………………………………………………………………………………31*
Figure 2.11: *Compilation of the paleoseismiological data from the MFS……………………34*

Figure 3.1: *Schematic diagram showing the preferred inception angle of fractures forming in a dextral strike-slip zone…………………………………………………………………42*
Figure 3.2: *Map of surface geology of an eastern part of the Kekerengu Fault …………48*
Figure 3.3: *Example of a ("well-evolved") section of ground rupture…………………………52*
Figure 3.4: *Example of a ("less evolved") section of ground rupture …………………………54*
Figure 3.5: *Moletrack structure at Shag Bend, Clarence River, Kekerengu ………………55*
Figure 3.6: *Moletrack located on the flanks of Deadman Stream, Kekerengu……………55*
Figure 3.7: *Fissured, bulged up moletrack at the paleoseismic trench site…………………56*
Figure 3.8: *"Less evolved" moletrack located along a fault strand of low slip……………56*
Figure 3.9: *Example of a section of the rupture in the Napoleon segment…………………58*
Figure 3.10: *Map showing locations of elevation profiles at Locations A-D ………………60*
Figure 3.11: *Location A ………………………………………………………………………………63*
Figure 3.12: *Location B ………………………………………………………………………………64*
Figure 3.13: *Location C ………………………………………………………………………………65*
Figure 3.14: *Location D…………………………………………………………………………………66*
Figure 3.15: *Tirohanga segment of the Kekerengu Fault ……………………………………69*
Figure 3.16: *Line drawing of the features mapped in Figure 3.15……………………………71*
Figure 3.17: *Schematic diagram illustrating the reconstruction of a marker line…………71*
Figure 3.18: *Reconstruction of the Tirohanga paddock…………………………………………74*
Figure 3.19: *Simple block rotation model showing rotational deformation processes…80*
Figure 3.20: *Block rotation model using values specific to the trench site…………………80*
Figure 3.21: *Block rotation model including a component of contractional heave …….83*
Figure 3.22: *Schematic illustration of the depth to detachment of a turf raft……………86*
Figure 3.23: *Excess raft area (bulge uplift) at Location A………………………………………87*
Figure 3.24: *Excess raft area (bulge uplift) at Location B………………………………………87*
Figure 3.25: *Excess raft area (bulge uplift) at Location C………………………………………88*
Figure 3.26: *Excess raft area (bulge uplift) at Location D………………………………………88*

Figure 3.27*: Graph of changes in moletrack characteristics with increasing displacement angle (α)*………*91*

Figure 4.1: *Tectonic map of the Cook Strait* *96*
Figure 4.2: *Map of fault traces near the three paleoseismic trenches from 2016* *97*
Figure 4.3*: Map showing GPS pinned locations of the pre- and post-earthquake locations of the margins of the original trench* *97*
Figure 4.4: *Pre-earthquake trench log of Trench 1, SW wall* *99*
Figure 4.5: *Post-earthquake structural map of the paleoseismic trench site* *100*
Figure 4.6*: Pre-earthquake and post-earthquake trench margins* *103*
Figure 4.7: *Post-earthquake trench log of the SW wall of TS1* *108*
Figure 4.8: *Post-earthquake trench log of the NE wall of TS1.* *109*
Figure 4.9: *Post-earthquake trench log of the SW wall of TN1*………………………………….*110*
Figure 4.10: *Area of the backfill unit on TS1, NE wall* *116*
Figure 4.11: *Area balancing calculations for the area of backfill in Figure 4.10* *117*
Figure 4.12: *Schematic and aerial view diagrams showing the effect of distributed deformation on the rupture zone.* *118*
Figure 4.13*: Intermediate state cross-section of the SW wall of TS1* *120*
Figure 4.14: *Intermediate state cross section of the SW wall of TN1* *121*
Figure 4.15: *Aerial orthophotography and DSMs used in topographic differencing* ... *124*
Figure 4.16: *Restored version of the post-earthquake orthophotograph and DSM* *125*
Figure 4.17*: Restored aerial view of trench site (1-part method)* *126*
Figure 4.18: *Restored aerial view of the trench site (2-part method)*………………………... *127*

1. Chapter One: Introduction

1.1 Research motivation and aims

Active faults pose one of the greatest natural hazards to New Zealand, yet, our knowledge about how they deform the ground during earthquakes is relatively poor. New Zealand's location on the Pacific-Australian plate boundary (Figure 1.1a) explains the abundance of active faults proximal to this boundary. A better knowledge of both the tempo of surface rupturing earthquakes occurring on these active faults, and the precision in paleoearthquake chronologies on these faults, will result in a better understanding of the seismic hazard in New Zealand. Because paleoseismologists interpret the geological record of past earthquakes based on an interpretation of the structural geology of the near surface sediments and soil, any opportunity to understand how this structure has evolved as a result of a single earthquake—especially where that rupture has experienced a known direction and magnitude of slip—can provide important new insight into the processes of coseismic ground deformation, and improve the paleoseismic interpretation of the geologic record. This is turn provides advantages in evaluating and modelling seismic hazard.

This thesis utilizes the rupture of the dextral strike-slip Kekerengu Fault during the 2016 Kaikōura earthquake in New Zealand to address two main research aims. First, I aim to update and refine the paleoseismic record of the Kekerengu Fault established by Little et al. (2018); second, I will attempt to evaluate how and where ~9 m of dextral strike-slip (and 1.3 m of contractional, fault-perpendicular heave was accommodated on this fault at the surface during the Kaikōura earthquake.

1.2 The Kaikōura earthquake in a seismic hazard context

Shortly after midnight on the 14th of November 2016, the Mw 7.8 Kaikōura earthquake struck the South Island of New Zealand. This earthquake ruptured ~20 faults in the Marlborough Fault System (MFS, Figure 1.1b) over a length of ~180 km, in a complex, multi-fault rupture sequence (Hamling et al., 2017). This thesis focusses on the Kekerengu Fault – one of five main northeast striking faults was involved in this (Figure 1.1c). Since the 2016 earthquake, researchers (e.g., Langridge et al., 2020) are striving to investigate whether past earthquakes in the MFS may similarly have involved a multi-fault rupture sequence, or whether the 2016 rupture was unusually complex. Knowing the answer to this question is important, because single vs. multi-fault rupture scenarios have very different seismic hazard implications. To further evaluate this important question, detailed and extensive paleoseismic records of active faults in the MFS are needed. Developing an accurate paleoseismic record for a fault is commonly achieved through fault trenching, and radiocarbon dating stratigraphic units logged in these fault trenches. Once these records are established for multiple faults in the MFS, the timings of the paleoearthquakes on each of these faults can potentially be compared in order to evaluate if: a) particular combinations of faults may have ruptured coevally in the past; b) multi-fault rupture is a chaotic process not necessarily involving any particular combination of faults; c) if multi-fault rupture is the exception, with single-fault rupturing being the "rule." Part of my thesis establishes a refined, detailed paleoseismic record for the Kekerengu Fault, which is one of the most rapidly slipping faults in the MFS (and in New Zealand). This type of detailed information needs to be collected before the research question mentioned above can be addressed with any resolution or clarity.

1.3 Research opportunities provided by the Kaikōura earthquake

Another opportunity provided by the Kaikōura earthquake is the opportunity to understand how large-magnitude slip has been partitioned into the near-surface ground materials of the rupture zone during a dominantly strike-slip earthquake. Advanced survey technology (including remotely piloted aircraft surveys, and Real Time Kinematic Ground Positioning Surveys, i.e., RTK GPS) used in the few weeks after the earthquake provided an abundance of aerial and ground surface data for the ruptured areas on the Kekerengu Fault (and others). These data provide a valuable opportunity to examine and map earthquake-related ground deformation and surface structures in detail – an opportunity for detailed description that has not been readily available in the past, especially for a very large coseismic displacement (as is the case for the Kekerengu Fault). Using these aerial datasets, I am able to examine earthquake related geological structures across an eastern part of the Kekerengu Fault rupture, at a detailed scale (mostly ~2 cm resolution). My analysis focuses on the morphology, structure, and origin of push-up structures (also called deformational bulges or moletracks) that characterize the inner part of most of the rupture zone along the Kekerengu Fault. In particular I strive to evaluate the kinematics of their development, the depth extent of the bulged material in the ground, and the role that the bulges (and associated structures) have played in accommodating a large coseismic displacement on a strike-slip fault.

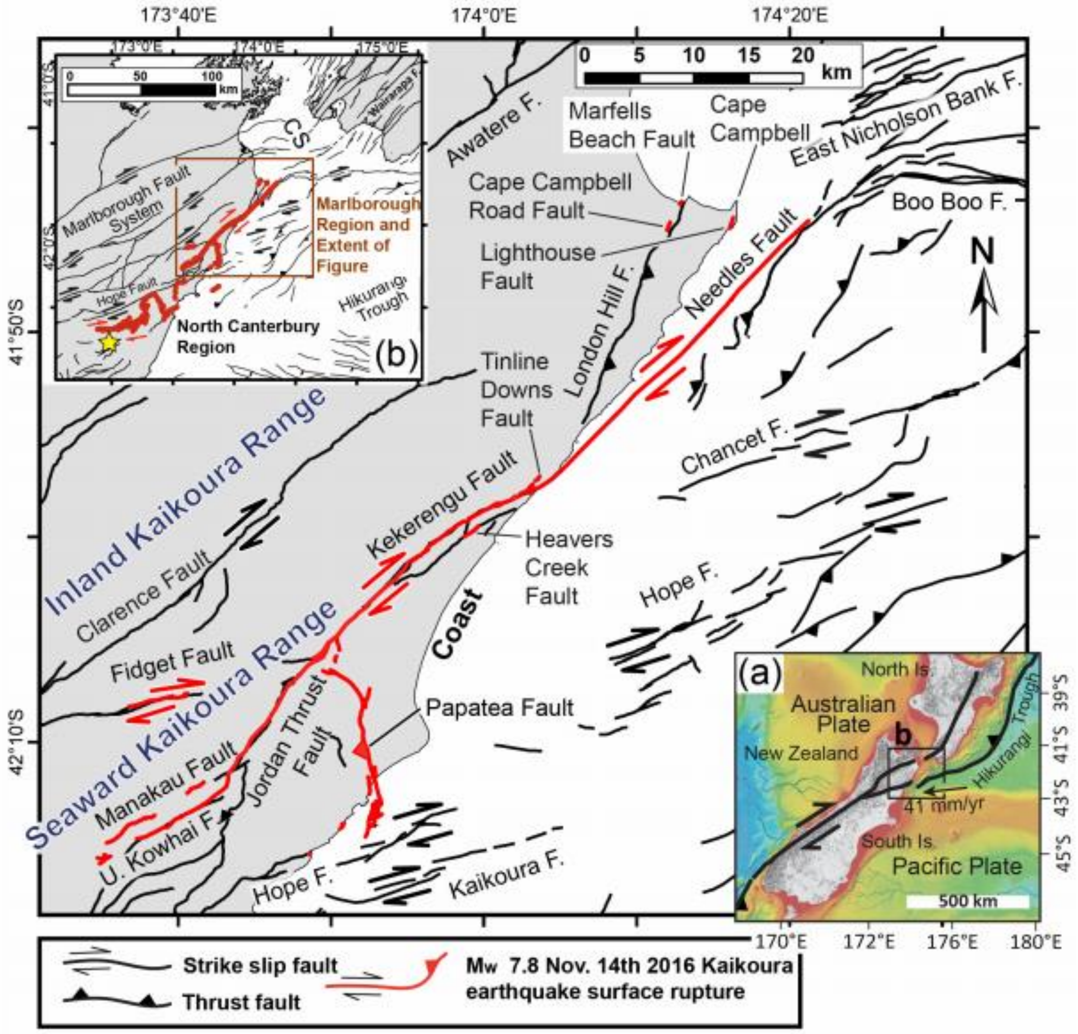

Figure 1.1: *Map of surface fault ruptures associated with the Kaikōura earthquake (red, Litchfield et al., 2018) and active faults that did not rupture in 2016 (black, from New Zealand Active Fault Database [NZAFDB]; Langridge et al., 2016). a) Regional plate boundary setting showing Pacific-Australian relative plate motion vector (black arrow, De Mets et al., 2010), and the extent of part b of the figure; b) All surface ruptures associated with the Kaikōura earthquake (red). Yellow star is the epicentre from Kaiser et al., (2017), brown box denotes the aerial extent of part c of this figure, CS = Cook Strait. Figure is from Kearse et al. (2018).*

Another opportunity provided by this earthquake was the ability to compare pre- and post-earthquake trench log data to understand changes in the structural geology of the fault zone in the uppermost few metres of the sub-surface. Approximately 10 months prior to the earthquake, several paleoseismic trenches were excavated near the coast by Little et al. (2018) to investigate the timing of past earthquakes on the Kekerengu Fault. One of these trenches was dextrally displaced by ~9 m during the earthquake — providing an opportunity to re-excavate the already-logged, original walls of the displaced trench, and to analyse the structure of these walls to assess the incremental effect of the last earthquake on the finite structure of the fault zone. This is the first time that this kind of comparison has been undertaken globally, and provides a unique method of understanding how slip is partitioned into the ground during a large magnitude strike-slip earthquake. Not only was a comparison of cross-sectional (trench) data possible following this earthquake, but aerial photography and Digital Surface Models (DSMs) from before and after the earthquake can also be compared to better understand where and how slip was accommodated on the surface during the earthquake.

1.4 Thesis structure

Following this Introduction, this thesis is presented in three main chapters. Chapters two, three and four each address a different research question. Each chapter is are designed as a self-contained research paper intended (with some modification) for later submission to a journal, although I occasionally cross-reference between them in the thesis. Because of this stand-alone format, each chapter contains its own Introduction and exposition of relevant background material. As there is some overlap in the data used in these chapters and the interpretations drawn from them, there is some unavoidable repetition between chapters. Finally, I draw together the results from all three of the main chapters to form an integrative conclusions section at the end of this thesis. For simplicity, the references cited in all the chapters in the thesis are listed together in a single master reference list that is presented at the end of the thesis (rather than within each chapter).

Funded by the Earthquake Commission (project 18/758, awarded to T. A. Little and R. J. Van Dissen), my project has benefitted from contributions from not only my supervisors (Little, Matthew Hill, and Van Dissen), but also several other project colleagues, particularly in the trench-logging. Notwithstanding these contributions, the presentation and processing of the data, their interpretation, the writing of the chapters drafting of the figures (unless otherwise attributed), and compilation of the Tables and Appendices was undertaken by myself. In the descriptions of the contents of each chapter below, I acknowledge the particular contributions of my colleagues to each chapter.

1.4.1 Chapter Two

Chapter two presents an updated, refined paleoseismic record of the Kekerengu Fault, based on a combination of radiocarbon data from before (Little et al., 2018) and after the 2016 earthquake. 15 new samples from the new trench excavations were submitted by me for ^{14}C analysis, six of which could be incorporated into a newly revised and extended preferred age model for paleoearthquakes on the near-coastal part of the Kekerengu Fault. This new model recognizes five paleoearthquakes since ~2000 cal. B.P. and is based on a total of 16 radiocarbon ages.

This chapter draws on both the pre- and post-earthquake trench log data. Researchers who contributed to logging and sampling of the new excavations include Tim Little, Russ Van Dissen (GNS Science), Jesse Kearse, Mark Hemphill-Haley (Humboldt State University, USA), Kevin Norton, Jessie Vermeer (University of Melbourne), Lynda Petherick, and Emma Watson. My role in this work (besides my own contribution to the trench logging and sampling) was to compile these datasets, draft the trench logs and all the other figures, submit and interpret the radiocarbon samples, and produce an updated chronology of this section of the fault through age modelling of the enlarged data set using OxCal 4.2.3. After considering the implications of the revised late Holocene earthquake chronology for the Kekerengu Fault, this chapter finishes with my comparison of this chronology with that of the nearby MFS faults. My supervisors Little, Hill, and Van Dissen provided guidance and advice in the presentation and interpretation of the data for this chapter, and Tim Little edited and commented upon my written drafts.

Appendix A and B both contain data used to produce this updated age model. Appendix A contains log of Trench 3 that was logged by Little et al. (2018) before the 2016 earthquake, and a table (Appendix A.2.2) of all the radiocarbon results as compiled prior to the 2016 earthquake by Little et al. (2018). Appendix B contains: detailed descriptions of all the stratigraphic units in the trenches, including newly introduced ones resulting from the post-earthquake trench excavations (Appendix B.2.3), a table of all the radiocarbon results collected after the 2016 earthquake (Appendix B.2.4), and an orthophotomosaic (Appendix B.2.5) of one of the newly introduced, post-2016 earthquake trenches (Trench 4, SW wall). Parts of the OxCal 4.2.3 age model that are not displayed in the main text are presented in Appendix B.2.6.

1.4.2 Chapter Three

Chapter three presents a detailed analysis of the moletrack structures along an eastern part of Kekerengu Fault rupture. In this chapter, I evaluate various features of the moletracks including their height, shape, and structure. I compare these moletrack features between different local kinematic settings (transpression, transtension, pure strike-slip), and between sites with different amounts of slip to evaluate how and where these structures accommodated the large magnitude slip seen throughout this eastern part of the rupture (7-9 m dextral strike-slip).

This chapter draws on post-earthquake aerial surveys of the rupture zone along an eastern (near-coastal) section of the Kekerengu Fault, taken using remotely piloted aircraft by Dimitrios Zekkos (University of Berkeley, CA, USA) and John Manousakis (Elxis Group, Greece) on the 28th of November 2016 (as part of the Kaikōura Earthquake Surface Rupture Mapping Team). Orthophotomosaics based on these images were compiled and processed by Matthew Hill (GNS Science). These post-earthquake orthophotomosaics were used as a base map for my digitization of moletrack structures. Matthew Hill also mentored me on the use of the ArcMap GIS program. Little and Hill provided guidance and advice in the presentation and interpretation of the data for this chapter, and Tim Little edited and commented upon the written drafts.

Appendix C contains information relevant to the understanding of moletracks structures in this chapter, including: the descriptions of the classes of sub-surface sediments within the mapped region, examples of map tiles showing digitized moletrack features, and the raw datasets and results from my mapping exercises and interpretation.

1.4.3 Chapter Four

Chapter Four takes presents a detailed, 3D analysis of the differences between the pre- and post-earthquake trench log data. Based on these differences, I am able to quantify where and how the ~9 m of dextral slip was accommodated at this site during the earthquake, using methods such as partial reconstruction of cross-sections, area balancing, and topographic differencing. I also document how this slip was expressed in a fault-orthogonal plane of view (i.e., the trench logs); this provides new insight into how large magnitude strike-slip ruptures may be expressed in paleoseismic trenches.

This chapter draws on both pre- and post-earthquake trench log data that was collected by a team of field team members, including Tim Little, Russ Van Dissen, Jesse Kearse, Mark Hemphill-Haley, Kevin Norton, Jessie Vermeer, Lynda Petherick, Emma Watson, and myself. In addition, I also use the aerial photography that was taken at and near the trench site using remotely piloted aircraft, by Dimitrios Zekkos and John Manousakis. The orthophotographic compilation and DSM processing from that photography was undertaken by Matthew Hill. He also provided me with access to aerial imagery and LIDAR from before the 2016 earthquake, sourced from Land Information New Zealand (LINZ). In addition to assisting with the trench logging, my contribution was to compile, compare, integrate and interpret the various datasets, and to interpret the processes by which deformation was partitioned and accommodated in the ground during the 2016 earthquake. I also created all the figures and tables in the chapter, and Tim Little provided advice on the writing and edited drafts of my written work. Lynda Petherick conducted preliminary analysis on pollen samples that were collected in the trenches, and drew some preliminary conclusions about the stability of the landscape at this site over the time spanned by the last several paleoearthquakes.

Appendix D contains a figure from Kearse et al. (2018) that documents a measurement of the slip vector at the trench site, as well as a measurement of the total rupture zone width at the site. I compare this with the slip vector and rupture width that I measure more accurately at the trench site (using a different method) in this chapter.

1.4.4 Conclusions

To conclude this thesis, I draw together the conclusions from each of the aforementioned chapters into a summary section at the end of this thesis.

2. Chapter Two: A revised paleoseismological record of the late Holocene ruptures on the Kekerengu Fault

2.1 Introduction

The Mw 7.8 Kaikōura earthquake of the 14th of November 2016 ruptured ~20 faults in the Marlborough Fault System (MFS), over a length of ~180 km, in an unusually complex, multi-fault rupture sequence (Hamling et al., 2017). The fault with the largest surface displacement was the NE-SW striking Kekerengu Fault, which commonly accommodated >8 m of dextral slip, locally reaching ~12 m. This slip is among the five largest coseismic surface displacements recorded globally to date (Kearse et al., 2018; Little et al., 2018). Approximately 10 months prior to this earthquake, three paleoseismological trenches were excavated across the northeastern part of the Kekerengu Fault near the coast. Little et al. (2018) used a suite of 13 radiocarbon samples from these trenches to identify three prior late Holocene surface-rupturing paleoearthquakes since ~1250 cal. B.P. Statistical analysis of the youngest four of these events yielded an estimate of a mean recurrence interval of 376 ± 32 yrs (1σ). Combined with the observed 9.1 ± 0.1 m of single-event displacement (SED) measured on this part of the fault during the 2016 earthquake, and assigning a coefficient of variation of 0.5 to this estimate of mean SED, Little et al. (2018) used this data to infer a mean (late Holocene) dextral slip rate of 24 ± 12 mm/yr (1σ) for the eastern Kekerengu Fault. The three paleoearthquakes identified by Little et. al (2018) were dated at 249-108, 528-356, and 1249-903 cal. B.P. respectively. They also suggested that a fourth paleoearthquake occurred at either >1605 cal. B.P. or in the interval 1673-1205 cal. B.P. This ambiguity arose from uncertainties in the best stratigraphic interpretation of (charcoal) radiocarbon ages in a coseismic fissure infill deposit, which they did not attempt to resolve in that paper.

In this chapter I update and revise the paleoseismic chronology for the Kekerengu Fault established by Little et al. (2018), based on a new overlay of stratigraphic data collected in the same study area. Approximately 3 months after the 2016 earthquake, the fragmented halves of one of the three pre-2016 trenches (Trench 1 of Little et al., 2018) were re-excavated as part of a study to compare equivalent trench logs from before and after the earthquake, in order to better understand the incremental deformation that was contributed by a single, large (9-10 m of slip) strike-slip rupture. In addition: 1) a new trench, “Trench 4”, was excavated across the 2016 zone of ground deformation (including the moletrack) adjacent to the Trench 1 (T1) fragments; 2) the exhumed T1 trench fragments were extended several metres across the fault zone to sample new fault zone material that had not been logged in the pre-earthquake (2016) study by Little et al. (2018); and 3), post-earthquake field observations were gathered regarding the process, source, and rate of infilling of the many earthquake fissures that had opened up during the Kaikōura earthquake, and infill material from a paleofissure that was reactivated in 2016 was also radiocarbon dated. A total of 34 ^{14}C samples were collected in the post-earthquake excavations, the results and implications of which are reported in this chapter.

My new synthesis of paleoseismicity for the Kekerengu Fault embraces at least one additional (older) paleoearthquake than was recognised by Little et al. (2018), thus allowing me to calculate a revised estimate of mean RI that is based on the last five surface rupturing events (rather than four). These new results provide important information about the timing and size of surface rupturing earthquakes on the fault—a result that is of direct relevance for seismic hazard evaluation in central New Zealand. In addition, my well constrained, detailed chronology of late Holocene ruptures for the Kekerengu Fault may prove valuable in future studies that aim to understand the seismic behaviour of the MFS as a whole - particularly comparative studies aimed at evaluating the possibility that other multi-fault rupturing earthquakes have involved the Kekerengu Fault prior to 2016, or that triggered earthquakes closely spaced in time as a result of stress interactions between the Kekerengu Fault and nearby structures to the south and north - such as the Hope and Wairarapa Faults respectively (Little et al., 2018).

A necessary first step in any such research is the construction of robust and precise earthquake chronologies for each of the key faults. Understanding how the faults of the MFS may (or may not) interact with one another is important for understanding local and regional seismic hazard, and crucial to understanding the nature and distribution of the Pacific-Australian plate boundary deformation through central New Zealand. The Kekerengu Fault is an important source of seismic hazard both locally and regionally, and that the implications of the tempo and activity on the fault are far-reaching (including the Wellington region).

2.1.1 Background

The active faults of the MFS are located in the northeast section of the South Island of New Zealand, where they have accommodated relative motion between the Pacific and Australian plates for at least the past ~7 Ma (T. Little & Jones, 1998). The MFS consists of a series of NE-striking, dextral/dextral-reverse faults, uplifted on their NW sides, that transfer motion from the Alpine Fault northeast into the upper plate of the Hikurangi Subduction margin. Across the Cook Strait, some of this motion is in part transferred to the NNE-striking dextral slip faults of the North Island Dextral Fault Belt, including the Wellington and Wairarapa Faults (Figure 2.1).

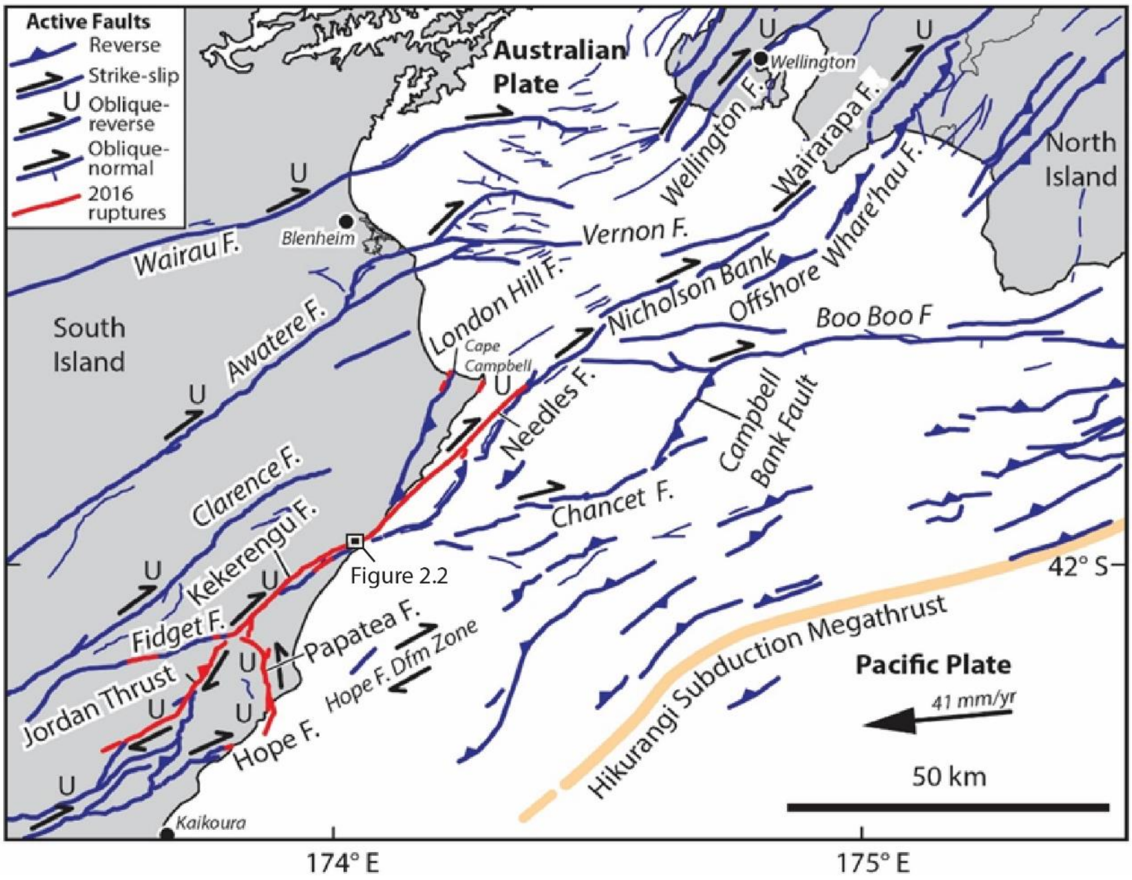

Figure 2.1: *Tectonic map of the Cook Strait, between the North and South Islands of New Zealand (from Little et al., 2018). Fault traces highlighted in red show the northern ruptures of the Kaikōura earthquake in 2016. Faults that did not rupture in the 2016 earthquake are shown in blue.*

The Kekerengu Fault typically strikes 060-070, and dips 60°- 80° NW (Little et al., 2018). At its SW end, it transfers slip northward off the Hope Fault through the intervening Jordan Thrust and adjacent fault splays. The Hope Fault is the most active fault in the MFS and is segmented, with slip rates of up to 23 ± 4 mm/yr (Langridge, Almond, & Duncan, 2013). To its NE end, the Kekerengu Fault continues offshore where it is renamed the Needles Fault, extending north into the Cook Strait.

Approximately 10 months prior to the Kaikōura earthquake, three near-coastal sites were chosen for the excavation of paleoseismic trenches on the Kekerengu Fault near its inferred intersection with the Heaver's Creek Fault to the south (Figure 2.2) - a dextral strike-slip splay of the Kekerengu Fault that also ruptured locally in 2016. These sites are located on a section of the fault that strikes ~5° more easterly than the average strike of the fault (~070) farther to the west. Near the coast, a long-term extensional part of the fault is manifested by a string of small sediment-filled pull-apart basins along the fault trace that are bounded by oblique-normal faults on one or both of their margins (Little et al., 2018). The three trenches were each excavated across linear fault depressions interpreted as transtensional fault furrows. Trench 1 was the farthest to the east and closest to the coast, and was excavated ~100 m to the east of a fault-bounded sag pond, and at right angles to a swampy, 2-3 m deep fault furrow (Figure 2.2). Although the NE wall of the trench collapsed prior to logging, the SW trench wall was scraped, cleaned, gridded, photographed, flagged and logged at a scale of 1:20. Approximately 10 months after it was excavated and backfilled, this trench was dextrally displaced during the Kaikōura earthquake by ~9.1 m (Little et al., 2018).

Differences in vegetative cover as a result of backfilling made the old trench margins easy to re-identify months after the earthquake. Although displacement initially appeared to be a discrete offset along a single linear fault trace, detailed analysis, including the renewed excavations, indicate that the strike-slip deformation was distributed across a rupture zone >1.5 m wide, and that the slip in this zone was in part accommodated by: a) vertical-axis rotation of fault-bounded, elongate blocks of near-surface sediment and soil, and b) by local pervasive shearing of sediment (see Chapter 3). One effect of the distributed rotation and shearing of the near-surface sediment was to cause a mismatch in the stratigraphic thickness, shape, and succession of units on opposite trench walls of the re-excavated trenches, as well as differences in the structure of the pre- vs. post-earthquake trench walls. These mismatches were probably caused by the out-of-plane nature of the distributed strike-slip motion (with respect to the trench walls) and lateral gradients in strain. For example, buckling and folding of the pre-earthquake stratigraphy caused by the transcurrent deformation generated a ~1 m high compressional mound or "moletrack" at the site, the amplitude and geometry of which varied laterally along strike (see Chapter 3).

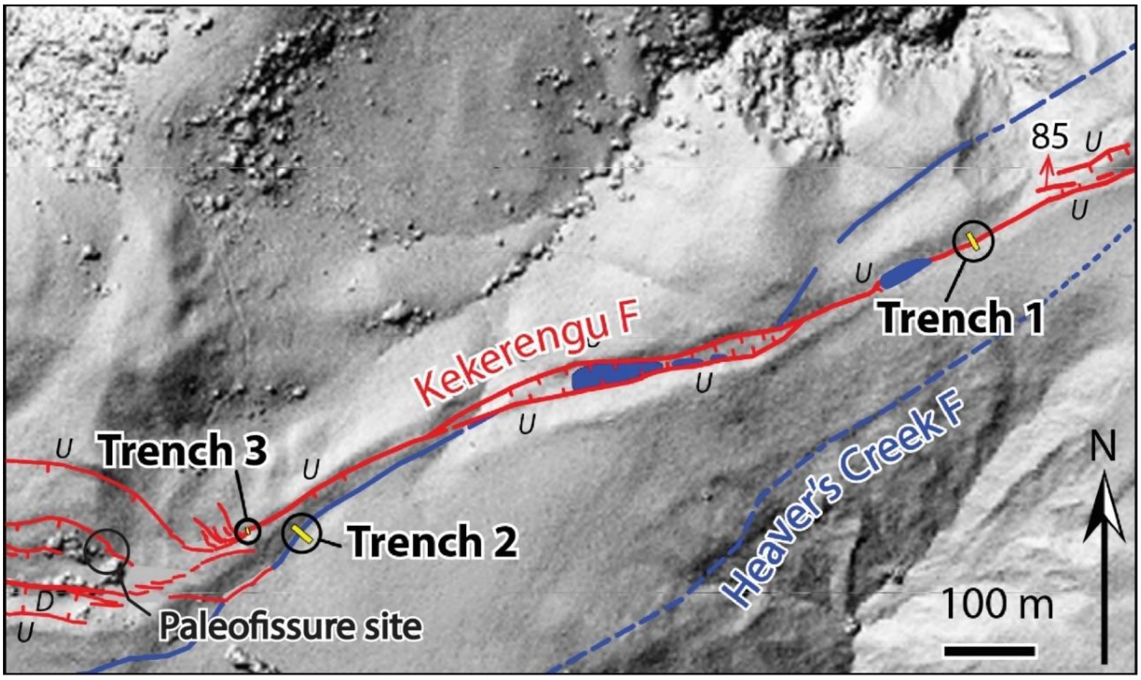

Figure 2.2: *Map of fault traces near the three paleoseismic trenches excavated in 2016 (adapted from Little et al., 2018), and the paleofissure site to the southwest (see also Figure 2.5). Red traces show faults strands that ruptured in the 2016 earthquake, while blue traces show fault strands that did not rupture in 2016. See Figure 2.1 for location. Background shaded DSM derived from analysis of 2014-2015 LINZ aerial imagery, gridded at 1m (Hill & Ashraf, 2017).*

2.1.2 Pre-earthquake stratigraphy and cross-cutting relationships (2016)

2.1.2.1 Trench 1, southwest wall (refer to Figure 2.3)

The fault furrow transected by Trench 1 of Little et al. (2018) contained several lenses of organic-rich sediment that were variably cut by faults (labelled 1-5) or deposited across their upward terminations, and also synclinally deformed (Figure 2.3). These lenses (units uc, lp, mp and up) were deposited in a swamp or pond that developed in the central ~2 m of the furrow and were within a metre of the ground surface. On some of the faults cutting these lenses within the syncline (faults 1-5), gently NE-plunging slickenlines were observed, indicating dextral-normal slip. The cross-cutting relationships observed in this trench allowed three paleoearthquakes to be identified by Little et al. (2018) – E1, E2 and E3. These are discussed in further detail below.

The oldest of these events, E3, caused slip on faults 3 and 4, offsetting the base of the uc unit but not cutting the overlying peat, unit lp (Figure 2.3). From this, it was inferred that samples 5 and 12 predated E3, while samples 3 and 9 post-dated it. This gave a bracketed age of 1716-729 cal. B.P. for E3. The next youngest paleoseismic event, E2, involved slip on fault 5, which displaced the peat unit lp. The overlying peat, unit mp, is not cut by fault 5, and so samples 1 and 2 postdate E2, while samples 3 and 9 pre-date it - bracketing this event between 538-331 cal. B.P. During the youngest paleoseismic event, E1, fault 2 displaced the unit mp; however, the overlying peat unit, up, was not displaced in this event, as it overlaps faults 1 and 2, and so must postdate E1. Although sample 4 from unit up gives an age that is apparently too old for this sequence, E1 can still be recorded as taking place at <273 cal. B.P.

With each paleoearthquake, the dip of the axes of the syncline progressively steepened and the syncline tightened. This is demonstrated by the steeper dip of unit uc (oldest in the basin) in comparison to unit up (youngest in the basin) and shows that each of these stratigraphic units was likely involved in a separate (older) event from the unit overlying them, to cause these differences in dip angle.

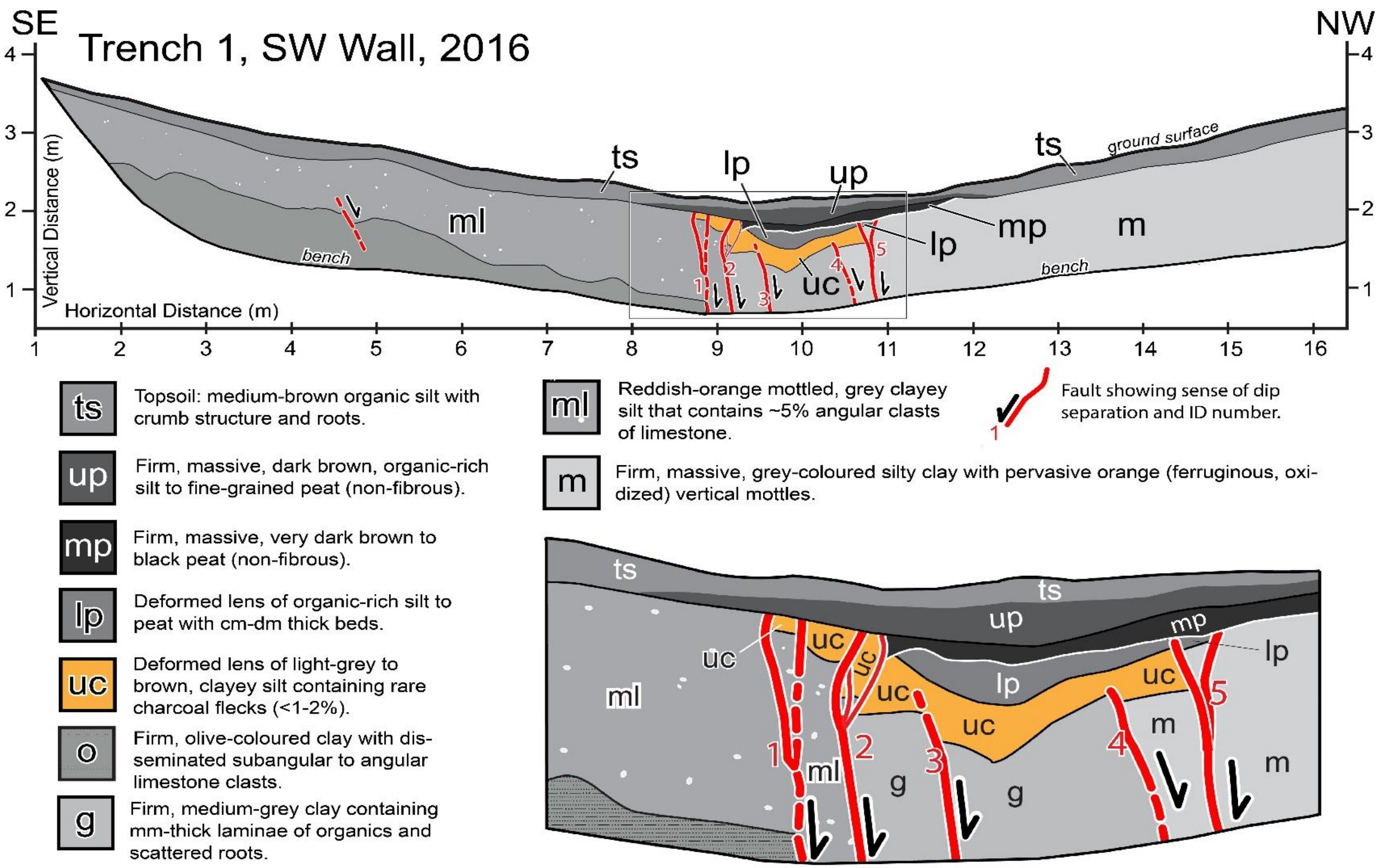

Figure 2.3: Pre-2016 earthquake log of southwest (SW) wall of Trench 1 (adapted from Little et al., 2018), showing numbered faults and basic stratigraphy. Only the upper half of the original trench is shown here (down to the bench) as this is the depth to which the trench was re-excavated in 2018; the northwestern end of the trench is also clipped, as it is not discussed in the current study. ^{14}C age ranges are quoted in cal. B.P. at 95% confidence. For more information on the ^{14}C samples, see Appendix A.2.2. Inset shows an enlarged version of inner rupture zone (see box on the main figure) so that detailed stratigraphic relationships can be more easily identified. No vertical exaggeration.

2.1.2.2 Trench 3, southwest wall (refer to Appendix A.2.1)

Trench 3 from Little et al. (2018) was excavated across an active fault strand that lies approximately 1 km to the SW of Trench 1. Only two paleoearthquakes were documented in this small trench; the older of these (E4) caused the opening of fissures up to 1 m deep and 10 cm wide, after which they were infilled and buried by younger sediments. Charcoal samples were taken from the top part of the largest fissure for radiocarbon dating (Sample T3-04, see Appendix A.2.1) and from the overlying unit that overlaps it (T3-01, see Appendix A.2.1). The ages of these samples were 1726-1605 cal. B.P. and 1270-1093 cal. B.P. respectively. If one interprets the infilling material as younger than the deformational event that opened the fissure, then the age result from Sample T3-04 (1726-1605 cal. B.P.) would indicate that there had been a paleoearthquake prior to the infilling at 1605 cal. B.P. An alternative interpretation is that the infilling material already existed on or just below the ground surface at the time of the fissure opening and was redeposited into that crack sometime after the earthquake. In the latter case, the age of 1726-1605 cal. B.P. would provide a maximum age for the earthquake that opened the fissure. Because of this ambiguity of interpretation, Little et al. (2018) did not include this oldest paleoearthquake in their reconstructed paleoseismic sequence.

2.2 Methods of excavation, sampling and age modelling (2018)

2.2.1 Excavation

The two displaced fragments (T1N, to the north of the fault; and T1S, to the south) of the pre-earthquake trench, T1, were re-excavated (Figure 2.4). The margins could still be recognised based on the difference in vegetation across the trench perimeters – where the trenches had been filled in, the grass had not quite grown back as much as the undisturbed ground. Moreover, Real Time Kinematic Ground Positioning Survey points (RTK GPS) along the margins were recorded both before and immediately after the earthquake. These observations affirmed a dextral slip at the site of 9.0 ± 0.3 m across the <4 m wide fault zone, and a shortening component (heave) of 1.3 ± 0.4 m; while also allowing the walls of the original trench (T1) to be reoccupied exactly. Due to gravitational failure of the NE wall, only the SW wall of the original trench had been logged by Little et al. (2018), whereas in this study both the NE and SW walls of trench fragment T1S were logged, as well as the SW wall of T1N. Although the original trench was ~4 m deep, the re-excavated trench was only to ~1.75 m depth in both trench fragments. This was due to the saturated and unsafe ground conditions at the time of the re-excavation; however, this limitation did not hinder our study because the most correlatable and paleoseismically significant part of the deformed stratigraphy (e.g., deformed lenses of organic sediment) is in the upper metre of the trench.

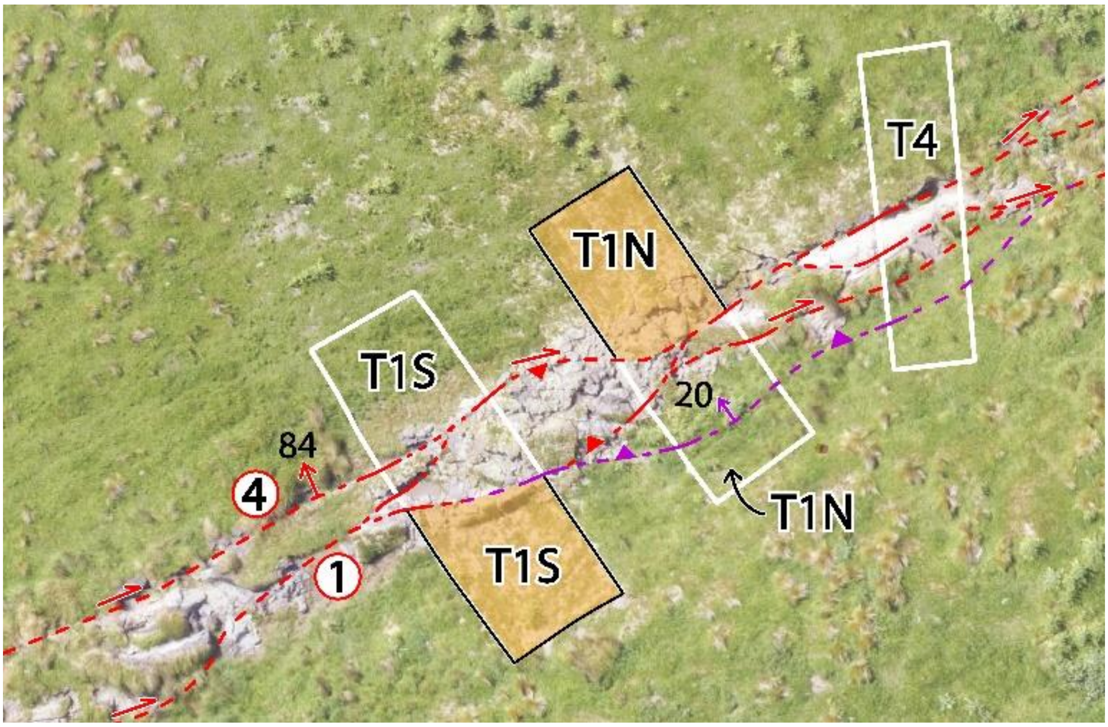

Figure 2.4: *Structural map of the trench site (T1 on Figure 2.2) showing 2018 excavations and fault traces as mapped in the trench logs (solid lines) and extrapolated between trenches (dashed lines); red faults accommodate strike slip motion, purple faults accommodate both strike slip and reverse motion. Triangles on some faults also show reverse motion. Dip direction is shown by fault perpendicular arrows, with dip angles written adjacent. Numbers 1 and 4 in circles next to faults correspond to numbered faults in the trenches. Black lines represent 2016 excavation margins, and orange shading represents the displaced halves of the original trench, labelled T1S (southern half) and T1N (northern half). White lines represent 2018 excavation margins including the new trench (T4). Underlying orthophotography taken by Zekkos et al. (2018) days after the earthquake.*

Trench 3 was not re-excavated, as it was unrecognizable after the earthquake, apparently as a result of pervasive ground deformation. Instead, a new, ~12 m long trench (T4) was excavated ~6 m northeast along the fault trace from trench T1N, at an ~110° angle to the main fault trace (Figure 2.4). This oblique direction is orthogonal to most fissures and/or Riedel faults that cut the rupture zone internally, and was chosen in attempt to section the moletrack in as simple (i.e., nearly 2D) a way as possible. All 2018 trench walls were scraped, cleaned, gridded, flagged, photographed, and logged at a scale of 1:20. Stratigraphic units were described in detail (Appendix B.2.3) using, wherever possible, the previously established stratigraphic nomenclature of Little et al. (2018). Several new units were added where necessary; for example, in the new trench (T4), which does not cut down through the same stratigraphy as T1.

2.2.2 Sampling

During the renewed excavations, 28 organic-bearing samples were collected for potential radiocarbon analysis. The target material consisted of charcoal fragments, wood, or peat. From these 28 samples, I short-listed 15 samples for ^{14}C analysis. Charcoal samples were preferred as they were deemed most likely to provide the most robust and interpretable approximation of the detrital age of the sediments. Samples were given a priority based on their potential to add precision to the pre-existing (pre-earthquake) stratigraphic and paleoseismic chronology; or to extend that chronology further back in time than was documented by Little et al. (2018). Additionally, a continuous vertical transect of 30 samples was taken from organic-rich or peat units expressly for the study of fossil pollen, microcharcoal, and clastic sediment grainsize by Lynda Petherick (work in preparation). After processing (following the method of Van der Kaars (1991), these pollen samples were examined under a microscope to identify and count pollen taxa and microcharcoal. This allowed for the reconstruction of past vegetation, and thus paleoenvironmental variability at the site during the period spanned by the last 4 earthquakes (2016 earthquake, and paleoearthquakes E1-E3). This work is an aspect of a larger study in preparation that will be presented elsewhere.

In addition to the samples taken during the re-excavation, a further three charcoal samples (PF-01, PF-02, PF-03) were taken from a paleofissure located ~1 km to the southwest of the re-excavated trenches (along fault strike). This paleofissure was reactivated and incrementally re-opened during the 2016 earthquake. The sampled material was not modern infill, but older material that infilled a shallower version of the same fissure during a paleoevent (see Figure 2.5). These three samples, as well as the 15 selected samples from new trenches were submitted to the Rafter Radiocarbon Laboratory, Lower Hutt, New Zealand. There, the target organic grains were processed and concentrated by picking, sieving, and chemical pre-treatment. Following processing, the concentrated separates of organic material included charcoal pieces, wood fragments, and undifferentiated plant material, as well as one charcoal rich bulk soil sample (Appendix B.2.4).

Figure 2.5: *Paleofissure that re-opened during the 2016 earthquake, located ~100 m southwest of Trench 1 along fault strike, and ~25 m southwest of Trench 3 along fault strike (see Figure 2.2). Infill of the paleofissure is shaded yellow, whereas the deepened cavity that opened in 2016 is what the geologist is occupying. Three radiocarbon samples were taken from the shaded area of this fissure, which were used to constrain an older paleoearthquake, E5 (see section 2.3.2.4). Photograph taken by Kate Clark, 27th of November 2016.*

2.2.3 Age modelling (see Appendix B.2.7 for OxCal code)

A Bayesian statistical approach was adopted to refine the chronology of the paleoseismic events on the Kekerengu Fault. The original (pre-earthquake) preferred age model from Little et al. (2018) was based on an aggregation of radiocarbon data from Trenches T1 and T3, under the assumption that a correlated event labelled E3 was the same in these two trenches. In the present study, I inserted one new sample (S1-21) from unit ff (Figure 2.7) into the pre-existing age sequence for T1 to refine the age model in that specific trench; in addition, I combined three new ^{14}C ages in the unit uc of T1 (S1-07, S1-20, N1-03) to form a new "phase" within that sequence. Samples plotted in phases are "pooled" – this means that they are not organised in stratigraphic order in the model, rather, they are plotted arbitrarily between two boundaries in a sequence, and therefore provide less information than sequentially ordered samples do. Hence, samples from parts of the uc unit that were not able to be precisely slotted into the previously established age sequence for the uc unit were aggregated into a generic "phase" for this unit.

Additionally, a new sequence ("Sequence Trench 4") was created using the two post-earthquake samples (T4-01, T4-09) from T4. T4 was physically disconnected from the offset fragments of T1, and thus samples collected from it could not be assigned exactly into the paleoseismic sequence for that trench. However, the pt unit could be correlated between them on the basis of its physical similarity to the peat sequence in T1, and the similarity in age between sample T4-09 (904-735 cal. B.P) from unit pt and sample S1-21 from unit ff in T1 (905-745 cal. B.P.). Combining all the pre- and post-earthquake age data together based on an argued set of correlations (see section 2.3.2), I produced a new, updated age model for the paleoearthquake events on the Kekerengu Fault using the program OxCal 4.2.3, following methods outlined in Ramsey (2008) and Lienkaemper and Ramsey (2009). This new model incorporates the new radiocarbon data from the pre-2016 earthquake trenches T1 and T3 as presented in Little et al. (2018), as well as the re-excavated (post-earthquake) offset fragments of T1, including T1S (both the SW and NE walls), T1N (SW wall), and the entirely new trench, T4 (SW wall). This results in a new preferred age model that includes a total of 16 radiocarbon samples.

2.3 Results

2.3.1 Post-earthquake stratigraphy and cross-cutting relationships (2018)

2.3.1.1 Trench 1 (2018)

The re-excavated, extended fragments of the original displaced trench were re-logged to document changes in stratigraphy, cross-cutting relationships, and geological structures. Here I focus only on new information that refines the paleoseismic chronology of the Kekerengu Fault.

TS1, SW wall (refer to Figure 2.6):

To the northwest of fault 4, material has been displaced into this plane of view from (relatively) ~9 m to the southwest. The presence of almost identical stratigraphic units and sequence on this faulted trench wall to those originally logged in 2016 suggests that the "faulted-in" stratigraphy was laterally continuous along strike to the SW, and thus did not change much in the plane of view, despite the large out-of-plane motion during the earthquake. Relative to the pre-earthquake log (Figure 2.3), the stratigraphy in the post-earthquake trench between faults 1 and 4 (Figure 2.6) is slightly altered, presumably because of pervasive strike-slip shearing and/or rotation of sediment blocks into the plane of the trench wall during the earthquake (see Chapter 4 for detailed analysis of changes in stratigraphy). Southeast of fault 1, the exact same wall of T1 from 2016 was exhumed, as evidenced by our recovery of buried nails and string on this trench wall. In the pre-earthquake trench (Figure 2.3), the youngest event (E1) was recognized on the basis of fault 2 cutting the mp unit but terminating beneath the overlying up unit. This relationship could not be observed in the 2018 excavation of this trench wall because both peat units were faulted in the earthquake, and the original stratigraphic relationships were destroyed as a result of slip and shearing on fault strands 1 and 2 (Figure 2.6). Importantly, however, the other key relationships that allowed the recognition and dating of the two older paleoearthquakes (E2 and E3) in the SW wall of T1 prior to the 2016 earthquake (Little et al., 2018) were still preserved even after deformation. In the deformed and dextrally offset southern fragment of that trench wall (TS1), E2 could still be recognized by the angular unconformity between lp (tilted) and mp (nearly horizontal) in the area just to the NW of fault 2 (See Figure 2.6). In the pre-earthquake trench, E3 was recognized by faults 3 and 4 that offset the base of uc unit, but do not cut through it to the upper contact. These relationships were still evident in the 2018 trench (see fault 3 in Figure 2.6).

TS1, northeast wall (refer to Figure 2.7):

During the 2016 earthquake, material to the NW of the major strike-slip fault strand labelled "A" in this trench was translated into the plane of this trench wall from an original location up to ~9 m to the SW of its current one; however, it contains a sequence of units (Figure 2.7) that resembles those logged on the SW wall of the original, pre-earthquake trench (Figure 2.3). This is perhaps not surprising, because prior to the 2016 earthquake this material on the current NE wall of TS1 would have been located only a couple of metres southwest of the wall of T1 that was logged by Little et al. (2018) (Figure 2.3). One new unit on this part of the wall, unit ff, was described during the post-earthquake trenching. This organic clay unit lies between the previously defined units uc and lp. Charcoal fragments from sample S1-21 (within unit ff) were dated at 905-745 cal. B.P., which overlaps in age with the age result from unit lp in Little et al. (2018) (sample T1-3, 800-502 cal. B.P.). I interpret this new unit ff as an older part of the lp unit that was present to the southwest of the original T1 excavation, that has now been displaced into the plane of view of this trench wall as a result of the 2016 earthquake.

The central rupture zone between faults A and B bounds a volume of deformed backfill (unit tbf) from the 2016 excavations. Importantly, it was noted that event E2 of Little et al. (2018) is identifiable on this trench wall, where the fault furthest to the NW offsets the uc unit and the base of lp, but does not cut the overlying mp unit. If any evidence for E1 and E3 were present in the material of this trench wall prior to the 2016 earthquake, that evidence was destroyed during that earthquake as the backfill (tbf) was rotated and sheared through this central rupture zone (between faults A and B).

TN1, southwest wall (refer to Figure 2.8):

Material to the NW of fault 4 on the SW wall of the post-earthquake trench TN1 (Figure 2.8) is equivalent to that logged to the NW of that fault in the pre-earthquake trench, T1 (Figure 2.3). The upwardly bifurcating trio of faults labelled "fault 4" in Figure 2.8 was the major locus of dextral displacement during the 2016 earthquake, and this zone encloses a volume of T1 backfill (unit tbf) that was pervasively sheared during the earthquake. Between faults 1 and 4, units o and ml have been tilted NW and uplifted along fault 1. The overturned topsoil (unit ts) on this upthrust wedge has overridden to the SE across the same material in the footwall, thus partially burying the pre-2016 ground surface. Evidences for E2 and E3 are still preserved on this wall after the 2016 earthquake. This includes greater tilting of lp than mp (E2), and greater tilting of uc than lp (E3), as expressed by the two angular unconformities logged on this trench wall.

2.3.1.2 Trench 4, SW wall (refer to Figure 2.9, also Appendix B.2.5):

This trench does not re-occupy any part of the pre-earthquake T1, but was excavated into new material 5-6 m to the NE of T1 in 2018. Most stratigraphic units exposed in T4 cannot be correlated with those in T1.

Thin, deep cracks are exposed in the central rupture zone of this trench (shown in the inset, Figure 2.9), which I interpret to be fissures – similar to the style of those from Trench 3 in Little et al. (2018). The inferred fissure furthest to the NW along the trench wall (label g, Figure 2.9) contains a newly defined unit of blocky peat (unit ffb), which is overlain by a peat layer (unit pt). These same units are observed in another fissure on the SE side of the central rupture zone (label e, Figure 2.9. I interpret that this fissure (label e) contains infill material from at least two paleoearthquakes; first, unit ffb filled in the fissure during or after a paleoearthquake. It was subsequently overlapped by the deposition of a silty clay, unit cff, which was not necessarily tectonically deposited. A second potential paleoearthquake occurred, in which unit pt was deposited (either during or after the earthquake) into both fissures either side of the central rupture zone in Figure 2.9. To date these two potential paleoearthquakes, two charcoal infill samples (T4-01, T4-09, see inset on Figure 2.9) were taken from units ffb and pt for radiocarbon dating.

Evidence of the 2016 earthquake is also clear on this trench wall. A large fault is observed on the SE side of the trench (label a, Figure 2.9) which thrusts up the modern topsoil (unit ts) to form a moletrack at the surface (see Appendix B.2.5 for photograph). Additionally, the spoil from the 2016 excavations (unit psp) and the modern, previously undeformed topsoil (ts) can be seen faulted into the older stratigraphy (units pt and ml) in several places (see labels b, c, d, and f on Figure 2.9).

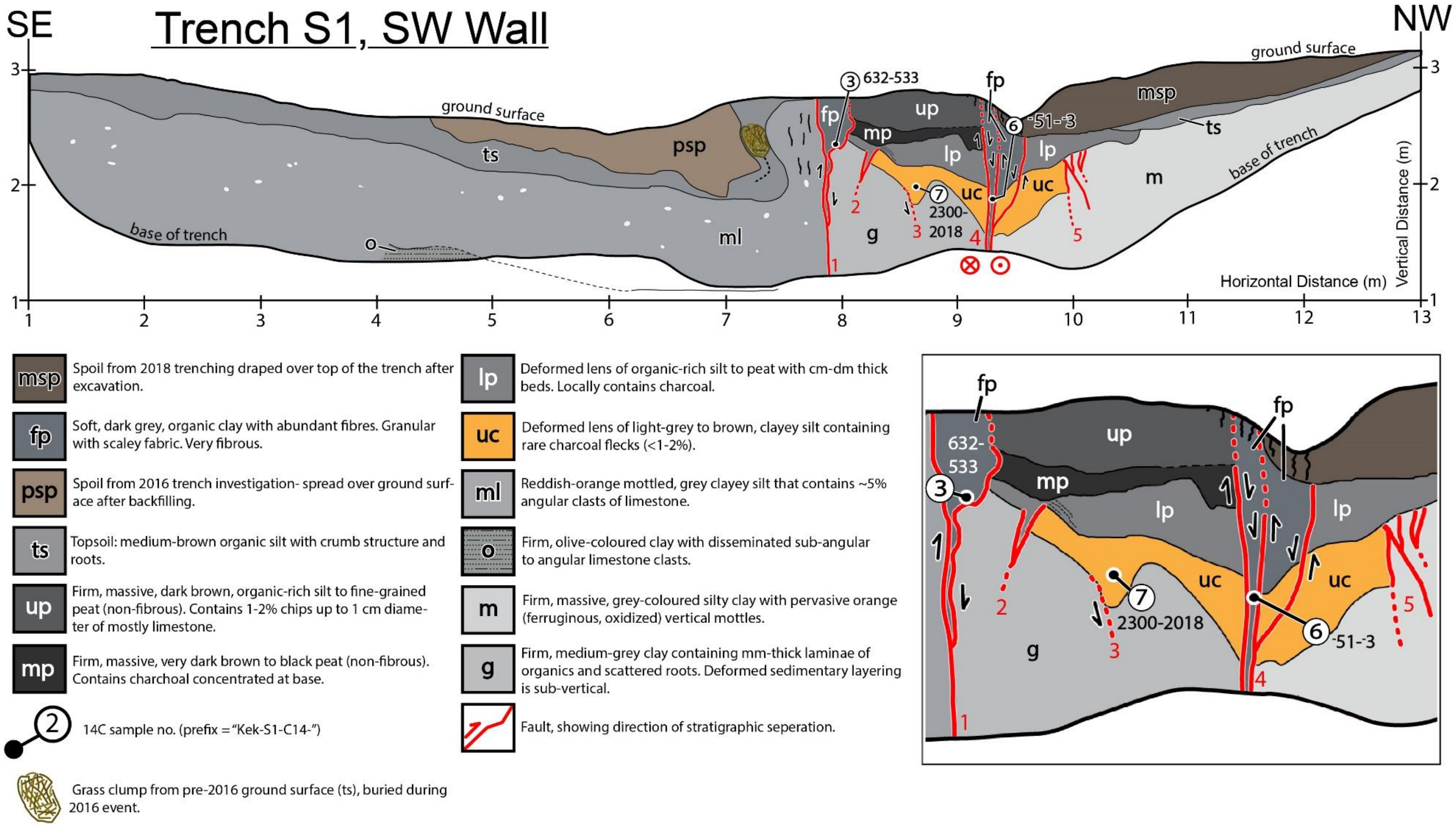

Figure 2.6: *Log of the re-excavated (post-2016 earthquake) southwest (SW) wall of Trench 1, fragment S1, showing numbered faults and basic stratigraphy. ^{14}C age ranges are quoted in cal. B.P. at 95% confidence (negative ages are given where samples were younger than 1950 AD). For more information on the ^{14}C samples, see Appendix B.2.4. Inset shows enlarged version of the inner rupture zone to enhance observation of the key stratigraphic relationships. No vertical exaggeration.*

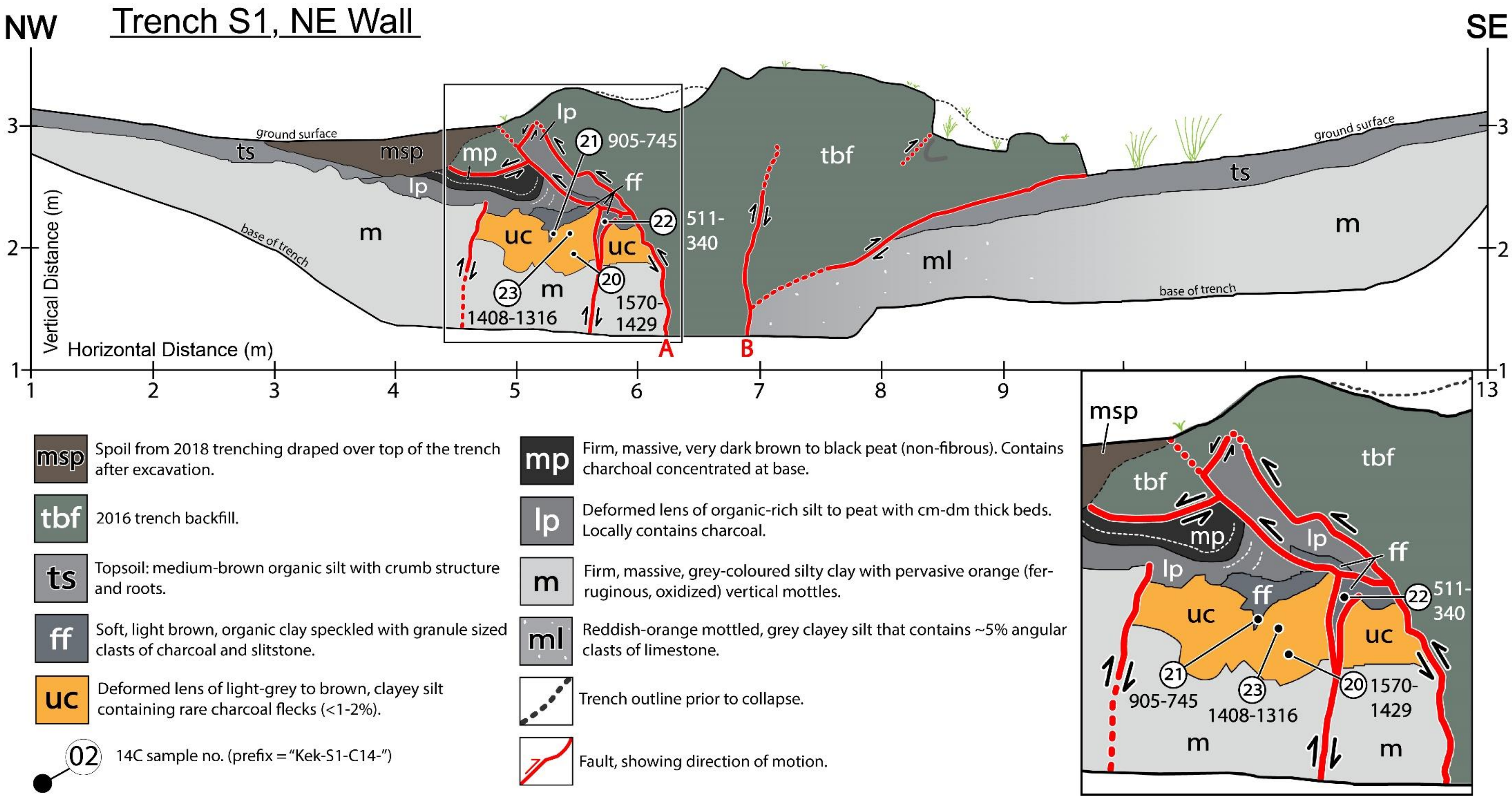

msp	Spoil from 2018 trenching draped over top of the trench after excavation.
tbf	2016 trench backfill.
ts	Topsoil: medium-brown organic silt with crumb structure and roots.
ff	Soft, light brown, organic clay speckled with granule sized clasts of charcoal and slitstone.
uc	Deformed lens of light-grey to brown, clayey silt containing rare charcoal flecks (<1-2%).
02	14C sample no. (prefix = "Kek-S1-C14-")
mp	Firm, massive, very dark brown to black peat (non-fibrous). Contains charchoal concentrated at base.
lp	Deformed lens of organic-rich silt to peat with cm-dm thick beds. Locally contains charcoal.
m	Firm, massive, grey-coloured silty clay with pervasive orange (ferruginous, oxidized) vertical mottles.
ml	Reddish-orange mottled, grey clayey silt that contains ~5% angular clasts of limestone.
	Trench outline prior to collapse.
	Fault, showing direction of motion.

Figure 2.7: *Post-earthquake log of northeast (NE) wall of Trench S1. Main faults are labelled A and B. ^{14}C age ranges are quoted in cal. B.P. at 95% confidence. For more information on the ^{14}C samples, see Appendix B.2.4. Inset shows enlarged version of the material that is correlated to the pre-earthquake trench (T1), to enhance observation of the key stratigraphic relationships. No vertical exaggeration.*

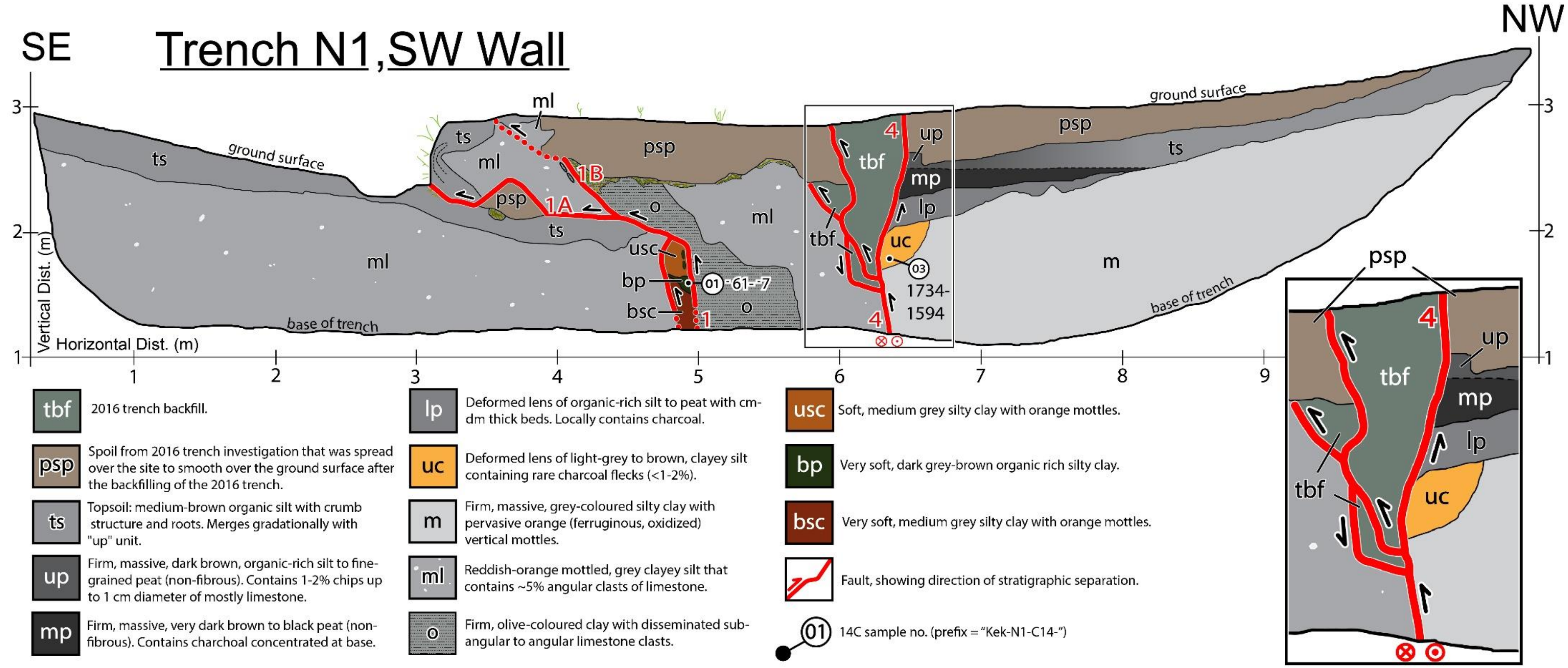

Figure 2.8: *Log of the re-excavated (post-earthquake) southwest (SW) wall of Trench 1, fragment N1, showing numbered faults (1 and 4, correlated to original trench from 2016) and basic stratigraphy. ^{14}C age ranges are quoted in cal. B.P. at 95% confidence (negative ages are given where samples were younger than 1950 AD). For more information on the ^{14}C samples, see Appendix B.2.4. Inset shows the enlarged version of the tail end of the trench backfill from the 2016 excavation (unit tbf), displaced into plane from the SW. No vertical exaggeration.*

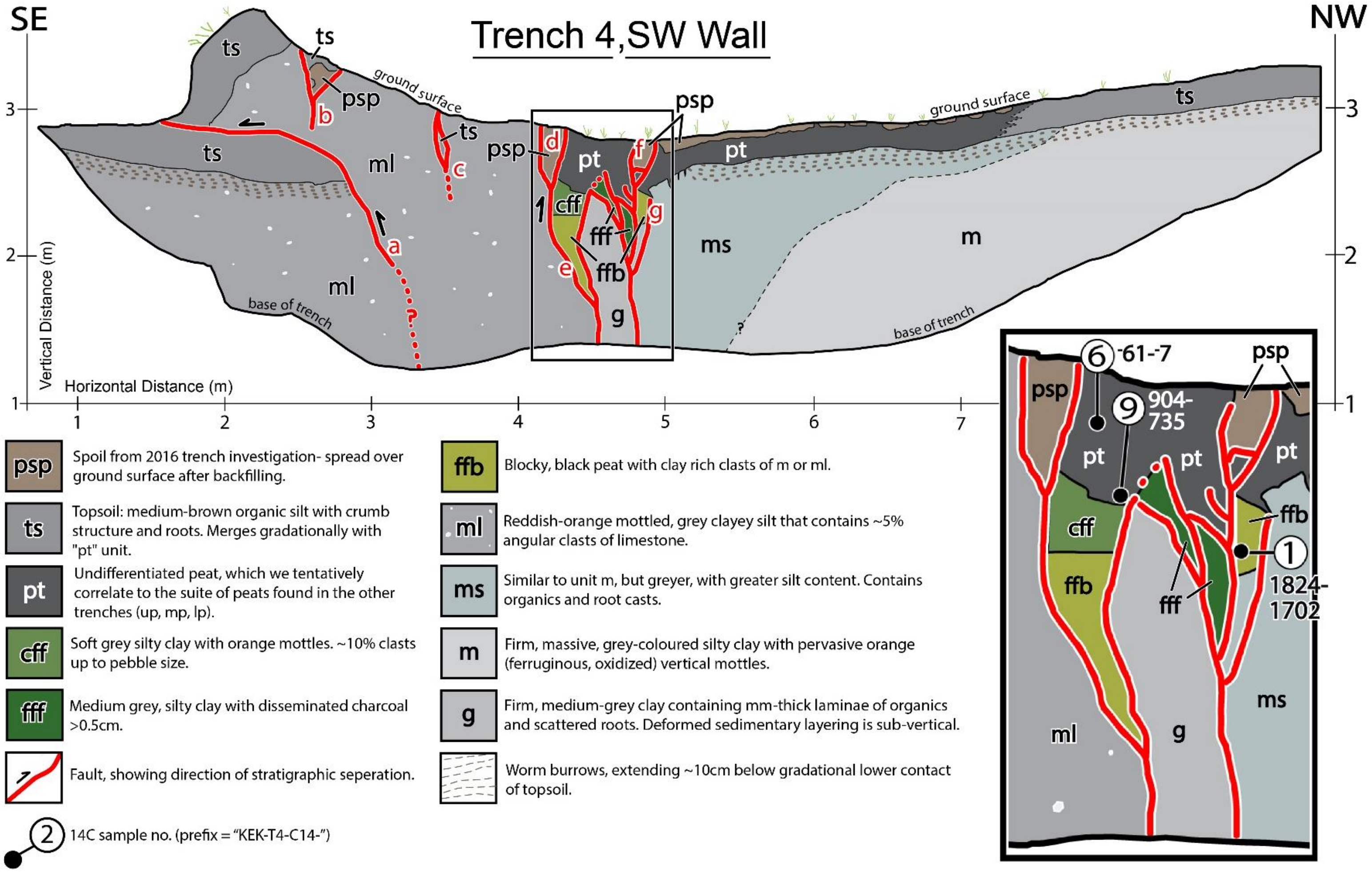

Figure 2.9: *Log of southwest (SW) wall of Trench 4, showing faults (labelled a-g) and basic stratigraphy. Inset shows enlarged version of the central rupture zone in the trench, and the location of the ^{14}C samples, quoted in cal. B.P. at 95% confidence (negative ages are given where samples were younger than 1950 AD). For more information on the ^{14}C samples, see Appendix B.2.4. No vertical exaggeration.*

2.3.2 Age Modelling and Chronology (2018)

2.3.2.1 Samples from the 2018 excavations that were included in the new, preferred age model

Of the 18 samples that were submitted for radiocarbon analysis in this study, only six were incorporated into the revised (preferred) age model (Appendix B.2.4). Sample S1-21 from unit ff (an older part of unit lp) in TS1 was inserted into the pre-existing stratigraphic sequence, as it provides an older minimum age for E3 (905-745 cal. B.P.) than previously established by Little et al. (2018).

In some cases, the stratigraphic ordering between some of the other new samples relative to those incorporated into the original age model of Little et al. (2018) was uncertain, due to changes in shape and thickness of units as a result of out-of-plane motion during the 2016 earthquake (although the unit designation of the sample was clear). Accordingly, these samples were entered into the new age model as a "phase" for that unit rather than as ordered samples in a sequence through that unit (see Appendix B.2.6 and B.2.7). This includes samples S1-07, S1-20, and N1-03 from the unit uc, which predate E3 (Figures 2.6, 2.7, and 2.8). In my new preferred age model, these pooled ages are assigned to a 'virtual trench' (Trench 5), in which the samples are plotted as a phase in OxCal (as explained in section 2.2.3 of this thesis). This allows these ages to provide further constraints regarding the maximum age for E3, but weights them such that they are less impactful in the final statistical analysis than the samples that were originally mapped in an ordered sequence on the T1 walls prior to the earthquake.

Samples T4-1 and T4-9 (T4, Figure 2.9) pre-date and post-date a paleoearthquake that could not be correlated with the others defined in T1. The age of sample T4-9 (904-735 cal. B.P.) from unit pt (Figure 2.9) is almost identical to the age of sample S1-21 from unit ff in TS1 (905-745 cal. B.P., Figure 2.7), the latter of which provides a minimum age for E3 (as stated above). This suggests that the earthquake that faults unit pt in Trench 4 is the same event as E3 in Trench 1, and so I correlate these in my new age model. Furthermore, the age of sample T4-1 from the fissure infill unit ffb (1824-1702 cal. B.P., Figure 2.9) overlaps in age with that of the fissure infill in Trench 3 (T3-4, 1726-1605 cal. B.P., see Appendix A.2.1). As these samples of overlapping age both fill deep fissures (although in different trenches), I attribute them to a common paleoearthquake that is older than E3. I call this paleoearthquake E4.

2.3.2.2 Samples from the 2018 excavations that were omitted from the new, preferred age model

The other nine samples that were submitted for radiocarbon dating were not included in my new age model for several reasons. The ml unit outside of the fault zone was interpreted as stratigraphically older than unit uc, and so was sampled to potentially provide a maximum age for an event that predates E3 (assuming that it was faulted separately from unit uc), i.e., E4. However, these samples (N1-02, Figure 2.8, T4-07 and T4-08, Figure 2.9) each provided older maximum ages for E4 than samples T3-4 and T4-01 (see section 2.3.2.1, Appendix B.2.4 for ages), and were therefore omitted from the preferred age model as they do not further constrain the age of that paleoearthquake.

Sample S1-22 from unit ff (511-340 cal. B.P., Figure 2.7) was omitted from the age model as it is completely fault bounded and has an unknown stratigraphic relationship to the other samples. Sample S1-23 from unit uc (1408-1316 cal. B.P., Figure 2.7) was a bulk, charcoal rich soil sample, which was submitted to potentially provide a younger maximum age for E3. The age yielded was significantly younger than the other uc sample ages (see Figures 2.3, 2.6, 2.7, 2.8, Appendix A.2.2 and B.2.4), leading me to infer that the charcoal flecks in this soil sample may have been incorporated into the soil after it was deposited, providing a false (younger) maximum age for the associated event (E3).

As the pre-earthquake appearance of T1 is known (Figure 2.3), sampling the structures created in the 2016 earthquake would potentially provide an accuracy test for the resulting radiocarbon ages when compared to the known age of the earthquake (November 2016). For this reason, two samples S1-03 and S1-06 (Figure 2.6) were submitted for radiocarbon dating; however, neither were anticipated to be included in the new age model, as the event age for the 2016 earthquake is known exactly. Sample S1-03 (632-533 cal. B.P., Figure 2.6) was from a fault wedge, and provided an older age than the 2016 earthquake, likely because the material displaced into the wedge was from an adjacent peat (most likely unit lp based on the age). Sample S1-06 (Figure 2.6) yielded a modern radiocarbon age, as did samples N1-01 (Figure 2.8) and T4-6 (Figure 2.9), and hence, these were omitted from the preferred age model.

2.3.2.3 Preferred age model

My new preferred age model for the timing of paleoseismic events on the Kekerengu Fault is based on a total of 16 samples: 10 pre-earthquake samples from Little et al.

(2018), and 6 new samples (from this study). Based on my recognition of E4, this new model embraces four paleoearthquakes rather than three (Figure 2.10). These paleoearthquakes are dated at: 249-108 (E1), 528-356 (E2), 1247-930 (E3), and 1666-1205 cal. B.P. (E4) (Figure 2.10d). In comparison to the previous age model in Little et al. (2018), the minimum age constraint for E3 has been made more precise, by ~30 yrs. Little et al. (2018) also speculated about the age of E4, but did not model this event due the ambiguity in interpreting fissure infill samples as maximum or minimum ages.

Following the 2016 earthquake, field observations showed that most of the fissures that opened up during this earthquake were largely infilled in less than two years, and that the material filling them in was topsoil and colluvium that had already existed on, or just below, the ground surface prior to earthquake. If dated, the age of this redeposited material would be older than 2016 (or perhaps statistically indistinguishable in age from it), and thus would provide a maximum age constraint for the earthquake. More generally, we infer that the ^{14}C ages of fissure-infilling material, including in paleofissures, do not provide minimum age constraints for fissure-opening earthquakes, but maximum ones. This is because the infill consists chiefly of recycled material that has toppled downward into the crack, rather than juvenile organic material that was deposited after the earthquake. Once the fissure is filled in, any younger layers draped over the fissure will potentially provide minimum age constraints for the fissure-opening earthquake. Thus, we are now able to date E4 (first recognized by Little et al. (2018) in T3, using fault fissures, see section 2.12) using a combination of fissure infill samples from Trench 3 (old, re-interpreted, T3-4 as a maximum age, T3-1 as a minimum age, see Appendix A.2.1) and T4 (new samples, T4-01 as a maximum age, T4-09 as a minimum age; refer to Figure 2.9).

This new preferred age model includes these four paleoearthquakes as well as the 2016 earthquake and calculates a revised mean recurrence interval (RI) for the Kekerengu Fault of 375 ± 32 yrs (1σ) (Figure 2.10e), which is almost identical to the RI indicated in Little et al. (2018). This concordance reflects stratigraphic consistency in the 16 total ^{14}C samples (six of them new) that are brought together in this updated model.

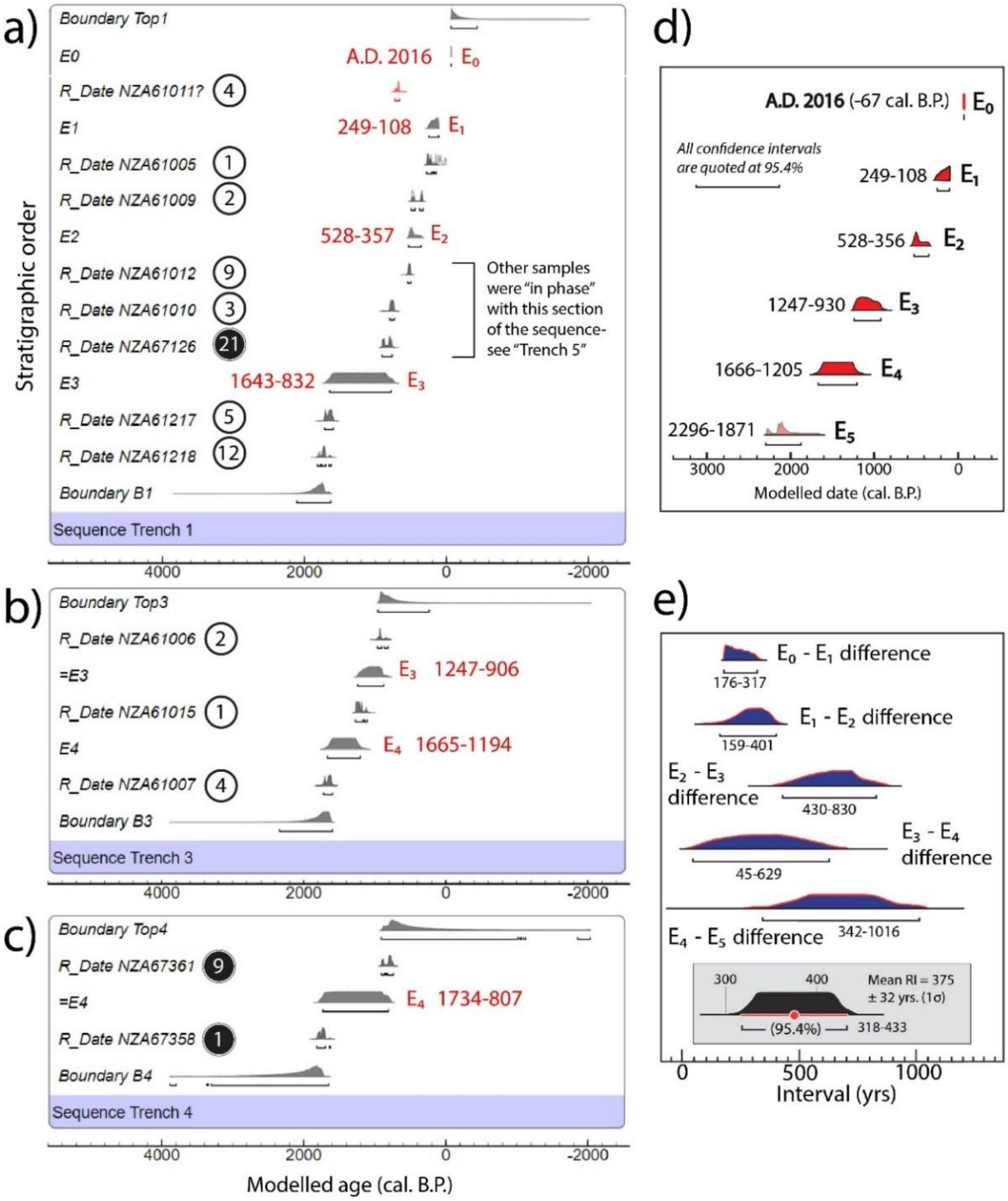

Figure 2.10: *Age modelling results: a), b), and c) show the sequences for Trench 1, T3 and T4 respectively (adapted from Little et al. (2018) to include both pre-earthquake and post-earthquake data), showing samples in stratigraphic order, with youngest at the top. Events are labelled in each trench sequence with age ranges based on samples from individual trenches only, rather than a correlation between trenches. Numbers in white circles are samples that correspond to the pre-earthquake (2016) excavations, while those in black circles are samples added from the post-earthquake (2018) excavations. d) Modelled probability density functions for each paleoevent, including E5 (not necessarily in sequence with E4). e) Modelled probability density functions for the intervals between paleoevents, and the re-calculated mean recurrence interval (RI) for the fault, with the associated probablitity density function.*

2.3.2.4 Alternative, expanded age model

The three charcoal samples that were taken from a paleofissure ~1 km to the SW (along fault strike, Figures 2.2 and 2.5) of T1 were remarkably similar in age to one another at 2300-2148 cal. B.P., 2296-2096 cal. B.P., and 2295-2094 cal. B.P. respectively (Appendix B.2.4). As argued in section 2.3.2.3, these provide maximum age constraints for the opening of the paleofissure. The concordance of these ages suggest that they were derived from a common source, presumably the pre-earthquake topsoil at the time; if so, they may approximate the age of the fissure-forming paleoearthquake (Figure 2.10d). This event (2296-1871 cal. B.P.) is not necessarily in immediate sequence with any of the paleoearthquakes describe in the trenches to the east; however, because it is older than E4, I call this event "E5", with the acknowledgement that there may be one or more unrecognized (and unnamed) events intervening between E4 and E5. By adding these three ^{14}C ages to my previously described age model as another "virtual" trench, I derive an expanded, alternative model that uses 19 total radiocarbon samples. This model embraces (a minimum of) six ruptures of the Kekerengu Fault (including the 2016 earthquake) and nominally produces a mean (maximum) RI of 433 ± 22 yrs (1σ).

2.4 Discussion

2.4.1 Comparison of the paleoseismic record of the Kekerengu Fault to paleoseismic data for other faults in the Marlborough Fault System (MFS)

The updated paleoseismic chronology presented in this study constrains the timing of that last 5 to 6 earthquakes on the Kekerengu Fault - one of the fastest slipping faults in the New Zealand plate boundary zone. Underpinned by 19 radiocarbon samples in three trenches in a small area (one of them re-excavated and enlarged), this unusually robust earthquake chronology for the eastern Kekerengu Fault makes it one of the best constrained late Holocene paleoseismic records for an active fault in the Marlborough Fault System.

The main source of slip onto the Kekerengu Fault comes from the Hope Fault to the southwest, through the Jordan Thrust system and allied strands, such as the Kowhai Fault (Figure 2.1) (Khajavi et al., 2016; Langridge et al., 2013; Langridge et al., 2003; Van Dissen & Yeats, 1991). The Hope Fault is fastest slipping fault of the four primary faults in the MFS, at 23 ± 4 mm/yr (Langridge et al., 2013), taking up most of the slip from the Alpine Fault. A compilation of paleoseismic data for the faults in the MFS has recently been presented by Hatem et al. (2019), including data from Khajavi et al. (2016) and Langridge et al. (2013) for the Hurunui section of the Hope Fault, and Langridge et al. (2003) and Hatem et al. (2019) for the Conway section of the Hope Fault; Howarth et al. (2018) and Wells et al. (1999) were used for the Alpine Fault. The compilation also includes data for the timing of earthquakes on the Kekerengu Fault from Little et al. (2018), and for the Wairarapa Fault in the North Island of New Zealand (Little et al., 2009). For Figure 2.11, I have modified this compilation by adding the revised earthquake chronology data for the Kekerengu Fault presented in this chapter; in particular, for its oldest-recognized events, E4 and E5.

The pink horizontal boxes on Figure 2.11 represent potential cases of past clustered events (<100 yr interval) or perhaps multi-fault ruptures. These are time periods in which most (or all) of the major faults in the MFS experienced surface ruptures of a similar (statistically overlapping) age. The last four paleoearthquakes on the Kekerengu Fault (E1-E4) overlap with others on the Hope and Alpine Faults, suggesting that the Kekerengu Fault may often rupture synchronously (or in close sequence) with other nearby faults (Figure 2.11). The Kekerengu Fault does not appear to have ruptured in an isolated earthquake in the last ~2000 years; however, the uncertainties in both my data as well as data from the rest of the faults (Hatem et al., 2019) shown make it difficult to rule this out, especially because all three of these faults have short RIs of ~300-500 yrs, which makes robust differentiation of individual events difficult. The oldest event that I document for the Kekerengu Fault (paleofissure opening, E5; labelled KE5 in Figure 2.11) is older than events documented on the other faults (as of writing, 2020).

In addition to the Hope Fault, the Papatea Fault also transfers slip onto the Kekerengu Fault at its southern end (Figure 2.1). This fault slips sinistrally, with a component of reverse slip, forming a block that is uplifted between the Hope Fault and the Jordan Thrust (R. M. Langridge et al., 2018). The Papatea Fault was not recognized as an active fault prior to the Kaikōura earthquake of 2016, but since the earthquake, much work has been undertaken to understand how it contributes to the system of faults surrounding it. This work includes trenching the fault to gain an understanding of its paleoseismology and whether the tempo is similar to that of either the Hope Fault, the Jordan Thrust, or the Kekerengu Fault (or all of the above). This work is still in progress, but preliminary results (Langridge et al., 2020) suggest that the timing of some late

Holocene paleoevents on the Papatea Fault may overlap with those that I have established for the Kekerengu Fault.

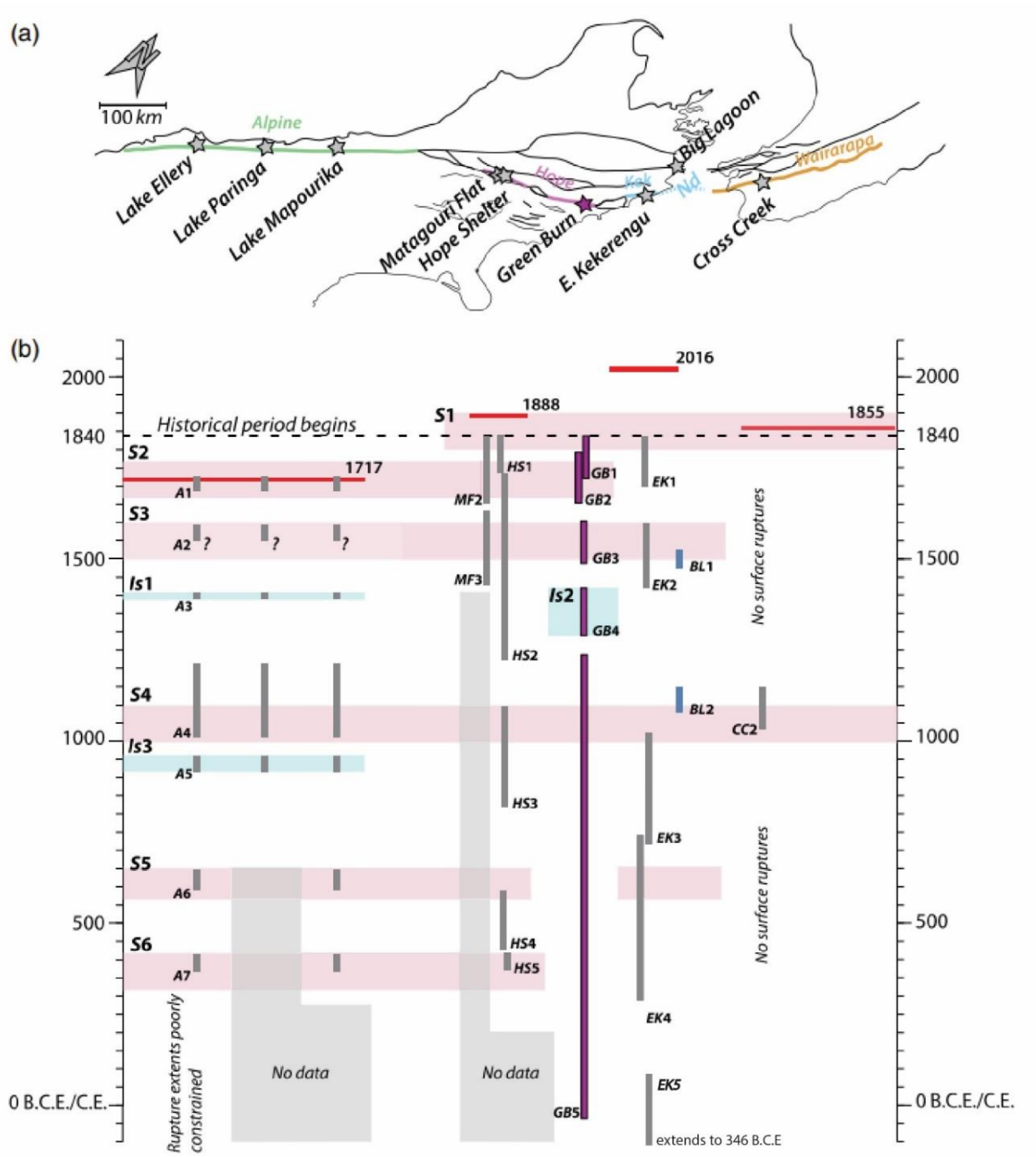

Figure 2.11: Compilation of the paleoseismiological data from the MFS as of 2019- adapted from Hatem et al. (2019); a) faults and individual paleoseismic sites on these faults are labelled; b) Grey vertical bars show the temporal range of individual events (2σ age range), and labels correspond to sites in a). Updated data (from this study) as been added for the two oldest recognized events on the Kekerengu Fault (EK4 and EK5). Pink horizontal bars show possible correlations (made by Hatem et al., 2019) between earthquakes at different sites and on different faults; and, in particular, identifying potential cases of multi-fault rupture. Blue horizontal bars represent isolated events.

2.4.2 Implications for future paleoseismic studies

An informative lesson for future paleoseismic studies is derived from our opportunity to re-excavate a paleoseismic trench that was previously documented, prior to a large strike-slip earthquake. This earthquake dextrally displaced this original trench by ~9 m. The post-earthquake, 2018 trench logs (Figures 2.6-2.8) show that following a large surface rupture, subtle stratigraphic relationships that indicate paleoearthquakes (angular unconformities, upward fault truncations, infilled fissures) may remain in the stratigraphic record despite the large slip and deformation associated with the last rupture. Thus in the exhumed trenches (TN1, TS1) and in a newly excavated trench nearby (T4), key stratigraphic relationships that had been observed before the earthquake were re-observed, and in some cases, further evidence corroborating (and in some cases, refining) the recognition of the originally defined events E2, E3, and E4 was found. An exception is the evidence for E1 (the mp unit being faulted, the up unit overlapping the fault and not being displaced, see Figure 2.3), which was observed along fault strand 2 at shallow depth (<15 cm) in the original study. In 2016, that strand (fault 2) broke again, accommodating only a small amount of slip, but enough to disrupt this stratigraphic relationship; a small thickness of unit lp now overlies fault 2, such that this fault no longer cuts unit mp (see Figure 2.6). Rupture on fault 1 also truncated units lp and mp (Figure 2.6), eliminating the possibility of evidence for E1 being observed southeast of fault 2.

In addition to these subtle changes, the large increment of out-of-plane fault slip and related soil and sediment deformation that was introduced during the 2016 earthquake overprinted and/or disrupted some stratigraphic relationships more clearly, and on a much larger scale. An example of this is the SW wall of TN1 (Figure 2.8). All the faults on this trench wall slipped in 2016, yet, without prior documentation of this trench, some of these faults might have been interpreted as cross-cutting one another (e.g., fault 1B cutting fault 1A). However, much of the structural complexity in this log (i.e., bulge emplaced along a low-angle contractional fault over a pre-existing, steeply dipping fault fissure) may have been established sequentially — and coseismically — over a period of just a few seconds. Sample N1-01 from this trench wall (Figure 2.8) yielded a modern radiocarbon age, which leads me to infer that this fault ruptured in at least two stages; first, a small fissure opened up at the ground surface and was filled in by material that was already lying on the ground surface (units bsc, bp and usc). Shortly afterward, this fissure was overridden by a fault that displaced units o, ml and psp overtop of the fissure and sealed it (further explained in Chapter 4). This demonstrates that large rupture events may not be easy to recognize and/or interpret in trenches, and could lead to misinterpretation of and/or contradictions within paleoseismic data and sequences.

Another interesting observation that arose from these new excavations is the apparent range in event age for the 2016 earthquake as inferred from radiocarbon samples collected in the post-earthquake trenches. In TS1 (Figure 2.6), two structures that formed in the 2016 earthquake were sampled on opposite sides of the central fault zone (between faults 1 and 4). Sample S1-06 (unit fp, fault 4, Figure 2.6) was modern in age, which could be expected given that the fissure formed and infilled in 2016. Sample S1-03 (unit fp, Figure 2.6) dated at 632-533 B.P; this structure is a fault wedge, meaning that the material (and charcoal) within it was sliced into plane from the southwest (likely from the lp unit). This sample therefore gives a false (much older) maximum age for the 2016 event than Sample S1-06, which if modelled would result in a much less accurate recurrence interval for the fault. In future trenching studies, distinguishing structures as either fissures or fault wedges should be carefully considered by paleoseismologists to avoid this potential uncertainty in modelled dates. Although these situations cannot necessarily be resolved without prior knowledge (as we have in this case), the style of fissuring may give some clues as to the source of the infill material; for example, wedge shaped fissures (like the fissure containing Sample S1-03) are more likely to be contaminated with material from adjacent units (or out-of-plane material) than thin, deep fissures (see fault 4 on Figure 2.6, fault e and g on Figure 2.9, T3 fissures in Appendix A.2.1).

2.6 Conclusion

Following the 2016 earthquake, the re-excavation and enlargement of a displaced paleoseismic trench and digging of a new trench nearby provided an opportunity to test and refine the paleoseismic sequence for the Kekerengu Fault. Radiocarbon samples taken from the walls of these trenches reinforced and refined the original chronology of Little et al. (2018). Including the 2016 earthquake, I now recognize and provide age constraints on six surface ruptures, two more than was reported by the previous authors based on their original excavations prior to the 2016 earthquake. This is based on OxCal modelling of a total of 16 radiocarbon samples collected in four trenches in a small area near the eastern end of the Kekerengu Fault. Based on the last five events (E0 to E4), the new analysis yields an updated estimate for the mean recurrence interval for the fault of 375 ± 32 yrs (1σ) since ~1650 cal. B.P.

Samples of charcoal infilling a deep paleofissure that reopened again in 2016 along an oblique-normal fault in a pull-apart graben provided information about a fifth and older event on the fault; this oldest dated event (E5) may not have immediately preceded E4, but is incorporated into the alternative model for earthquakes on the fault based on an assumption that all events up to the time of E5 have been recognised. This alternative age model yields a mean recurrence interval estimate of 433 ± 22 yrs (1σ). In reality, this represents a maximum estimate of the mean RI because there may be missed events between E4 and E5.

In addition to this refined chronology, the re-excavation of this paleoseismic trench also showed that earthquakes with a large displacement may create complicated structures in the sub-surface geology that pose challenges for a paleoseismologist's interpretation of the event history and paleoseismic record of future trench walls.

3. Chapter Three: Formation and evolution of moletrack structures during a M_w 7.8 strike-slip earthquake

3.1 Introduction

The rupture zones of strike-slip earthquakes typically host a variety of geological structures as they accommodate coseismic slip, including Riedel faults (Figure 3.1), pull-apart structures, and push-up structures (moletracks) (Deng, Wu, Zhang, & Chen, 1986). These structures are often short lived, as either erosional or depositional processes restore the landscape over time (e.g., push-up structures are eroded, fissures and pull-apart structures are filled in). The rupture of the Kekerengu Fault during the 2016 M_w 7.8 Kaikōura earthquake in New Zealand was marked by a welt of deformed ground that contained a variety of fractures, fissures and push-up structures with differing attitudes and kinematics that collectively accommodated ~9 m of slip. These push-up structures are often referred to as “moletracks”, loosely defined as mounds of turf that have been ‘bulged up’ during an earthquake, forming a line of jumbled material along the ground.

In this chapter, I provide a working definition of “moletracks” such that I can describe the push-up structures that formed during the earthquake and evaluate how they accommodated slip in different sections along the Kekerengu Fault. Extensive aerial orthophotography and Digital Surface Models (DSMs) created from this orthophotography after the earthquake allow me to study these structures in detail, both qualitatively (distribution of different types of structures and their map patterns) and quantitatively (fracture density and strikes, changes in ground elevation, shapes and widths of deformed ground), and compare these observations to previous field studies that have described similar structures following strike-slip earthquakes. In this chapter, I use these datasets to evaluate how the moletracks and other structures in the rupture zone evolved during the earthquake. I then describe and compare rupture zone structures along segments of the dominantly strike-slip Kekerengu Fault that slipped with slightly different kinematics, either purely transcurrent, slightly convergent, or slightly extensional - and interpret how these structures evolved with increasing slip. To further investigate the processes identified from regional-scale data, two key study sites were selected for a more detailed structural analysis.

The first site was a section of the Kekerengu Fault near its intersection with the east coast of the South Island. This section includes a paleoseismic trench that was displaced ~9.1 m during the earthquake, for which I have pre- and post-earthquake datasets including aerial photography, Digital Surface Models (DSMs), Real Time Kinematics (RTK) surveys and sub-surface stratigraphic records from the logs of this trench (see Chapter 4 for detailed comparison of these datasets). At this location, the Kekerengu Fault was slightly transpressive during the 2016 earthquake and slipped dextrally by 8-9 m. I call this section of the fault the “Napoleon segment” (Figure 3.2a). Because this and many other places along the Kekerengu Fault accumulated >7 m of slip (Kearse et al., 2018), I can use this area as a natural case study to evaluate how rupture zones and moletracks form in response to large-magnitude strike-slip fault displacements. This chapter will focus on the rupture zone – how it was fractured, how these fractures slipped and were deformed, and the height and width of the uplifted welt of deformed ground within the rupture zone (moletrack). I also estimate a minimum depth extent of the layer of detached turf and near-surface materials that was fractured, rotated about a vertical axis within it, and bulged upward within this welt.

The second study area I selected for comprehensive analysis is a paddock just inland of the intersection of the Kekerengu Fault with the east coast of the South Island. At this location, the 2016 rupture includes two fault strands, one of which I infer to have slipped dextrally by ~3.2 m (northern strand), while the other slipped dextrally by ~3.5 m (southern strand). My detailed analysis focusses on this southern fault strand, which I refer to as the “Tirohanga segment”. The paddock was ploughed only a few days before the earthquake, creating a strength anisotropy in the soil that influenced the style of ground deformation during the earthquake. The style in which this paddock deformed during the earthquake was quite similar to that in other parts of the rupture zone, but it can be quantified more exactly because the plough marks provided a continuous set of marker reference lines that could be mapped in detail using post-earthquake orthophotography. This site exemplifies the mechanisms by which relatively small amounts of displacement (~1.5-3.5 m) were accommodated in the rupture zone, presumably providing a snapshot of how other, higher-slip locations (7-9 m) on the fault appeared during early stages of the earthquake rupturing process. As it was possible to trace the ploughing marker lines through the full width of the ground deformation zone at this site, I was able to retro-deform a part of paddock to an approximation of its pre-earthquake state, allowing me to measure and evaluate where, and by what processes, slip was partitioned during the earthquake.

3.2 Background and previous work

Geological structures forming near the ground surface as a result of deeper strike-slip deformation have been extensively described in the laboratory and in the field. Experiments in the laboratory simulating strike-slip deformation in various near-surface analogue materials resulting from tectonic boundary conditions imposed at depth and/or on the sides of the model (Cloos, 1928; Davis et al., 2000; Dooley & Schreurs, 2012; Eisenstadt & Sims, 2005; Mandl, 1988; Naylor et al., 1986; Riedel, 1929; Schopfer & Steyrer, 2001; Schreurs, 1994, 2003; Withjack et al., 2007) have provided insight into the origin of natural deformation structures, including those observed on the ground along strike-slip earthquake ruptures around the world (Bergerat et al., 2003; Deng et al., 1986; Jackson, 1997; Kearse et al., 2018; Kotô, 1893; Lin et al., 2004; Quigley et al., 2010; Tchalenko, 1970).

3.2.1 The Coulomb failure criterion and Riedel fracture zones

One concept that has been widely applied to help understand the inception of earthquake related structures in the ground is the Coulomb failure criterion. This theory was first suggested by Coulomb (1776), but further developed and applied by Mohr (1906), such that it is often referred to as the Mohr-Coulomb failure criterion. Essentially, it is a linear equation describing the conditions at which various materials will fail, in response to a combination of shear and normal stresses:

$$\sigma_s = C + tan\varphi \cdot \sigma_n$$

where σ_s and σ_n are shear and normal stresses on a fault plane, C is cohesion, and φ is the internal friction angle. The Coulomb criterion also predicts the orientation of two potential fault planes, assuming a homogenous material; these fault planes will be oriented at ($45° \pm \varphi/2$) to the maximum principal stress (σ_1) direction. For a “perfect strike- slip faulting” scenario, laboratory experiments (Atmaoui et al., 2006; Cloos, 1928; Eisenstadt & Sims, 2005; Mandl, 1988; Naylor et al., 1986; Richard & Cobbold, 1990; Riedel, 1929; Schopfer & Steyrer, 2001; Schreurs, 1994, 2003; Tchalenko, 1970; Withjack et al., 2007) assumed that a) the (previously unstressed) ground deforms in response to an imposed simple shear boundary condition, and b) the ground accumulates elastic strain homogeneously through this deformation. These conditions predict that σ_1 is oriented at 45° to the strike of the strike-slip zone, while σ_2 is vertical, and σ_3 is orientated at right angles to both σ_1 and σ_2. Assuming a typical ("Byerlee") angle of internal friction of φ= 30°, the Mohr-Coulomb failure criterion predicts that a conjugate set of ideally oriented fault planes (vertical strike-slip faults) will cut previously intact rock at strike angles of ~15° (R faults, which slip synthetically to the main fault zone) and ~75° (R' faults, which slip antithetically). Where developed, either alone or together, these fault sets are known as Riedel faults (Figure 3.1).

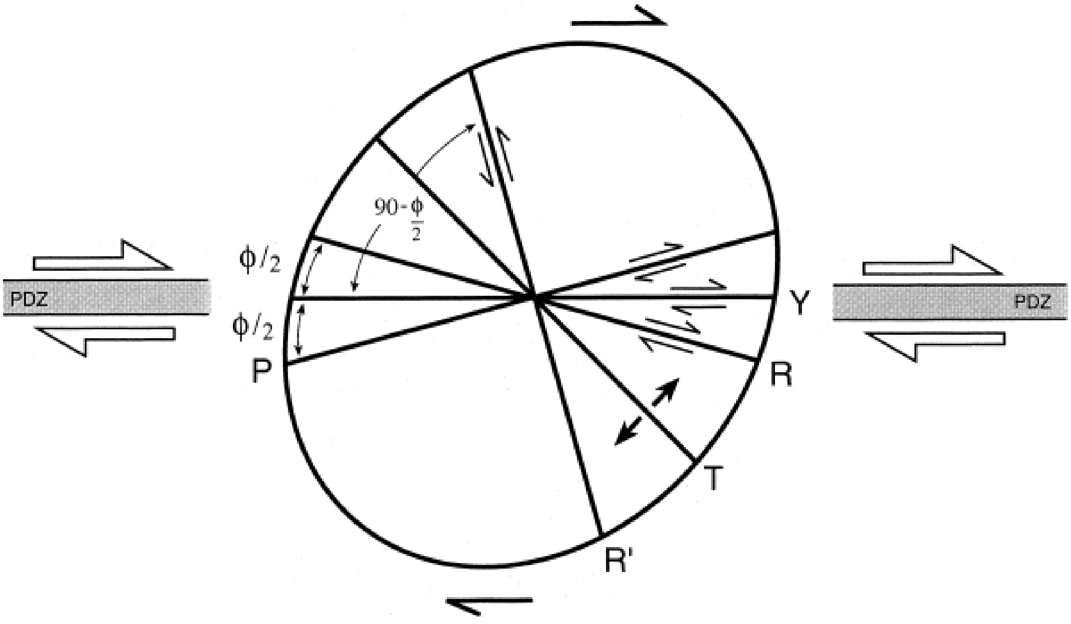

Figure 3.1: *Schematic diagram showing the preferred inception angle of fractures forming in a dextral strike-slip zone (from Davis et. al, 2000). R faults form approximately 15° clockwise from the Principal Deformation Zone (PDZ), R' faults form approximately 75° clockwise from the PDZ, and T fractures form at approximately 45° (or σ_1) to the PDZ. Also shown are throughgoing Y faults, which form parallel to the PDZ, subsequent to the other fractures.*

Riedel faults have been produced in many analogue experiments, first in clay by Cloos (1928) and Riedel (1929), and later in sand and many other analogue materials (Atmaoui et al., 2006; Eisenstadt & Sims, 2005; Mandl, 1988; Naylor et al., 1986). The typical boundary condition used in these experiments involves a vertical, planar basement fault that slips horizontally, overlain by an undeformed overburden which deforms in a distributed manner in response to this slip. This scenario is a highly simplified simulation for earthquake ruptures in the field – generally faults do not have such simple geometry in nature, nor is the sub-surface geology homogeneous. Nonetheless, these experiments provide a basis for understanding the types of structures that can be found in nature and what the expected orientations of such structures would be. During these experiments, the uppermost layer of the overburden breaks and fractures during deformation; R faults are the most common fracture type produced, typically forming earliest in the deformation sequence at a strike angle of ~15° to the Principal Displacement Zone (PDZ) of the main, deeper-seated fault, and with the same sense of slip (Figure 3.1)(Davis et al., 2000). In some, but not all, experiments, R’ faults form at a high angle to the PDZ, preferentially in the zone of overlap between two R adjacent faults, either synchronously with the R faults or subsequent to their formation (Davis et al., 2000). T fractures are extensional fractures that typically form at ~45° from the PDZ, often forming sigmoidal gashes (Figure 3.1).

3.2.2 Laboratory deformation experiments—effect of material properties on fault zone structure

Dooley and Schreurs (2012) review the results of previous analogue experiments of strike-slip deformation zones and evaluate the various controls on their structural development. Important parameters on the structures that form include the type (and thickness) of analogue material (e.g., dry sand, wet clay), and the boundary conditions used in the experiment (e.g., the location, dip, and slip-sense of any basement faults, the width of any basal zones of distributed shearing, and also the thickness of the unfaulted overburden). Dooley and Schreurs (2012) place particular emphasis on comparing results from experiments using dry sand versus wet clay (Atmaoui et al., 2006; Eisenstadt & Sims, 2005; Schopfer & Steyrer, 2001; Withjack et al., 2007), and they determined that while the cohesive strength and internal friction angles of these materials are similar, they behave differently during deformation due to differences in grain size, shape and distribution, the presence or absence of strain hardening or softening in the material, and the role of pore dilatation and fluid pressure variation (especially in clays). Eisenstadt and Sims (2005) and Withjack et al. (2007) compared deformation patterns between dry sands and wet clay under identical boundary conditions, and found that faults develop and link faster in dry sand models, with major faults accommodating most of the deformation; while in clay models, smaller faults develop slowly and deformation is more distributed until the faults link together (Dooley & Schreurs, 2012).

3.2.3 Laboratory deformation experiments—effect of boundary conditions on fault zone structure

Boundary conditions strongly influence deformation of surface materials in zones of dominantly strike-slip deformation. The original experiments by Cloos (1928) and Riedel (1929) both featured a single, vertical basement fault overlain by an initially undeformed overburden. Since these early experiments, variations on these boundary conditions have been evaluated extensively. Dooley and Schreurs (2012) selected representative studies for both clay (Tchalenko, 1970) and sand models (Naylor et al., 1986).

Tchalenko (1970) found that the thickness and shear strength (cohesion and co-efficient of friction) of the clay slab used as an overburden strongly affected both the width of the deformation zone and the distribution of shear fractures within that zone. For a given shear strength, increasing slab thickness results in a wider deformation zone and more widely spaced fractures. For a constant slab thickness, increasing shear strength also widens the deformation zone, and produces more R’ faults and relatively fewer R faults (the latter are more widely spaced).

Experiments in dry sand by Naylor et al. (1986) showed that the R faults initially develop as an *en echelon* array on the surface, but at depth are connected and merge downwards into a vertical strike-slip fault in the basement. There were also small amounts of bulging uplift in between adjacent, overlapping R faults near their tips, yielding some reverse slip at the ground surface. Generally, experiments in granular, dry materials demonstrated less structural variability than those in clay models (Dooley & Schreurs, 2012), which displayed many different types of faults and fractures, pull-apart structures, push-up structures and tension fractures.

Experiments have also been conducted to track deformation in a previously unfaulted cover layer that results from distributed strike slip shearing at depth. In these experiments, Naylor (1986, in Mandl, 1988) observed that R faults were much longer than in the classic Riedel experiments. Arrays of short antithetic (R’) faults commonly cut between the longer R faults; either appearing synchronously with the R faults (conjugates), or subsequently (linking across the blocks between R faults). The attitude of later-forming structures is commonly influenced by local rotation of σ_1 that occurs in the compressive and extensional zones that surround the tips of the R faults (e.g., Naylor et al., 1986).

3.2.4 Relevance of laboratory structures to natural earthquake rupture zones

The most common structure observed in laboratory experiments of strike-slip deformation above a buried basement fault are *en echelon* arrays of R faults and/or extension fractures (the latter striking at a higher angle to the main fault than R faults, Figure 3.1). In some experiments, these fracture types are accompanied and linked by shorter R’ faults. The inception angle of both types of fractures is influenced by the attitude of σ_1; while σ_1 is expected to be 45° in a pure strike-slip faulting scenario, often this is not the case in the field. Many rupture zones have an aspect of either transpression or transtension associated with them, which affects $\sigma_{1.}$ For example, in transpressional zones, the trend of σ_1 >45°, which increases the inception strike of the R faults and T fractures that form in the rupture zone (and vice versa for transtensional zones). This change in inception angle as a result of variation in σ_1 has been demonstrated in experiments that replicate zones of either transpression or transtension (Naylor et al., 1986; Richard & Cobbold, 1990).

As slip on the main fault at depth increases, the near-surface array of faults typically becomes linked together into one or more throughgoing faults, striking subparallel to the basement fault; these may be called “Y faults”. A similar suite of structures has been observed on the ground in many natural strike-slip rupture zones globally (Ambraseys & Zatopek, 1969; Bergerat et al., 2003; Deng et al., 1986; Kearse et al., 2018; Lin et al., 2004; Quigley et al., 2010), suggesting that the “Riedel” boundary condition (buried strike-slip fault at depth) may provide some insight into how near-surface materials deform during large strike-slip ruptures (Atmaoui et al., 2006; Davis et al., 2000; Dooley & Schreurs, 2012; Eisenstadt & Sims, 2005; Mandl, 1988; Naylor et al., 1986; Schopfer & Steyrer, 2001; Schreurs, 1994, 2003; Tchalenko, 1970; Withjack et al., 2007). In these rupture zones, both in nature and in laboratory experiments, push-up structures form to accommodate horizontal compression, either on restraining bends of the fault or in the tip regions between two sub-parallel synthetic faults (where they overlap) (Atmaoui et al., 2006; Deng et al., 1986; Lin et al., 2004; Naylor et al., 1986). These push-up structures form in both clay (Atmaoui et al., 2006) and sand (Naylor et al., 1986) models, however, the push-ups are more pronounced in clay models as the clay is more cohesive (Dooley & Schreurs, 2012). When applied to field studies, the push-up structures that form between the tips of sub-parallel synthetic faults are often referred to in literature as “moletracks” (Ambraseys & Zatopek, 1969; Deng et al., 1986; Kotô, 1893; Lin et al., 2004; Quigley et al., 2010).

The word “moletrack” was first used by Koto (1893) to describe push-up structures associated with the 1891 M_w 8.0 Mino-Owari strike-slip earthquake in Japan: “the line of the fault appears on the surface like a rounded ridge of soft earth 30 to 60 cm high and, as I have already stated, resembles very much the pathway of a gigantic mole”. Since then, the term “moletrack” has been used to describe similar push-up structures associated with strike-slip ground ruptures, to varied levels of detail (Ambraseys & Zatopek, 1969; Deng et al., 1986; Lin et al., 2004; Quigley et al., 2010). These studies use the term slightly differently: Ambraseys and Zatopek (1969) use it to describe areas of the rupture trace that have “evolved” from a zone of ground fractures into sections of “humped up” ground that are uplifted (between 0.1 and 1.5 m high), but are not considered to be a fault scarp. Deng et al. (1986) use the term “moletrack” rather loosely to describe push-ups that formed in between adjacent R faults or fractures. In this study, I focus on comparing the push-up structures I observe along the Kekerengu Fault following the Kaikōura earthquake with those described by Lin et al. (2004) and Quigley et al. (2010), as these studies are more recent and descriptive than those previously mentioned.

Lin et al. (2004) describe large push-up structures as coseismic moletracks in association with the Kunlun earthquake (China) in 2001, and distinguish between two main types of moletracks: angular ridge structures, which were more rigid and formed in consolidated or frozen sediments, and bulge pattern structures, which accommodated flexural folding of the ground and occurred in semi-consolidated sediments. Quigley et al. (2010) describe moletrack structures associated with the Darfield earthquake (Christchurch, New Zealand) of 2010. This earthquake produced a maximum of 4.5 m of strike-slip and ruptured through alluvial gravels. In areas with a wider deformation zone, slip was primarily accommodated by horizontal flexure (distributed deformation), where the ground bends rather than breaks. In areas where the deformation zone was narrower and slip more concentrated, push-up structures formed, and these were termed "moletracks".

In this study, I use a working definition of moletracks that describes them as volumes of spatially repeating, bulged up ground associated with a strike-slip rupture that form in the central rupture zone along a fault. My work differs from the studies listed above in that it examines how moletracks evolve in response to a larger (up to ~10 m) magnitude of coseismic strike-slip, including ground features that may be peculiar to large displacement earthquakes. The studies with which I compare the Kaikōura moletracks with more closely include: the Darfield earthquake, which accommodated <4.5 m slip (most commonly <1.5 m of slip) (Barrell et al., 2011; Quigley et al., 2010) and the Kunlun earthquake, which accommodated <16.3 m slip - but 3-8 m slip in areas that contained moletracks (Lin et al., 2004). How displacement manifested in the Kaikōura earthquake has allowed us to better understand how the ground accommodates large magnitudes of strike-slip during earthquakes, and perhaps the likely paleoseismic expressions of large strike-slip earthquakes that one might observe in trench excavations (see Chapter 4).

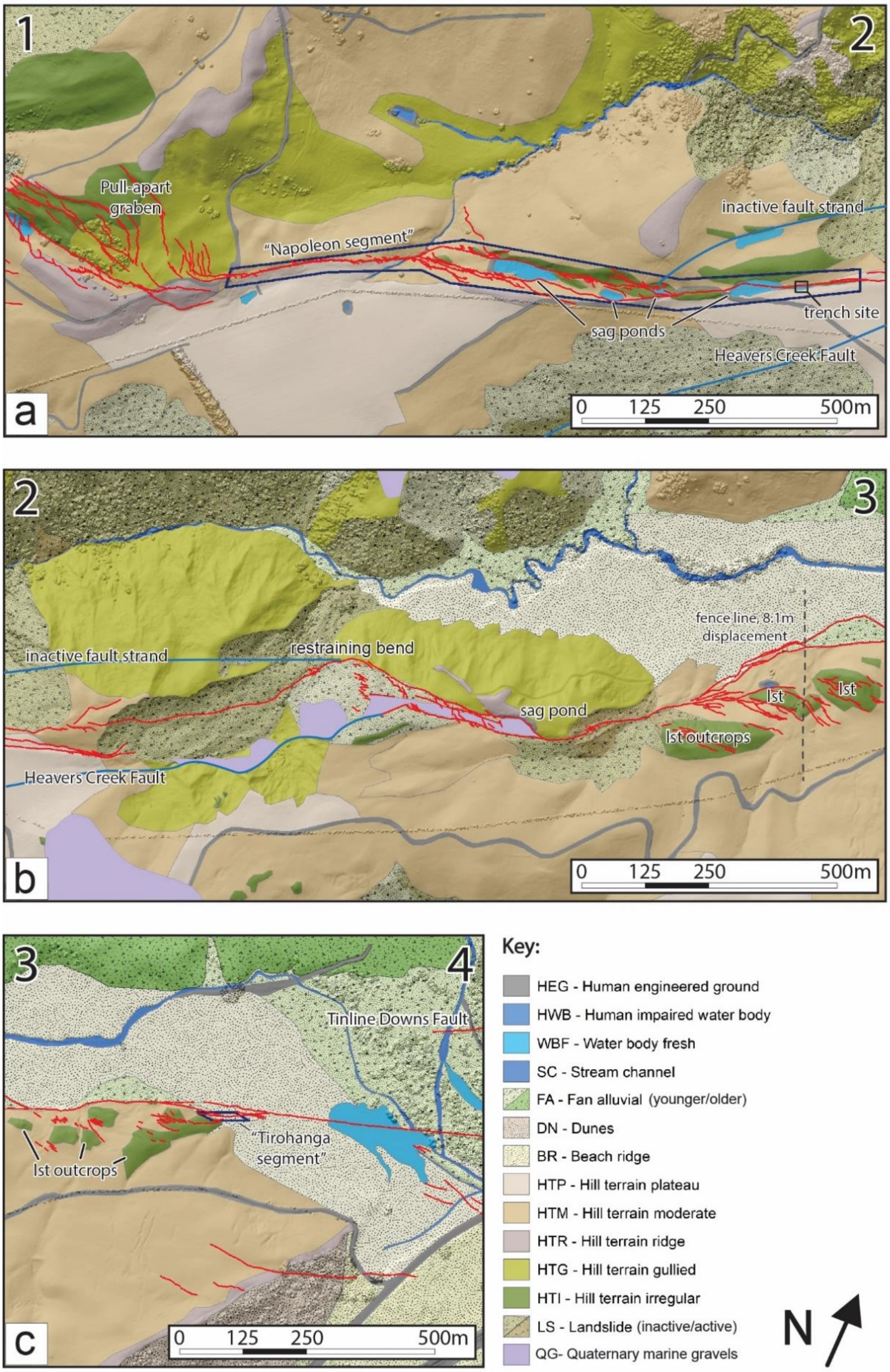

Figure 3.2: *Map of surface geology of an eastern part of the Kekerengu Fault, showing fault rupture traces from the 2016 earthquake in red (Kearse, 2018), fault traces that did not break in 2016 in blue, and specific study areas (dark blue boxes, labelled "Napoleon segment" and "Tirohanga segment"). Numbers in the top corners of each box show the order of the map tiles, which are labelled a-c and are referred to in the text. Background topography is hill-shaded LIDAR DSM (from Land Information New Zealand, 2016). For descriptions of geomorphic units shown in the Key, see Appendix C.3.1.*

3.3 Geomorphology and structural geology of an eastern part of the 2016 rupture on the Kekerengu Fault

3.3.1 Structure, geologic setting, and 2016 event displacement along the near-coastal Kekerengu Fault

The eastern, near-coastal section of the Kekerengu Fault varies in geology and geomorphology, including the local fault strike, and the lithology and topography of the rocks and the landscape that it cuts (Figure 3.2). The study area for this thesis covers a ~4 km-long segment of the onshore Kekerengu Fault from near the coast (in the east) to a large releasing bend and pull-apart graben (in the west, Figure 3.2a). Two sub-areas along this section of the fault were mapped in detail. These include the “Napoleon segment,” to the west, (Figure 3.2a) and the “Tirohanga segment,” to the east (Figure 3.2c). The underlying basement rock throughout this section primarily consists of Amuri Limestone. Surface geology has been mapped across the section, shown in Figure 3.2. More detailed descriptions of the different classes used in this mapping are listed in Appendix C.3.1. Generally, distinction was made between the following; hill terrain, landslide deposits, alluvial fans, water features (e.g. sag ponds) and man-made features (i.e., roads, dams). Below, most specifications of fault displacement, fault attitude, and rupture zone width are taken from the observations of Kearse (2018), who undertook field work soon after the 2016 earthquake.

The dip of the Kekerengu Fault throughout this section is steep (60-90°) and generally to the northwest. Closer to the coast in the east, the fault reverses dip direction at irregular spatial intervals, dipping (steeply) towards the southeast. The 2016 rupture zone includes multiple strands in this map area, shown in Figure 3.2. The faults within the pull-apart graben shown in Figure 3.2a generally strike 50° clockwise relative to the surrounding fault traces. This pull-apart graben includes an up to 300 m-wide zone of subparallel fault strands (also open fissures) that are chiefly dextral-normal in slip-sense. At the graben during the 2016 earthquake, dextral displacement exceeded 7.5 m (an exact value was difficult to determine because of the distributed nature of the deformation). Northeast of the pull-apart graben, the fault deflects to a more typical strike that varies between 060-080 as it traverses eastward towards the Napoleon segment. Along this part of the fault, the 2016 rupture trace was relatively linear and simple, and the zone of ground deformation was <5 m wide (which is narrow compared to other sections of the Kekerengu Fault rupture). This section of the fault accommodated ~9 m of dextral slip during the 2016 earthquake. Farther northeast from the southwestern end of the Napoleon segment, the fault bends ~10° to the east to follow a strike of 080 along a ~400 m part of the segment that functions—at least in the long-term—as a subtle releasing bend. There, a series of sag ponds, bounded by one or two oblique-normal faults on their margins, have formed over many earthquake cycles to accommodate a slight component of fault-orthogonal extension. The ground deformation zone in the 2016 earthquake locally ranged in width up to as much as 30-50 m in this section, where it spanned a small pull-apart graben. The dextral slip along this reach of the fault in 2016 was ~9 m. The paleoseismic trench site that was displaced ~9.1 m (Kearse et al., 2018) is located towards the northeast end of the Napoleon segment (Figure 3.2a).

To the northeast of the faulted trench site (Figure 3.2b), the fault bends northward around an outcrop of the Amuri Limestone, forming a restraining bend. Farther north, the 2016 fault rupture bends back towards the east to achieve a slight releasing bend, along which a sag pond, bounded by oblique normal faults on each side, is developed. There, the rupture zone is up to ~25 m wide in this ponded area and accommodated ~7.1 m of dextral strike-slip. Northeast from the sag pond, the fault rupture trace bends northward again and narrows, before bifurcating into a series of mostly discontinuous strands. The northernmost strand is continuous, striking ~050-055, and mostly accommodates reverse fault motion. To the south are several smaller, sub-parallel strands (also shown in Figure 3.2c) that strike roughly east through hard bedrock of the Amuri Limestone. These strands opened up during the earthquake as extensional fractures, while also rotating clockwise about a vertical axis to accommodate a cumulative dextral slip of ~8.1 m. This slip was accommodated in a gradational, distributed way across a zone width of ~100 m, as documented by the almost uniform deflection of a surveyed fence line spanning these fractures.

Farther to the northeast (Figure 3.2c), the fault trace simplifies as it traverses across the valley flank and alluvial plain of Tirohanga Stream. Here the rupture trace is narrow (mostly ~1.5 m, in places up to 5 m wide) and linear, striking ~075 towards the coast, and is downthrown on its northern side. On the floor of Tirohanga Stream Valley, this Tirohanga segment of the Kekerengu Fault transects a farm paddock that was freshly ploughed at the time of the 2016 earthquake. No displacements were measured across this paddock by Kearse et al. (2018); however, my analysis of aerial photographs (see section 3.3.2, Figure 3.3 and 3.4) yields a dextral slip estimate of ~3.5 m for the fault strand that traverses the paddock on the southern side of Tirohanga Stream, based on the cumulative offset of individual plough cuts across the rupture zone. This reduction of slip compared to the nearest horizontal displacement values measured in either direction along fault strike by Kearse et al. (2018) (~8.1 m to the southwest, ~6.7 m to the northeast) could be due to the presence of the Tinline Downs fault on the north side of the valley which also accommodated <1.5 m of the horizontal displacement (Figure 3.2c), as measured by Kearse et al. (2018).

3.3.2 Field description of the eastern Kekerengu Fault rupture and its moletracks

In this section I use field and aerial photographs taken soon after the earthquake by members of the Kaikōura Earthquake Surface Rupture Team as a means to describe the appearance and structure of deformed ground along the 2016 rupture of the eastern Kekerengu Fault. The following descriptions do not consider aspects of the rupture zone structure that can be attributed chiefly to gravitational collapse of scarps (Figures 3.3, 3.4) or other steep slopes. In these descriptions I distinguish between features in the inner and outer rupture zone. The inner rupture zone is the central part of the rupture zone in which ground deformation is focused and slip is relatively concentrated, commonly bounded by throughgoing faults; this is where moletracks form (Figure 3.3c). The outer rupture zone encompasses the deformation that occurs outside this inner, concentrated zone of the rupture. It typically displays fractures (including extensional fractures) and can include smaller splays of the main fault strand that do not accommodate much slip (Figure 3.3c).

Along the Napoleon segment of the fault (Figure 3.2a) most of the moletrack structures were conspicuous zones of up-bulging that were generally 0.5-1 m high (but <2 m high relative to the less deformed ground farther away from the fault trace) and ~5 m wide. Large volumes of turf are deformed in these moletracks and they generally form rounded bulges (rather than angular fold-ridges as reported by Lin et al. (2004) with regards to the Kunlun earthquake). Several different fracture types are observed in the aerial photography of the moletracks (Figure 3.3b): the first type are R faults, which

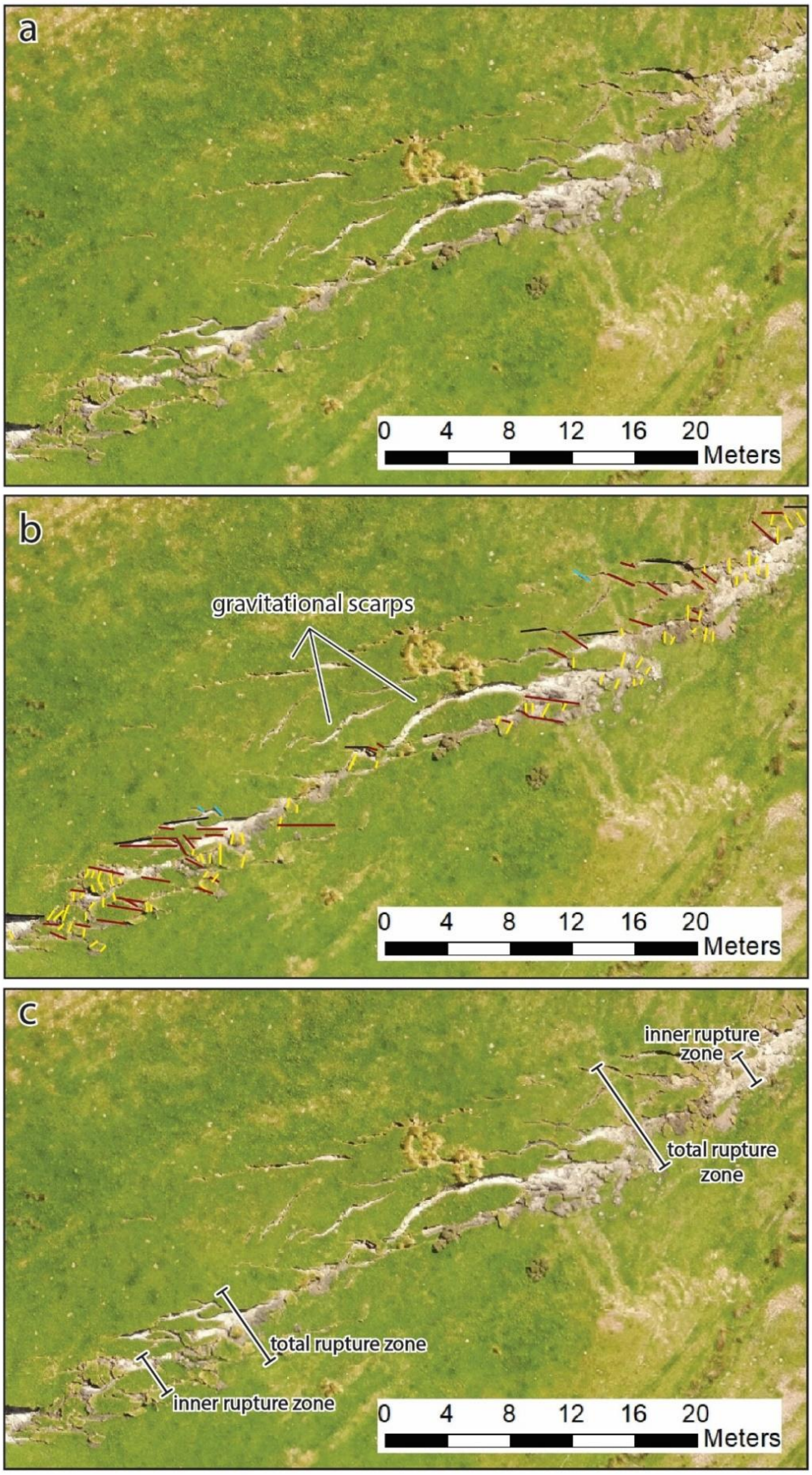

Figure 3.3: *Uninterpreted orthophotograph (a) and interpreted orthophotograph (b, c) of a section of ground rupture in the western section of the Napoleon segment that strikes 065. Part b) shows a series of fractures: black lines represent R faults, red-brown lines are rotated R faults, yellow lines are rotated R' faults, and blue lines are extensional fractures (see Table 3.1 for further descriptions). Gravitational scarps are also labelled. Part c) shows examples of where measurements of the inner and total rupture zone widths were taken (referred to in text).*

occur just outside the inner rupture zone, commonly striking ~20° clockwise from the main fault trace. Within the inner rupture zone, the turf is broken into a series of relatively evenly spaced, well defined “rafts” that are bounded by clockwise-rotated R faults. These rafts are separated by fissures or gashes (Figure 3.3, labelled on Figure 3.5) and are presumably decoupled from underlying material at some shallow depth. The depth of this decoupling must have been deep enough to produce <1 m of elevation in response to the horizontal shortening that has been absorbed by the rotated turf rafts. As deformation progressed, the rafts were rotated clockwise about a vertical axis and broken up by internal faults which also rotate with the rafts during deformation (Figure 3.3). These turf rafts appear to tear away from one side of the fault (commonly the upthrown side of the fault), leaving a barren (grassless) scar in its wake. While the rafts tend to rotate away from the uplifted side of the fault, on the opposite side they are thrust outward along a low-angle fault contact that is expressed on the ground surface as a turf roll. It should be noted that in contrast to the relatively intact rafts shown in Figures 3.5 and 3.6, in other places, deformed turf rafts are more broken up or shattered in appearance (Figure 3.3, 3.7) especially where the slip was large (<~8 m) and/or focused in a particularly narrow (<5 m) zone.

The above descriptions apply to most of the field area that I considered in my analysis; however, there are some notable exceptions. In areas where slip is distributed across one or more strands or splays of the fault, the moletracks were less developed, likely due to the lesser amount of slip accommodated by individual strands in comparison to sites where there is only one main fault rupture (~9 m in this area). Fractures are present in the rupture zone but are less rotated and deformed than those in areas of concentrated slip. Typically, one can observe some poorly defined turf rafts in these lower slip areas; they are poorly defined because the rupture ceased before the turf rafts have accommodated much slip, and so these rafts are less developed than those that formed in areas with ~9 m of slip (Figure 3.4). One example of an area with this distributed type of slip is the pull-apart graben located in Figure 3.2a. As previously mentioned, this section of the fault strikes 50° clockwise from the main rupture trace, accommodating extension over a ~300 m wide zone. This geometry results in a multitude of dextral-oblique faults, as well as extensional surface fractures. The moletracks along these graben strands are dominated by these extensional fractures

(Figure 3.4). R faults are hard to identify at this location, although some rafts have begun to form in places. The up-bulged moletrack along the Tirohanga segment of the fault (Figure 3.8) also formed along a dextral-splay fault strand (Figure 3.2c) which accommodates ~3.5 m of dextral displacement. The height of this Tirohanga moletrack is between 0.3 and 0.8 m relative to the pre-earthquake ground surface. Turf rafts are abundant at this site, bounded by pre-existing (anthropogenic) plough cuts at the site ~0.3 m deep, that were reactivated as antithetic-slipping strike-slip fractures and rotated clockwise during the earthquake. This makes the Tirohanga moletrack somewhat more pervasively fractured than might be expected along these splay-like fault strands with low or distributed slip (such as the pull-apart graben, Figure 3.4).

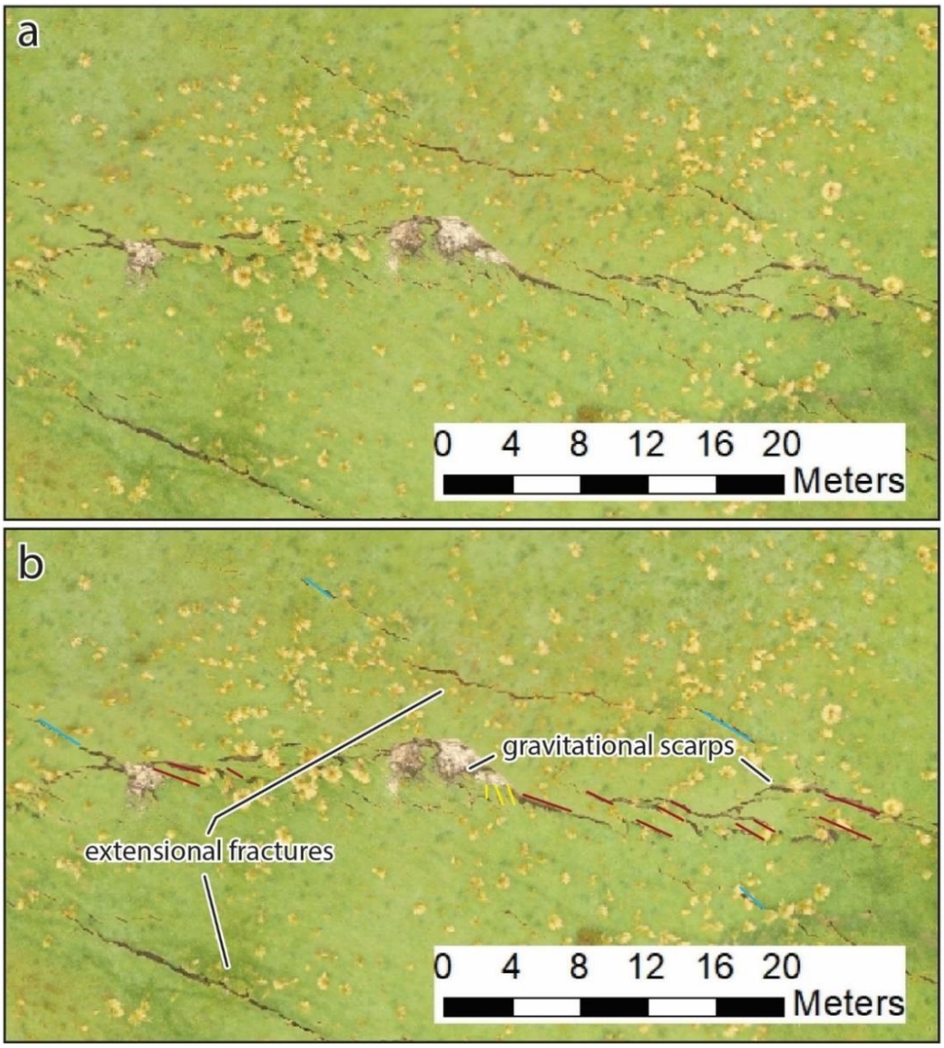

Figure 3.4: *Uninterpreted orthophotograph (a) and interpreted orthophotograph (b) of a section of (less evolved) ground rupture along a strand of the Napoleon segment 160 m west of the pull-apart basin in Figure 3.2a. Large scale extensional fractures and gravitational scarps are labelled in 'b', as well as some rotated R faults (brown-red lines) and some small extensional fractures (blue lines). See Table 3.1 for further descriptions of faults and fractures.*

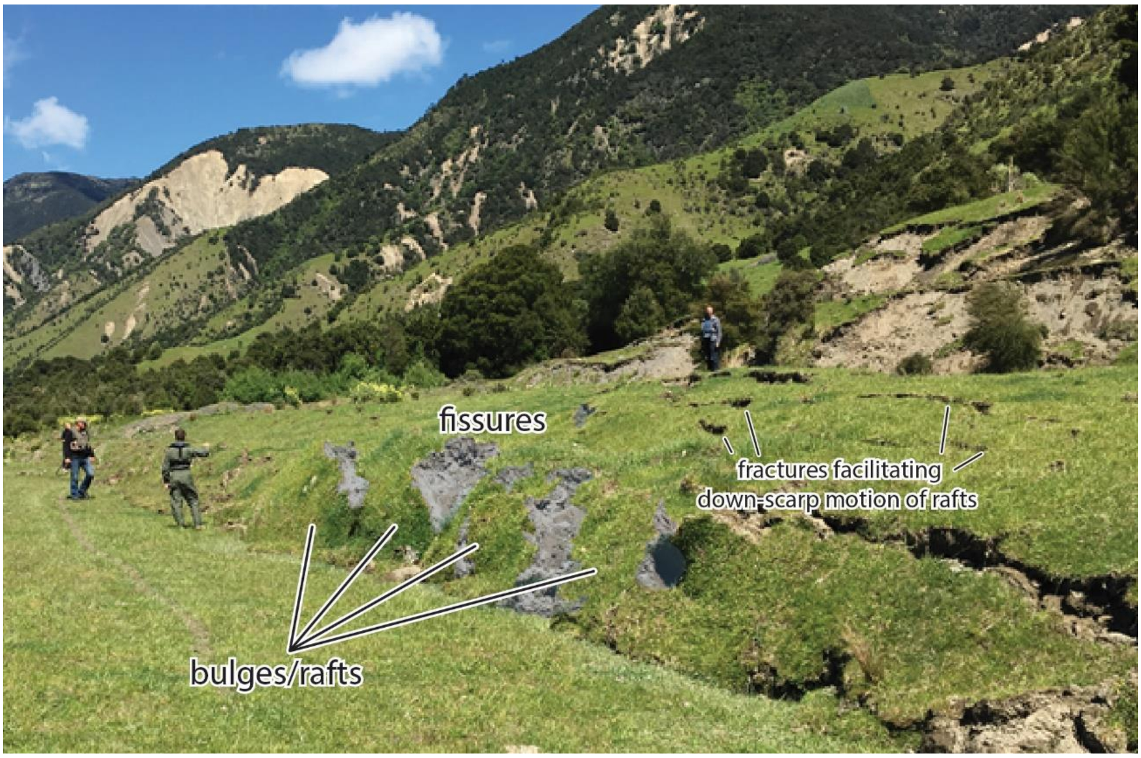

Figure 3.5: *Moletrack structure located on a 1-2 m high scarp at Shag Bend, on the Clarence River, Kekerengu. Fissures are labelled and shown in shading. Rafts are also labelled, and have moved down-scarp, facilitated by fractures up slope (labelled). 5.5 m of dextral slip was measured at this site (Kearse, 2018). Photograph taken by Matthew Hill, 18/11/2016.*

Figure 3.6: *Moletrack located on the flanks of Deadman Stream at its intersection with the Kekerengu Fault (adjacent to Valhalla Stream), looking west. 8.7 m of dextral slip was measured ~100 m southwest of this site along fault strike (Kearse, 2018). Photograph taken by Russ Van Dissen, 25/11/2016.*

***Figure 3.7:** Fissured, bulged up moletrack at the paleoseismic trench site along the Napoleon segment, shown in Figure 3.2a. Russ Van Dissen is pictured (centre) standing on the largest intact turf raft at the site (see also Figure 3.14); the rest of the up-bulged material is fairly jumbled and disorganised. This is partially because the sub-surface material is backfill from the original trench excavation, which more easily detached from its roots (see Chapter 4 of this thesis for further detail). Photograph taken by Mark Hemphill-Haley, 23/11/2016.*

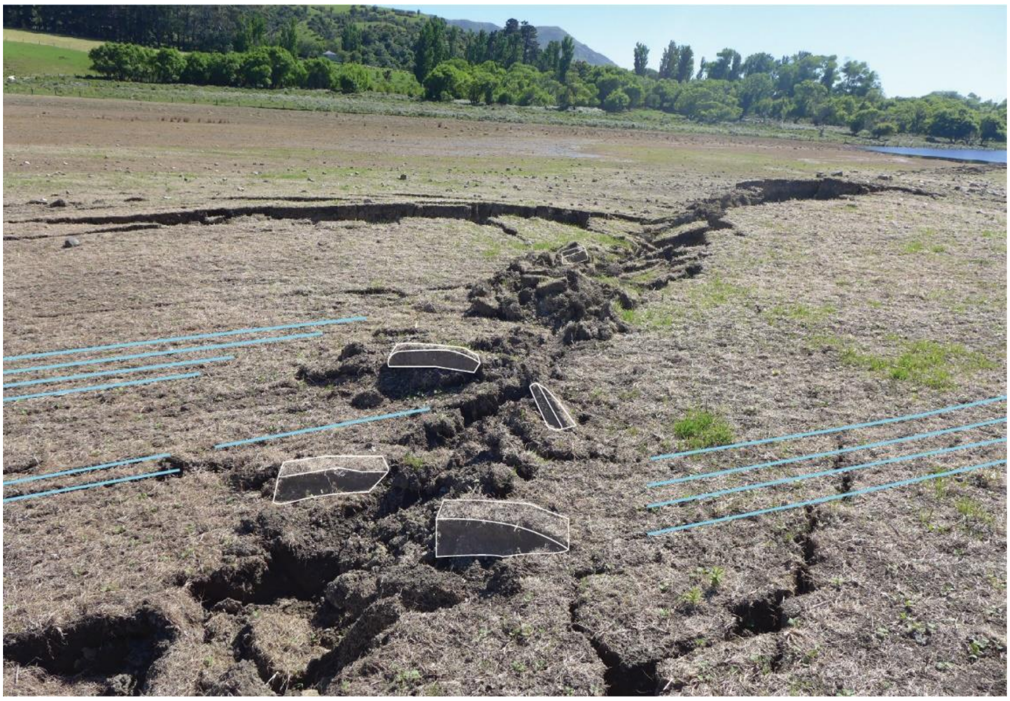

***Figure 3.8**: Small moletrack located along an <80 cm high scarp (southwest side upthrown) in the Tirohanga segment (Figure 3.2c), looking northeast. Total dextral slip is ~3.5 m. Examples of plough cuts are traced on the surface (shown in blue). Examples of turf rafts or blocks are also traced in white - see Figure 3.15b for further detail. Photograph taken by Tim Little, 19/11/2016.*

3.3.3 Description of ground deformation along the Napoleon segment

This area was selected for more detailed moletrack analysis for several reasons: first, the rupture trace through this segment is relatively simple and single-stranded, and displacement values are known from both pre- and post-earthquake Real Time Kinematic surveys (RTK) and field observations from Kearse et al. (2018). Displacement was dextral strike-slip between ~7 and ~9 m. The displacement vector varied by ~10° throughout the fault segment (averaging 067), which produced a variation in the local displacement angle (α). The rupture zone structures are also relatively continuous and spatially repeating along this segment. Additionally, this section of the fault also hosts the site of the displaced paleoseismic trench (see also Figure 3.7), which is a particular research focus of this thesis (see Chapter 4).

3.3.3.1 Approach to mapping of moletrack structures (Napoleon segment)

To aid in the description of the rupture zone structures along this section of the fault, I adopt a simple classification scheme for fractures based on their spatial arrangement, strike, and kinematics. This scheme shares some terminology with the widely applied nomenclature for strike-slip zones that was derived from analogue experiments (e.g., (Dooley & Schreurs, 2012; Riedel, 1929). Four main types of surface fractures were recognized (Table 3.1). Using this scheme, I examined the detailed orthophotography of this part of the fault, digitized fracture traces visible on the images in ArcMap GIS, and colour-coded each fracture segments with my interpretation as to the type of fracture it represented. The key goals of this analysis are to: a) document the average change in strike of the deformed R faults resulting from their clockwise rotation, and b) describe the average initial (or little rotated) strike of the R faults and T fractures in the little deformed, outer part of the rupture zone. A script in the GIS program calculated the strike of each fracture segment relative to the (variable) local fault strike of the main trace of the Kekerengu Fault at the site, and these values were tabulated. Examples of fractures mapped in this way are shown in Figure 3.9 (see Appendix C.3.2 for further examples of fracture mapping across the Napoleon segment, and Appendix C.3.3 for tabulated measurements of fracture strike). Because of the large amount of finite deformation in the narrow, large-slip rupture, assignment of “fracture type” was often interpretive; for example, recognizing a rotated R fault was difficult where it was no longer attached, and/or in continuity with its unrotated (or perhaps less rotated) equivalents in the exterior parts of the rupture zone.

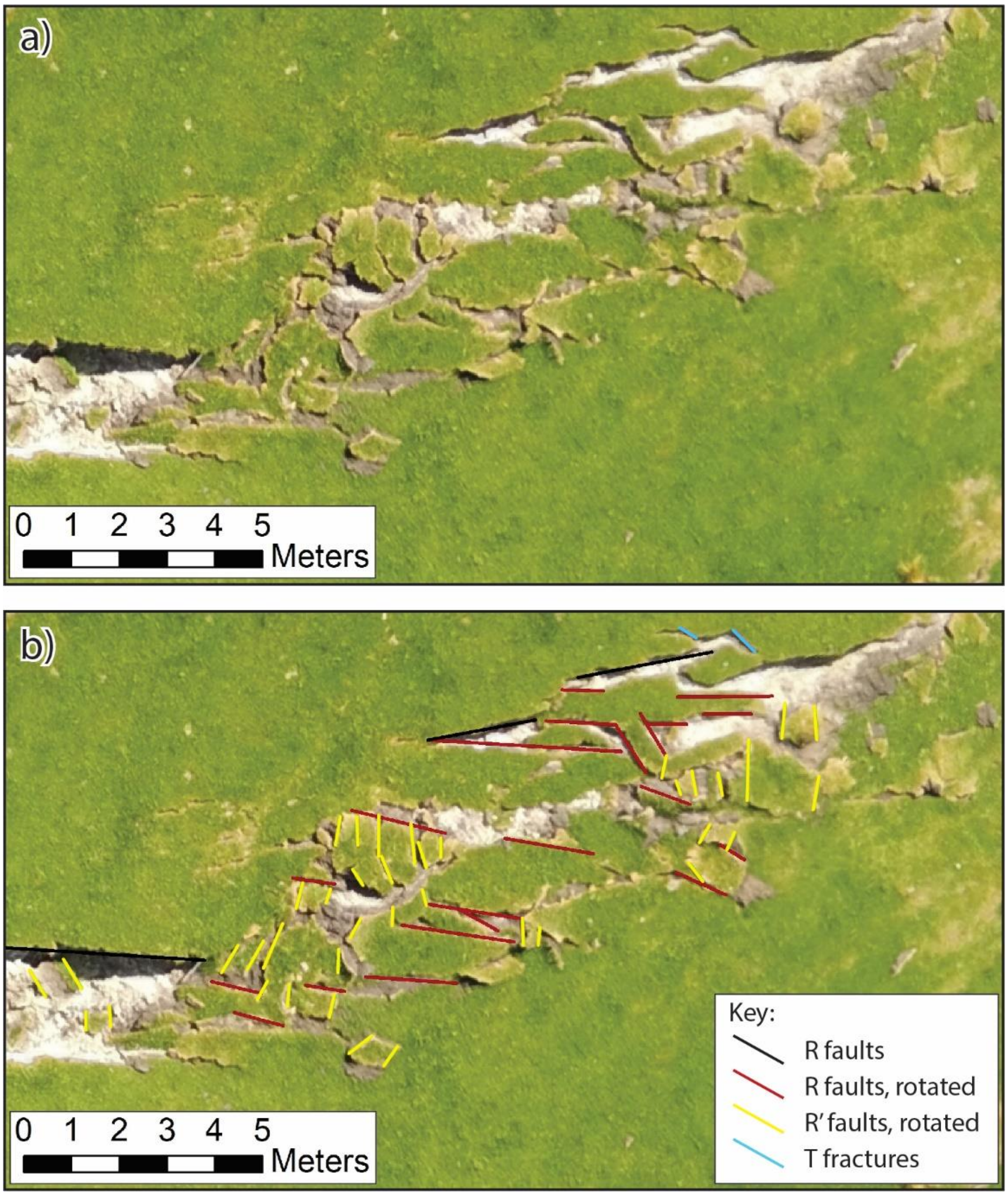

Figure 3.9: *Example of a section of the rupture zone within the Napoleon segment, showing the uninterpreted (a) and interpreted orthophotograph (b). Orthophotography sourced from aerial imagery taken by Zekkos et al. (2018) in November 2016.*

Table 3.1: *Kinematic classification scheme for fractures observed in the field.*

Fracture type	Description
R fault, initial	R faults preserved in an intact or little-rotated state in the outer part of the rupture zone. They have a synthetic (dextral) sense of slip. Often appear as barren “scars” where the turf rafts have torn away from their origin, while rotating about a vertical axis to form a rotated R fault.
R fault, rotated	R faults that are inferred to have rotated clockwise about a vertical axis in the strongly deformed, inner part of the rupture zone. As they rotate, extensional fissures open up along the walls of the original R fault, and these fissures separate one turf raft from another. The rotated R faults ultimately acquire an antithetic (sinistral) sense of strike-slip, with rotation that is larger than the original magnitude of dextral slip.
R’ fault, rotated	Short fractures, now at a high angle to the main trace, that transect the (R-fault bounded) turf rafts into smaller pieces. Inferred to have rotated clockwise to some degree, but probably less than the rotated R faults that they commonly cut and offset. Inception of these fractures must at least in part postdate R faults. Sense of strike-slip is antithetic (sinistral), but the displacement also includes some extension. Interpreted to have initiated as antithetic (R’) Riedel faults.
T fracture, rotated	Gaping extensional fractures most commonly observed in the outer part of the rupture zone, some of which have acquired a small component sinistral strike-slip shear (perhaps during clockwise rotation).

3.3.3.2 Results - Fracture strikes and inferred rotations

The strike of each digitized fracture was measured clockwise from the local strike of the main Kekerengu Fault, in degrees. In the Napoleon segment study area, a total of 102 R faults were mapped. These faults have a range of strike angles between 14-32°, with an average of 22° ± 5° (1σ). I also calculated the average strike angle of R faults in both transtensional and transpressional settings separately; these were 19° and 22°, respectively. 149 fractures classified as rotated R faults were digitized. The range of strikes of these faults was 21-68°, with an average strike angle of 41° ± 12° (1σ) relative to the main fault. This suggests an average vertical-axis clockwise rotation of 19° ± 13° (1σ) for the (originally) synthetic Riedel faults in the highly deformed, inner (and up-bulged) part of the rupture zone. A total of 216 fractures were classified as rotated R' faults, based on their high angle to the fault (and their relationship to the rotated rafts). Their strike angles ranged between 66 and 155° relative to the main fault strike, with an average of 114° ± 24° (1σ). Only 34 of the little-deformed T fractures were mapped, ranging from 32-83° in strike angle with an average of 57° ± 14° (1σ). These results are tabulated in full in Appendix C.3.3.

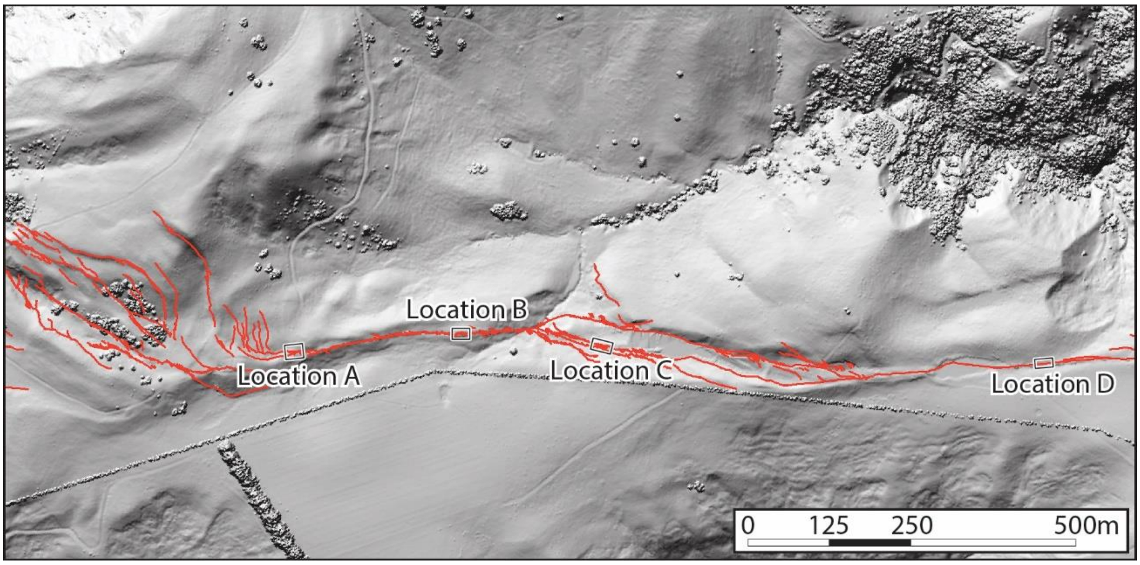

Figure 3.10: *Map showing locations of elevation profiles at Locations A-D within the Napoleon segment. 2016 rupture traces are shown in red. Background topography is a hillshade model derived from 1 m LIDAR (Land Information New Zealand, 2016), compiled and produced by Matthew Hill (GNS Science).*

3.3.3.3 Results - elevation profiles of some sections of moletrack structures

Four locations along the Napoleon segment of the fault were selected for detailed topographical analysis of the rupture zone (Figure 3.10), to measure the shape and height of moletrack bulges and their intervening fissures in profile view across a range of α values. Profiles were taken both parallel and perpendicular to the strike of the local fault rupture. The elevation differences between adjacent bulges and their flanking fissures were measured along the strike-parallel profiles. Rupture zone widths and moletrack heights (relative to a projected "pre-deformation" ground surface) were best measured along the strike-perpendicular profiles. In these perpendicular profiles, I extrapolate topography from outside the rupture zone across the area affected by the up-bulged moletracks (inner rupture zone) to estimate a pre-deformation ground surface, and compare this surface with the bulges of the moletracks to estimate the true height of these bulges. For each locality, I also establish the degree to which the fault slip is locally transpressional or transtensional (i.e., value of α). I compare the azimuth of the displacement vector for the Kaikōura earthquake near each site (calculated from local GPS displacement surveys by Howell et al., 2019) with the average local fault strike measured in ArcMap GIS. This difference is the local displacement angle (α). Positive α values correspond to a transpressional setting, while a negative α value suggests transtension.

Location A (Figure 3.11): This section of the moletrack is located just to the northeast of the pull-apart graben (Figure 3.2a) on a section of the fault that strikes 067, resulting in a slightly transtensional displacement angle (α) of -2° (Figure 3.11a). The inner rupture zone at this locality is ~5 m wide (Figure 3.11c). Examination of the strike-parallel profile (Figure 3.11b) showed that elevation differences between adjacent fissures and bulges along the moletrack ranged between 0.12 m and 1.03 m, with an average difference of 0.5 ± 0.3 m (1σ). This is also depicted in the strike-perpendicular profile in Figure 3.11c, where the peak bulge of the moletrack is about 0.5 m higher than the dashed pre-deformation ground surface.

Location B (Figure 3.12): This section of the fault strikes 065, a geometry that resulted in a slightly transpressional coseismic displacement vector during the 2016 earthquake (α = 1°, Figure 3.12a). The inner rupture zone width is ~6 m; however, the perpendicular profile in Figure 3.12c shows a wider measure of the inner rupture zone - as it also includes turf that is bent upwards in the outer rupture zone. Elevation differences between adjacent fissures and bulges along fault strike (Figure 3.12b) are between 0.12 and 0.95 m, with an average difference of 0.41 ± 0.27 m (1σ). This agrees with the measures of height in the strike-perpendicular profile (Figure 3.12c), where the elevation is generally 0.6-0.7 m, but <1 m at the peak of the bulge.

Location C (Figure 3.13): This section of the fault strikes 075, creating a transtensional displacement vector during the 2016 earthquake (α = -5°, Figure 3.13a). The inner rupture zone width is ~7 m, which is reflected in the fault perpendicular profile (Figure 3.13c). The strike-parallel profile (Figure 3.13b) shows that the elevations between adjacent fissures and bulges range between 0.14 and 0.59 m difference, with an average of 0.3 ± 0.12 m (1σ). The strike-perpendicular profile (Figure 3.13c) shows elevations of 0.4-0.5 m.

Location D (Figure 3.14): This section of the fault strikes 063 and includes the paleoseismic trench site. Here α= 8° (Figure 3.14a), indicating that transpression was accommodated during the 2016 earthquake. The inner rupture zone at this locality is ~2.8 m wide. The range in elevation differences between adjacent fissures and bulges here is 0.18-1.01 m (Figure 3.14b), with an average of 0.53 ± 0.26 m (1σ). This is also reflected in the strike-perpendicular profile (Figure 3.14c) where elevations range between 0.4-1.2 m.

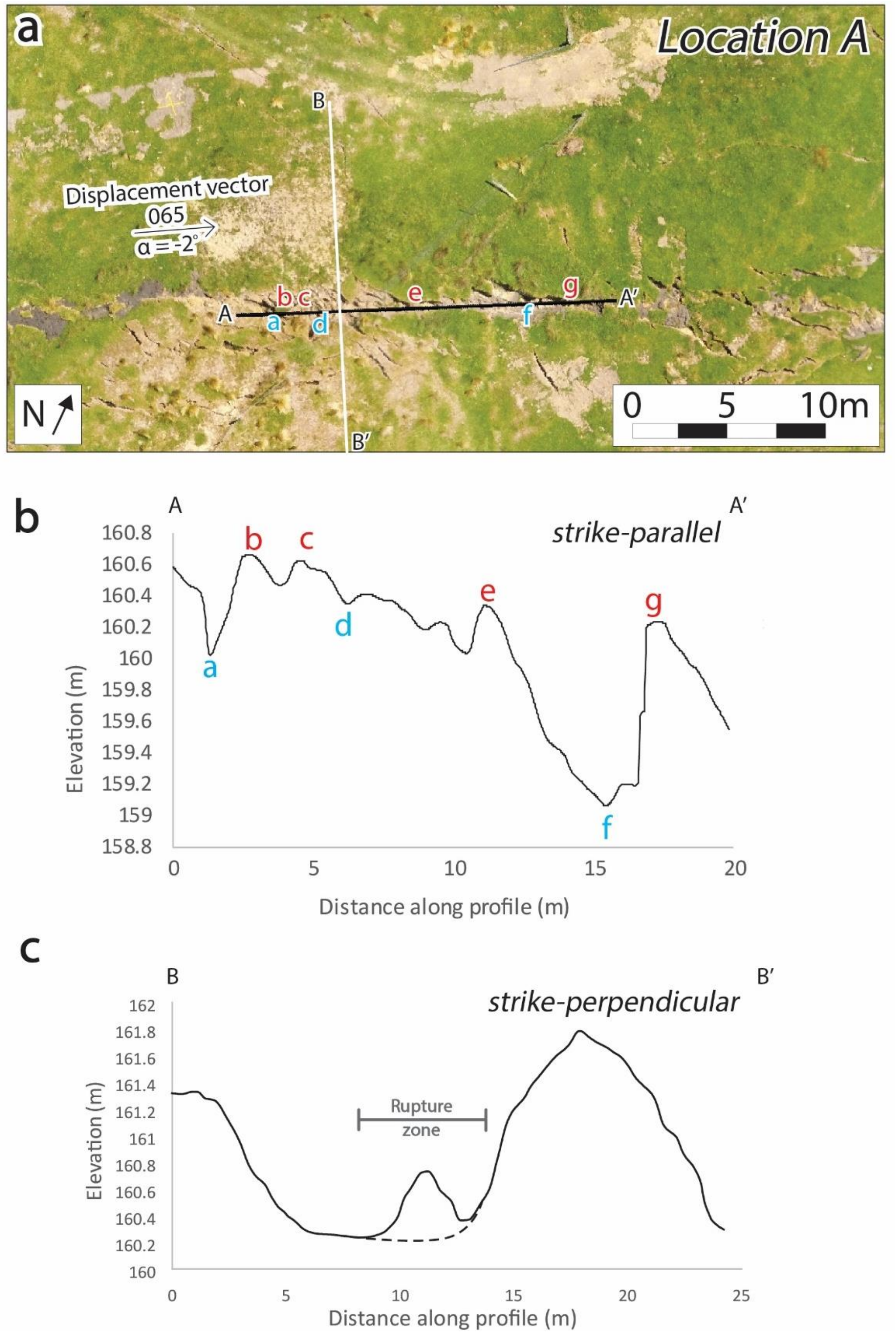

Figure 3.11: *Location A (Figure 3.10 for location), showing: a) annotated map view, with the labelled local displacement vector (almost pure strike-slip), b) a cross section in the fault-parallel direction, showing elevation of adjacent fissures and bulges (5.6x vert. exaggeration) and c), a cross section in the fault-perpendicular direction, showing the width of the rupture zone (labelled) and the total change in height (5.8x vert. exaggeration) of the raft bulge at this location as a result of deformation, above a (projected) pre-deformation ground surface for the rupture zone (dashed black line). Labels (a-g) along the profile A-A′ in 'a' and 'b' denote fissures and/or depressions (in blue) and rafts and/or bulges (in red). These profiles traverse a narrow set of rafts along a strand of the fault that is located just northeast of the large pull apart basin shown in Figure 3.2a.*

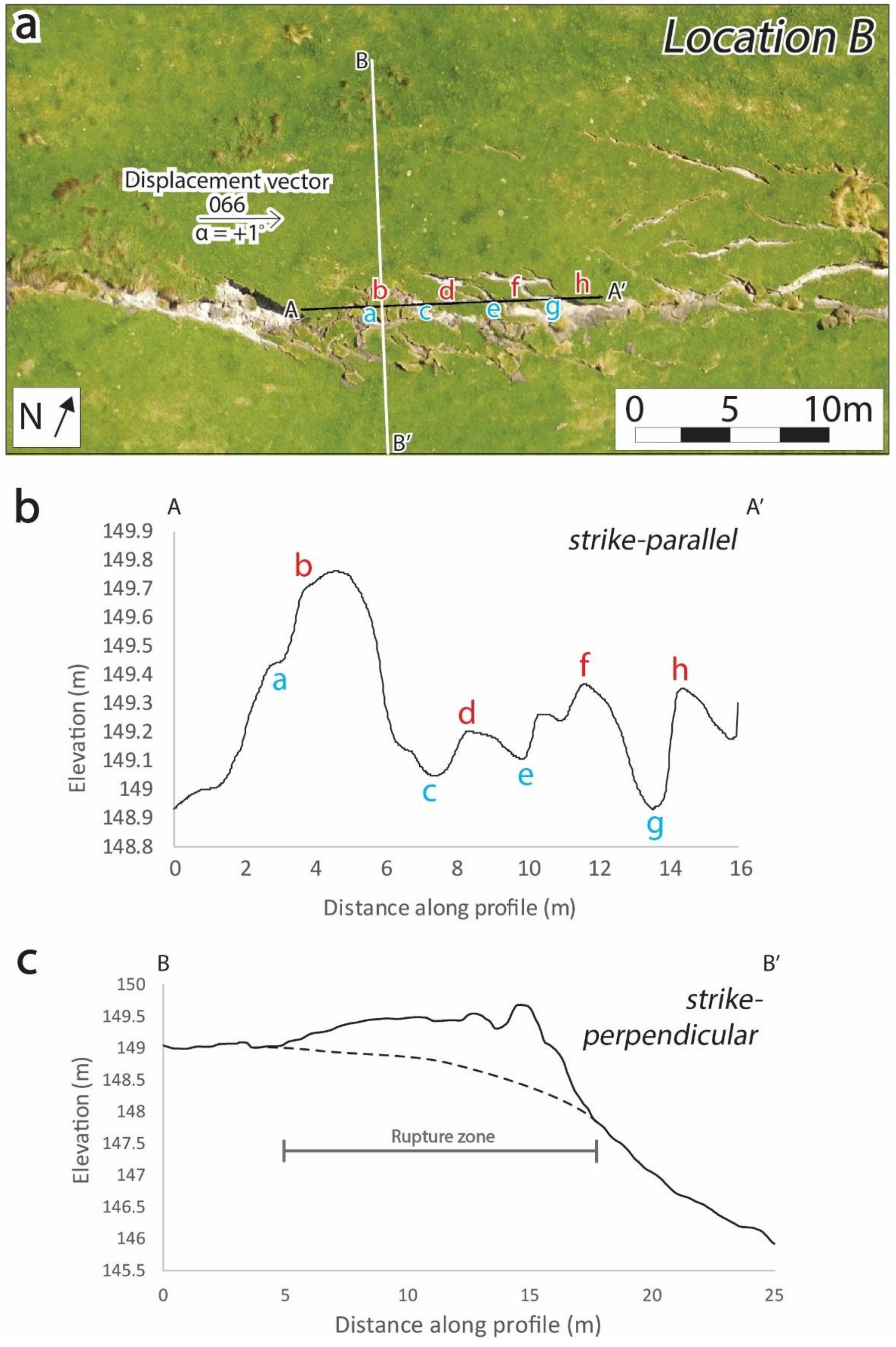

Figure 3.12: *Location B (Figure 3.10 for location), showing: a) annotated map view, with the labelled local displacement vector (almost pure strike-slip), b) a cross section in the fault-parallel direction, showing elevation of adjacent fissures and bulges (5.6x vert. exaggeration) and c), a cross section in the fault-perpendicular direction, showing the width of the rupture zone (labelled) and the total change in height (5.8x vert. exaggeration) of the raft bulge at this location as a result of deformation, above a (projected) pre-deformation ground surface for the rupture zone (dashed black line). Labels (a-h) along the profile A-A′ in 'a' and 'b' denote fissures and/or depressions (in blue) and rafts and/or bulges (in red). These profiles traverse a series of rafts which have begun to break apart into smaller rafts.*

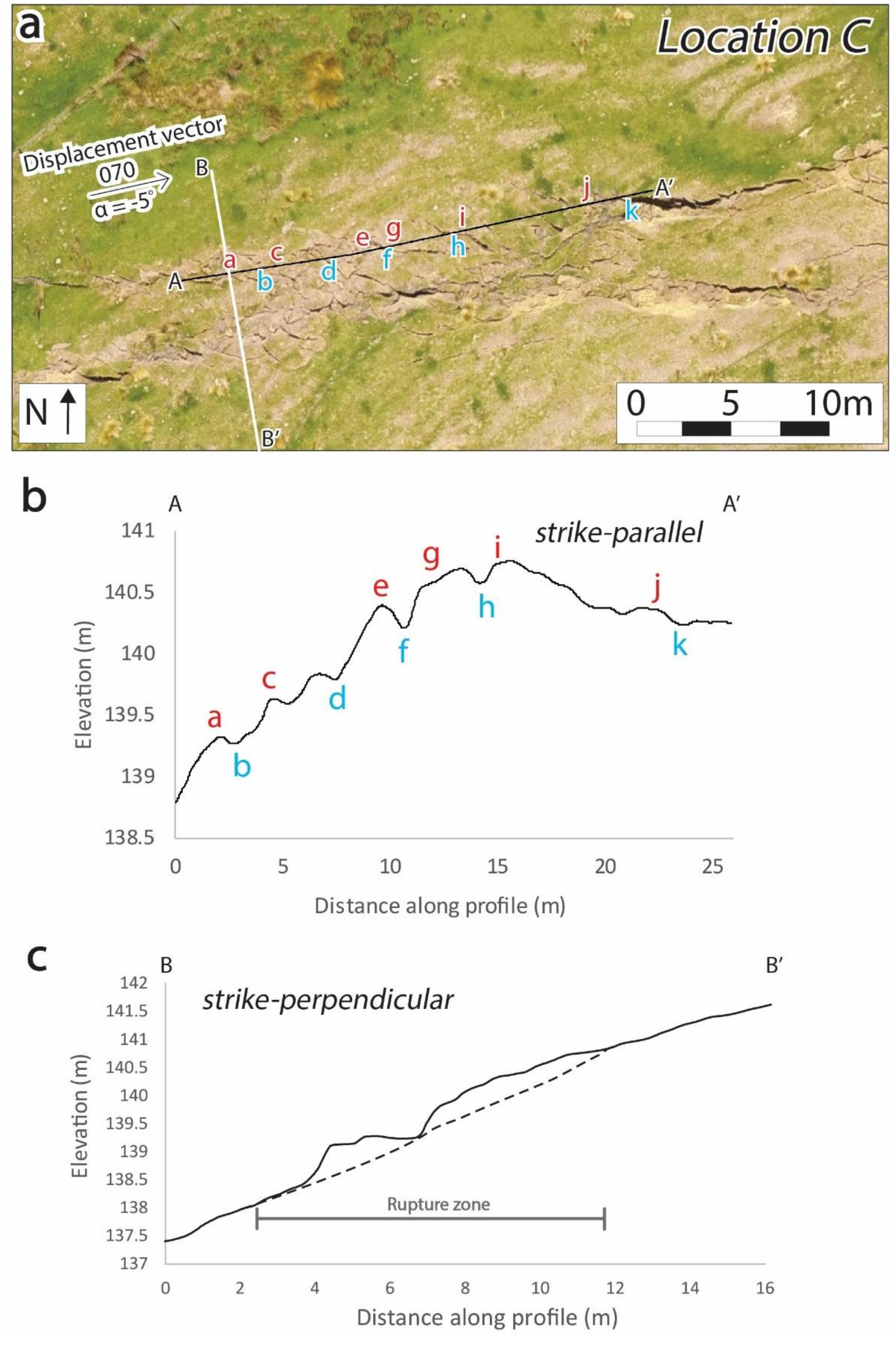

Figure 3.13: *Location C (Figure 3.10 for location), showing: a) annotated map view, with the labelled local displacement vector (slightly transtensive), b) a cross section in the fault-parallel direction, showing elevation of adjacent fissures and bulges (5.6x vert. exaggeration) and c), a cross section in the fault-perpendicular direction, showing the width of the rupture zone (labelled) and the total change in height (5.8x vert. exaggeration) of the raft bulge at this location as a result of deformation, above a (projected) pre-deformation ground surface for the rupture zone (dashed black line). Labels (a-k) along the profile A-A′ in 'a' and 'b' denote fissures and/or depressions (in blue) and rafts and/or bulges (in red). These profiles are located on a releasing bend of the fault and traverse a series of narrow, closely spaced rafts.*

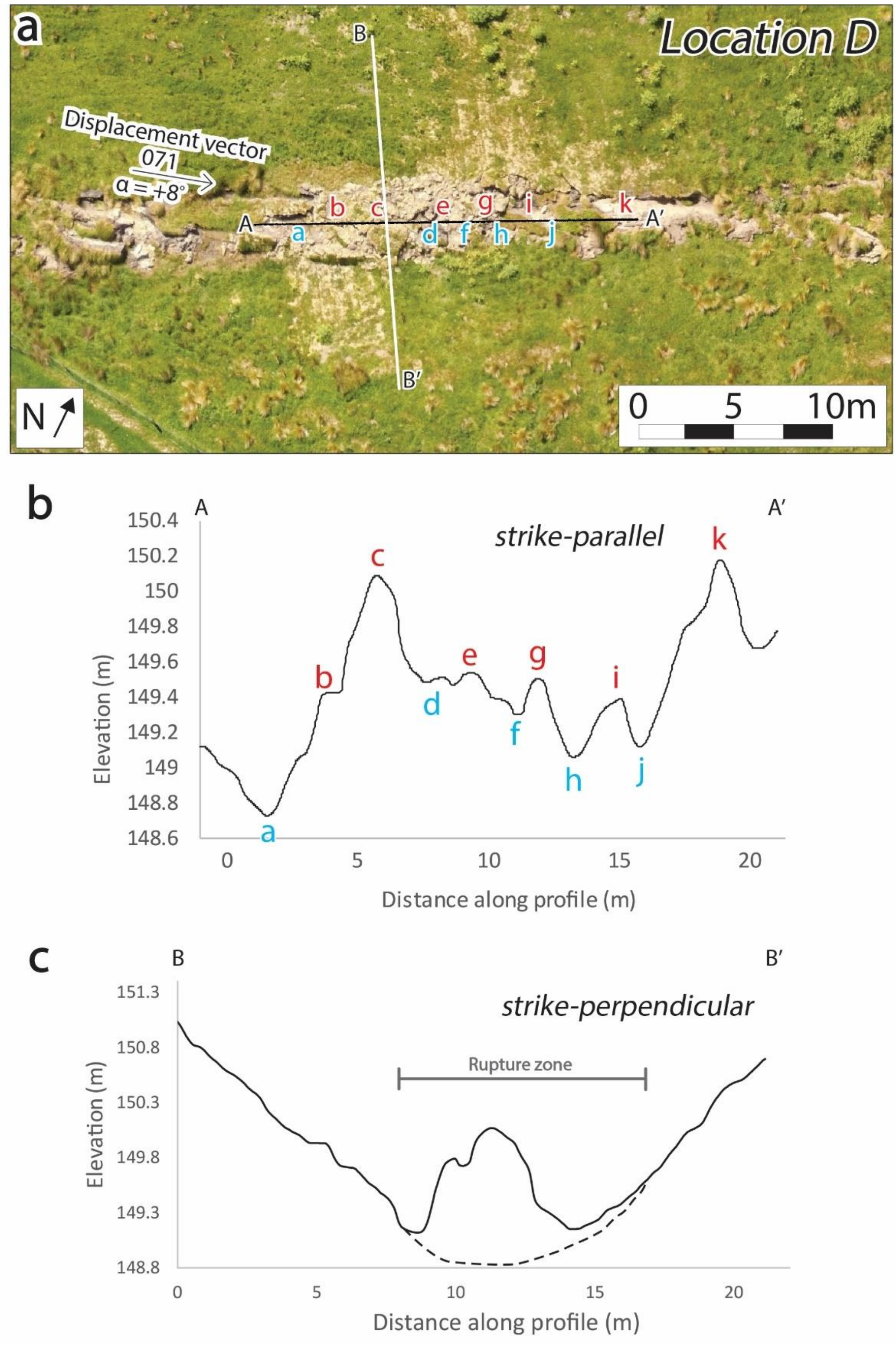

Figure 3.14: *Location D (Figure 3.10 for location), showing: a) annotated map view, with labelled local displacement vector (slightly transpressive), b) a cross section in the fault-parallel direction, showing elevation of adjacent fissures and bulges (5.6x vert. exaggeration) and c), a cross section in the fault-perpendicular direction, showing the width of the rupture zone (labelled) and the total change in height (5.8x vert. exaggeration) of the raft bulge at this location as a result of deformation, above a (projected) pre-deformation ground surface for the rupture zone (dashed black line). Labels (a-k) along the profile A-A′ in ‘a’ and ‘b’ denote fissures and/or depressions (in blue) and rafts and/or bulges (in red). These profiles traverse the site of the paleoseismic trench that was displaced in 2016 (see also Figure 3.8). The peaks (and troughs in ‘b’) appear more prominent in these profiles, possibly an effect of the previous excavation at this site (see text).*

Comparison of measurements from all four localities shows that the average elevations of deformational bulges (relative to a pre-deformation ground surface) at sites that featured local displacement angles varying between α = -5 to +8° ranged from 0.44 to 0.66 m, based on both the strike-parallel and strike-perpendicular measurements (with an average of 0.54 ± 0.3 m). Location C was the most transtensive (obliquely extensional) of the four sites, at α = -5°. Bulges at this location have the lowest mean transverse elevation compared to the others, an observation that is not unexpected because the amount of raft shortening strain (for the same amount of strike-slip) would have been less. On the other hand, Location D was the most transpressive (obliquely compressional) of the sites with a displacement angle of α = 8°. Bulges at this location have the highest mean transverse elevation, which again is not unexpected, as it would have had a higher amount of raft shortening strain for the same amount of strike-slip. It should be noted that many of the moletrack bulges most likely collapsed or toppled over following their uplift during the earthquake, and so the measured heights are in fact minimum estimates.

At face value, the profiles suggest that bulges are generally higher relative to this pre-deformation ground surface than the adjacent fissures are deep; however, this apparent asymmetry is likely at least in part an artefact of the fact that the DSM's cannot sample the true depth of the fissures because they are largely filled in with water and collapsed debris. Thus, the apparent fissure depths on the profiles are also minimum estimates.

In addition to the strike-perpendicular profiles that were taken at these four detailed study localities, 39 other rupture zone widths were measured at other places along the fault trace (both Napoleon and Tirohanga fault segments). The complete set of measurements (Appendix C.3.4) indicate an average total rupture zone width (for both of these segments) of 6.3 ± 1.7 m (1σ), and a mean inner rupture zone width of 2.1 ± 0.58 m (1σ). The average outer zone width is 4.1 ± 1.9 m (1σ), which is the difference between these values. Examples of these widths are shown in Figure 3.3c.

3.3.4 Reconstructing ground deformation along the Tirohanga segment of the Kekerengu Fault

The mapped part of the Tirohanga segment of the fault is ~23 m long and cuts across a paddock that had been recently ploughed at the time of the earthquake. The subsidiary strike-slip fault strand that I mapped and analyse here in detail is ~14 m to the south of the main fault trace that transects the southern part of Tirohanga Stream Valley (Figure 3.2c). The outer reaches of the rupture zone of this strand are up to 5 m in width, but generally <1.5 m wide. A total of ~3.5 ± 0.2 m of dextral displacement was accommodated across this strand of the fault (Tirohanga segment). This was estimated by using the up-raised, southwestern margin of the paddock as a linear marker. The area was selected for detailed analysis for two reasons: first, it has a lower amount of dextral slip than many other parts of the 2016 rupture trace, possibly giving insight as to how moletrack structures appeared elsewhere during early stages of the coseismic deformation. Second, well-defined plough cuts had been inscribed across the paddock just prior to the earthquake.

During the 2016 earthquake, the cuts influenced the way coseismic deformation evolved at the site, promoting fracturing parallel to the ~30 cm deep plough marks at an angle of ~40 degrees to the main fault trace. The plough cuts could still be observed days after the earthquake, and in places were able to be traced through the rupture zone (Figure 3.15), providing an opportunity to reconstruct the fabric (defined by the plough cuts) of the paddock back to its pre-earthquake state in attempt to further understand how different components of deformation (e.g., fault slip, bending of turf, rotation of fracture-bounded rafts/panels) contributed to a net accommodation of dextral slip at the site.

3.3.4.1 Approach to understanding moletrack structures (Tirohanga segment)

Due to the unique structure imposed by the plough marks at this site, the terminology used to describe natural (non-anthropogenic) fractures on the Napoleon segment (Table 3.1) could not be directly applied to the Tirohanga segment. At the latter site, I recognized and mapped three types of structures: 1) faults, 2) plough cuts, and 3) turf rafts, bounded by those cuts (see Table 3.2 for descriptions and refer to Figure 3.15).

This fault segment is shown in Figures 3.15a (orthophotography) and 3.15b (annotated orthophotography). Individual faults are mapped in Figure 3.15b. They are only observed on the southern side of the main fault trace (which strikes ~070) and generally have a strike that is 15-20° clockwise from this main fault trace. A small fault scarp formed at this location during the earthquake that was <1 m high (southwest side

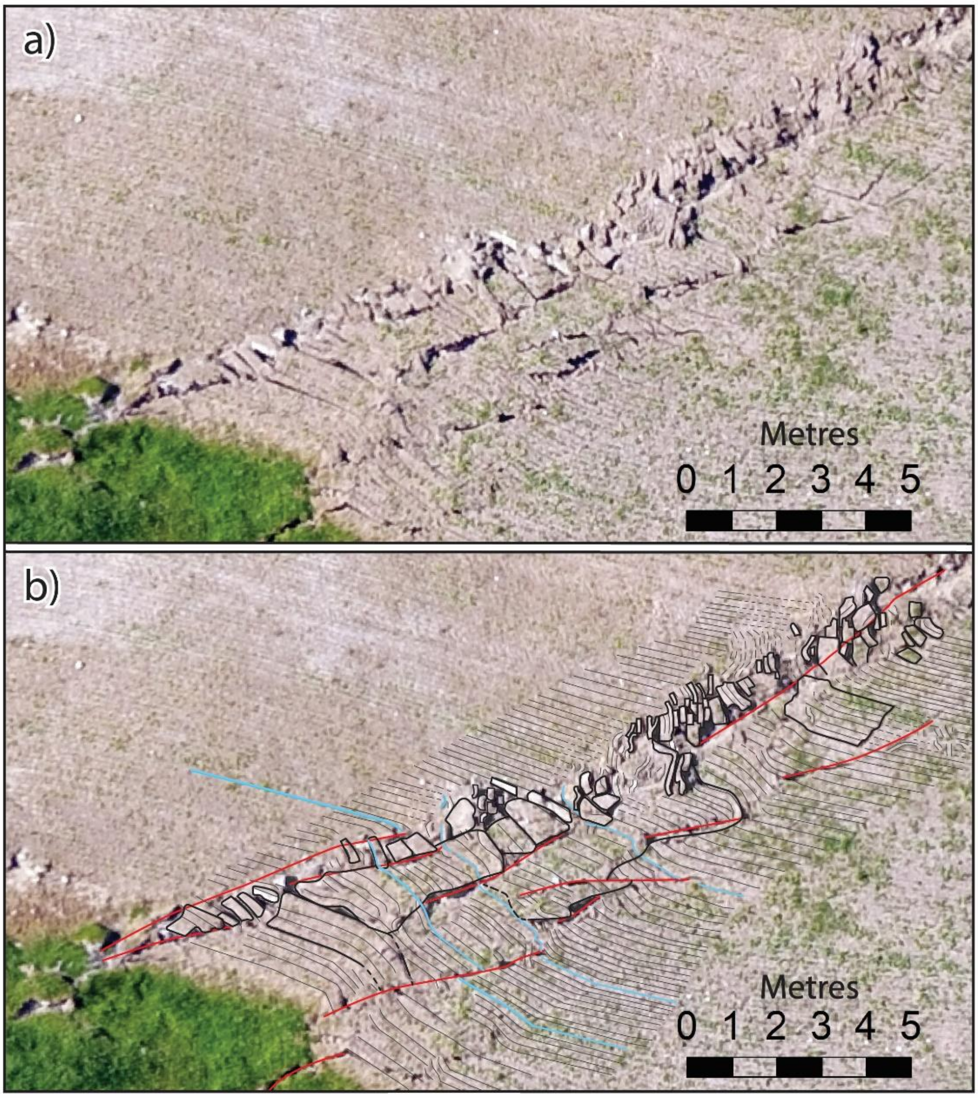

Figure 3.15: *Tirohanga segment of the Kekerengu Fault (Figure 3.2c) showing: a) orthophotograph taken by Zekkos et al. (2018), b) annotated orthophotograph showing faults (red), turf raft margins (black), and plough cuts that have been traced across the paddock (grey). Blue lines show single plough cuts that can be traced through the rupture zone.*

Table 3.2: Descriptions of different classes of ground breaks or fractures along the Tirohanga segment, shown in Figure 3.15b.

Type of fracture	**Description**
Faults (red lines)	Breaks in the ground that cut across the fabric lines and are not apparently influenced by the pre-existing fabric.
Plough cuts (grey lines)	Traces of the plough marks along the ground that in places can be tracked into (but rarely out the other side of) the deformation zone.
Turf rafts (black lines)	These are elongate rafts or panels of turf that are bounded by plough cuts on either side. Some are one plough spacing wide, forming narrow, elongate rafts, while others encompass several plough spacings, forming wider and more equant rafts.

upthrown), but subsequently collapsed. Individual plough cuts (shown by grey lines in Figure 3.15b) are 10-15 cm wide and approximately 30 cm deep. Often turf rafts broke along individual plough cuts, but were commonly several plough cuts wide towards the southwest end of this segment. These rafts range between 0.1 and 0.8 m wide and appear to be only a few tens of cm deep (depth of the cuts made by the plough).

In some places, individual plough cuts could be traced through the deformation zone to the other side (blue lines on Figure 3.15b). In other locations, it is extremely difficult to trace sections of deformed turf back to their pre-earthquake dispositions, particularly where the slip is localized and the strain is high, and/or where there is a local absence of traceable plough cuts. These limitations became more evident towards the northeast end of the fault segment. This segment of the fault has a known total strike-slip of 3.5 ± 0.2 m, which, together with the dense marker lines provided by the (now deformed) plough cuts, provides enough information to reconstruct the finite deformation accommodating that slip through the southwestern section of the ploughed paddock (blue lines on Figure 3.15b). Only the southwest part of the paddock was reconstructed, because plough cuts could not be traced through the rupture zone in the northeastern section.

The traces of the faults, plough cuts and turf rafts from Figure 3.15b were extracted to form a line drawing of the observed features (Figure 3.16). The offset of each of the blue plough cuts from Figure 3.15b was retro-deformed along each fault that transects them, and the deflection or bending of the plough cuts was straightened out by identifying and back-rotating the fracture-bounded turf rafts. The incremental slips that were accommodated by each of these processes can be measured. The first blue plough cut (furthest southwest) was analysed in this way, shown in Figure 3.16 - where each label (a-e) is associated with a different deformation mechanism and magnitude of displacement. These measurements of slip are shown in Table 3.3. The sum of these contributions on a transect spanning the rupture zone (farthest southwest blue line shown on Figure 3.15b) yielded an estimate for the total strike-slip of 3.7 ± 0.2 m for this segment, which is within the margin of error of the total displacement measured using the edge of the paddock (3.5 ± 0.2 m). This exercise shows that discrete slip is the main way that displacement is accommodated along the boundaries of the inner deformation zone, whereas rotational deformation, including distributed bending and raft rotation, dominates in the interior of that zone. Notably, there is also some distributed deformation in the outer deformation zone, at the location labelled e in Figure 3.16. Farther to the northeast along fault strike, tracing the plough cuts through the deformation zone was difficult, because the turf rafts commonly broke along single-spaced plough cuts, were quite narrow, and consequently were easily twisted. This means that incremental displacement estimates in these places are imprecise, and only the southwestern half of this fault segment could be restored to its pre-earthquake state (shown by the purple lines in Figure 3.16).

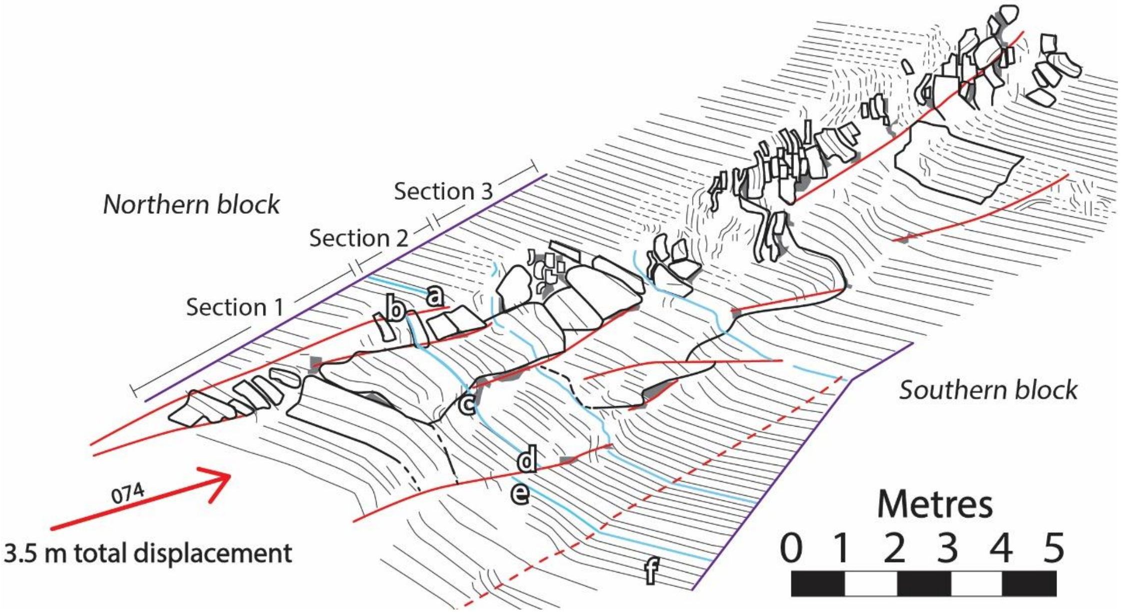

Figure 3.16: Line drawing of the features mapped in Figure 3.15b. Total displacement vector (of the northern block relative to southern block) is measured by the offset edge of the paddock, shown on the bottom left of the figure. Labels a-e show areas where displacement (either slip or rotational distributed deformation) could be measured (by offset or deflection, respectively) of a plough cut (blue line). These spot displacement measurements are shown in Table 3.3. Label f shows an example of the assumed original orientation of the plough marks for restoration purposes. The marginal purple lines are used as a start and end point for pre-earthquake restoration of the paddock, shown in Figure 3.18. Sections 1-3 were used as stages in the process of reconstruction (see section 3.3.4.2).

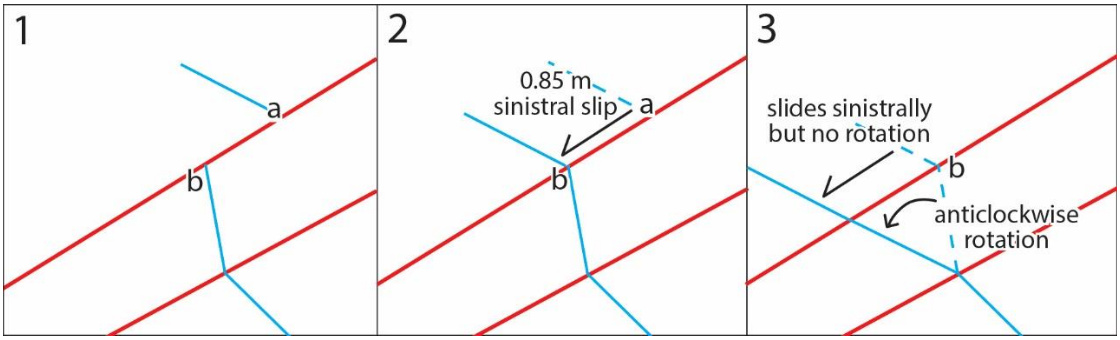

***Figure 3.17:** Schematic diagram illustrating the first stages of reconstructing a marker line (see section 3.3.4.2).*

3.3.4.2 Pre-earthquake restoration of a section of the Tirohanga segment

I made a reconstruction of this section of the paddock by: 1) keeping the far-field southwestern block fixed, 2) sliding the far-field northeastern block 3.5 m in the southwest direction, and 3) in the intervening deformed zone, incrementally "undoing" the displacement in order to restore the ploughing fabric to its original, nearly linear disposition (See Table 3.3). This process was done using line length balancing. The purple lines in Figure 3.16 are an arbitrary start and end point for these line length measurements, the only considerations being that they are placed outside the deformation zone and are roughly perpendicular to the original orientation of the plough lines, for simplicity. The area that was to be restored was broken up into three sections, based on the blue marker lines shown in Figure 3.16. These sections were restored successively from southwest to northeast. To do the reconstruction, I assumed that the plough lines were originally straight and parallel, aligned as they are outside the deformation zone at transect location 'f' (Figure 3.16). I also assumed that there was no shortening of any line lengths during deformation. This is equivalent to an assumption that the turf rafts were not internally deformed and behaved more or less rigidly, with all deformation accommodated by slip (also opening) along their margins.

Table 3.3: Measurements of displacement for the transect along the southwestern fabric trace (Figure 3.16).

Transect location	Amount of displacement	Deformation mechanism
a	0.85 ± 0.1 m	Discrete fault slip
b	0.57 ± 0.05 m	Distributed deformation - Turf raft rotation
c	0.4 ± 0.15 m	Distributed deformation - Pervasive shearing of plough cuts, turf raft rotation
d	0.5 ± 0.1 m	Discrete fault slip
e	1.35 ± 0.1 m	Distributed deformation - subtle rotation and pervasive shearing of plough cuts
f	0 m	Original orientation of plough cuts, undeformed

Section 1: The blue marker line was repositioned to its assumed original trend (straight, see Table 3.3). Working from the assumption that the southwest side of the fault is "fixed," I began undoing deformation at transect location a and continued toward the south along the blue plough line until I reached transect location 'e'. Because the deformation accumulates across the deformed zone, transect location 'a' represents the point that is the most deformed relative to the southwest end of the blue fabric line, and has been subsequently deformed by the motion of each of the other labels. By this logic, the part of the marker line northeast of label 'a' was slipped back sinistrally along the small fault by 0.85 m, until it was adjacent to the once contiguous blue line on the other side of the fault (see Figure 3.17, box 1 and 2). Next, the section of the blue line at label 'b' was rotated anticlockwise by fixing the southwest corner and rotating until it was parallel to the original orientation of the plough marks shown at label 'f' (Figure 3.16). Through this rotation, the section that was previously sinistrally slipped to match with b also moves backwards - however, its orientation relative to the fault does not change (see Figure 3.17, box 3).

Applying these methods to each datum (transect locations a-e), the blue marker line (plough cut) was restored back to its assumed original (straight) orientation (Figure 3.18). The rest of Section 1 of the fault segment (Figure 3.16) was then reconstructed using line length balancing techniques, including turf rafts, which were also straightened out to their pre-deformed state. Adjacent rafts that had to be rotated anticlockwise often involved an aspect of dextral slip to undo the deformation- indicating that sinistral (antithetic) slip was induced along turf raft margins during the earthquake. In addition to restoring the plough cuts of the paddock, I can also envision what faults would have looked like before they were deformed. To do this, rather than just measure from one end of a marker line to the other, points were marked along marker lines where they intersected faults. These points were then joined between adjacent marker lines to estimate where faults were located prior to deformation (Figure 3.18). Using these methods, and assuming parallelism between marker lines, Section 1 of the paddock was reconstructed (Figure 3.18). Areas of overlap between plough cuts or turf rafts were coloured green. This mainly occurred around faults and the edges of blocks as they were rotated anticlockwise. This could be a result of some stretching of line lengths during deformation and/or an artefact of the back-rotation of rafts. Gaps were also produced in several places and represent areas where undoing the deformation meant that some plough cuts (in their deformed state) were too short to cover the distance that they would have covered before they were deformed. These gaps were coloured grey (Figure 3.18) and are likely a result of line lengths being shortened during deformation, which was not accounted for. These overlaps and gaps suggest that contrary to our assumptions, line lengths did change during deformation, and the turf rafts that formed were not rigid but were themselves deformed as a result of this line length change.

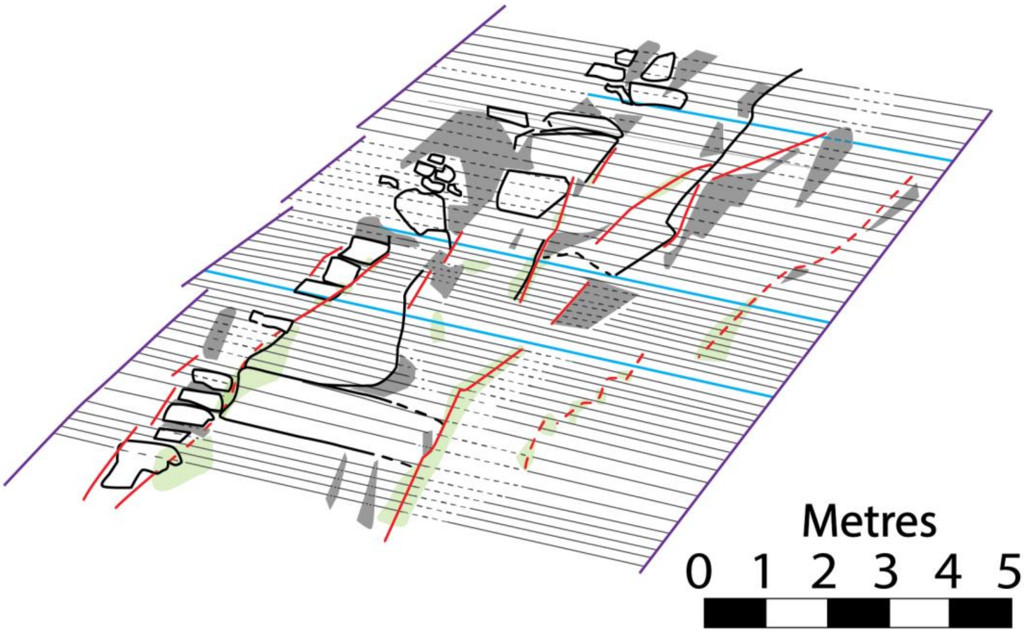

Figure 3.18: *Reconstruction of Sections 1-3 of the Tirohanga paddock (Figure 3.16). Green areas represent overlaps (apparent extensional zones); grey areas represent gaps (apparent contractional zones); and dashed grey lines represent parts of the ploughing fabric that could not be traced through the deformation zone. Red lines represent faults as they may have appeared prior to the earthquake.*

By attempting a restoration of this section of the Tirohanga paddock, it became clear that even at low amounts of slip, coseismic deformation of the ground surface was complex. Even with pre-existing markers to trace, restoring the paddock to a pre-earthquake state involved assumptions that do not appear to best represent the deformation process. Firstly, through the reconstruction process it became evident that some change in line lengths occurred during deformation and that this mostly involved shortening (rather than extension) (Figure 3.18). This likely occurred in a relatively uniform way to each plough cut; however, the way that sections were divided for ease of reconstruction may have affected where gaps appeared, making it seem as if shortening only occurred in certain areas. The assumption of originally straight, parallel plough cuts is also not necessarily valid, at least in some places. While generally this applies outside the deformation zone, nearer to the paddock edge, the plough lines bend as the farmer navigated the curved sides. This means that although I have forced lines to be straight and parallel in the pre-earthquake state, it may not best represent what the paddock actually looked like. However, without these assumptions, an already complex restoration process would become near impossible. This attempt still provides information about the process and accommodation of deformation, however simplified. The total amount of slip accommodated by distributed deformation was ~2.32 m, while finite slip accommodated ~1.35 m. This suggests that at low amounts of slip, distributed deformation plays a more important role in accommodating slip than finite slip.

3.4 Discussion

3.4.1 Are the Kaikōura earthquake moletracks different from previously described ones?

To understand if the moletracks that formed in the Kaikōura earthquake are unique when compared to other moletracks described in literature, a more detailed, numerical comparison of their morphologies is needed. Consequently, for this analysis I compare displacement, height (relative to a pre-deformation ground surface) and rupture zone width measurements of the Kaikōura moletrack bulges (from section 3.3 of this thesis) with those described by Lin et al. (2004) in association with the Kunlun earthquake in China, and with those from the Darfield earthquake in Christchurch, New Zealand, described by Quigley et al. (2010).

3.4.1.1 Comparison of slip magnitude and rupture zone width between earthquakes

The Kaikōura earthquake accommodated an average of 5-6 m of slip at the surface along the Kekerengu (onshore) and Needles (offshore) Faults (Kearse et al., 2018). In the Napoleon segment (Figure 3.2a), the Kekerengu Fault slipped dextrally by 7-9 m, whereas the Tirohanga segment (evaluated in Figures 3.15 and 3.16) slipped by only ~3.5 m. The measurements of the average outer and inner rupture zone widths (of both of these fault segments) are 6.3 ± 1.7 m and 2.1 ± 0.58 m respectively (1σ). These are narrower than the rupture zone widths reported in the studies of the Kunlun and Darfield earthquakes. The Kunlun earthquake generally had between 4 and 8 m of sinistral slip, distributed across a zone between 5-50 m wide (Lin et al., 2004), whereas the Darfield earthquake accommodated an average of ~2.5 m of dextral slip across a zone that was between 30 and 300 m wide (Quigley et al., 2010).

This comparison shows that the rupture zones in both these earthquakes experienced a lower magnitude of finite shear strain in the ground than the eastern Kekerengu Fault during the Kaikōura earthquake. This difference in the degree of strain localization and magnitude of finite shear strain is probably responsible for differences in the degree and style of evolution of their respective moletrack structures.

3.4.1.2 Comparison of moletrack elevations (above a pre-deformation ground surface)

Although a higher finite shear strain was absorbed in the ground along the Kekerengu Fault during the Kaikōura earthquake, this difference is not apparently reflected in the elevations of the moletracks (relative to a pre-earthquake ground surface) compared to those formed in the two other earthquakes. In our study area, the Kaikōura moletracks average about 0.54 m in height (relative to a projected pre-deformation ground surface), reaching 1-2 m in places (Figures 3.6, 3.7 and 3.14). These height measurements are not dissimilar from the bulge heights measured in the Darfield earthquake. During the Darfield earthquake, moletracks formed in alluvial materials along the Greendale Fault in response to 1.5-4.5 m of dextral slip, and were generally <0.5 m high, but reached ~1 m in places (Quigley et al., 2010). The Kunlun earthquake moletracks were generally between 0.5 and 1 m high, but locally reached up to ~3 m in places where the fault ruptured through frozen alluvial materials (Lin et al., 2004).

These comparisons show that the elevation of moletracks (relative to undeformed ground) is not necessarily tied to the width of the total rupture zone or the amount of strike-slip accommodated by it. In the case of the Kunlun earthquake, the extreme moletrack heights of <3 m (relative to the undeformed ground surface) were observed only in frozen alluvial materials. In contrast, unfrozen alluvial sediments were bulged up to heights of between 0.3 and 1 m (Lin et al., 2004). This difference in height suggests that the elevation values of <3 m in this earthquake were a result of the frozen sediments, which would have a higher cohesion, and therefore not collapse like unfrozen or unconsolidated alluvial sediments would (creating higher elevations).

3.4.1.3 Impact of cohesion of sediments on moletrack morphology

The Kekerengu Fault moletracks feature rotated turf rafts, bounded by original synthetic Riedel faults that rotated to accommodate deformation, while slipping sinistrally and opening up as fissures (Figures 3.5, 3.11-3.14). Such structures were not described for the Darfield earthquake (Quigley et al., 2010). Ground deformation during the Darfield earthquake featured a series of *en echelon* surface traces of R faults; however, although these faults broke up the turf into semi-rectangular blocks, they did not apparently experience measurable clockwise rotations about a vertical axis. Quigley et al. (2010) states that the ruptured paddocks likely consisted of “a considerable thickness of poorly consolidated alluvial gravels”. This lack of consolidation or cohesion in the sediments could be a reason that well-defined rafts did not form or rotate, as the rafts could not hold together as they rotated coseismically.

As stated in Dooley and Schreurs (2012), in the strike-slip faulting experiments conducted in sand (i.e., very little cohesion), faults formed rapidly and linked together to accommodate the majority of the deformation; this is analogous to the way deformation was accommodated in the Darfield earthquake, where gravels simply slid past one another and formed faults rather than coherent rafts or blocks. Contrastingly, along the eastern Kekerengu Fault, the Kaikōura earthquake produced a multitude of coherent rafts that rotated to accommodate deformation. The deformed ground materials generally consisted of several metres of wet (old, and consolidated) clay-rich sediments capped by a several dm-thick layer of grass-bounded topsoil or turf. This material suggests an analogy with the clay experiments from Dooley and Schreurs (2012).

Based on this comparison, I suggest that the cohesion of the material involved in the deformation of a rupture zone has an impact on the shape of the associated moletracks, as well as the fractures that form and the way that these fractures and moletracks (or push-ups) accommodate slip during an earthquake. This interpretation agrees with the findings from Lin et al. (2004) in regards to the Kunlun earthquake in China, where two primary types of moletracks were distinguished based on differences in the shape between structures that had formed in frozen, consolidated sediments (angular ridge structures), and the structures that formed in semi-consolidated sediments (bulged ridges). The moletracks that formed in the consolidated sediments formed slabs that are comparable to the turf rafts observed in the Kaikōura moletracks; however, these slabs were not described with regards to any aspect of coseismic rotation.

3.4.2 Evolution of moletrack structures

3.4.2.1 Comparison of moletracks on parts of the fault with different slip magnitudes

To understand the structure and morphology of strike-slip rupture zones, one must understand the path by which they evolved from their initial to final states. One method that can help us to achieve this is to compare sites along the fault with low displacement magnitudes (“less evolved”) to those with high displacement magnitudes (“well evolved”), inspect the differences between them, and then attempt to “fill in the blanks” in the evolutionary process that might have linked these differing states of moletrack development. Using the Tirohanga segment (Figure 3.2c) as an example of a section of the fault with low slip (~3.5 m), one might understand the early stages of the deformation process. In Figure 3.15, in the southwest corner of the segment, the rupture zone is ~5 m wide and narrows towards the northwest. As shown in the method of reconstruction in Figures 3.15-3.18, this southwest section of the paddock accommodates motion not only by discrete slip along small faults, but also through distributed deformation that occurs in both the inner and outer deformation zone. In this stage of development (lower slip), the bending and shearing of the turf bounded by plough cuts is a more prominent deformation mechanism than their clockwise rotation - although raft rotation does become a more dominant part of the deformation process toward the northeast end of the Tirohanga fault segment shown in Figure 3.15.

Comparing these mechanisms of deformation to those within the Napoleon segment (~7-9 m displacement), processes accommodating deformation are similar, but rotation of R-fault bounded turf rafts is a more visually prominent part of the deformation process along the Napoleon segment. This is because there, the rupture zone is more evolved (larger total slip), and any subtler mechanisms such as shearing and bending were overwhelmed by the rotation of the natural turf rafts which, are wider and deeper-seated than the narrow turf rafts bounded by the plough cuts in the Tirohanga segment. With progressive slip, the turf rafts in the Napoleon segment were broken up and disaggregated by a later set of fractures that I infer to have had an initially antithetic sense of slip (R' fractures), thus complicating the structure of the inner rupture zone on the surface. Some strips of ground were laterally displaced away from their site of origin by slip on (throughgoing) strike-slip fault strands (Y faults), making it difficult to reconstruct the moletrack without having pre-earthquake information (such as exists at the trench site, and along the Tirohanga segment).

3.4.2.2 Quantification of slip partitioning during the earthquake (Napoleon segment)

Applying a simple block rotation model (Figure 3.19) to the information on Riedel faults I gathered from the structural maps, I quantify the relative importance of rotational distributed deformation (of the turf rafts) in accommodating the total displacement along the Napoleon segment of the Kekerengu Fault. Because the average displacement vector trend (067) is parallel to average fault strike (067) for this ~1.2 km-long section of the fault, I assume that the heave (or fault-perpendicular convergence) across this segment is relatively negligible - though locally it is important, where the local fault strike swings away from the mean value (i.e., at Locations C and D in Figures 3.10, 3.13 and 3.14). Thus, the rupture zone width is not allowed to change during coseismic slip, which means that the turf rafts are forced to shorten as they are rotated clockwise to fit within a constant width of rupture zone.

To estimate the average shortening magnitude according to this geometrical model, I used the averages of the following quantities measured along the Napoleon segment: fault strike, inner rupture zone width, and the strikes of both R faults and rotated R faults (relative to the local fault strike). Structural interpretation of the detailed orthophotography along the Napoleon segment of the fault showed that the average angle of R faults relative to local fault strike was 22°, while their rotated counterparts

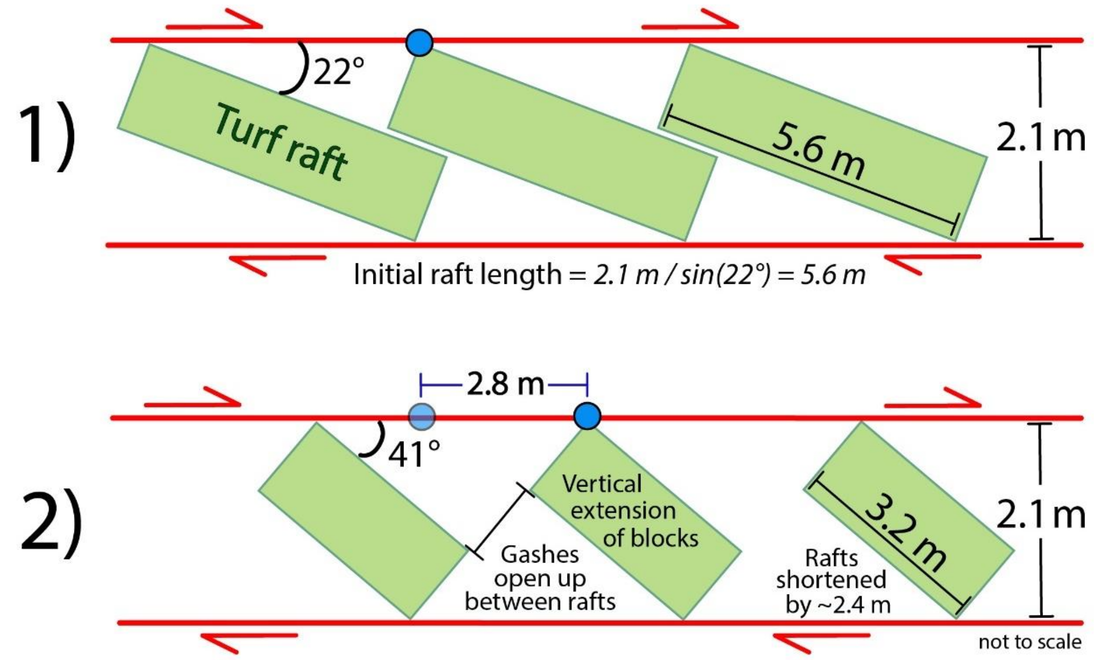

Figure 3.19: *Simple block rotation model (aerial view) showing the mechanism by which raft rotation might accommodate pure strike-slip motion. Values of inner rupture zone width, and initial and deformed strikes of R faults (relative to main fault strike) presented are based on the mean values for the entire Napoleon segment of the fault. Blue dots show the pre- and post-deformation points of the corner of a raft, with the inferred mean amount of dextral slip that this average raft rotation accommodated coseismically (~2.8 m). Rafts are shortened by ~2.4 m on average to fit within a fixed final width of rupture zone (2.1 m). Any change in rupture zone width during deformation as a result of heave is not considered in this model.*

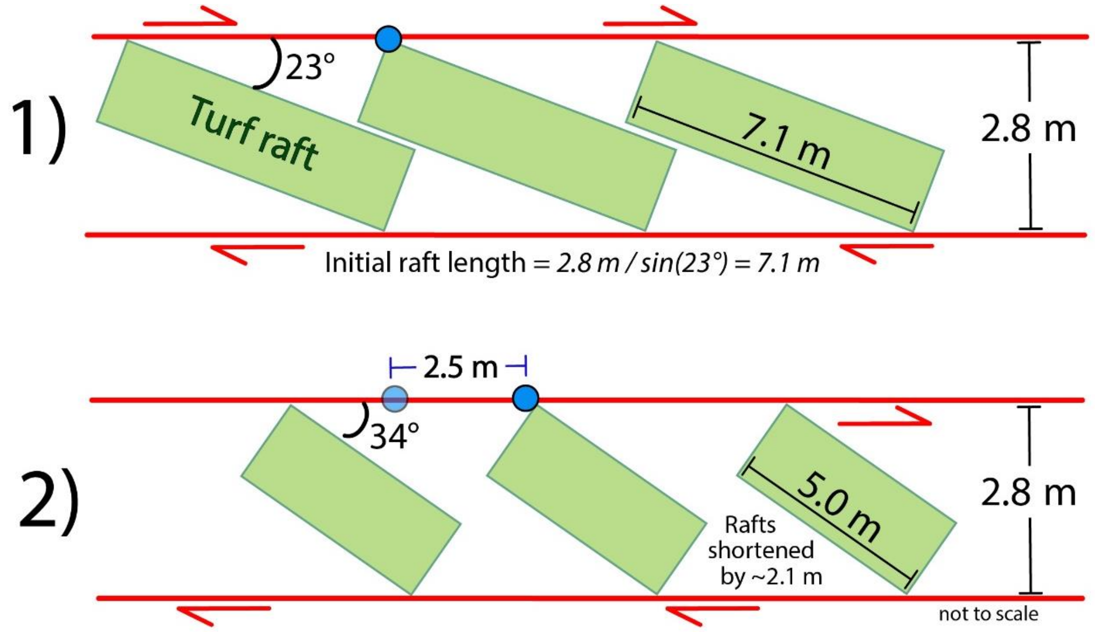

Figure 3.20: *See Figure 3.19 and section 3.4.2 for explanation of block rotation model. These values of rupture zone width and R fault strike (both initial and deformed) are specific to the paleoseismic trench site (see also Figure 3.2a, 3.7, 3.14). Blue dots show the pre- and post-deformation points of the corner of a raft, with the inferred amount of slip that this raft rotation accommodated coseismically (~2.5 m). Any change in rupture zone width during deformation as a result of heave is not considered in this model.*

averaged a strike of 41° (examples in Figure 3.3b, 3.9b, see also Appendix C.3.2). As previously stated, this suggests an average clockwise rotation of the R faults and turf rafts by 19° during the 2016 earthquake. Furthermore, the average width of the inner rupture zone (the zone containing the rotated turf rafts) is measured as ~2.1 m (see Appendix C.3.4). Assuming that the inception angle of 22° for R faults relative to the main fault strike is representative of the initial angle at which turf rafts generally form, I estimate an average elongate length for the rafts prior to deformation using simple trigonometry; this mean raft length is 5.6 m (Figure 3.19). Given this set of parameters, for a section of fault that accommodated 9 m of dextral displacement, ~30% of the dextral slip component of displacement seems to have been accommodated by the rotational deformation (coseismic rotation of the rafts) - that is, ~2.8 m of dextral slip on average (Figure 3.19). During this rotation, rafts were shortened on average by ~2.4 ± 0.9 m parallel to their bounding rotated R faults.

The relative amount of slip accommodated by rotational deformation appears to be nearly constant across the Napoleon segment, despite variations in total slip from site to site. This follows from the nearly constant final rupture zone width from place to place, and the only minor variation in the original strike of the R faults and the magnitude of their rotation, despite large differences in the total displacement. These relationships suggest that there is a point at which raft rotation ceases to accommodate slip early on in the earthquake, and after this point, slip is transferred either onto throughgoing faults or fault strands and is accommodated as discrete slip. By increasing the total slip in the model shown in Figure 3.19 and noting the change(s) in the partitioning of this total slip (ratio of slip accommodated by distributed deformation vs discrete slip), I determine that the transition point at which rotation ceases to accommodate slip is at (up to) ~3 m. This value agrees with my data from the Tirohanga segment of the fault, that had only ~3.5 m of slip, most of which was accommodated by distributed and rotational deformation.

3.4.2.3 Quantification of slip partitioning during the earthquake (trench site/Location D)

Although the estimate of slip partitioning calculated in section 3.4.2.2 above is based on a set of averages across the whole length of this fault segment, applying this model to specific sections of the fault yields similar results. For example, using values specific to the paleoseismic trench site implies a similar partitioning of finite slip and distributed deformation (Figure 3.20). This site is transpressional (α = 8°) and accommodates 9.1 m of dextral slip. Turf rafts have been rotated ~11° (from 23° to 34°) within a 2.8 m wide inner rupture zone. Based on simple trigonometry, the rafts were initially ~7.1 m long (measured parallel to the rotated R faults). Using these data, the block rotation model predicts that ~27% of the dextral displacement was accommodated by rotational deformation (equivalent to ~2.5 m of slip, see Figure 3.20); and that the rafts were shortened by ~2.1 m during their rotation (see Figure 3.14a).

3.4.2.4 Effect of local contractional heave of the rupture zone on slip partitioning

According to the block model, a decrease in the rupture zone width during deformation would cause a corresponding decrease in the length of the rafts – i.e., for the same net rotation angle, the shortening magnitude experienced by the raft (measured in meters) increases, as does the amount of strike-slip accommodated by rotational deformation. While the main control on the shortening strain accommodated by turf rafts in this model is their original strike and their rotation angle (discordance between strike of R faults and rotated R faults), an additional control is imposed by the heave, as this will shorten the width of rupture zone that the rafts are contained within – contributing to the raft shortening (perhaps significantly, if the site is transpressive and has a high value of α).

For example, the paleoseismic trench site has a displacement angle of α = 8°, resulting in a heave of 1.3 m; this means that during deformation, the rupture zone is shortened from 4.1 m to 2.8 m as a result of the heave (see Figure 3.21). This difference in rupture zone width affects the calculated change in raft length (i.e., shortening) during its rotation. Introducing an extra contractional heave to the displacement vector means that the unrotated rafts would have resided in an initially wider zone and had greater pre-deformational lengths than would be the case for pure strike-slip displacement (i.e., lacking any heave). Restoring the heave yields an initially wider rupture zone, containing initially longer rafts — whereas the final rupture zone widths and final raft lengths in these two cases (either with or without heave) are the same (see Figures 3.20 and 3.21).

Put another way, where there has been a contractional heave (transpression), turf rafts are forced to experience an additional increment of shortening in order to fit within the narrowed, contracted width of rupture zone (Figure 3.21). As shown in Figure 3.20, if one ignores heave (assumes perfect strike-slip), the model predicts that rafts at the trench site were shortened by ~2.1 m during their rotation, but this estimate increases to ~5.5 m when the 1.3 m heave is included in the displacement (Figure 3.21). This results in ~50% of the total slip being accommodated as discrete slip, and 50% as distributed deformation. This shows that the calculated raft shortening for a given amount of raft rotation is greater for a transpressive displacement than for a strike-slip one, even though the strike-slip component is equivalent (Figure 3.20 vs Figure 3.21).

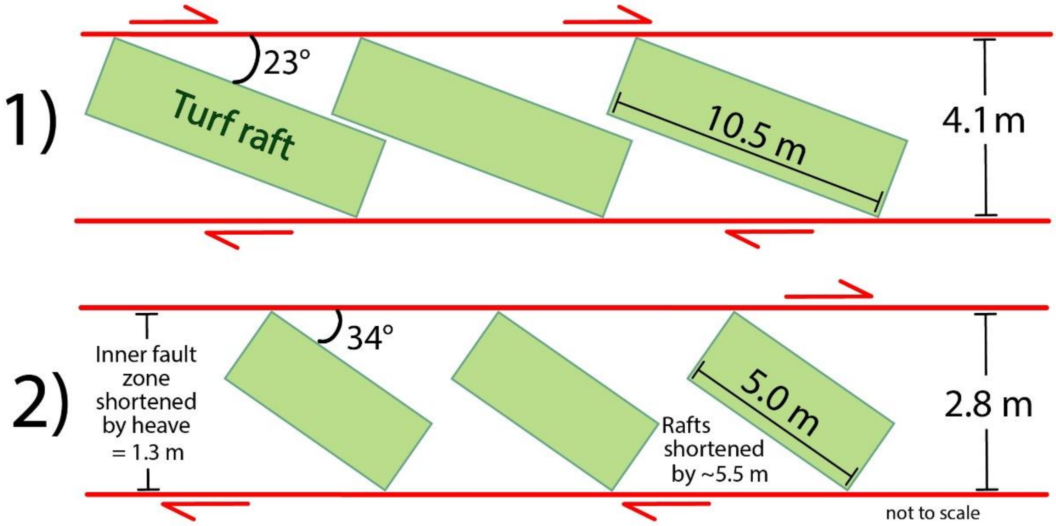

Intial raft length = *4.1 m / sin(23°) = 10.5 m*

Final raft length = *2.8 m / sin(34°) = 5.0 m*

Rafts shortened by an additional ~3.4 m as a result of heave

Figure 3.21: *Modification of Figure 3.20 to show how the simple block rotation model can accommodate deformation that is slightly transpressional (i.e., includes component of contractional heave) rather than pure strike-slip. This site (α = 8°) has a heave of 1.3 m; the inner rupture zone initiates at 4.1 m wide but is shortened by this 1.3 m during deformation. The addition of this contractional heave increases the total raft-parallel shortening from 2.1 m (see Figure 3.20) to 5.5 m, as rafts are forced to fit within a narrower rupture zone.*

3.4.3 Detachment depth of turf rafts

The depth to detachment for the rotated rafts (below a pre-deformation ground surface) can be estimated if we know the following: 1) the final length of a turf raft parallel to the rotated Riedel faults, 2) the deformation-induced “excess” volume (or in a profile parallel to the raft axis, the “excess” area) of material in that raft that has been bulged upward above the pre-deformational ground surface; and 3) the magnitude of horizontal shortening of the raft that drove the upward bulging, some part of which may have been contributed by any contractional fault heave (i.e., transpression). If one assumes that the total volume (or in profile, area) of a raft does not change during the deformation, then for a given amount of raft shortening, greater magnitudes of bulge excess area indicate deeper detachment depths (below a pre-deformation ground surface, see Figure 3.22 for further explanation). In this analysis I am assuming: 1) that the deformed ground does not experience a significant dilatation (volume change) during the earthquake; and 2) the rafts are shortened uniaxially as they rotate without changing in transverse width (as they abut open fissures on each side). The assumption that the rafts do not change in width reduces the problem to 2D area balancing, as observed in a profile parallel to the long axis of the raft (i.e., parallel to the rotated Riedel faults).

I use topographical profiles in this direction to measure the excess area of some raft bulges above the pre-deformational ground surface (see Figures 3.23-3.26). To estimate the amount of contractional shortening (change in horizontal length) parallel to the raft axis, I use the change strike of its bounding R faults. Using the block rotation model, and (in this example) assuming a deformation zone of fixed width perpendicular to strike, the change between the initial and final strike angles determines to a unique value of shortening in order for the rotated rafts (assumed to be non-rigid) to remain inside the fixed transverse width of that deformation zone. Based on a (final) mean inner rupture zone width of 2.1 ± 0.58 m, and the mean (assumed original) strike of the R faults relative to the main fault strike in the outer rupture zone (22 ± 5°), I estimate that the average raft length prior to deformation was ~5.6 ± 0.5 m. My data indicates that during the earthquake, the rafts rotated clockwise by an average of ~19°, which results in a final raft length of 3.2 ± 0.4 m, and an average raft shortening of 2.4 ± 0.9 m (see Figure 3.19). All ranges in the data above are 1σ.

3.4.3.1 Estimating detachment depth for the Napoleon segment

Profiles were drawn parallel to the axis of the deformed rafts at 28 locations along the Napoleon segment of the fault. Examples of these profiles are shown in Figures 3.23-3.26. The range in excess area for these rafts is 0.2-5.4 m^2 (calculated from values presented in Appendix D.3.7), with an average of 1.67 ± 1.56 m^2 (1σ). Dividing this average excess area by the average raft shortening that is calculated using the block model (~2.4 m) indicates an average detachment depth of ~0.7 ± 0.6 m (1σ) below a pre-deformation ground surface. This is an estimate of the thickness of the turf rafts that were detached at depth and deformed into the observed moletrack bulges. The standard deviations of the individual parameters used to calculate excess raft area and detachment depth are large, consequently producing large standard deviations for the these resulting parameters. This is not unreasonable considering the variable local kinematic setting (transpression, transtension, pure strike-slip), the frequent changes between one simple rupture trace and multiple rupture strands, and the complex moletrack patterns that was produced throughout the Napoleon segment during the earthquake. It is also likely that changes in the local stratigraphy of the near surface sediments contributes to lateral variations in raft thickness/detachment depth. The parameters listed above each contribute somewhat to the measured differences in raft length and height, which in turn affect the excess raft area and detachment depth.

Other information relevant to an assessment of the detachment depth of these rafts is the minimum fissure depths shown on the profiles in Figures 3.11-3.14. These are minimum depths because the LIDAR cannot survey the true depths of the fissures, as after the earthquake they were soon infilled with water and debris. The depth of these fissures prior to infilling should reflect an approximate detachment depth for the turf rafts, as they show the approximate depth to which ground deformation penetrated. Examining these profiles, it is difficult to determine a pre-deformation ground surface, as profiles are parallel to the rupture zone, however, the fissure depths reach a maximum of ~1 m (which is within error of the average detachment depth, 0.7 ± 0.6 m). Fissures observed in the field soon after the earthquake (by Kearse et. al., 2018 and others) also reached up to ~1 m in depth. The agreement in results from these different methods of estimating detachment depths suggests that while there is a large standard deviation for my average estimates of detachment depth, the results are robust.

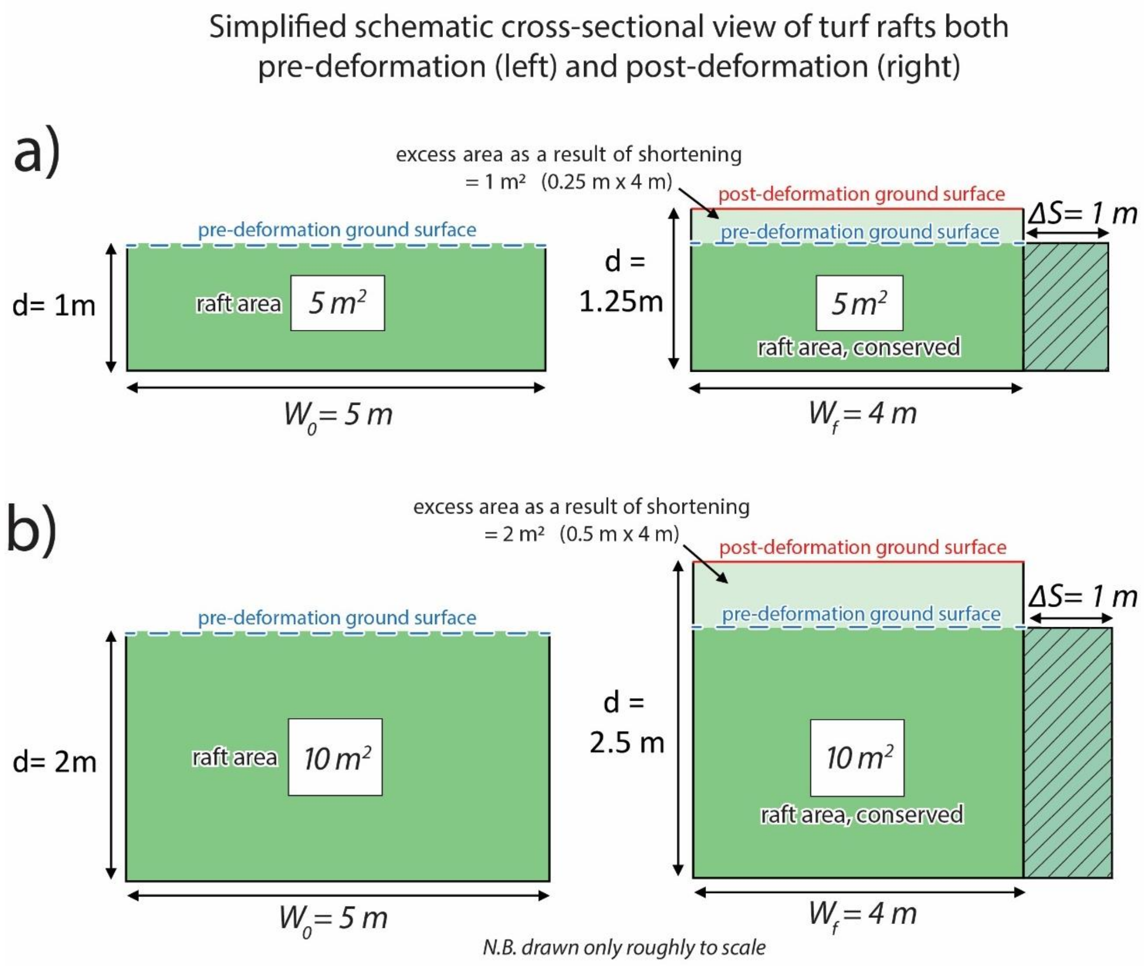

Figure 3.22: *Assuming area is conserved within a 2D, cross-sectional plane of view during deformation, for a given amount of raft parallel shortening (in this example, $\Delta S = 1$ m), greater values of excess area indicate deeper detachment depths. For example, in a), the area of a raft is fixed at 5 m^2, with an initial width $W_0 = 5$m, and a depth of 1 m below a pre-deformation ground surface (dashed in blue and labelled). After 1 m of shortening parallel to the raft, the final raft width $W_f = 4$ m, and so to conserve the 5 m^2 area, the depth below the new ground surface (shown in red and labelled) increases from 1 m to 1.25 m. This results in an excess area of 1 m^2 (light green shading, labelled). In b), the same amount of raft parallel shortening is applied to a 10 m^2 raft with a depth of 2 m below the pre-deformation ground surface (dashed in blue, labelled). The raft width reduces from 5 m to 4 m during deformation, which increases the depth by 0.5 m to conserve the 10 m^2 area. This results in an excess area of 2m^2 above the new, post-deformation ground surface (shown in red) - demonstrating that the greater excess area produced in ‘b’ has a greater associated detachment depth (2.5 m below the ground surface) compared to ‘a’ (1.25 m). This indicates that in the field, greater observed excess areas of turf rafts or bulges above the ground surface indicate deeper detachment depths, and vice versa.*

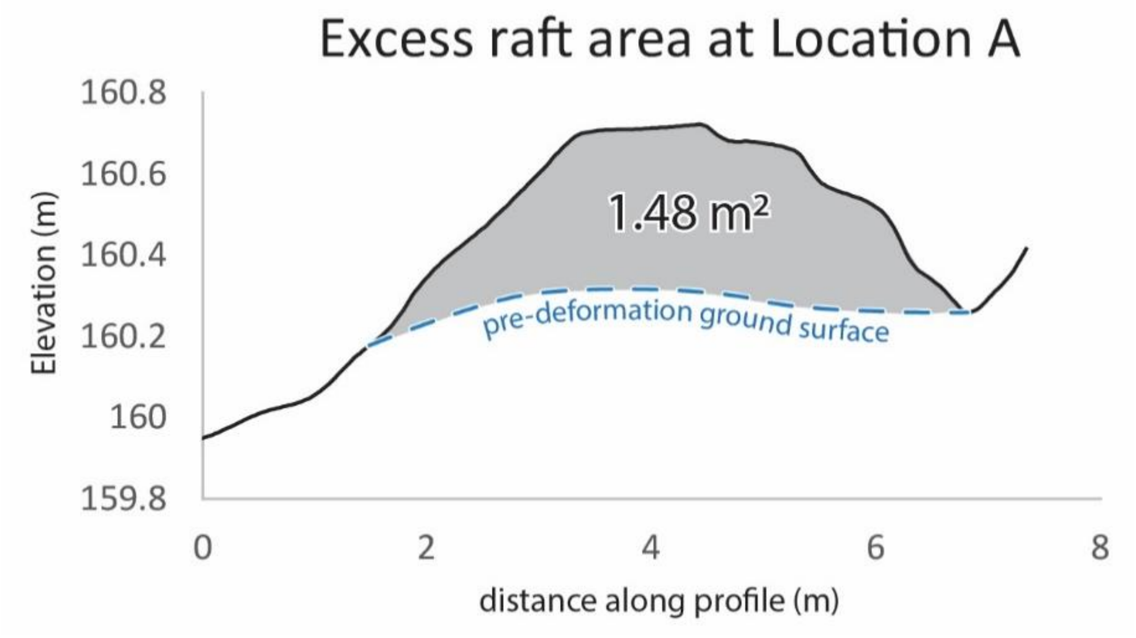

__Figure 3.23:__ Excess raft area (bulge uplift) shown in grey shading along a turf raft at Location A (α= -2°), above a projected pre-deformation ground surface (blue dashed line). This excess area is introduced from out of plane (perpendicular to this plane of view), and is theoretically balanced by adjacent fissures or depressions between the rafts, along fault strike (also perpendicular to this plane of view, see profiles in Figures 3.11b-3.14b).

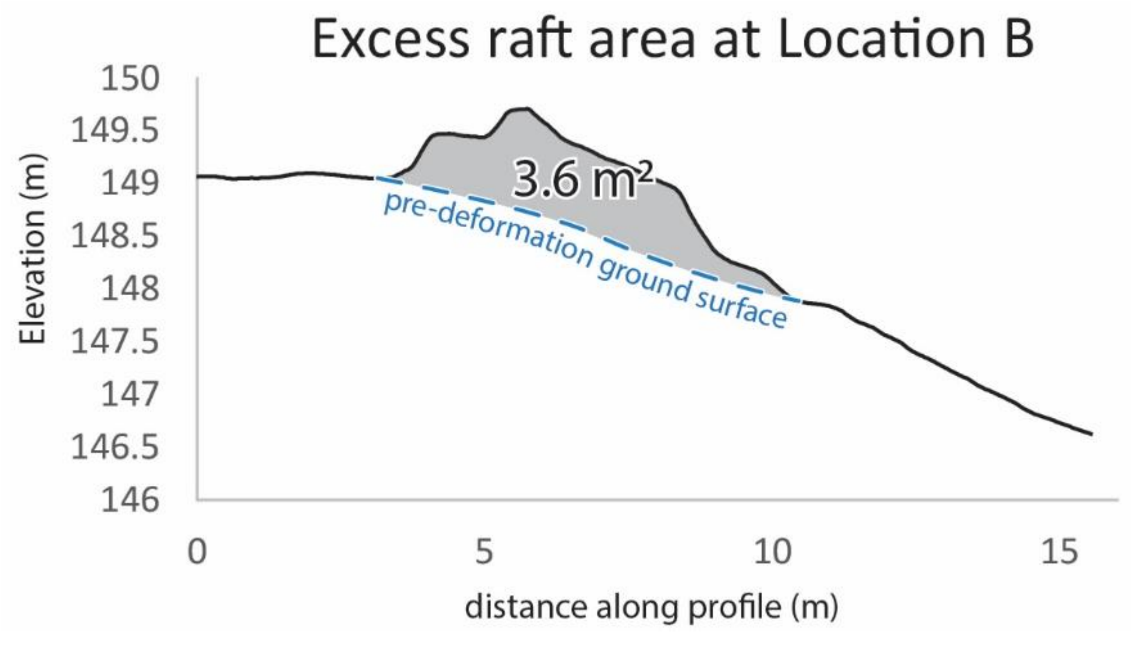

__Figure 3.24:__ Excess raft area (bulge uplift) shown in grey shading along a turf raft at Location B (α = 1°), above a projected pre-deformation ground surface (blue dashed line). This excess area is introduced from out of plane (perpendicular to this plane of view), and is theoretically balanced by adjacent fissures or depressions between the rafts, along fault strike (also perpendicular to this plane of view, see profiles in Figures 3.11b-3.14b).

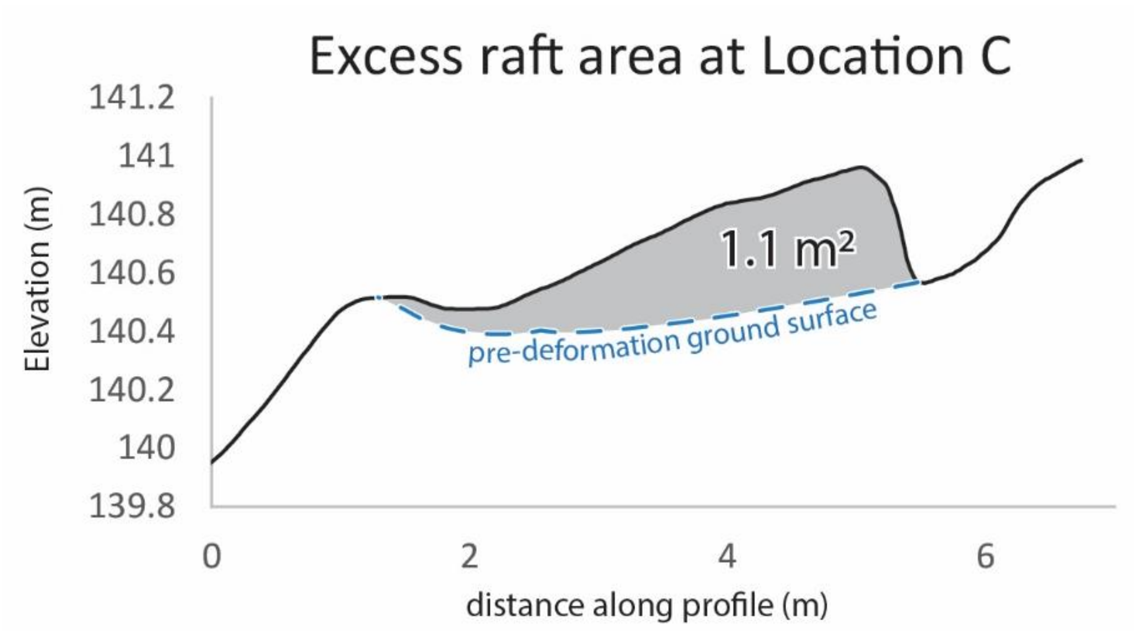

Figure 3.25: *Excess raft area (bulge uplift) shown in grey shading along a turf raft at Location C (α = -5°), above a projected pre-deformation ground surface (blue dashed line). This excess area is introduced from out of plane (perpendicular to this plane of view), and is theoretically balanced by adjacent fissures or depressions between the rafts, along fault strike (also perpendicular to this plane of view, see profiles in Figures 3.11b-3.14b).*

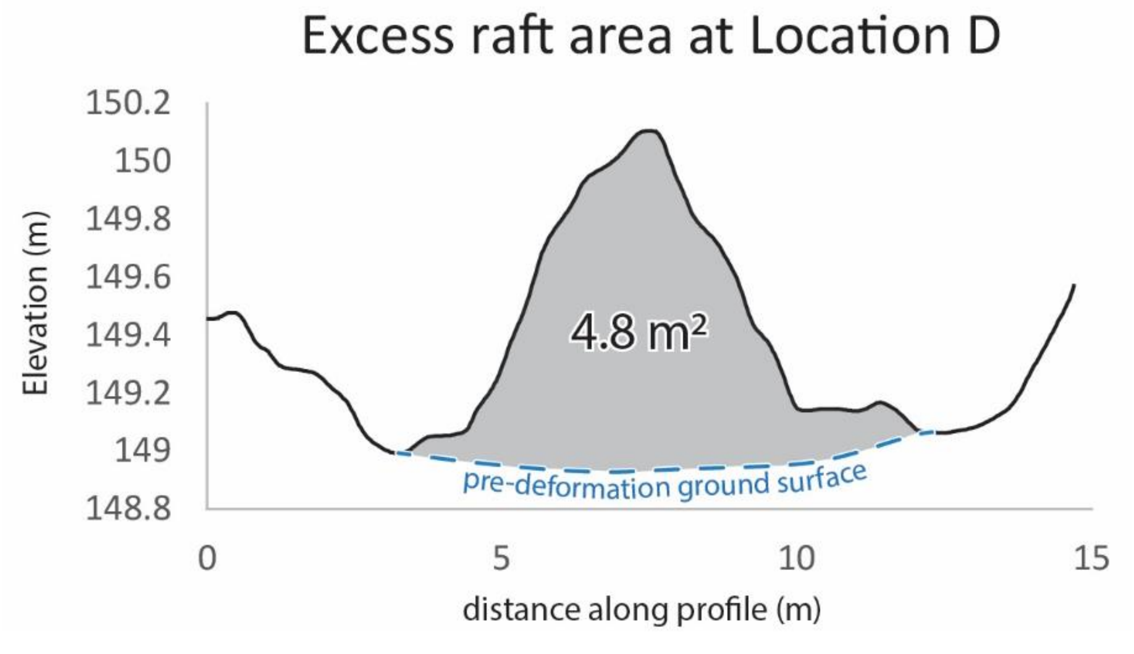

Figure 3.26: *Excess raft area (bulge uplift) shown in grey shading along a turf raft at Location D (α = 8°), above a projected pre-deformation ground surface (blue dashed line). This excess area is introduced from out of plane (perpendicular to this plane of view), and is theoretically balanced by adjacent fissures or depressions between the rafts, along fault strike (also perpendicular to this plane of view, see profiles in Figures 3.11b-3.14b).*

Table 3.4: *Estimates of parameters involved in calculating: a) local excess raft area, b) longitudinal raft parallel strain absorbed by a raft for a fixed value of detachment depth, and c) aspect ratios of height to width for these rafts. Results include data from both transpressional (α = positive) and transtensional (α = negative) kinematic settings at four sites within the Napoleon segment of the fault (Figure 3.10). See Figures 3.23-3.26 for excess raft area calculations. Results highlighted in bold are plotted on the graph in Figure 3.27.*

	Location A (α = -2)	*Location B (α = 1)*	*Location C (α = -5)*	*Location D (α = 8)*
R fault strike rel. to main fault	25°	19°	21°	23°
Rot. R fault strike rel. to main fault	44°	38°	42°	34°
Inner rupture zone width (final)	2.6 m	2.7 m	3.5 m	2.8 m
Local heave [tan(α) x total slip (9m)]	-0.31 m	+0.16 m	-0.79 m	+1.3 m
Inner rupture zone width (original)	2.29 m	2.86 m	2.71 m	4.1 m
Final raft length (parallel to rotated R faults) based on block rot. model	3.7 m	4.4 m	5.2 m	5.0 m
Excess raft area measured perpendicular to turf rafts (A_R)	**1.48 m^2 ± 0.1 m^2**	**3.6 m^2 ± 0.2 m^2**	**1.1 m^2 ± 0.1 m^2**	**4.8 m^2 ± 0.3 m^2**
Modelled, local raft parallel shortening (including heave)	1.7 m	4.4 m	2.3 m	5.5 m
Original raft length (RL_O) [final raft length + modelled local shortening]	5.4 m	8.8 m	7.5 m	10.5 m
Fixed average detachment depth (<1.3 m, >0.3 m for error margins)	0.7 m	0.7 m	0.7 m	0.7 m
Local (normalised) shortening (S_{LN}) [A_R /av. detachment depth]	2.1 ± 0.53m	5.1 ± 0.93m	1.6 ± 0.49m	6.8 ± 1.22m
Longitudinal raft parallel strain (e) [S_{LN} / RL_O]	**0.39 ± 0.32m**	**0.58 ± 0.43m**	**0.21 ± 0.31m**	**0.65 ± 0.49m**
Maximum raft height (relative to pre-deformation surface, Figs. 3.23-3.26)	0.42 m	0.90 m	0.42 m	1.18 m
Aspect ratio for rafts (height : width) [(1/max height) x inner rupture zone width] (above a pre-deformation ground surface)	**1 : 6**	**1 : 3**	**1 : 8**	**1 : 2.5**

3.4.4 Is there a change in moletrack characteristics or morphology as a result of an increasing displacement angle (i.e., α = increasingly positive/transpressional)?

To understand how variation in local displacement angle (α) affects moletrack structure and shape, I evaluate and compare excess raft area, longitudinal strain and aspect ratio of bulges in four selected sites (both transtensional and transpressional). I took two profiles from each kinematic setting; the excess areas measured in Figures 3.23 and 3.25 (1.48 m^2 and 1.1 m^2 respectively) are both from transtensional settings, while the excess areas measured in Figures 3.24 and 3.26 (3.6 m^2 and 4.8m^2 respectively) are from transpressional settings. These graphs suggest that areas that experienced transpression during the 2016 earthquake have higher values of excess raft area above a pre-deformation ground surface (Figure 3.27).

3.4.4.1 Longitudinal strain absorbed by moletrack bulges

To compare these sites independently from the modelled values of shortening, I define moletrack bulges in terms of the longitudinal strain (e) accommodated by an individual raft, parallel to its bounding, rotated R faults. The longitudinal strain is a measure of raft parallel shortening that has been normalised by the original length of the deformed raft. To calculate this longitudinal strain, I first use the local excess area of a raft (A_R), and divide it by an assumed value of detachment depth (d = 0.7 m, see above) to give a (normalised) local shortening value (S_{LN}).

$$S_{LN} = A_R/d$$

This local shortening value (S_{LN}) divided by the original raft length (RL_O) at the site gives an estimate of the longitudinal strain of a raft (e):

$$e = S_{LN}/RL_O$$

In these calculations, I include the local heave (derived from the known coseismic displacement vector as determined by Howell et al., 2019), and combine it with the (final) inner rupture zone width to estimate the original width of the zone prior to deformation (Table 3.4), as this affects the original raft length, which is the denominator of longitudinal strain. The results of these calculations suggest that the ground at transpressional sites has experienced higher values of longitudinal strain, and that this strain seems to scale with the displacement vector trend (Figure 3.27). This relationship is qualitatively an expected one, because transpressional sites have additional shortening derived from their contractional heave, and therefore the rotated turf rafts should absorb greater strain. That said, this small sample size is not necessarily representative of all the moletracks along the Napoleon segment of the fault, as it samples only a few displacement angles (ranging between α angles of -5° to +8°). This range in displacement angles may not be representative of the kinematic variation throughout the entire Napoleon segment.

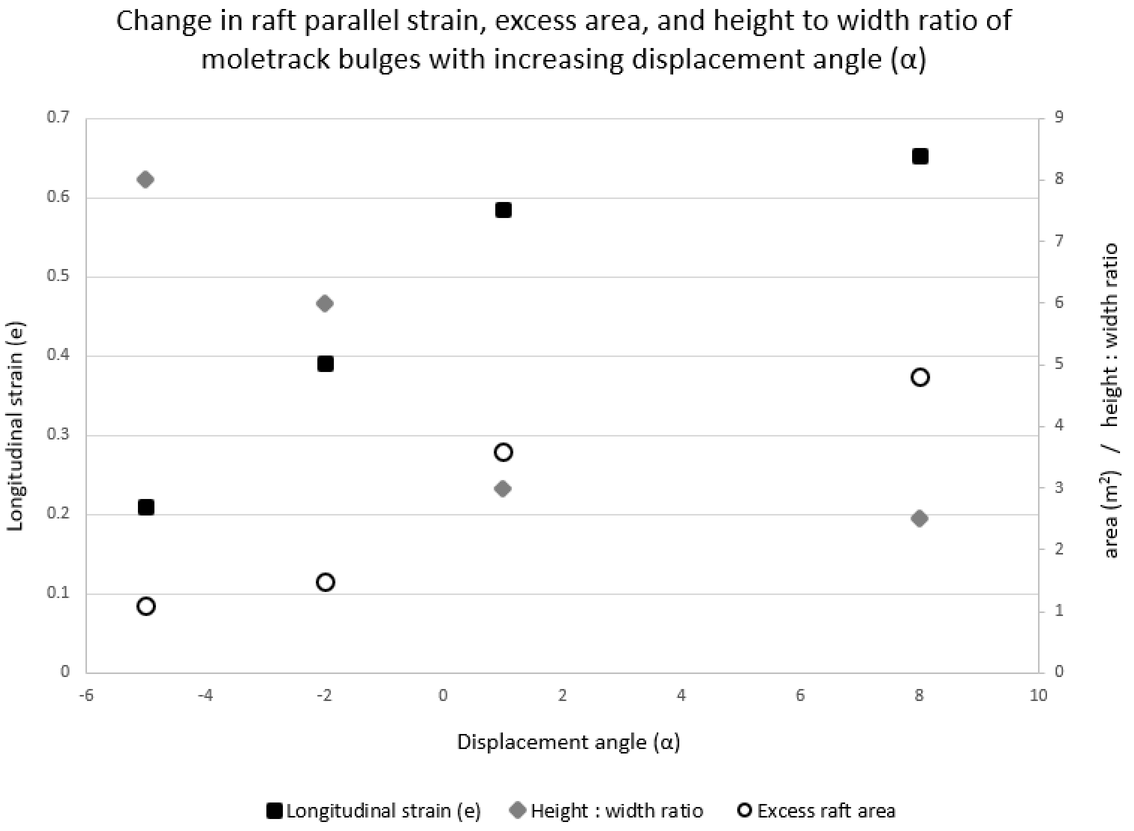

__Figure 3.27:__ Changes in longitudinal (raft parallel) strain, excess raft area, and height : width ratio of moletrack bulges with increasing displacement angle (α). Longitudinal strain values (black squares) are plotted with respect to the left vertical axis, while raft area (white circles) and height to width ratio (grey diamonds) are plotted with respect to the right vertical axis. This graph shows that with an increasingly transpressive (positive) α, the longitudinal strain and excess area of the rafts or bulges both increase, and that the aspect ratio may decrease – creating slightly more rounded bulges. These values are gathered from the four locations (A-D) shown in Figure 4.10.

3.4.4.2 Aspect ratios of moletrack bulges

In addition to knowing how longitudinal strain varies with displacement angle (α), I also calculate aspect ratios for the moletrack bulges (perpendicular to the fault) at these four sites as a measure of any variation in moletrack morphology related to a changing α value. To do this, I first measured the maximum height (H_M) of the turf rafts above a pre-deformation ground surface, using the profiles shown in Figure 3.23-3.26 (values shown in Table 3.4). To estimate the height to width ratio for these bulges, I assume that their width is equal to the local inner rupture zone width (W_I) at each of the sites (Table 3.4). The ratio is then given by:

$$\text{Height : Width ratio} = (1/H_M) \times W_I$$

These calculations (Table 3.4) suggest that rafts that formed in transpressional settings during the earthquake had slightly higher elevations, and slightly lower aspect ratios - meaning that their bulges are narrower and higher (Figure 3.27). This fits with my previous analysis that discusses the effect of heave on rupture zone width; the inner rupture zones in areas that have experienced transpression are shortened during the earthquake, which should result in narrower and higher bulges. However, the differences in the aspect ratios between transpressional and transtensional sites are small and are not statistically robust given the small sample size (as only four sites were sampled in this way).

Generally, I can conclude that a greater displacement angle creates a greater longitudinal strain in the turf rafts, and a greater excess area parallel to their bounding rotated R faults. This greater α angle also may create slight increases in bulge height, and hence decrease the aspect ratio for the moletrack bulges within the Napoleon segment.

3.5 Conclusion

Past authors have simulated the structural development of fractures associated with strike-slip rupture zones in laboratory experiments to explore the effect of different boundary conditions and materials on the orientation and shape of the structures that form during an artificial earthquake. These structures, including push-up structures (moletracks), pull-apart structures, and arrays of *en echelon* Riedel faults have been observed in the field subsequent to many large strike-slip earthquakes. I use the framework established by previous authors to describe a series of push-up moletrack structures that formed along an eastern part of the Kekerengu Fault during the M_w 7.8 Kaikōura earthquake as a way of accommodating some of the 7 - 9 m slip in this region. I compare these moletracks to the structures described by Lin et al. (2004) in association with the Kunlun earthquake in China, and Quigley et al. (2010) in regards to the Darfield earthquake in Christchurch, New Zealand. These comparisons showed that a controlling factor on the height and shape of moletrack structures was not the degree of slip, rather, it was the material that was deformed in the moletrack formation; consolidated materials formed higher and more defined moletracks. I define the moletrack structures associated with the Kaikōura earthquake as spatially repeating, bulged up areas of ground that form in the inner rupture zone along a fault during a strike-slip rupture. These moletracks accommodated slip during the earthquake both through a distributed, rotational deformation (primarily the coseismic rotation about a vertical axis of turf rafts, bounded by synthetic R faults), and discrete dextral strike-slip on (later forming) throughgoing faults that were roughly parallel to the main fault strike. The accommodation of dextral strike-slip through raft rotation accommodated on average ~2.8 m of dextral strike-slip (of a total of ~9 m of slip), and apparently ceased after ~3 m of slip regardless of the magnitude of the total strike-slip at a site and the details of local kinematics (i.e., degree of transpression or transtension).

Variance in the local displacement angle (α) also affects several characteristics of the moletracks. A greater α value introduces contraction of the rupture zone during deformation (heave), which creates additional shortening of the rotating rafts. This increase in shortening within transpressional settings causes a greater bulged up excess area of the associated rafts (in a 2D view), and greater internal longitudinal strain within these rafts or bulges. An increase in transpression may also result in moletracks that are slightly higher in elevation, without being significantly wider; however, more analysis is needed to further test this preliminary result. The analysis of moletrack structures along the Kekerengu Fault that I present in this chapter provides a basis for how moletracks can be analysed in the future, with reference to the mechanisms and processes through which they accommodate slip in large strike-slip earthquakes.

4. Chapter Four: 3D analysis of incremental ground deformation as a result of ~9 m of strike-slip: Comparison of “before” and “after” logs of a displaced paleoseismic trench

4.1 Introduction

The most common way to measure earthquake displacements is to document the offset of natural and cultural markers. If one knows the pre-earthquake location of a point, or the original configuration of a once linear marker spanning a fault, then changes in their position after the earthquake can yield an estimate of the coseismic ground displacement. Both planar and linear natural and cultural markers have been used to estimate displacements in past earthquakes, including fences, roads, fluvial or glacial landforms, and ridges. In addition to displacing these common types of markers, the November 2016, M_w 7.8 Kaikōura earthquake in New Zealand resulted in a ~9 m dextral strike-slip displacement of paleoseismic trench that had been logged and back-filled only ~10 months prior to the earthquake. To my knowledge, this is only the third time globally that a paleoseismic trench has been displaced during an earthquake. The first was during the Borah Peak earthquake of 1983 (Idaho, United States), at which time a normal fault (Lost River Fault) displaced a 7-yr old trench by 2 m (Haller, Crone, & Wood, 2004). Parts of this trench were exposed and re-examined, and the expression of slip on the exposed trench wall was found to be essentially the same as in previous earthquakes. In the recent (2016) Kumamoto earthquake in Japan, two trenches were laterally displaced by ~0.5 m, but neither was re-excavated (Shirahama et al., 2016).

In this chapter, I use the well-documented ~9 m displacement of a recently logged paleoseismic trench, and re-excavation of that trench after the earthquake as an opportunity to identify and quantify the partitioning of ground deformation during a large magnitude, mostly strike-slip coseismic displacement. My goal is to understand the processes by which this coseismic oblique-slip was accommodated, not only on the ground surface, but also in the top few metres of sediments and soil. To harness this opportunity to its fullest potential, both halves of the original (displaced) trench were re-excavated and re-logged. In this way, the pre- and post-earthquake views of identical segments of trench wall could be compared in three dimensions. In addition, the walls of each trench-fragment were extended across the fault zone in order to expose material on the opposite fault block that had been newly juxtaposed against the original trench walls during the 2016 earthquake. The detailed datasets used in this chapter include: 1) original trench log data collected prior to the earthquake; 2) post-earthquake trench log data corresponding to the originally documented walls; 3) post-earthquake trench log data for newly extended walls (not previously logged); 4) pre- and post-earthquake aerial photography, as well as Digital Surface Models (DSMs) derived from them; and 5) the positions of selected survey points measured using Real-Time-Kinematic (RTK) Global Positioning System (GPS) methods both before and after the 2016 earthquake, including points along the perimeter of the (original and displaced) trenches.

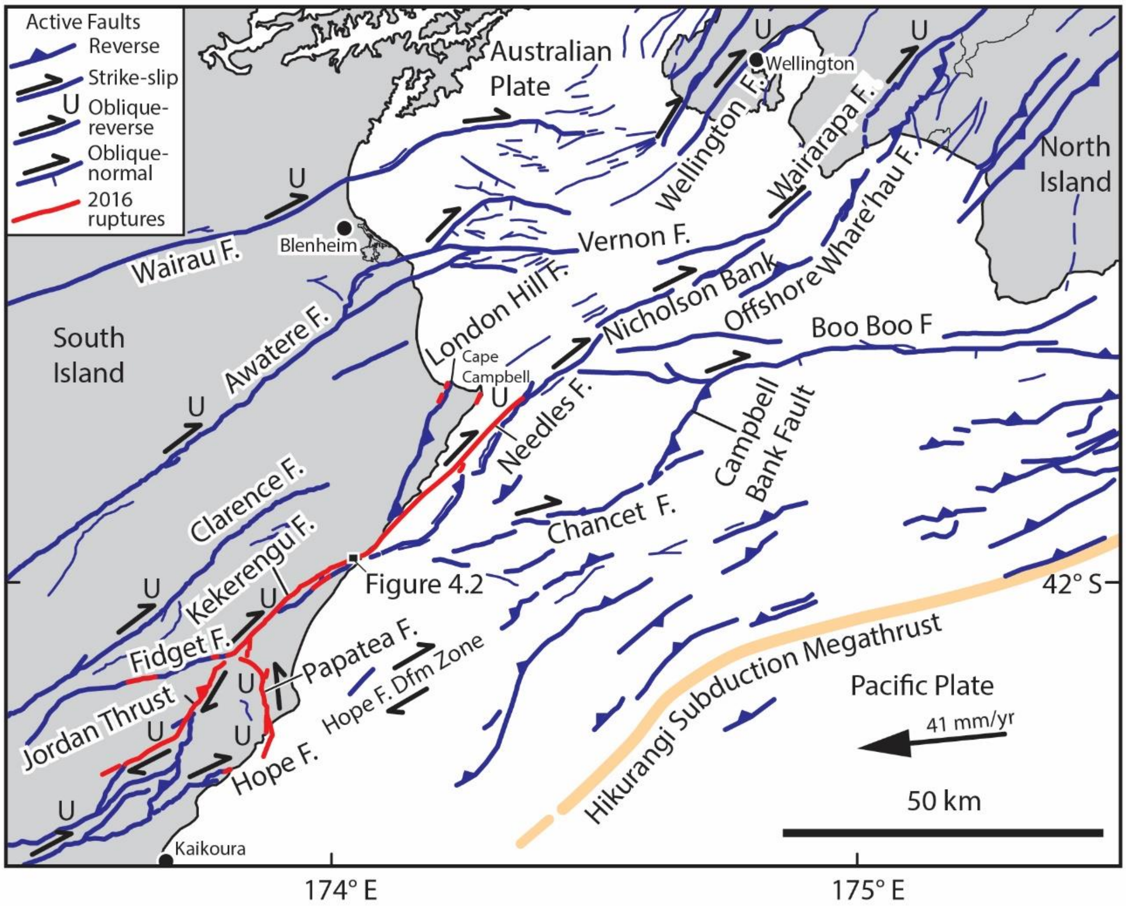

Figure 4.1: *Tectonic map of the Cook Strait, between the North and South Islands of New Zealand (from Little et al., 2018). Red fault traces show the northern ruptures of the Kaikōura earthquake in 2016. Faults that did not rupture in the 2016 earthquake are shown in blue. Location of the paleoseismic trenches from Little et al. (2018) is labelled (for Figure 4.2).*

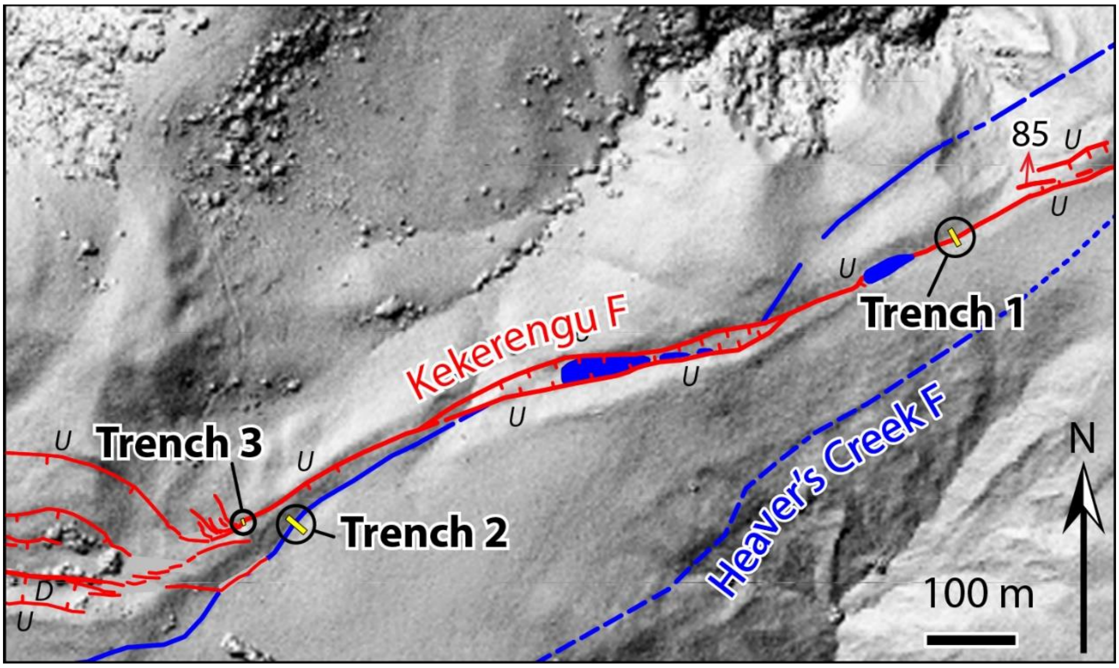

***Figure 4.2:** Map of fault traces near the three paleoseismic trenches excavated prior to the earthquake in January 2016 (adapted from Little et al., 2018). Red traces show faults strands that ruptured in the 2016 earthquake, while blue traces show fault strands that did not rupture in 2016. See Figure 4.1 for location. Background is shaded DSM derived from analysis of 2014-2015 LINZ aerial imagery, gridded at 1 m (Hill & Ashraf, 2017).*

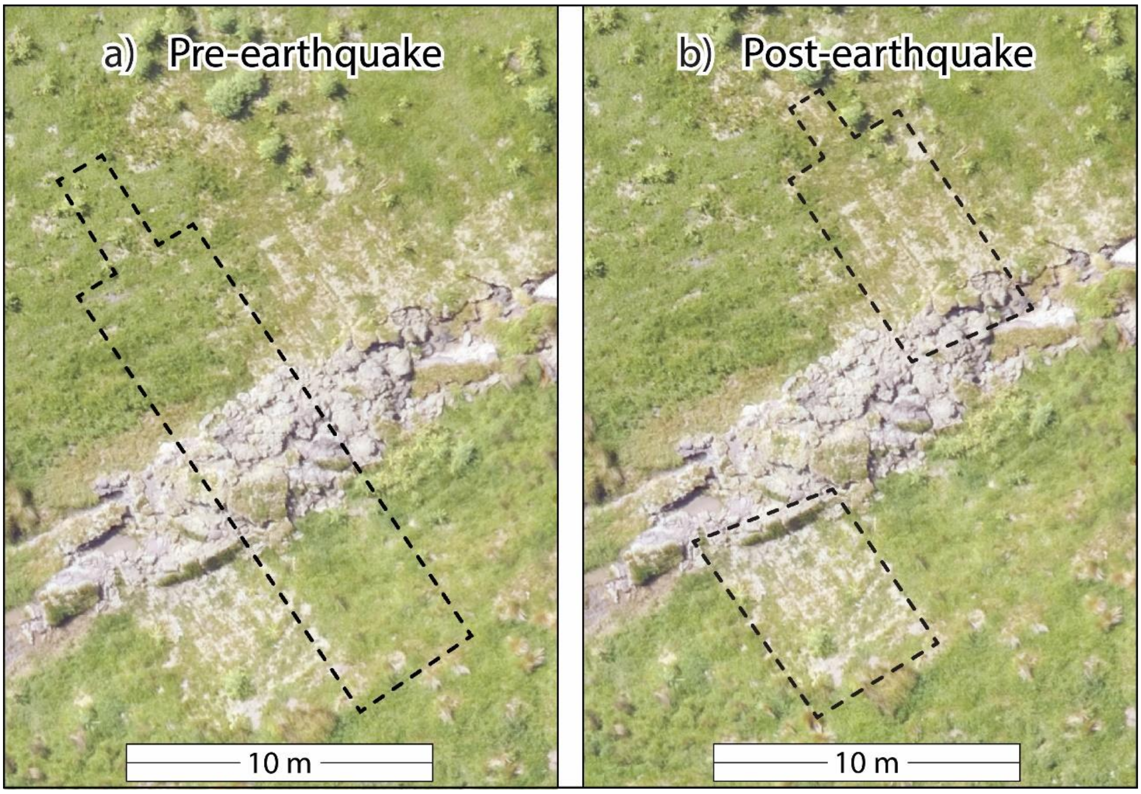

***Figure 4.3**: Map showing GPS pinned locations (NZGD 2000) of a) the pre-earthquake trench margins (T1 on Figure 4.2), excavated in January 2016, and b) the post-earthquake locations of these margins as surveyed on 28/11/2016 by Zekkos et al. (2018) after ~9 m of dextral displacement. Underlying orthophotograph is from Zekkos et al. (2018), as the pre-earthquake aerial photography is not detailed enough to show the trench site at this scale.*

4.2 Background and previous work

The trench that was dextrally displaced in the 2016 earthquake was one of three paleoseismic trenches along the Kekerengu Fault excavated by Little et al. (2018) in January 2016 (Figures 4.1 and 4.2). During the earthquake, Trench 1 (previously mentioned) was dextrally displaced by ~9 m (Figure 4.3), Trench 2 was left untouched on a fault strand that did not rupture during 2016, and the smaller (~7.5 m long) Trench 3 was ruptured and effectively destroyed. In this chapter, I will focus only on the pre-earthquake stratigraphy and deformation style of Trench 1 (T1), as this is the only trench for which I have detailed post-earthquake datasets with which to compare the corresponding pre-earthquake data.

4.2.1 Pre-earthquake stratigraphy and cross-cutting relationships (refer to Figure 4.4)

Because of slope failure, only the southwest wall of this trench was logged prior to the 2016 earthquake. In the centre of this trench, the Kekerengu Fault had been expressed as a ~2 m wide, trough-shaped fault furrow, cut by oblique-normal faults. The closed, synclinal basin was a depocenter, accumulating organic and clay-rich sediments over the span of last several surface-rupturing paleoearthquakes at the site, since ~1650 cal. B.P. The dips of the flanking limbs of this shallow basin steepened structurally downward into older units - a relationship that can be attributed to the incremental effect of multiple paleoearthquakes that each deepened the extensional basin and caused progressive synclinal tilting. As observed before the 2016 earthquake, the basin had first been infilled by a layer of clayey silt (unit uc), and later by a succession of three peaty units (units lp, mp, and up). The fault furrow was cut by an array of at least five dextral-normal faults near the centre of the trench. Importantly, some of these faults terminated upward into the uc unit (faults 3 and 4), another cut the lp unit but not the overlying mp unit (fault 5), and still others (faults 1 and 2) cut the mp unit but not the up unit, which drapes unbroken across them (Figure 4.4). On the basis of this incremental deformation, three paleoearthquakes were identified in the walls of the pre-2016 trench; from oldest to youngest, Little et al. (2018) called these E3, E2, and E1. The 2016 earthquake, which took place prior to publication of that paper, was called E0. Wherever possible, the names of these five faults will be retained later in this chapter where I describe the post-earthquake version of the same trench wall (section 4.4.2).

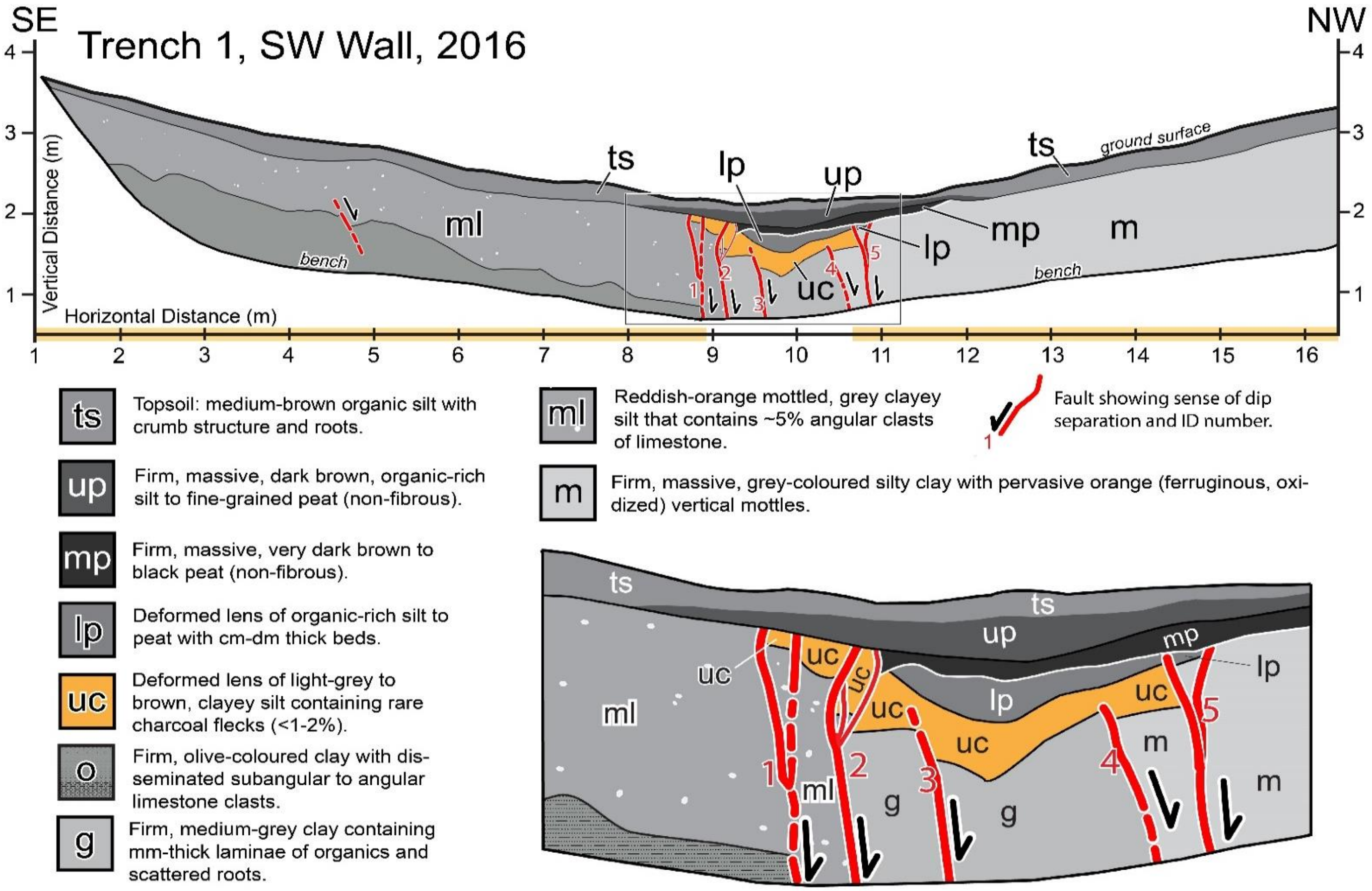

Figure 4.4: *Pre-earthquake trench log of Trench 1 (SW wall) from Little et al. (2018), showing numbered faults (referred to in text) and basic stratigraphy. Only the upper half of the original trench is shown here (down to the bench) as this is the depth to which the trench was re-excavated in 2018 as part of the present study; the northwestern end of the trench is also clipped, as it is not discussed in the current study. Orange bars along the scale at the base of the trench show material that is to be logged in the post-earthquake trench (2018). Inset shows an enlarged version of central rupture zone (see box on the main figure) so that detailed stratigraphic and structural relationships within the synclinal basin can be more easily identified.*

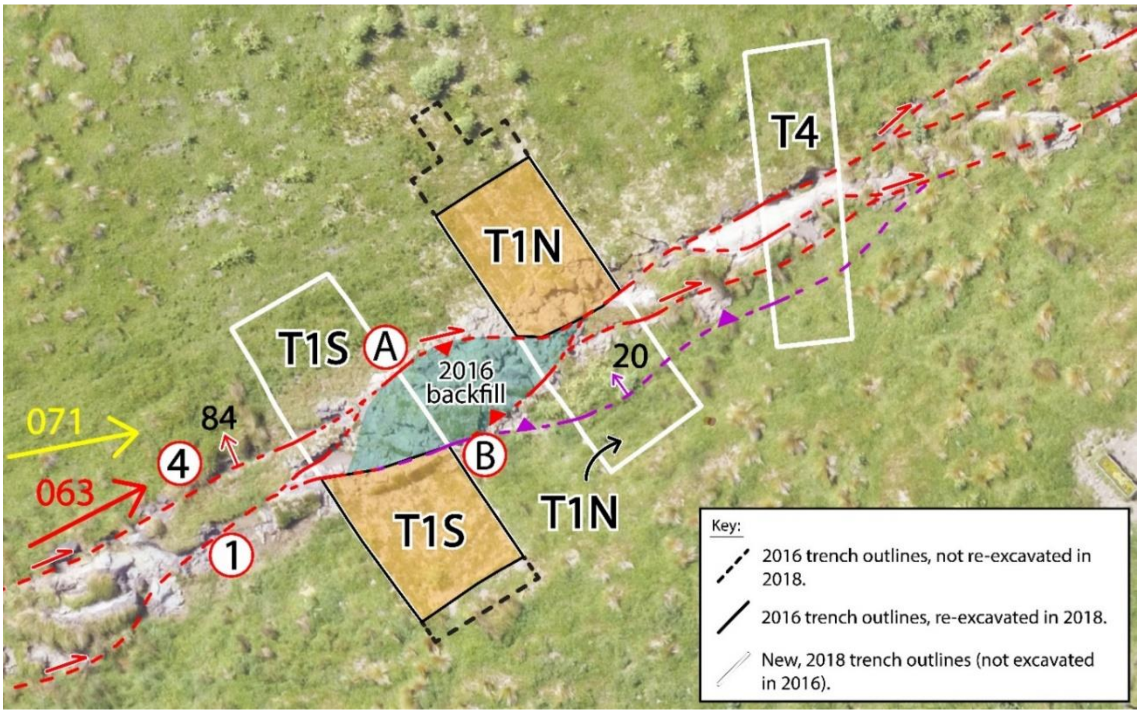

Figure 4.5: *Post-earthquake structural map of the paleoseismic trench site showing the outlines of the 2018 excavations and fault traces as mapped in the post-earthquake trench logs (solid lines) and extrapolated between trenches (dashed lines). Faults coloured red accommodated primarily strike-slip motion in 2016, whereas faults coloured purple accommodated both strike-slip and reverse motion. Some faults also have triangles attached; these indicate that the fault accommodated some contractional heave. Arrows attached perpendicular to faults indicate dip direction and angle. Numbers 1 and 4 in circles next to faults correspond to numbered faults in the trench logs of Figures 4.7 and 4.9. Labels A and B adjacent to faults correlate to faults labelled in Figure 4.8. Black lines represent pre-earthquake trench margins (see also Figure 4.3), and orange shading represents the displaced halves of this original trench, labelled T1S (southern half) and T1N (northern half). White lines outline the extended dimensions of the re-excavated, post-earthquake trenches (T1N, T1S), and also the perimeter of the entirely new trench (T4). In the central part of the 2016 rupture zone, the blue shading shows the location of the earthquake-deformed and up-bulged backfill of the originally excavated trench (T1). Arrows on the left of the map indicate a) the mean strike of the fault zone at this locality (red arrow, 063); and b) the trend (azimuth) of the 2016 coseismic displacement vector at this site (yellow arrow, 071, see section 4.4.1 of this chapter). Underlying orthophotography was taken by remotely piloted aircraft in a survey by Zekkos et al. (2018), on 28/11/2016.*

4.2.2 Contrast in ground deformation style between the previously recognised paleoearthquakes and the 2016 earthquake

The obliquely extensional style of fault slip during the paleoearthquakes E1, E2, and E3 at this site produced cm to dm-sized normal dip-separations of the surficial layers in fault-perpendicular view of the trench wall, and incremental subsidence of the synclinal basin. Structural up-bulges of the coeval ground surface (i.e., moletracks, up to ~1 m high) did not form; however, the 2016 earthquake produced moletrack structures along most of the Kekerengu Fault, including in this small basin (Figure 4.5). This apparent contrast in the style of ground deformation between the 2016 earthquake and its several most recent paleoearthquakes raises questions about the cause of this contrast. One possible explanation is that the azimuth of the slip vector in 2016 was more locally convergent at this site than it had been previously. Another possible explanation is that the mechanical properties of the soil changed since the last documented paleoearthquake (at 249-108 cal. yrs. B. P.), perhaps as a result of the introduction of exotic grasses that caused the turf to become less granular, and more tightly grass-bounded and cohesive. This change may have promoted the formation of moletracks in 2016. Deforestation and colonization of the soil by exotic grasses followed the European arrival at circa 1840 A.D., a timing that fits in the transition period between the last paleoearthquake (E1) and the 2016 earthquake (E0). These explanations for the difference in ground deformation style are explored and addressed in section 4.5 of this chapter (discussion).

4.3 General approach to evaluating how and where slip was accommodated at the trench site during the 2016 earthquake

To assess where and how slip was partitioned into the ground in 2016 at the site of the displaced paleoseismic trench, re-excavation of both halves of the original trench was undertaken in February 2018 (Figure 4.5). This enabled me to identify the coseismically induced structural changes in its walls, by comparison of the pre- and post-earthquake trench logs. A reduced density of grass cover on the infilled ground of the original trench (artificially re-seeded following the 2016 excavations) could be identified visually, and was used to fix the locations of the old trench margins. This provisional location of the original walls was confirmed by digging shallow soil pits on either side of their inferred position. Recognising the lighter colour of the backfill (in comparison to the dark, undisturbed topsoil that remains outside of the trench) allowed us to refine the location of the original trench walls to within 3 cm. Finally, we also knew the exact dimensions and shape of the original trench margins as fixed by GPS survey points during their excavation (Little et al., 2018), and could use this information to fix the location of parts of the post-earthquake trench perimeter that were not otherwise obvious.

The two halves of the displaced trench were 1) re-excavated on either the north (TN1) or south (TS1) side of the fault; and 2) extended into “new ground” on the opposite side of the fault in order to embrace the full width of the 2016 rupture zone (Figure 4.5). A new trench (Trench 4, Figure 4.5) was also excavated several metres northeast along fault strike from these trenches, orthogonal to the fault, with the goal of better understanding the internal structure of the up-bulged moletracks in cross-section. Each of these new trench margins were scraped, cleaned, gridded, photographed, and logged at a scale of 1:20.

4.4 Analysis of how and where displacement was partitioned during the 2016 earthquake, through comparison of pre- and post-earthquake datasets

4.4.1 Revised coseismic displacement vector at the trench site

Kearse et al. (2018) estimated the coseismic slip vector near T1 by re-surveying individual fence posts (with Real Time Kinematic Ground Positioning Surveys, or RTK GPS) that had originally been surveyed ten months prior to the earthquake (see Appendix D.4.1). The two re-surveyed fence posts on the southern side of the fault were only ~10-20 m away from the trench site; however, the single re-surveyed fence post on the northern block of the fault is located over 200 m to the northeast of the trench site, and so may not provide the most accurate depiction of coseismic motion at the trench. In addition, the wooden posts have a diameter of ~20 cm, and were originally surveyed by placing the antenna rod on an unspecified part of their outer circumference. This exact position (being unrecorded) was not able to be reoccupied during the post-earthquake survey. This introduced a ± 0.1 m uncertainty in the displacement vector additional to the nominal surveying precision of ± 0.25 m (Kearse et al., 2018). Most importantly, the displacement vector probably varied over distances of ~200 m due to local changes in the structure of the rupture zone and in the style and distribution of coseismic ground deformation within it.

To define a more precise slip vector for the site, I use a) the observed dextral strike-slip offset of the original trench margins (9.0 ± 0.3 m), measured parallel to the 063-trending fault trace (Figure 4.6a), and b), the coseismic change in the distance between the outer ends of the trench on both the northern and southern fault blocks - measured parallel to the long walls of the trench and perpendicular to the fault trace (1.3 ± 0.4 m, Figure 4.6b). The deformational change in this axial trench length is a measure of the fault-perpendicular convergence (heave) during the earthquake. In addition, this site also experienced ~0.1 m of vertical displacement during the earthquake (Howell et al., 2019).

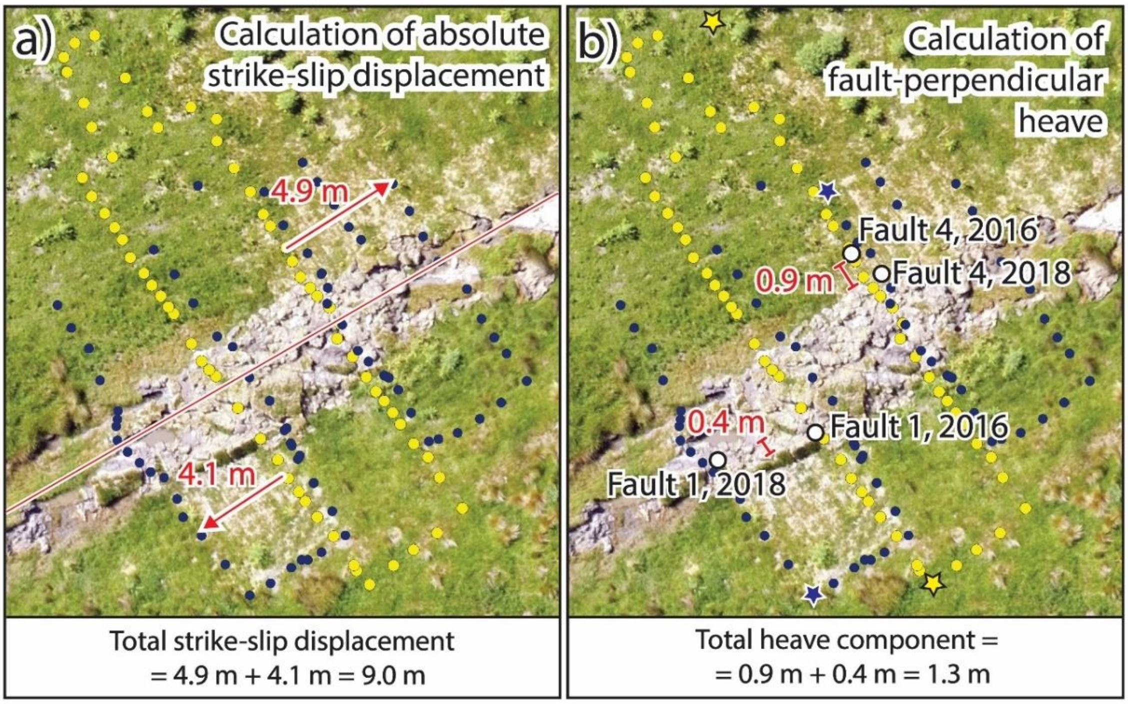

Figure 4.6: *RTK GPS points of the pre-earthquake (yellow) and post-earthquake (dark blue) trench margins; a) shows the absolute dextral strike-slip displacement of the original trench margins, on both the northern (4.9 m) and southern (4.1 m) sides of the fault. An average fault trace is shown in red. b) shows a measure of the fault-perpendicular contractional heave, on both the northern (0.9 m) and southern (0.4 m) sides of the fault. The heave was calculated using the difference in the pre- and post-earthquake position of fault 4 (for the northern side) and fault 1 (for the southern side) in aerial view. These locations were measured using the distance on the trench logs from the end of each trench (marked as stars in map view, yellow = 2016 trench end, blue = 2018 trench ends) to each fault; these distances were plotted on the map as white circles. The difference in distance between the fault locations in map view (distance between 2016 and 2018 circles, for each fault) is the heave. For further explanation see section 4.4.1. Total values for both the strike-slip and heave components of slip are given underneath the boxes a) and b).*

The strike-slip offset of the trench walls was measured by surveying points along the walls of the displaced trench fragments using RTK GPS (Figure 4.6a). Relative to the New Zealand Geodetic Datum (2000), the “absolute” strike-slip displacement of the northern fault block (walls of TN1) was eastward by 4.9 ± 0.2 m, whereas that of the southern fault block (walls of TS1) was westward by 4.1 ± 0.2 m. Combined together, these indicate a total dextral slip displacement of 9.0 ± 0.3 m.

The coseismic change in the axial length of the trench walls (i.e., the contractional heave during the earthquake) was measured by identifying and conspicuous geological features in both the pre- and post-earthquake trench logs (fault 1 and 4), and comparing the difference in map distance between them before and after the earthquake. In doing this, I am assuming that faults 1 and 4 can be correlated between the pre- and post-earthquake trenches, and that they were rigid during deformation (i.e., any change in their map position is related to contractional heave, rather than coseismic deformation of the faults themselves). I measured the distance on the 2016 (pre-earthquake) trench log between its NW end and fault 4, and plotted a point on the map (white circle, Figure 4.6b) which corresponds to the location of this fault on the surface (along the 2016 trench outline). I repeated this process for fault 4 in the 2018 log, and fault 1 in both the 2016 and 2018 trench logs (in the latter cases, distances were measured from the SE end of the trench logs). I then compared the pre- and post-earthquake map positions of these faults; this distance is a measure of the contractional heave that either side of the fault experienced during the earthquake. The northern fragment of the trench experienced 0.9 ± 0.3 m of southward displacement perpendicular to the fault, whereas the southern fault block recorded a northward motion of 0.4 ± 0.3 m. Added together, these indicate a heave (change in overall fault-transverse trench length) of 1.3 ± 0.4 m.

The trigonometric combination of the dextral strike-slip and heave measurements above defines a displacement vector for the site that trends 071, relative to the fault strike of 063 (Figure 4.5). This also creates a moderately transpressional displacement vector angle (α) of +8°. This result indicates that the slip vector in 2016 must have rotated clockwise by a minimum of 8° to change from a late Holocene transtensional angle ($\alpha<0$) during the youngest paleoearthquake (causing basin opening and subsidence), to a transpressional one in 2016 ($\alpha = 8°$), which caused conspicuous up-bulging of a moletrack. In fact, the displacement vector likely rotated more than this, because, as per my analysis of the kinematic conditions required for moletrack bulging in Chapter 3 of this thesis, moletracks can form in transtensional settings at α angles as small as -5°.

The fault zone survey data of Kearse et al. 2018 included a measurement of a dextral deflection (offset) by 9.4 ± 0.2 m of a fenceline located only ~20 m to the SW of the trench site, which is within the margin of error of my measurement (presented above) of 9.0 ± 0.3 m of dextral slip based on offset of the trench walls. In addition, the fenceline survey from Kearse et al. (2018) indicated that the rupture zone across which the ~9 m of strike-slip was accommodated was ~4 m wide. This was measured as the fault-perpendicular width of the zone over which the fenceline was dextrally deflected (see Appendix D.4.1). This width represents a total rupture zone width, and the estimate accords well with the rupture width that I measure in aerial view using post-earthquake drone orthophotography of the trench site (Figure 4.5).

4.4.2 Post-earthquake trench stratigraphy and cross cutting relationships (2018) (refer to Appendix D.4.2 for photographic comparison)

To compare the 2016 trench logs with those from 2018, it was important to re-identify the same structures and stratigraphic units in cross-section that were logged prior to the 2016 earthquake. This included a) the five primary faults (mentioned in section 4.2.1 of this thesis), the evidence for which remained preserved (to variable degrees) in the new trench logs; and b) the original sequence of stratigraphic units that infilled the synclinal depression in the centre of T1 (Figure 4.4). After the 2016 earthquake, these features were typically modified in their shape, dip, position, thickness, and/or clarity of expression.

4.4.2.1 Trench S1, southwest wall (refer to Figure 4.7)

Displaced westward by 4.1 ± 0.2 m from its pre-earthquake location (Figure 4.6a), the southern part of this trench wall is materially coincident with the logged southern part of the original trench (highlighted in orange in Figures 4.4 and 4.7). On the opposite side of the Kekerengu Fault, to the north, TS1 was extended northward into new material that had not been not logged prior to the earthquake. This part of the trench wall was originally located relatively ~9 m to the SW of T1, and was laterally transported into the plane of TS1 during the 2016 earthquake (Figures 4.6 and 4.7). In the resampled, southern part of TS1, 5 faults that I correlate to the previously labelled faults 1 through

5 in the original T1 trench were identified and logged (Figures 4.4 and 4.7). I describe these faults with reference to the inner rupture zone; this is defined as the central part of the rupture zone in which ground deformation is focused, and slip is relatively concentrated, commonly bounded by throughgoing faults (see also Chapter 3).

Faults that define the boundaries of the inner rupture zone

Fault 1: This steeply dipping fault is the fault splay furthest southeast that was recognized in both the 2016 and 2018 trenches. It bounds the southeastern margin of the 2016 inner rupture zone, both in aerial view (Figure 4.5) and on the trench walls (Figure 4.7). In the pre-earthquake trench (Figure 4.4), this fault had splays that bifurcated upward, both of which cut the uc unit and were overlapped by the up unit. During the 2016 earthquake, fault 1 was re-activated as a major locus of slip, cutting upward through the previously unbroken up unit. Retaining its upward splaying geometry, the post-2016 version of fault 1 encloses a fault slice that appears to be a tectonic mixture of the several peat units (evidenced by the contained radiocarbon age of sample S1-03 is 632-533 cal. B.P., which is similar in age to unit lp – refer to Figure 4.7 and Appendix B.2.4) but does not show evidence for the unit uc. Farther to the NW, on the original trench wall (between faults 1 and 2 on Figure 4.4), a ~15 cm-thick slice of unit uc was present to the northwest of fault 1 prior to the 2016 event; however, in the post-2016 version of this wall this slice appears to have been displaced dextrally out-of-plane as a result of strike-slip. Distributed strike-slip shearing adjacent to fault 1 may have either transported this material out-of-plane to the northeast, or destroyed the integrity of this thin layer beyond recognition. Fault 1 also accommodated considerable convergent motion during the earthquake, as evidenced by the steepening and up-folding of the ml unit and its topsoil (unit ts) to the southeast of fault 1, as well as folding of the overlying, anthropogenically introduced layer of the pre-earthquake trench spoil (unit psp).

Fault 4: Based on its spatial position relative to the other faults and stratigraphic units, I recognize fault 4 of the original trench (Figure 4.4) on the wall of TS1 (Figure 4.7). After the earthquake, this vertical fault bounded the northwest margin of the inner rupture zone at the displaced trench site, again in both an aerial view (Figure 4.5) and in cross-section (Figure 4.7). This fault consists of three upwardly bifurcating splays surrounded by sheared organic rich clay (unit fp), and cuts through all the stratigraphic units up to the ground surface. Some of the material enclosed (and sheared) within these splays was probably derived from the 2016 topsoil (unit ts), as evidenced by the modern radiocarbon age obtained for sample S1-06 (Figure 4.7). Interestingly, although fault 4 did not slip during either the E1 or E2 paleoearthquakes (as indicated by the un-faulted nature of the mp and up units overlapping it on the pre-earthquake trench log, Figure 4.4), the fault became a major locus of slip during the 2016 earthquake.

Deformation between the boundaries of the inner rupture zone (faults 1 and 4)

A >1.5 m wide zone was observed in TS1 after the earthquake, that was apparently affected by pervasive strike-slip shearing in the region between faults 1 and 4 (Figure 4.7). Within this zone, faults and stratigraphic units identified and logged in the pre-earthquake trench are difficult to re-identify in the post-earthquake trench, as their geometry, dip, thickness, or expression has changed. I attribute these changes to strong deformation of these soft materials, including vertical shearing, horizontal compression, and out-of-plane transport of 3D shapes. As a result of such processes, the thicknesses of the deformed units (Figure 4.7) have changed in comparison to their pre-earthquake counterparts (Figure 4.4); in some places, units may be omitted when the (horizontal) out-of-plane transport was in either up or down that unit's dip direction. Given the large amount of displacement at the site, it is difficult to specify the relative contributions of pervasive shearing, shortening, and/or out-of-plane transport in the creation of these coseismically induced geometrical changes to the post-earthquake trench wall.

Fault 2: In the wall of the pre-earthquake T1, two upwardly bifurcating splays of this fault were observed enclosing a thin faulted wedge of the uc unit, and were overlapped by an unbroken layer of the up unit. The faulted uc unit was no longer recognized in the post-earthquake version of the wall – instead, the fault now abuts an exposure of the lp unit. Possible reasons for such stratigraphic omissions or additions caused by the earthquake (including out-of-plane shearing down dip direction) are mentioned above.

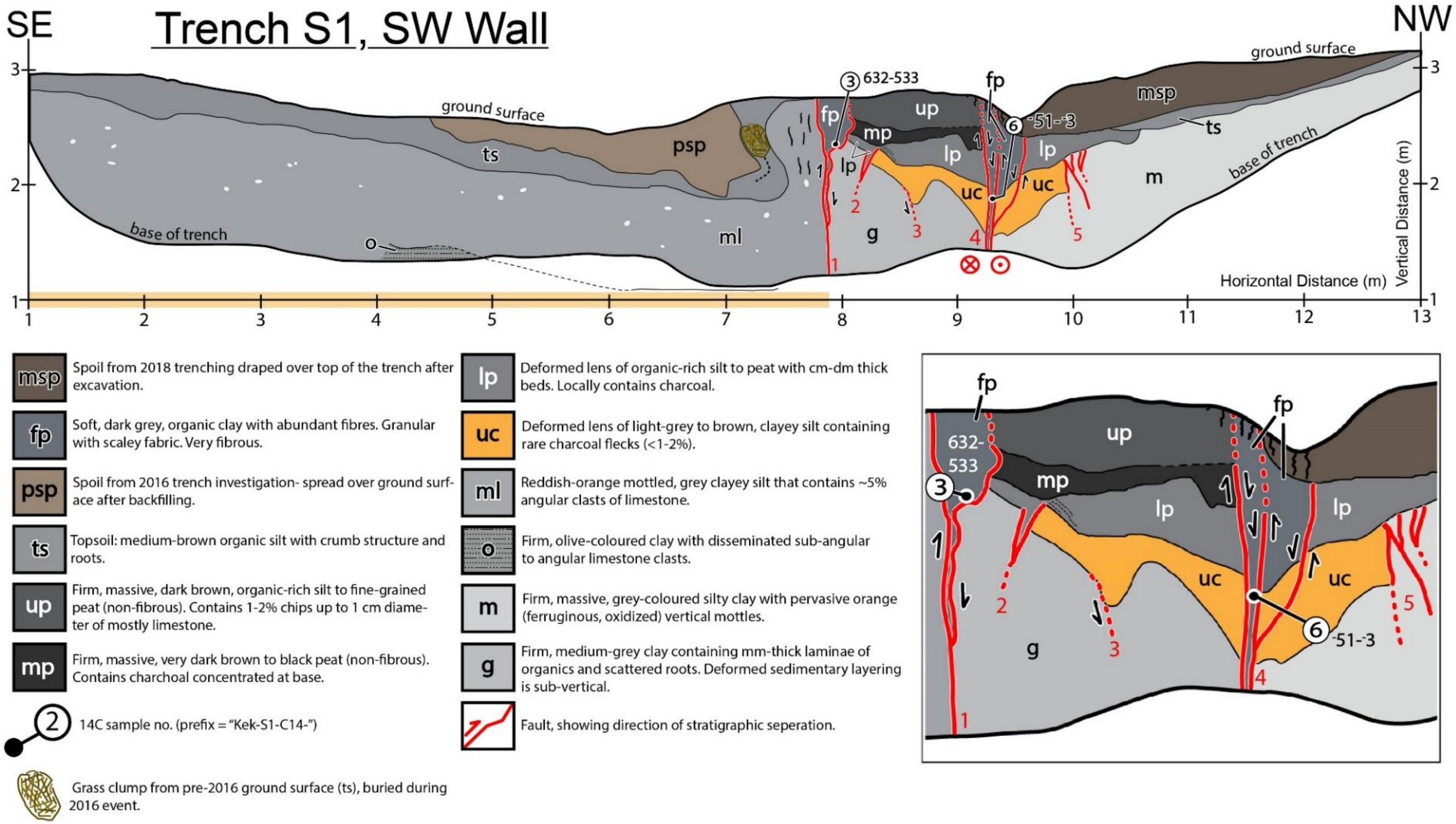

Figure 4.7: *Post-earthquake trench log of the SW wall of Trench 1 (fragment S1, re-excavated) showing numbered faults and basic stratigraphy. Faults are numbered to correlate with the pre-earthquake trench (Figure 4.4, see text). Orange bar along the scale at the base of the trench shows material that is the same as that logged in the pre-earthquake (2016) trench. Inset shows enlarged version of the inner rupture zone to enhance observation of the key stratigraphic relationships and structures. No vertical exaggeration.*

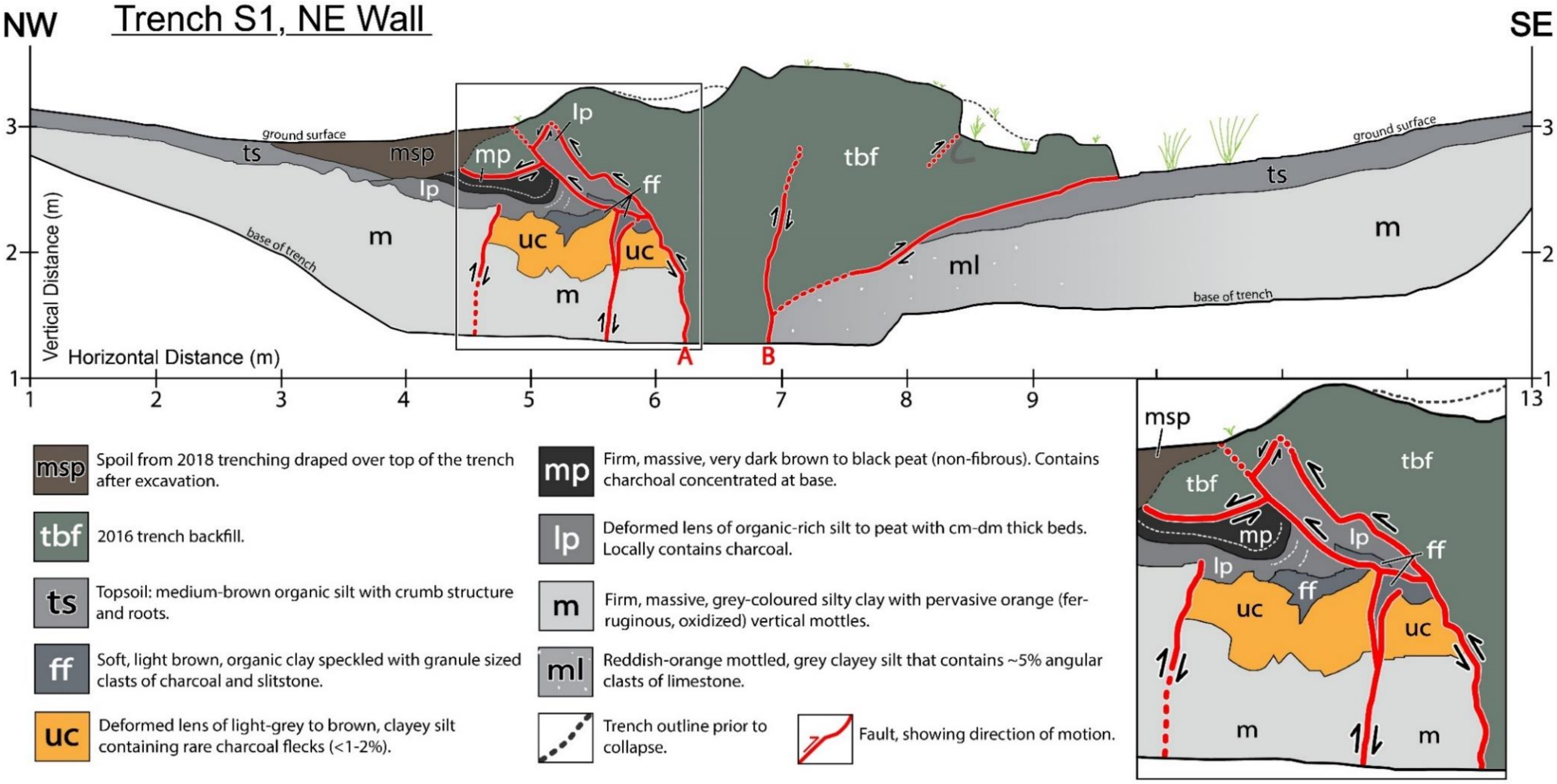

Figure 4.8: *Post-earthquake trench log of the NE wall of Trench S1. Faults bounding the inner rupture zone are labelled A and B (referred to in text). Inset shows enlarged version of the displaced, original stratigraphic sequence (just to the NW of the inner rupture zone). No vertical exaggeration.*

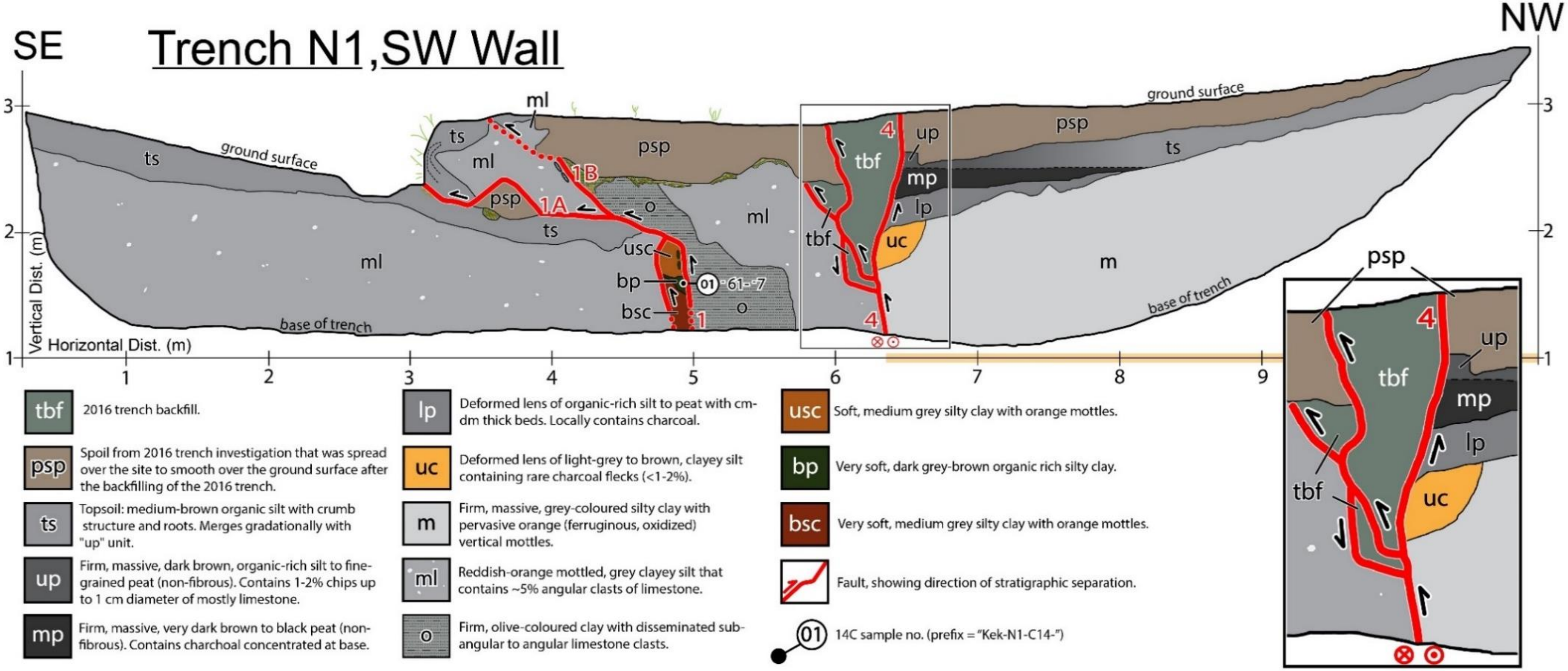

tbf	2016 trench backfill.
psp	Spoil from 2016 trench investigation that was spread over the site to smooth over the ground surface after the backfilling of the 2016 trench.
ts	Topsoil: medium-brown organic silt with crumb structure and roots. Merges gradationally with "up" unit.
up	Firm, massive, dark brown, organic-rich silt to fine-grained peat (non-fibrous). Contains 1-2% chips up to 1 cm diameter of mostly limestone.
mp	Firm, massive, very dark brown to black peat (non-fibrous). Contains charchoal concentrated at base.
lp	Deformed lens of organic-rich silt to peat with cm-dm thick beds. Locally contains charcoal.
uc	Deformed lens of light-grey to brown, clayey silt containing rare charcoal flecks (<1-2%).
m	Firm, massive, grey-coloured silty clay with pervasive orange (ferruginous, oxidized) vertical mottles.
ml	Reddish-orange mottled, grey clayey silt that contains ~5% angular clasts of limestone.
o	Firm, olive-coloured clay with disseminated sub-angular to angular limestone clasts.
usc	Soft, medium grey silty clay with orange mottles.
bp	Very soft, dark grey-brown organic rich silty clay.
bsc	Very soft, medium grey silty clay with orange mottles.
	Fault, showing direction of stratigraphic separation.
(01)	14C sample no. (prefix = "Kek-N1-C14-")

Figure 4.9: *Post-earthquake trench log of the SW wall of Trench N1, showing numbered faults (1 and 4, correlated to the pre-earthquake trench, Figure 4.4) and basic stratigraphy. Orange bar along the scale at the base of the trench shows material that is the same as that logged in the pre-earthquake (2016) trench. The ^{14}C age range of Sample 01 is quoted in cal. B.P. at 95% confidence (negative age is given as the sample is younger than 1950 AD). For more information on this ^{14}C sample, see Appendix B.2.4. Inset shows the enlarged version of the tail end of the trench backfill from the pre-earthquake excavation (unit tbf), displaced into plane from ~9 m to the SW. No vertical exaggeration.*

Fault 3: I recognize this fault on the post-earthquake trench wall based on the shape of the basal contact of unit uc (Figure 4.7). In the pre-earthquake trench log, fault 3 offsets the base of unit uc on the southeast limb of the synclinal basin (Figure 4.4). In the post-earthquake log, this contact retains a similar shape, even though the basin has been highly deformed (in particular, steepening of its limbs) during the earthquake.

Deformation outside the boundaries of the inner rupture zone

Fault 5: On the post-earthquake trench wall, several short faults are located to the northwest of fault 4 (Figure 4.7), placing them outside the boundaries of the inner rupture zone. I correlate this fault array to fault 5 from the pre-earthquake trench (Figure 4.4), as they truncate the unit (uc) at its northwestern extent in both the pre- and post-earthquake trench logs (Figures 4.4 and 4.7). In the pre-earthquake trench (Figure 4.4), fault 5 is overlapped by the unit mp, while in the post-earthquake trench (Figure 4.7), this array of faults is overlapped by the unit lp. This is likely the result of the down-dip migration of unit mp through out-of-plane motion – such that it is no longer observed in this plane of view.

4.4.2.2 Trench S1, northeast wall (refer to Figure 4.8)

This trench (TS1) exhumes the northeast wall of the southern fragment of the original trench, a wall that was not logged prior to the earthquake because of its gravitational collapse. The NE wall of this trench is dominated by a bulging mass of anthropogenically mixed, clay-dominant material (unit tbf) that had been used to backfill the original, pre-earthquake trench (T1) following the 2016 excavations. Unit tbf is located between two steep, upwardly convex faults (faults A and B on Figure 4.8). This strongly deformed, central part of the fault zone on this trench wall is designated as the inner rupture zone.

Fault A: This fault bounds the northwestern margin of the up-bulged mass of backfill (unit tbf) and upwardly bifurcates into two strands midway up the trench. Fault A accommodates a large dextral strike-slip, having displaced the northwestern half of the T1 trench ~9 m horizontally relative to the southeastern side. In addition to this strike-slip motion, fault A uplifts the tbf unit along its highly convex upper splay, emplacing the up-bulged mass of backfill over the lp and mp units to the northwest. A second, steeper-dipping, and structurally lower splay of fault A emplaces a “horse” or slice of unit lp (in its hanging wall) over units lp and mp (in its footwall). This splay crosscuts the higher and more shallowly dipping splay in an apparently out-of-sequence manner.

The stratigraphy to the northwest of fault A consists of stratigraphic units that are equivalent to those logged in the synclinal basin on the SW wall of the pre-earthquake trench (Figure 4.4). In addition, a newly recognized stratigraphic unit (unit ff, organic clay) was logged on the post-earthquake trench wall, where it occurs (inserted) between units uc and lp. I infer that prior to the 2016 earthquake, a lens of unit ff existed to the southwest of the original trench wall logged in 2016 (Figure 4.4), and that it was transported into the plane of the trench by strike-slip on Fault A during the earthquake – explaining its absence in the pre-earthquake trench.

Fault B: This fault acts as a low-angle (~20° dipping) oblique fault, accommodating both strike-slip and convergent motion. Opposite in vergence to Fault A, Fault B emplaced the mound of backfill (unit tbf) up and over the 2016 topsoil (unit ts) to the southeast. Fault B bifurcates upward into a second, subvertical splay cutting at least part way upward though the centre of the backfill mass. This splay was likely dominated by dextral slip.

4.4.2.3 Trench N1, southwest wall (refer to Figure 4.9)

Displaced eastward by 4.9 ± 0.2 m from its pre-earthquake location (Figure 4.6a), the northern part of this trench wall is materially coincident with the logged northern part of the original trench (highlighted orange in Figures 4.4 and 4.9). This material has been juxtaposed against new material (southeastern part) that was not logged in the pre-earthquake trench, through ~9 m of (relative) dextral slip on fault 4. Only two of the faults from the original, pre-earthquake trench could be identified on this trench wall, which were the two faults that accommodated most of the slip in the 2016 earthquake (faults 1 and 4).

Fault 1: This fault is inferred to be an along strike continuation of fault 1 that was active in the 2016 earthquake, mapped both in the original trench (Figure 4.4) and in its southern displaced fragment (Figure 4.7). Fault 1 here includes two steep strands that bound a slice of organic rich sediment (units bsc, bp, and usc) at a depth of ~1 m below the post-earthquake ground surface. The northern of these two steep strands bifurcates upward into two splays: a southern, structurally lower strand (Fault 1A) that shallows abruptly, displacing units ts (topsoil) and ml up and over the 2016 topsoil; and a northern, structurally higher strand (Fault 1B) that bifurcates upward from Fault 1A, emplacing units o and ml over themselves in an apparent thrust repetition. Between these two fault strands is an anticlinal wedge of material capped by an overturned limb of the pre-earthquake topsoil (unit ts). While upper part of Fault A accommodates a large contractional heave (~2 m, Figure 4.9), I interpret Fault A to have slipped with dominantly dextral motion, not only in this trench but also farther west (Figures 4.5 and 4.7).

Fault 4: As is also the case in the southern trench fragment TS1 (Figure 4.7), this steeply dipping fault bifurcates upward into several strands that cut upward all the way to the post-earthquake ground surface (Figures 4.5 and 4.9). On this trench wall, a downward tapering wedge of the pre-earthquake trench backfill (unit tbf) is enclosed between these fault strands. Located ~5 m to the northeast along fault strike of the main mass of backfill (Figure 4.5) logged in Figure 4.8, this <1m wide slice of the same material is inferred to be the highly deformed, northern end of the originally rectangular-shaped backfilled volume of the original trench. It is here displaced eastward and dextrally sheared into the plane of Figure 4.9.

4.4.3 Structural interpretation of 2016 coseismic deformation across the rupture zone of the Kekerengu Fault at the trench site

To understand the deformation in this rupture zone as a whole, it was imperative to combine information from these three adjacent trenches into a complete story of the sequence of events during the rupture. To do this, I used a variety of techniques including area balancing, and both 2D and 3D restoration of the trench site to its pre-earthquake state.

4.4.3.1 Area balancing

The local estimate of shortening (contractional heave) for the trench site is ~1.3 m, based on the difference in the fault-perpendicular trench margin lengths from before and after the earthquake; yet, there is an apparently greater amount of fault-perpendicular shortening observed in the trench logs, particularly on the northeast wall of TS1. On this trench wall, the backfill from the 2016 excavations (unit tbf) was squeezed horizontally and bulged upward during the earthquake, behaving in a (macroscopically) ductile way that contrasted with the largely brittle behaviour of the material surrounding it. This bulged mass of backfill was emplaced horizontally outward over less deformed ground on both of its margins, along an inwardly dipping pair of inferred dextral-reverse faults (labelled faults A and B on Figures 4.8 and 4.10). To evaluate if the bulging and shortening between these two faults was an expected consequence of the measured contractional heave (1.3 ± 0.4 m), area balancing of the backfill was attempted (Figure 4.10). If area was conserved in this plane, then the horizontal shortening (heave in m), the depth extent of the "squeezing" (in m) and the excess area of the deformational bulge (as measured above the trace of the pre-earthquake ground surface, in m^2) should be related in a simple way (see Figure 4.11a for the definition of these parameters and for the governing equation). If area was not conserved (e.g., if new material was brought into the plane as a result of dextral out-of-plane motion), then the predicted relationship between heave and excess area (Figure 4.11c) might be violated in that plane. This would show too large an excess area relative to the heave (Figure 4.10). In particular, my earlier work (see Chapter 3) predicts that dextral coseismic rotation of turf rafts about vertical axes within the inner part of the rupture zone should introduce excess material into the fault-orthogonal plane of view. This rotation causes an increase of fault-orthogonal horizontal shortening in the rafts to a magnitude beyond that of the fault heave (Figure 4.12a). Note that a lack of area balancing does not imply (or require) an overall change in volume of the deformed material in the zone, only a redistribution of material into the reference plane.

To estimate the original depth of the backfill in this plane of view, I consider the dimensions of the original trench. The trench had a bench at ~2 m below the surface that extended across its entire width. While the centre of the trench did extend to 4 m depth, that section was very narrow, so the basal contact for the majority of the backfill would have been located at ~2 m depth. I therefore assume a detachment depth of ~2 m when describing deformation that has been localised into the backfill volume in this plane of view (Figure 4.10).

The final width (W_f) of the backfill as measured on the NE wall of TS1 is 0.66m (shown on Figure 4.10). The contractional heave at the trench site was 1.3 ± 0.4 m (ΔS), as previously calculated in section 4.4.1. To estimate the original width of the backfill (W_0) in this plane of view prior to deformation and shortening, I add the measured fault-perpendicular shortening (1.3 m) to the final width:

$$W_0 = W_f + \Delta S = 0.66 \text{ m} + 1.30 \text{ m} = 1.96 \text{ m (Figure 4.11b).}$$

Combined with the estimated depth (d = 2 m), I estimate the original area of the backfill (A_0) in this reference plane of view:

$$A_0 = W_0 \text{ x } d = 2.0 \text{ m x } 1.96 \text{ m} = 3.92 \text{ m}^2 \text{ (see Figure 4.11b).}$$

To predict the expected excess area (A_{exp}) for a case of constant area in the chosen plane, given the known amount of contractional heave or shortening (ΔS) at the site, one multiplies this shortening (ΔS) by the depth of the backfill (d):

$$A_{exp} = \Delta S \text{ x } d = 1.3 \text{ m x } 2.0 \text{ m} = 2.6 \text{ m}^2 \text{ (see Figure 4.11c).}$$

Based on the logged topographic profile on the NE wall of TS1 (Figure 4.8), the actual deformational excess area of the backfill in this plane is ~4 m^2 (above the projected pre-deformation ground surface), which is a greater than that predicted for the case of constant area (Figure 4.11c). The apparent increase in area on this plane as a result of deformation indicates that either: a) my assumed depth of the backfill and/or the shortening magnitude were too small; or b) that additional material (area) was brought into the plane of view as a result of macroscopically ductile (pervasive) deformation of the backfill - most plausibly a consequence of out-of-plane dextral shearing and/or turf raft rotation. My estimate of shortening (ΔS) based on exact measurement of the deformational change in length of the original trench walls is known to within ± 0.4 m. The depth of the backfill may be underestimated (i.e., too shallow), however, as previously stated, ~2 m is the most reasonable estimate for its depth. Thus, the most plausible explanation for a lack of area conservation on the fault-orthogonal plane is that material derived from out of plane has been introduced into this plane as a result of dextral deformation (Figure 4.12, also confirmed by my analysis in Chapter 3).

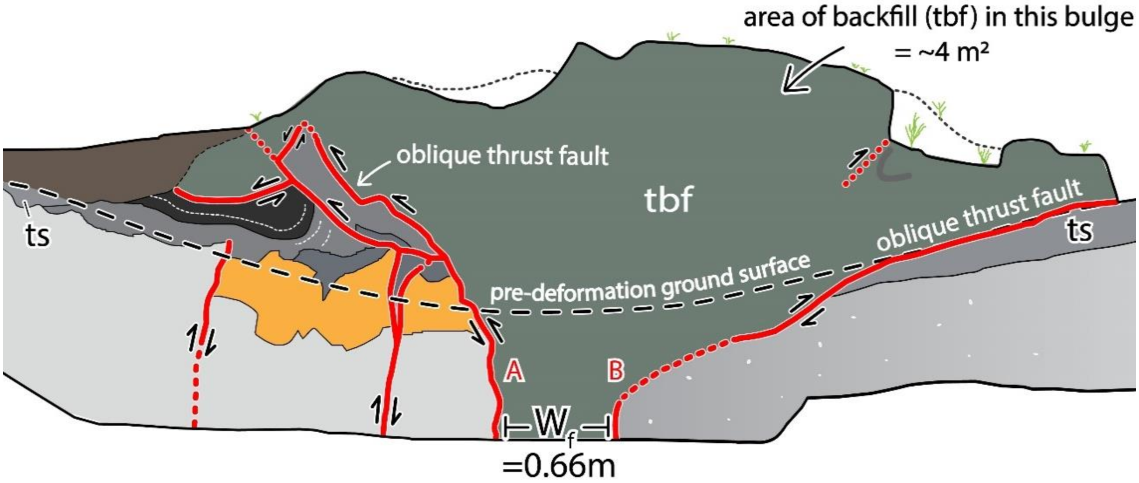

Figure 4.10: *Enlarged version of the trench backfill (unit tbf) within the inner rupture zone, as observed on the NE wall of TS1 (see Figure 4.8 for full version). This section of the backfill was used to determine if area was conserved in this plane of view during the earthquake. Low angle contractional faults (oblique thrusts) are labelled and are referred to as Fault A and B in the text (also labelled). The final width of the backfill (labelled) can be measured between these faults (W_f = 0.66 m). A pre-deformation ground surface is extrapolated across the trench wall, through projection of the upper contact of the topsoil (as this represents the ground surface prior to the earthquake); the excess deformational area above this surface is ~4 m^2.*

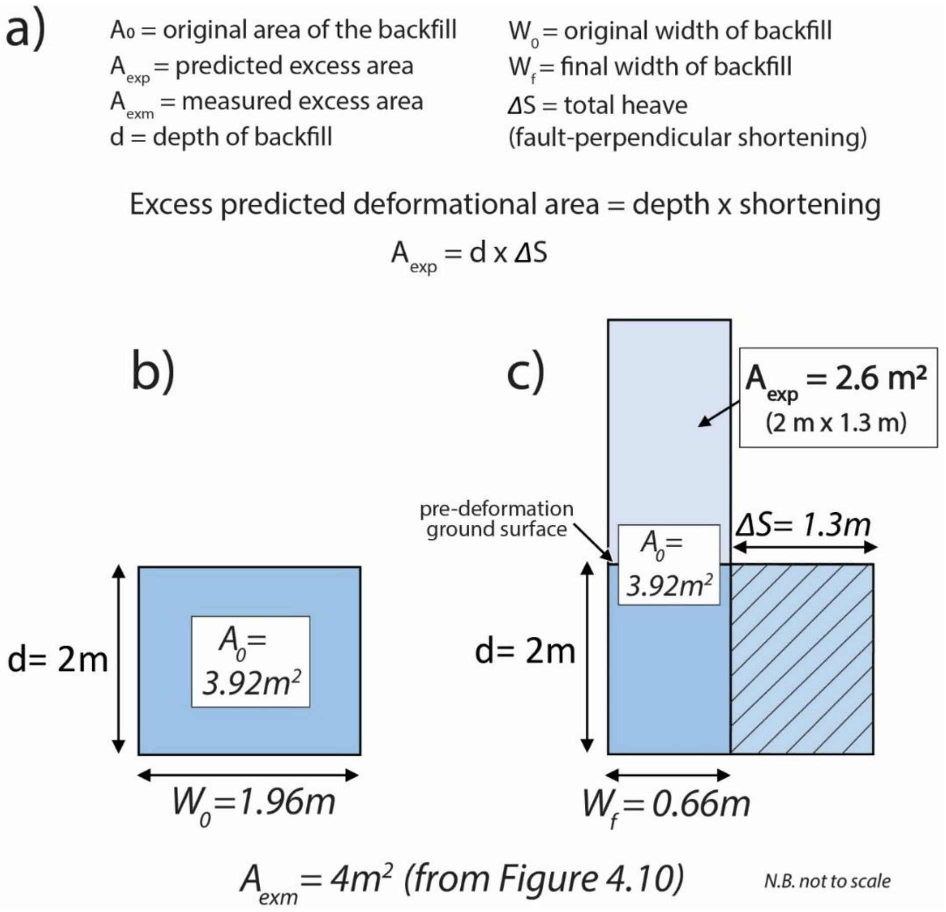

Figure 4.11: *This diagram shows a schematic cross-sectional view of the deformational bulge of backfill shown in Figures 4.8 and 4.10. Part a) shows the definitions of terms used in the area calculations, and the governing equation for deformational excess area; b) shows the estimated original area of the backfill (A_0 = 3.92 m^2) using the original depth of the backfill (d = 2 m) and the estimated original width ($W_0 = W_f + \Delta S$ = 1.96 m); c) shows the predicted final excess area of the backfill (A_{exp}) above a pre-deformation ground surface (labelled), after 1.3 m of shortening (assuming that the total area of 3.92 m^2 is conserved). This predicted value of excess area (A_{exp}= 2.6m^2) is much smaller than the measured value (A_{exm}= 4 m^2, from Figure 4.10), by a factor of almost 50%.*

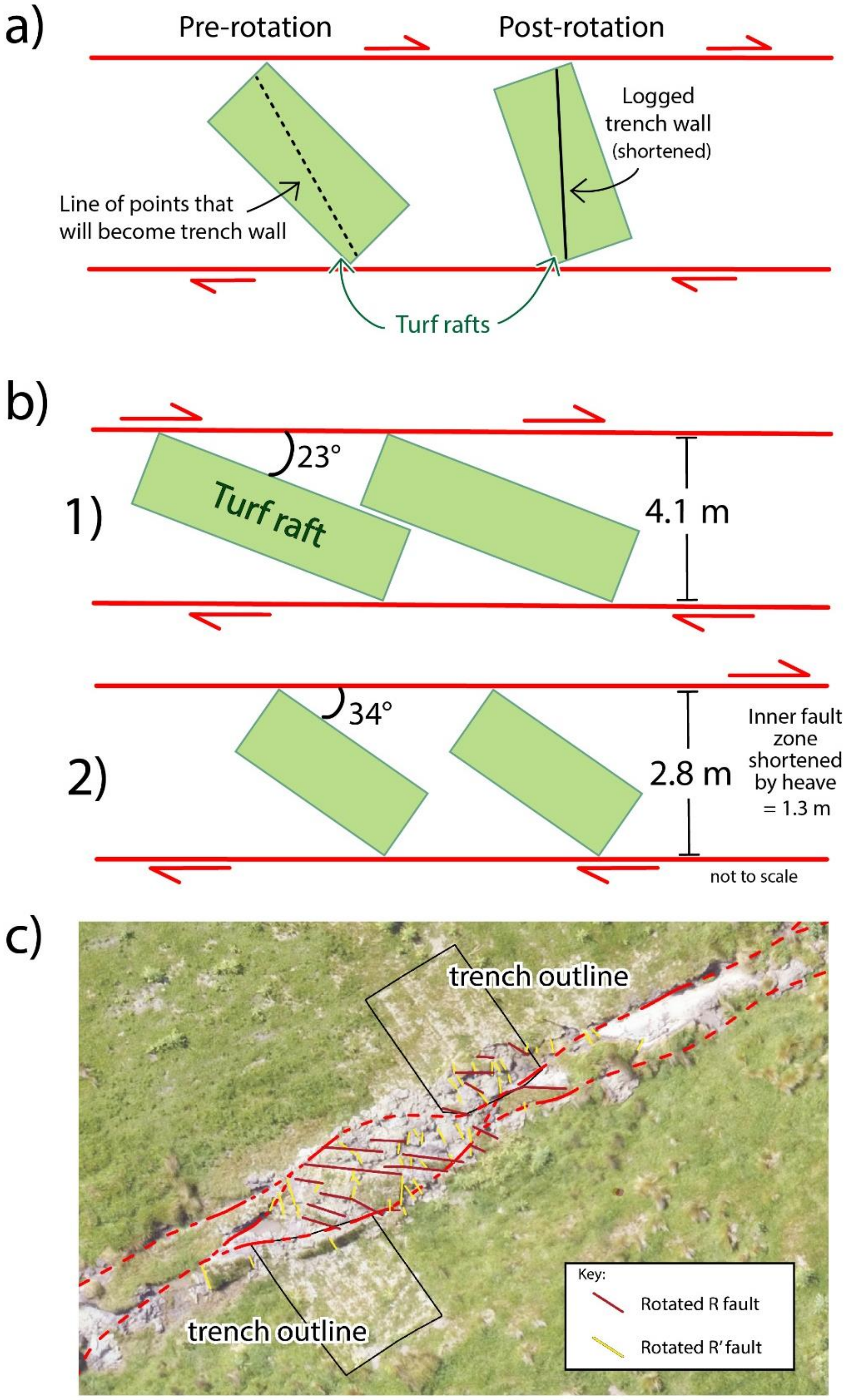

Figure 4.12: *Aerial view diagrams showing: a) the process by which a line of points that is to become a trench wall is rotated and shortened with a turf raft to become perpendicular to the fault; b) a schematic block rotation model based on the measured values from the trench site (R fault strike = 23°, R fault rotated strike = 34°, and initial and final rupture zone widths), used to calculate the partitioning of discrete slip and distributed deformation at the site (see section 4.5.1); c) the rotated R faults at the trench site that bound the turf rafts at this location. R fault strikes were measured further northeast outside of this selected aerial extent.*

4.4.3.2 Partially restored cross-sections

By comparing trench logs from before (Figure 4.4) and after the earthquake (Figures 4.7 and 4.9) one can quantify changes in the thicknesses, dip, and shape of the stratigraphic units on the logged plane, that have changed as a result of deformation during the earthquake. Evaluating these changes may provide information on the mechanisms and distribution of coseismic deformation in the plane of the trench, and insight into how and where different components of displacement were partitioned into the rupture zone. To aid in the visualisation of the stratigraphic and structural changes, I have created "intermediate state" (i.e., syn-earthquake) cross-sections of the displaced SW walls of the original trench (Figures 4.7 and 4.9). These cross sections (Figures 4.13 and 4.14) represent a "semi-deformed" snapshot in time that postdates the beginning of the rupture but precedes the final deformed state which is shown in the 2018 trench logs.

To create these semi-deformed cross-sections, I compared the dip angles, shape, and thicknesses of the units between the pre- and post-earthquake trench logs, and chose a midpoint between these two states to represent syn-earthquake versions of each of these units. I also estimated semi-deformed versions of the faults - in this case examining the shape of the faults and the number of strands in both the pre- and post-earthquake trench logs. In creating these intermediate state cross-sections, I am assuming that throughout the duration of the earthquake, deformation was occurring homogenously (i.e., the discrete strike-slip, convergence, and distributed aspects of the deformation were all occurring synchronously), rather than in distinct phases (i.e., discrete strike-slip occurred first, ceased, and was succeeded by convergence and/or shortening).

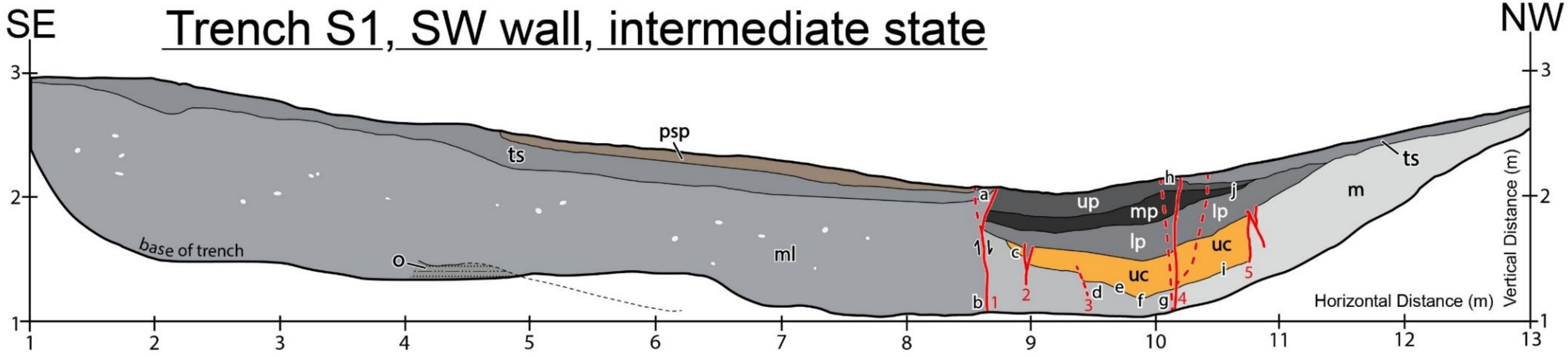

Figure 4.13: *Intermediate state cross-section of the SW wall of TS1, showing numbered faults (dashed if they are yet to form) and stratigraphy that has been partially retrodeformed. Letter labels show areas of particular intrest:* ***a)*** *in 2016, unit ts extends over the entire ground surface, but in the final 2018 log, it is folded (with unit psp) by fault 1. This state shows the point in time where the topsoil (ts) is truncated by fault 1 and is just beginning to fold;* ***b)*** *fault 1 still appears as a single strand in this state;* ***c)*** *in the pre-earthquake trench at this location, unit uc was present both within and to the SE of fault 2, but in the post-eartquake trench, unit lp both fills fault 2 and is present to the SE of it. In this intermediate state, the splays of fault 2 contain the lp unit, but a small slice of unit uc is still present to the SE as it has not yet been dextrally sheared out of plane;* ***d)*** *fault 3 was present in the pre-earthquake trench, but is only inferred in the post-earthquake trench. In this intermediate state log, it s presence is inferred, based on the abrupt change in shape of the lower contact of unit uc;* ***e)*** *in the pre-earthquake trench, the dip of the lower contact of uc between fault 3 and 4 was moderate and to the SE, but in the post-earthquake trench it dips steeply to the NW. In this intermediate state it dips shallowly NW, to approximate a "halfway" point between these two differing pre- and post-earthquake dip directions and angles, while maintaining a subtle (gentle) synclinal structure;* ***f)*** *this point represents the maximum depression of the basin, which is less defined here compared to either the pre- or post-earthquake logs;* ***g)*** *fault 4 acts as one strand in this state, and has not yet accommodated enough motion to facilitate small vertical offsets of the unit uc across it;* ***h)*** *in the final log, unit ts has been displaced by fault 4 and no longer exists adjacent to it– but in this state it is still present as there has not yet been enough slip on fault 4;* ***i)*** *in the pre-earthquake trench log, the dip of uc between faults 4 and 5 is sub-horizontal, while in the final logs, it is steep and to the SE. In this state it dips moderately to the SE to represent a halfway point between these two states;* ***j)*** *in the pre-earthquake log, the peat units (lp, mp, up) extend across fault 4 to the NW, but in the post-earthquake log they are truncated by it. In this state the peat units are still present, but are beginning to thin out NW of fault 4 as they are replaced by narrower thicknesses of the same units from the SW, through dextral slip.*

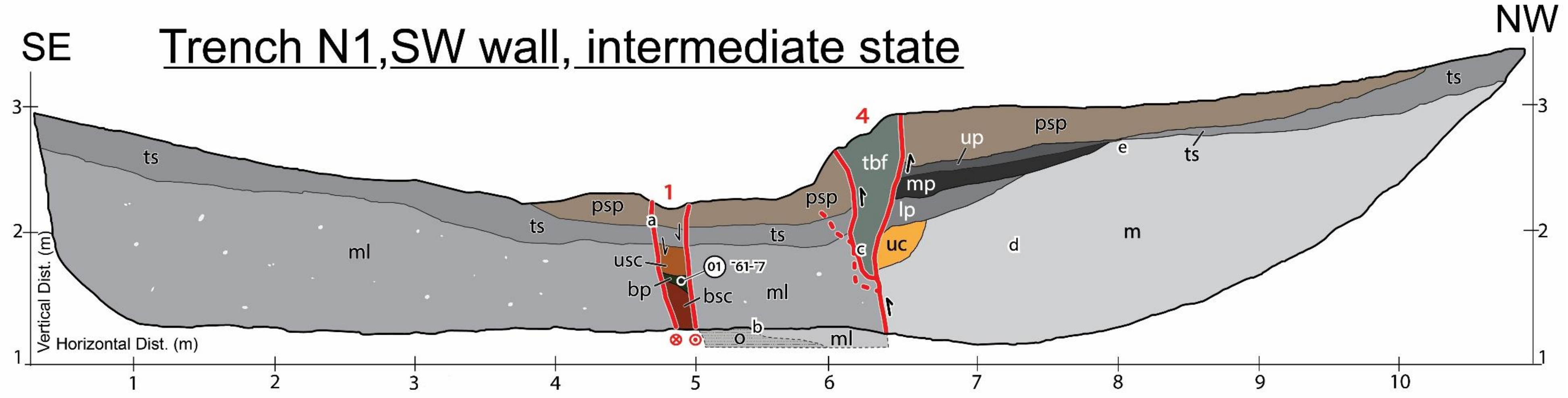

Figure 4.14*: Intermediate state cross section of the SW wall of TN1, showing numbered faults (dashed if they are yet to form) and stratigraphy that has been partially retrodeformed. Letter labels show areas of particular interest:* ***a)*** *as Riedel faults form, begin to rotate clockwise, and open-up as fissures, fault 1 opens up and is partially infilled with down-faulted and/or gravitationally collapsed 2016 topsoil and related near-surface organic sediment (units usc, bp, bsc);* ***b)*** *the oblique dextral-reverse fault strands identified in the post-earthquake trench (faults 1A and 1B, Figure 4.9) have not yet activated, with units o and ml sitting just below the depth of the trench in this state;* ***c)*** *fault 4 is dashed in places as all the strands have not yet activated. Less area of unit tbf therefore exists in this plane of view, as a greater quantity of this unit is still to be sheared dextrally into plane by the fault strands of fault 4 that will soon develop;* ***d)*** *all of the material on the northwestern side of fault 4 is the same as that logged in the pre-earthquake trench, but eventually will be displaced ~9 m dextrally relative to the trench fragment on the southeast side of fault 4;* ***e)*** *in the pre-earthquake trench the unit up is very thin at this location and pinches out underneath the topsoil, while in the post-earthquake trench, no contact was logged between them and they laterally merge. This changed contact topology is inferred to be the result of different unit morphologies from out of plane to the SW being sheared dextrally into this trench wall (as discussed in text); I represent this intermediate state in contact topology by the tapering out of these two units before they contact one another.*

Trench S1, SW wall - intermediate state (refer to Figures 4.4, 4.7 and 4.13)

This cross-section represents a point in time where fault 4 had not yet bifurcated into two strands. In this "snapshot", the synclinal basin structure seen in the pre-earthquake trench is still present, but the limbs of the syncline dip more shallowly, as the basin is progressing towards the partially inverted (up-bulged) state seen in the final post-earthquake log (Figure 4.7). In this state, the topsoil (unit ts) southeast of fault 1 is, at the surface, still almost horizontal (as it is prior to the earthquake), but it is beginning to fold adjacent to fault 1. This attempts to depict the earliest stages of the folding of the topsoil (ts) seen in the post-earthquake log (Figure 4.7). Other more subtle stratigraphic and structural changes are detailed in the figure caption of this log (labelled a – j, Figure 4.13).

Trench N1, SW wall - intermediate state (refer to Figures 4.4, 4.9 and 4.14)

This partially restored cross-section highlights the temporal evolution of fault 1 on the southeast side of the trench log. A radiocarbon sample taken from unit bp adjacent to this fault (sample N1-01, Figure 4.9, Figure 4.14) yielded a modern age (refer to Appendix B.2.4); however, it was sealed by an overriding fault strand. This relationship leads me to infer that the lower section of this fault must have been opened at the surface early on in the rupture, and was filled in with ground-proximal material before it was sealed by the overriding fault strand (fault 1A, Figure 4.9). In this state, both the topsoil (unit ts) and spoil from the 2016 excavations (unit psp) are still unbroken, laterally continuous layers at the ground surface that have not yet been deformed. Other more subtle stratigraphic and structural changes are detailed in the figure caption of this log (labelled a – e, Figure 4.14).

4.4.3.3 Topographic differencing

Area balancing techniques and the restoration of the trench logs to an intermediate-state provides some comparison of "before" and "after" data from the earthquake, but this only quantifies changes in a specific (fault-perpendicular) 2D plane of view. To better understand deformational changes in 3D, I compare Digital Surface Models (DSMs) from before (2015 aerial survey, Hill and Ashraf (2017), Figure 4.15a and b) and after (Zekkos et al. 2018, Figure 4.15c and d) the 2016 earthquake. The difference in elevation between these two surfaces can provide information about the deformational excess volume that was incorporated into the bulged moletrack in 3D at the site. The contractional heave is known at the site (1.3 ± 0.4 m, section 4.4.1), and so assuming that there was at most a small change in volume during the earthquake, the excess volume should be proportional to the mean depth of detachment of the deformed rupture zone materials as averaged across the study site of Figure 4.15 (i.e., not specific to the ~1 m high up-bulge of trench backfill, as depicted in Figure 4.10 and analysed in Section 4.4.3.1).

The dataset I use to represent the topography prior to the earthquake is derived from an aerial survey taken in 2015 (Figure 4.15a), which produced a DSM with a grid spacing of 30 cm (Figure 4.15b). I compare this pre-earthquake surface model with that derived from a survey taken by a remotely piloted aircraft (Zekkos et al., 2018) 12 days after the earthquake (Figure 4.15c). The post-earthquake survey produced a DSM at a grid spacing of 2 cm (Figure 4.15d), which is much higher in resolution than the pre-earthquake one. The two datasets were loaded into CloudCompare (v2.10.2) - a program that allows data to be viewed in 3D. Datasets were clipped to an area around the paleoseismic trench (shown in Figure 4.15).

The southern fault block in the 2016, post-earthquake DSM was aligned to the southern block of the 2015 DSM, using common, identifiable fixed features such as fence posts and a water trough. After this alignment, the elevations of each grid cell for each surface model were sampled at a grid spacing of 20 cm (a value chosen to accommodate the differences in resolution between the two DSMs) and exported as a raster image. Once loaded into ArcMap GIS, the two DSMs were differenced to produce a new DSM that shows the change in elevation as a result of the earthquake. However, because the Kekerengu Fault slipped dextrally by ~9 m at the site, this comparison produced some noise (labelled on Figure 4.15e). The elevation differences at any given point on the northern fault block are influenced by the lateral shift of the topography during the earthquake; moreover, they do not compare points of identical material to one another. In this initial comparison, where a ridge or hill was laterally displaced into a region where they did not formerly exist, the grid cells record a positive change in elevation (red areas), while also leaving depressions, or negative elevation changes, at their original locations (blue areas).

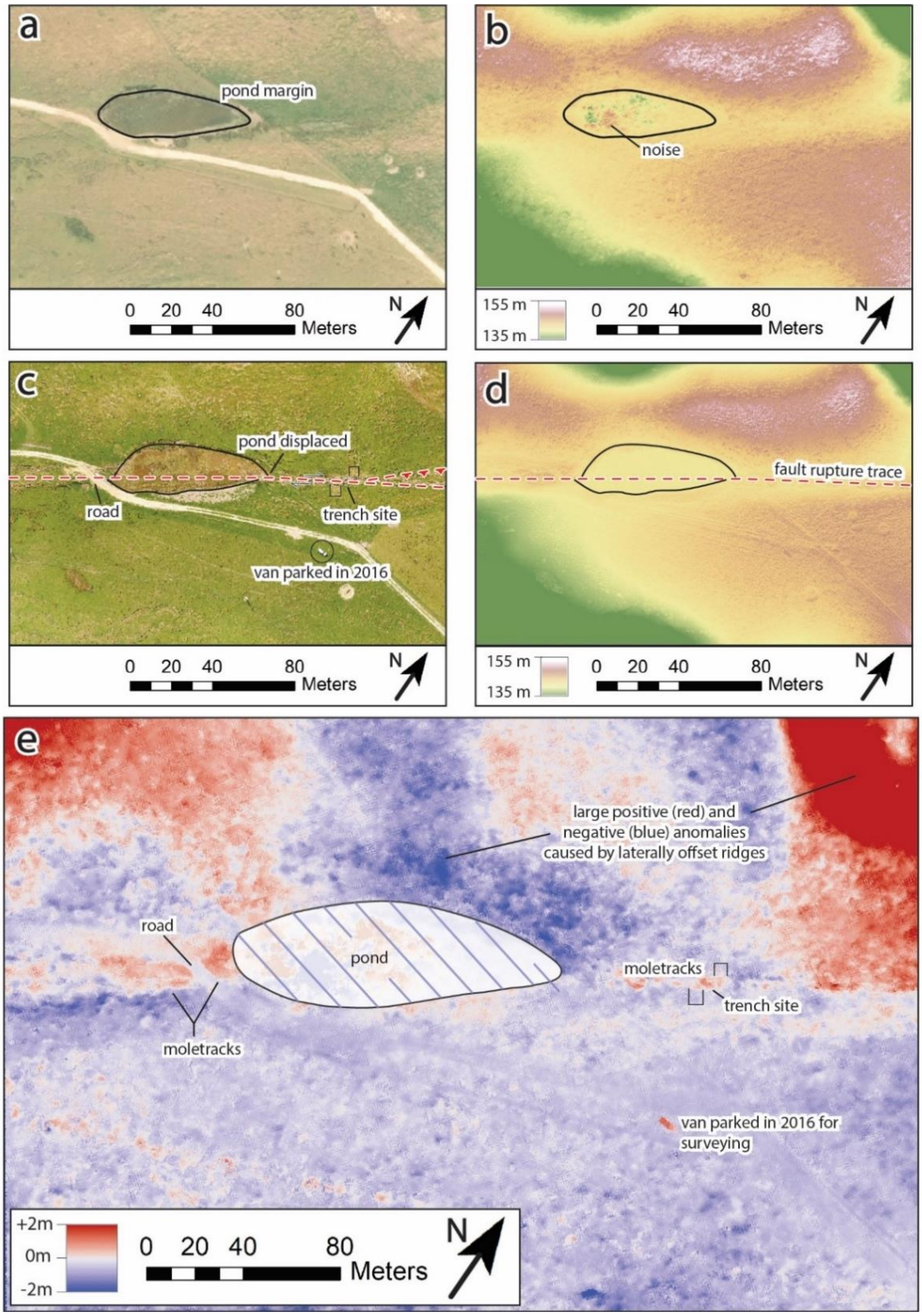

Figure 4.15: *Aerial orthophotography and DSMs used to estimate elevation changes at an area around the trench site. Boxes a) and b) show the pre-earthquake aerial photograph and DSM respectively. Boxes c) and d) show the post-earthquake orthophotograph and DSM respectively, with the labelled 2016 fault rupture trace and displaced features including the road, pond, and trench margins. Box e) shows the difference in elevation (from -2 m to +2 m) between the pre- and post-earthquake DSMs (in boxes b and d), with some labelled features (including moletracks and a survey van, see text). Artefacts/noise are created within the pond on the DSMs (in boxes b and e) as the water does not reflect true elevations – these are shaded out in e) such that the true differences in elevation are better observed.*

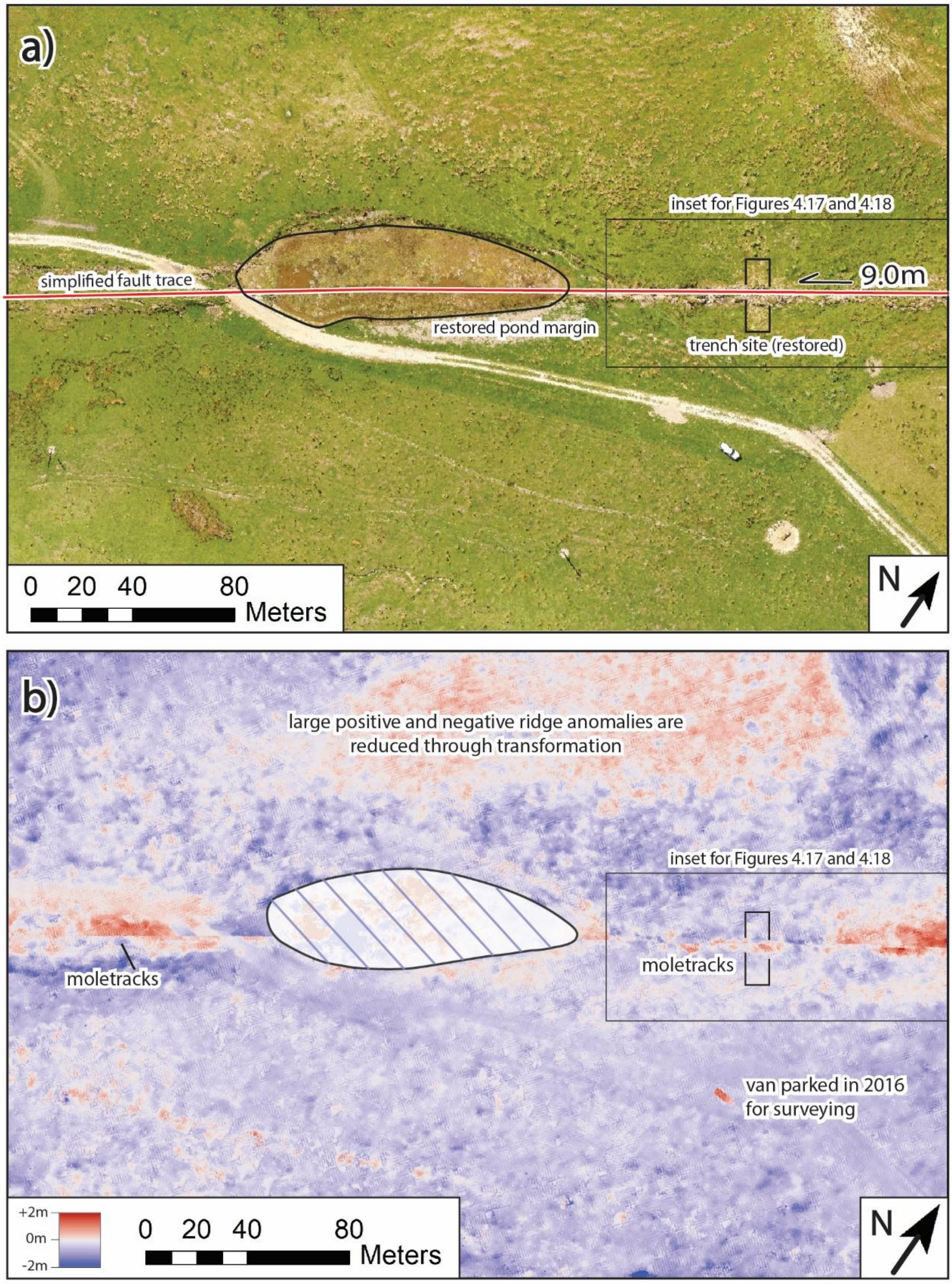

Figure 4.16: *Restored version of a) the post-earthquake orthophotograph and b) the differenced DSM (see text for method). Anomalies from Figure 4.15e (offset ridges) have been reduced through this restoration. The black box in 'b' is the location for Figures 4.17 and 4.18. The pond is again shaded out here due to the water creating artefacts and noise in the DSM.*

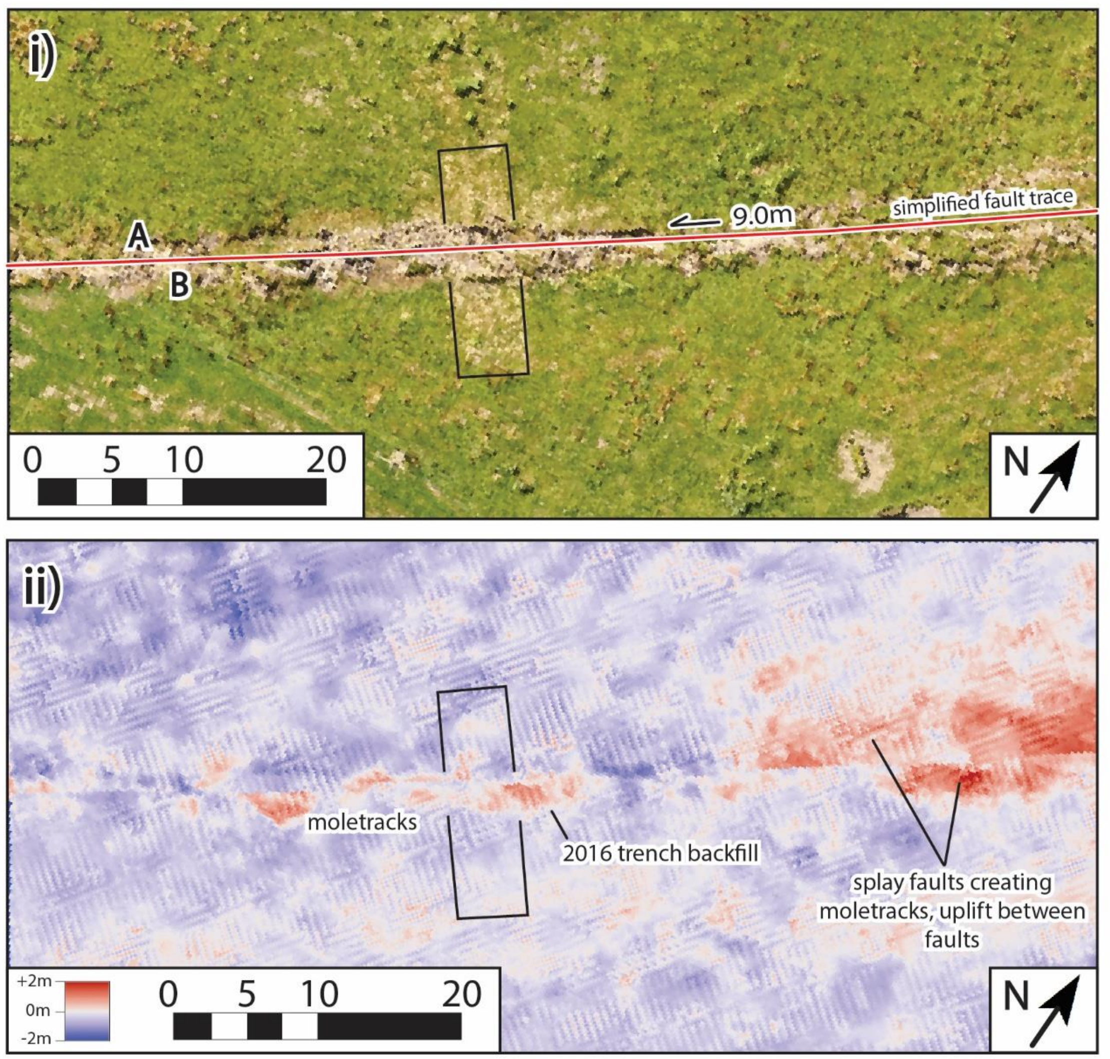

Figure 4.17: *Restored orthophotograph (i) and differenced DSM (ii) of the trench site using ~9 m of sinistral slip along one simplified fault rupture trace (see text for further detail). Restored trench margins are shown by the black lines in the centre of the figures. In ii), moletrack structures show up as positive elevation changes as expected, and are labelled. Trench backfill is also labelled.*

To overcome the shortcomings of this first approach, and to correct for the known ~9 m of dextral displacement (such that the height of the same material at any point before and after the earthquake can be compared), I drew a simplified fault trace along the post-earthquake DSM in CloudCompare (shown in Figure 4.16a), and restored the northern fault block ~9 m sinistrally (to the left) with respect to the southern fault block. In this way, the trench and pond margins (labelled) were restored to their pre-earthquake alignment (Figure 4.16). When this (laterally shifted) post-earthquake DSM is differenced with the pre-earthquake DSM, it produces a more accurate measure of the coseismic vertical shift experienced by each grid point on the ground (Figure 4.16b). Errors in the method are derived from our uncertainty in the precise dextral slip magnitude used in the restoration (± 0.3 m), our assumption of rigid fault blocks, and the mismatch in grid sizes between the 2015 and 2016 DSMs. A practical test of this method is the observation of the pixels coincident with the parked van that is present on the post-earthquake DSM – this van shows up clearly as an appropriately positive change in elevation on the differenced DSM (Figure 4.16b), which is expected as that vehicle was not present at the time of the 2015 survey.

Although topographic differencing at this scale does highlight some moletrack structures around the fault (labelled on Figure 4.16b), to estimate a more accurate deformational excess volume I consider a smaller, narrower area around the trench site (shown by the black boxes in Figure 4.16a and 4.16b). At this more detailed scale, I tried two different methods of restoration to correct for the ~9 m of slip.

Firstly, focusing on the smaller fault-proximal area, I again slid the northern block (labelled 'A' on Figure 4.17i) sinistrally along the mean fault trace by ~9 m relative to the southern block ('B') so that the trench margins were aligned before constructing the final DSM (of differenced elevations). In this DSM, the up-bulged moletrack is clearly visible (labelled on Figure 4.17ii); however, the mound of trench backfill from the 2016 excavations (discussed in section 4.4.2 of this thesis, see Figures 4.5, 4.8 and 4.9) appears in the DSM on the northeast margin of the pre-earthquake trench (refer also to Figure 4.3). Examining the post-earthquake orthophotography (Figures 4.3, 4.5, 4.14c), the mounded backfill is smeared out between the two halves of the displaced trench. Logically, if restored to a pre-earthquake state, this backfill would re-assume a rectangular, trench-like shape in aerial view. The lack of this relationship is an unavoidable consequence of our assumption of rigid fault blocks, and it also provides good evidence for considerable distributed ("ductile") deformation within that mound. In an attempt to improve the restoration, I back-slip two pieces of the post-earthquake DSM separately on two faults (relative to a more southern block). These faults (labelled faults 1 and 4 on Figure 4.18) bound either side of the up-raised moletrack ridge (section 4.2.2 of this thesis, see Figures 4.5, 4.7, 4.8 and 4.9). I assume that the dextral slip was evenly distributed between these two faults (i.e., ~4.5 m on each fault). I first slid the block labelled 'B' (Figure 4.18i) sinistrally by ~4.5 m along fault 1 with respect to block 'C'. Subsequently, I slid the block labelled 'A' (Figure 4.18i) sinistrally by ~4.5 m along fault 4 with respect to block 'B'. When the back-shifted, two-piece post-earthquake DSM is differenced with the pre-earthquake 2015 DSM, a more realistic restored location for the main mass of trench backfill is obtained (Figure 4.18ii). This improvement, in turn, should lead to a more accurate estimation of vertical deformation of the ground during the earthquake.

To calculate a spatially integrated value for deformational excess volume caused by mounding (also fissuring) in the rupture zone near the trench, I extracted the difference in heights from the two DSMs (which were between -2 and 2 m) in ArcMap GIS and imported them into a spreadsheet. I then multiplied these heights by the cell width and cell length of the DSM (both set at 0.2 m) to get the volume for each individual grid cell. The sum of these grid cell volumes was slightly negative in total (~-341 m^3, of a total of ~44,000 grid cells); however, the average change in volume was only -7.8mm^3. This suggests that overall, the amount of volume uplifted to create the moletracks is essentially balanced by the volume that subsided or formed fissures during the earthquake.

This slightly negative mean change in elevation would be expected if this site was located in a transtensional environment, as the ground would subside during the earthquake; however, the trench site is transpressional ($\alpha = 8°$). The heave at this site should induce a slightly positive mean change in elevation as a result of the earthquake, creating an excess deformational volume. Of the cells that showed a positive change in elevation in this differencing method, the average change was ~9 cm^3. Given the uncertainties in the method, both in the pre-earthquake restoration of the DSM (metre scale lateral change to the grid cells of the DSM), and in the difference in cell size between the 2015 and 2016 DSMs (10s of cm scale difference in resolution), it is not surprising that this small mean positive change in elevation of only 9 cm^3 is masked amongst these larger uncertainties.

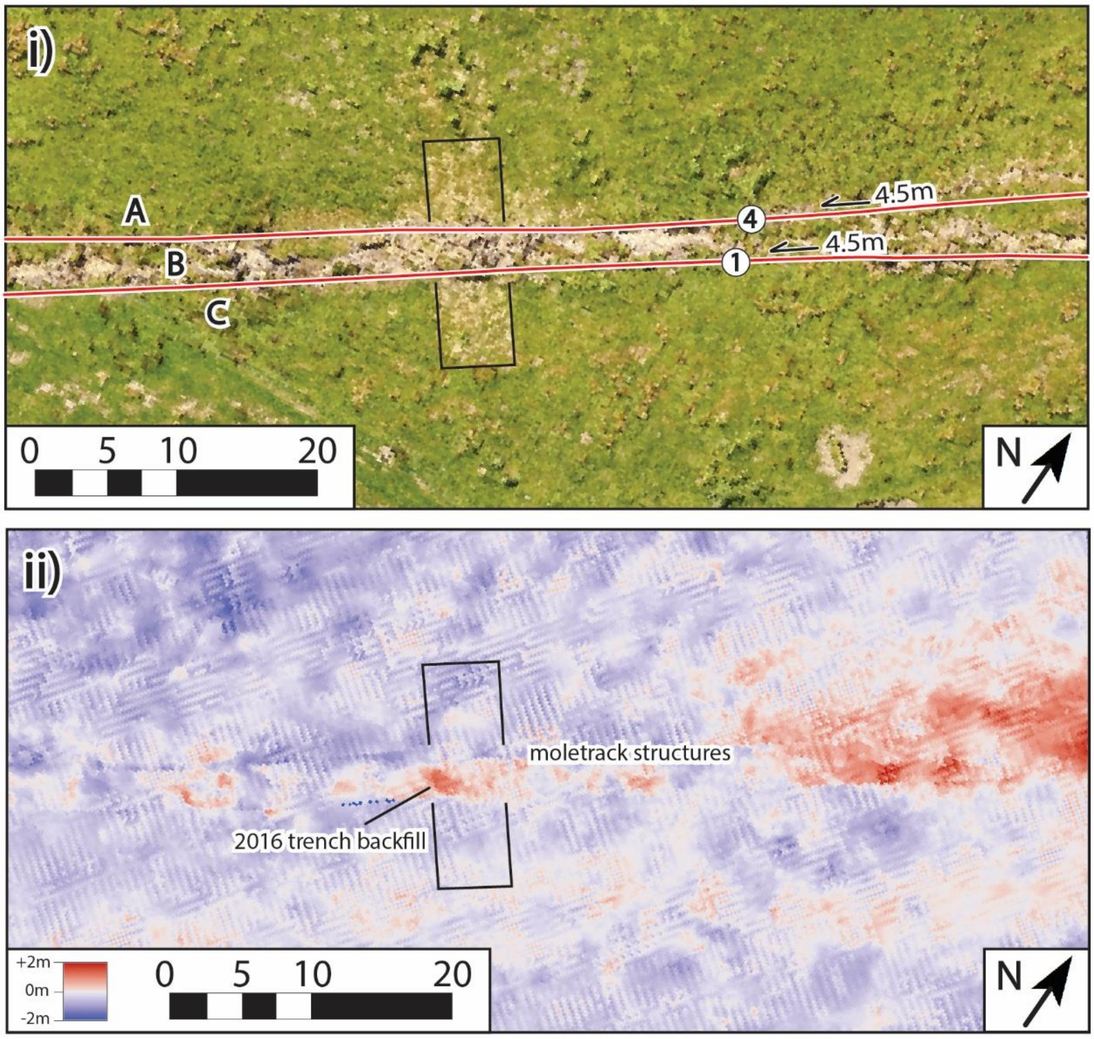

Figure 4.18: *Restored orthophotograph (i) and differenced DSM (ii) of the trench site using ~4.5 m of sinistral slip along two fault strands that represent the approxiamte boundaries of the inner rupture zone (see text for further detail). These faults are labelled 1 and 4 in i), to correlate with faults 1 and 4 from Figures 4.5, 4.7, and 4.9. Restored trench margins are shown by the black lines in the centre of the figures. In ii), moletrack structures show positive elevation changes as expected, and are labelled. Trench backfill is also labelled, and is restored to within the margins of the original (pre-earthquake) trench using this method.*

4.5 Discussion

4.5.1 How and where ~9 m of dextral slip was accommodated at the paleoseismic trench site

Through my analysis of the coseismic changes between the pre- and post-earthquake data in both 2D and 3D, I have gained insight into the deformational processes at the trench site that led to an accumulation of 9.0 ± 0.3 m of dextral slip across part of the rupture zone. This slip was accommodated within the strongly deformed and up-bulged ground ("inner rupture zone") between faults 1 and 4 (labelled in Figures 4.5, 4.7, 4.8. 4.9, 4.17) through a combination of discrete strike-slip on those faults, and distributed deformation between them. The latter is inferred to have included some pervasive dextral shearing of the near-surface materials, and also the clockwise vertical-axis rotation of turf rafts bounded by synthetic Riedel faults (Figure 4.12c, see also Chapter 3). Aerial orthophotography of the trench site (Figure 4.5) indicates that the inner rupture zone is 1.5-3.5 m wide and is bounded by faults 1 and 4 (Figures 4.7, 4.8 and 4.9), which were reactivated in 2016 from pre-existing faults (Figure 4.4).

Aerial and trench log data indicate that clockwise rotation of Riedel-fault bounded rafts, and pervasive ("ductile") shearing in the inner rupture zone were both important in accommodation of the ~9 m of total slip at the site. Interestingly, the mechanical properties of the trench backfill from the 2016 excavations seemed to play role in accommodating this distributed deformation, as it is this material that underlies the highest culmination (~1 m high) of the moletrack bulge near the trench site. I interpret that a detachment surface (much like those discussed in Chapter 3) unhinged along the base of this backfill (unit tbf) during the earthquake. This anthropogenically induced, locally deepened detachment level (~2 m deep, based on the depth to the bench in the original trench, Figure 4.4) converted the contraction at the site into a compressional mound consisting of highly deformed backfill. At its margins, this contractional mound was outwardly emplaced along low-angle oblique-reverse faults (labelled A and B in Figure 4.8), and bulged up at the surface (forming a moletrack, Figure 4.5). The accumulated heave along these marginal faults was larger than the contractional heave of the fault at the site (1.3 ± 0.4 m).

Examining Figures 4.8 and 4.9, there is an apparent contractional heave on the two faults of ~2 m, based qualitatively on the conspicuous up-bulging of unit tbf above the pre-deformation ground surface (Figure 4.8), and quantitively on the outward emplacement of units ts and ml over the 2016 ground surface along fault 1 (Figure 4.9). This difference between the locally observed shortening (~2 m) and the measured heave (~1.3 m) can be reconciled by reference to the block (turf raft) rotation model (discussed also in Chapter 3), the basics of which are outlined in Figure 4.12a. This figure schematically illustrates how a line of points that will become the logged trench wall undergoes both rotation and shortening to become oriented perpendicular to the fault. This creates, in this plane of view, an amount of “ductile” shortening that is greater than the fault-orthogonal displacement between the two rigid fault blocks. This interpretation of “extra” fault-transverse shortening caused by transcurrent distributed deformation is supported by: a) my area balancing exercise (see section 4.4.3.1), which showed that extra material entered the plane of the trench wall during deformation, and b) my topographic differencing exercise, which showed that – despite this excess area – there is no (or very little) deformational excess volume (i.e., up-bulging) beyond that expectable as a result of the known contractional heave (i.e., transpression) at the site (Figures 4.16, 4.17 and 4.18).

Considering these lines of evidence, I infer that deformation during the earthquake was primarily accommodated by discrete slip on faults that bound the inner rupture zone, and by distributed deformation within that zone, including rotation of turf rafts, axial-shortening of the clockwise rotating turf rafts, and pervasive shearing of soft sediments. To estimate the relative partitioning of discrete slip to distributed deformation, I measured strike angles of the R faults and their rotated counterparts (that bound the turf rafts, Figure 4.12c) relative to local fault strike and input these values in a simple block rotation model, along with the measured rupture zone width and the heave (see Figure 4.12b). This simple model (also discussed in Chapter 3) suggests that ~50% of the total slip was accommodated by distributed deformation, and ~50% was accommodated as discrete slip on faults (presumably faults 1 and 4). This style of deformation is significantly different to that expressed in the last several paleoearthquakes (E1, E2 and E3, Little et al., 2018) at the site (Figure 4.4).

4.5.2 Contrast in deformation style at the trench site between the last paleoearthquake and the 2016 earthquake

In the Introduction, I suggested two possible explanations for the apparent contrast in ground deformation style between the last several paleoearthquakes and the 2016 earthquake. The last three paleoearthquakes involved minor extension that was manifested as incremental subsidence of the central synclinal basin at the trench site during each earthquake, and activation of oblique-normal faults (Figure 4.4). By contrast, the 2016 earthquake formed compressional moletrack structures within the inner rupture zone, and slipped with a measurable contractional heave of ~1.3 m at the site.

One explanation for this contrast in deformation style is that there was a rotation in the local coseismic displacement vector at the trench site, such that it rotated from transtensional ($\alpha<0°$) to ($\alpha = +8°$). My analysis of the processes by which deformation was accommodated (discussed in section 4.5.1) and my calculated orientation of the slip vector (based on the resurveyed positions of the walls of the trench after the earthquake) indicate that transpressional kinematics in 2016 did play a significant role, perhaps the chief one, in this change in ground deformation style.

Another possible explanation for this contrast, not mutually exclusive to the first, is that there was a change in mechanical soil properties since the last paleoearthquake, resulting from the introduction of exotic grasses at the time of European arrival - this colonization may have led to a stiffer and less granular soil. These properties may have promoted the formation of coherent turf rafts, and led to their clockwise rotation, shortening, and consequent up-bulging to form moletracks - even where there was no transpression across the fault. Paleoenvironmental and palynological work addressing this hypothesis is in progress by Lynda Petherick (VUW), who undertook detailed sampling at the trench site. As of writing (2020), pollen species assemblages in these samples have been analysed for the three peat units (up, mp and lp) and the modern topsoil (ts). These units represent the respective topsoils during the last three paleoearthquakes on this section of the Kekerengu Fault, and the 2016 earthquake (ts). Preliminary results show that the pollen species assemblages have not changed significantly over the last 1000 years (see Chapter 2 of this thesis for unit ages). This suggests that the soil properties (and by inference, the landscape) have been relatively stable over this period of time, so are unlikely to have contributed to the change in deformation style between the last paleoearthquake and the 2016 earthquake. Further information that may support these preliminary findings includes grainsize analysis and measures of the moisture content of each of these soils; such data would provide further information about potential changes in (or stability of) the cohesion of the soil over time.

4.5.3 Expression of large magnitude strike-slip rupture in a fault perpendicular plane of view

As previously stated, strike-slip earthquakes on this section of the Kekerengu Fault have accommodated minor amounts of fault-orthogonal extension (i.e., transtension) in the past. Prior to the earthquake, this was manifested in T1 as dm-scale normal dip-separations of the stratigraphic units that infilled and were synclinally deformed within the axial depression (basin) along the fault trace. The post-earthquake trench logs showed some large (~2 m) fault-perpendicular shortening in the trenches (e.g., the outward emplacement of unit tbf along faults A and B in Figure 4.8, and the offset of units ts, ml and o along fault 1 in Figure 4.9); however, the overall the dip-separations of faults that slipped in 2016 were still mostly small (cm scale), despite the site accommodating ~9 m of dextral slip. Overall, the cross-sectional expression of the strike-slip component of the 2016 earthquake remained subtle in the re-excavated trenches. For example, in Figure 4.7, the unit uc is only offset vertically by a few centimetres across fault 4, yet according to my measurements of slip on the surface, this fault accommodated ~9 m of relative dextral slip, and ~4.9 m of absolute dextral slip during the earthquake. This demonstrates (as one might expect) that large strike-slip ruptures may only show cm-dm scale offsets in a fault-perpendicular plane of view, especially where a stratigraphic depocenter is elongate parallel to the strike of the fault (and so its infill is relatively homogenous or unchanging in that direction). Furthermore, the similarities in expression of the strike-slip component of motion between the 2016 earthquake and paleoearthquakes suggests that previous earthquakes at this site on the Kekerengu Fault may have also accommodated large dextral strike-slip (<9 m), even though they were only expressed as dm-scale offsets (Figure 4.4). This relationship reiterates the importance of using surface markers to measure true offsets associated with earthquakes on strike-slip faults. Another point is that without the knowledge that this earthquake accommodated ~9 m of dextral strike-slip, one might interpret from the large, contractional heaves of its central bulge that the earthquake accommodated a large component of reverse slip, whereas in reality its throw (NW-side up) was <0.1 m (Howell et al., 2019).

The post-earthquake trench logs also illustrate that if cross-cutting relationships are observed between individual fault strands in a trench in fault-perpendicular view, they could easily be misinterpreted as a result of a sequence of earthquakes, rather than a progression of structures that developed (possibly over just seconds) during a single earthquake. This is exemplified in Figure 4.9 (see also Figure 4.13), where fault 1 is interpreted to have ruptured coseismically in 2016, as two (possibly three) temporally distinct strands: first, a small fissure or gape opened up in the ground and filled in with surface material (units bsc, bp and usc), possibly as a result of gashes opening up in the ground as rafts rotated coseismically (see Chapter 3 for further detail). During this rotation, the rafts were forced to shorten, activating oblique thrust faults (Faults 1A and 1B in Figure 4.9). These thrusts overrode the aforementioned fissure, sealing it and displacing older stratigraphic units overtop it (units ml, o, and ts). These three fault strands were possibly activated only seconds apart, but represent different deformation mechanisms.

Without the radiocarbon data of sample 1 from unit bp within this sealed fissure (modern age, see section 4.4.3.2), this temporal relationship may have been interpreted differently i.e., as two temporally distinct earthquakes. This potential misinterpretation would cause the mean recurrence interval to be underestimated, and would also affect the interpretation of the slip kinematics of the fault. In this study, the interpretation of where and how slip was distributed and accommodated during the earthquake was influenced by the rich, multidimensional 2016 datasets such as detailed post-earthquake orthophotography, which indicated that moletracks forming in the inner rupture zone were a key part of the deformation process (see Chapter 3). However, in paleoearthquake studies, such information would not usually be available.

In strike-slip zones in particular, there are subtle kinematic complexities involved in a rupture that are not well represented in a fault-perpendicular view. For example, many strike-slip faults have a varied local degree of transpression or transtension, which impacts the style of deformation that this fault would experience during an earthquake. In this study, because of the pre- and post-earthquake GPS datasets, I could establish a displacement angle of α = 8° for the trench site, which suggested that there would be an expected component of shortening (heave) in the trench logs. Additionally, in strike-slip ruptures where a narrow (inner) rupture zone forms, elements of distributed deformation are also introduced into the rupture process (such as rotation and shearing of material within this zone, as described earlier in this chapter, Figure 4.12), which can complicate the expression of slip in the corresponding zone in the sub-surface (see Figures 4.8 and 4.9, and section 4.4.2 of this chapter). Although these complications cannot necessarily be resolved in future studies, they demonstrate that caution and precision is needed when interpreting fault-perpendicular structures and the way(s) in which these structures accommodate deformation, if one wishes to gain a comprehensive and accurate understanding of how and where slip was partitioned during an earthquake.

4.7 Conclusions

The opportunity to re-excavate a displaced paleoseismic trench is one that has only been provided twice before in history (and not fully seized). In the case of the Kaikōura earthquake, a trench was dextrally displaced by ~9 m, vertically by ~0.1 m, and had a contractional heave of 1.3 ± 0.4 m. This is the largest globally recorded offset for a paleoseismic trench. The re-excavation of this trench allowed me to compare detailed datasets from before and after the earthquake (including trench logs, orthophotography, and DSMs), such that I could understand where and how this ~9 m of slip was accommodated. Reflected in each of these datasets was the existence of an inner rupture zone, bounded by two main faults (faults 1 and 4) that together accommodated ~50% discrete dextral slip during the earthquake. The remaining ~50% of the deformation was also accommodated within this inner rupture zone, through coseismic clockwise rotation of turf rafts and pervasive shearing of soft sediments between these two bounding faults. This type of distributed deformation had a complicated expression, especially in a fault-perpendicular plane of view (i.e., the trench logs), which made deformation processes harder to identify, quantify, and interpret. The most visually dominant was the discrepancy between the calculated contractional heave (~1.3 m) and the apparent fault-perpendicular shortening observed in the trench logs (~2 m). This discrepancy is explained by the distributed deformation processes outlined above, which force blocks to shorten during their rotation as they become perpendicular to the fault, creating extra apparent shortening in the logs.

The comparison of pre- and post-earthquake trench log data also illustrated that the expression of large magnitude strike-slip earthquakes in cross-section can vary significantly between earthquakes, from a difference of only a few degrees in local displacement angle. In both the last few paleoearthquakes and the 2016 earthquake, the offsets created along strike-slip faults were cm-dm scale. However, in the 2016 earthquake, a component of contractional heave was introduced at the site that dominated the expression of the earthquake in the re-excavated trenches. This contrast in deformation style is most likely the result of a change in the local slip vector from slight transtension in past earthquakes to slight transpression in the 2016 earthquake – highlighting the fact that small changes in local slip kinematics may have a large effect on the structures that form in the rupture zone of a subsequent earthquake. Preliminary analysis of pollen samples from the trenches also indicates that the pollen species assemblages have not changed significantly at this site over the last 1000 years. This indicates that the soil properties (and by inference, the landscape) have been relatively stable over this period of time, so are unlikely to have contributed to the change in deformation style since the last paleoearthquake.

Summary of Conclusions

This thesis has utilized the unprecedented opportunity of detailed datasets from both before and after the Kaikōura earthquake to understand how and where slip was accommodated during this earthquake on an eastern section of the Kekerengu Fault rupture, and also refine the pre-existing paleoseismic chronology of the fault. Each of the chapters of this thesis addresses different research questions associated with this earthquake, and therefore have their own individual conclusions.

Chapter two tested and refined the paleoseismic sequence for the Kekerengu Fault at this location. The previous age model established by Little et al. (2018) established three paleoearthquakes for the Kekerengu Fault based on a total of 10 radiocarbon samples, which resulted in a recurrence interval of 376 ± 32 yrs (1σ). I reinforced the chronology at this site with 28 new ^{14}C samples, six of which incorporated were into an updated OxCal model for earthquakes on the Kekerengu Fault. This new model embraces and five late Holocene paleoearthquakes in addition to the 2016 Kaikōura earthquake (E0). Based on the last five of these earthquakes (events E4 through E0), my new analysis yields an updated estimate for the mean recurrence interval for the fault of 375 ± 32 yrs (1σ) since ~1650 cal. yrs B.P. An alternative model that also includes oldest dated paleoearthquake (E5) yields a mean recurrence interval estimate of 433 ± 22 yrs (1σ) — interpreted as a maximum estimate of the mean RI because there may be a missed event between E4 and E5. As a result of this work, the Kekerengu Fault now has one of the best constrained late Holocene earthquake chronologies in the Marlborough Fault System—an important step forward in the general goal of assessing the rupturing behaviour of the MFS, including its potential for multi-fault rupturing earthquakes. In addition to this refined earthquake chronology, re-excavation of a dextrally displaced paleoseismic showed that strike-slip earthquakes with a large out of plane displacements may create, in some locations, only dm-scale separations on trench walls, while in others, complexly cross-cutting faults (within the same earthquake).

Chapter three analyses the push-up structures (or moletracks) that formed within the inner rupture zone along an eastern section of the Kekerengu Fault rupture. I compared these moletracks with those that have formed in other large magnitude strike-slip ruptures, and found that a controlling factor on the height and shape of moletrack structures was not the amount of slip accommodated in the earthquake, rather, it was the near-surface material that was deformed to form the moletracks, the thickness of this detached material, and the degree of transpression at a given site.

On the eastern part of the Kekerengu Fault, 7-9 m of dextral slip occurred during the 2016 earthquake. Distributed deformation and up-bulging of the moletracks that formed along the fault trace accommodated some of this slip, primarily through the rotation and horizontal shortening of rafts of clay-rich surficial sediment and grassy turf that were bounded by synthetic Riedel faults (R). During early stages of the coseismic displacement, the rafts rotated clockwise about a vertical axis and opened up as fissures between those rafts, before being cross-cut by younger, possibly antithetic (R’) faults and fragmented into blocks. The accommodation of dextral strike-slip through ~19° of clockwise rotation accommodated on average ~2.8 m of dextral strike-slip (of a total of ~9 m of slip), and apparently ceased after ~3 m of slip regardless of the magnitude of the total strike-slip at a site and the degree of transpression. During this rotation, the rafts shorten on average by ~2.4 m parallel to their bounding R faults. The remainder of the displacement was accommodated (presumably during later stages of the earthquake) by discrete strike-slip accumulating on later forming (Y) faults.

Changes in the local displacement angle, α (where $\alpha>0$ indicates transpression; and $\alpha<0$, transtension) affects several moletrack characteristics. A greater α value introduces contractional heave across the rupture zone, which causes additional shortening of the rafts or bulges, and a greater longitudinal strain within those bulges (compared to sites with a lower α value). Analysis of the fault-transverse cross-sectional shape or aspect ratio of these bulges suggests that bulges that formed in transpressional settings were slightly higher, without being significantly wider. The analysis I provide in this chapter provides a basis for better understanding the origin of moletracks, the nature of their internal deformation, and their role on accommodating coseismic slip in large strike-slip ruptures.

Chapter four compared, for the first time, the before and after cross-sections and aerial views of a displaced paleoseismic trench, providing insight into how large magnitude strike-slip ruptures are expressed in 3D. During the Kaikōura earthquake, this trench experienced ~9.0 m of dextral displacement, ~0.1 m of vertical displacement, and ~1.3 m of contractional heave. An inner rupture zone formed at this site bound by two steeply dipping strike-slip faults that together accommodated ~50% of the total (dextral) slip as discrete slip during the earthquake (based on a simple block rotation model). The remainder of the displacement was accommodated by distributed deformation within this inner rupture zone, involving coseismic clockwise rotation of turf rafts (as described above) and pervasive shearing of soft sediments between the two bounding faults.

The cross-sectional view of the rupture zone provided by the walls of the re-excavated trench fragments revealed that the coseismic deformation in 2016 included a conspicuously large shortening (<2 m) of the near-surface ground materials, despite the dominance of dextral slip (~9 m) in the total displacement (compared to the heave, ~1.3 m). This apparently large shortening component (i.e., greater than the heave) can be explained by the out-of-plane process of clockwise rotating turf rafts within the inner rupture zone, which forces blocks to shorten as they are rotated and become perpendicular with the fault. This process creates extra apparent shortening in the trench logs.

By contrast with the highly contractional surface expression of the 2016 earthquake (E0), the preceding three paleoearthquakes (events E1, E2, and E3, at 249-108, 528-356, and 1249-903 cal. B.P., respectively) were dextral-normal in their kinematics. Each of these paleoearthquakes caused renewed subsidence of an axial fault furrow and cm to dm-scale normal dip-separations of stratigraphic units infilling that furrow. In other words, the Kekerengu Fault near trench site had previously experienced transtensional ruptures since ~1605 cal. B.P., and was not a site that experienced any fault-perpendicular shortening. The abundance of sag ponds or small pull-apart basins along this reach of the Kekerengu Fault provides further evidence for longstanding transtensional slip along this part of the fault. I interpret this change in coseismic deformation style to have been the result of an abrupt rotation in the azimuth of the local slip vector during the Kaikōura earthquake - from a slight transtension ($\alpha<0$) to moderate transpression ($\alpha = 8°$).

References

Ambraseys, N., & Zatopek, A. (1969). The Mudurnu Valley, West Anatolia, Turkey, earthquake of 22 July 1967. *Bulletin of the Seismological Society of America, 59*(2), 521-589.

Atmaoui, N., Kukowski, N., Stöckhert, B., & König, D. (2006). Initiation and development of pull-apart basins with Riedel shear mechanism: Insights from scaled clay experiments. *International Journal of Earth Sciences, 95*(2), 225-238.

Barrell, D., Litchfield, N., Townsend, D., Quigley, M., Van Dissen, R., Cosgrove, R., . . . Begg, J. (2011). Strike-slip ground-surface rupture (Greendale Fault) associated with the 4 September 2010 Darfield earthquake, Canterbury, New Zealand. *Quarterly Journal of Engineering Geology and Hydrogeology, 44*(3), 283-291.

Bergerat, F., Angelier, J., Gudmundsson, A., & Torfason, H. (2003). Push-ups, fracture patterns, and palaeoseismology of the Leirubakki Fault, South Iceland. *Journal of structural geology, 25*(4), 591-609.

Cloos, H. (1928). Experimente zur inneren Tektonik. *Cetralblatt fur Mineralogie, 5*, 609-621.

Coulomb, C. (1776). An attempt to apply the rules of maxima and minima to several problems of stability related to architecture. *Mémoires de l'Académie Royale des Sciences, 7*, 343-382.

Davis, G. H., Bump, A. P., García, P. E., & Ahlgren, S. G. (2000). Conjugate Riedel deformation band shear zones. *Journal of structural geology, 22*(2), 169-190.

DeMets, C., Gordon, R. G., & Argus, D. F. (2010). Geologically current plate motions. *Geophysical Journal International, 181*(1), 1-80.

Deng, Q., Wu, D., Zhang, P., & Chen, S. (1986). Structure and deformational character of strike-slip fault zones. *Pure and Applied Geophysics, 124*(1-2), 203-223.

Dooley, T. P., & Schreurs, G. (2012). Analogue modelling of intraplate strike-slip tectonics: A review and new experimental results. *Tectonophysics, 574*, 1-71.

Eisenstadt, G., & Sims, D. (2005). Evaluating sand and clay models: do rheological differences matter? *Journal of structural geology, 27*(8), 1399-1412.

Haller, K. M., Crone, A. J., & Wood, S. (2004). Twenty years after the Borah Peak earthquake: Field guide to surface-faulting earthquakes along the Lost River fault, Idaho. *Geological field trips in southern Idaho, eastern Oregon, and northern Nevada*, 116-133.

Hamling, I. J., Hreinsdóttir, S., Clark, K., Elliott, J., Liang, C., Fielding, E., . . . Wright, T. J. (2017). Complex multifault rupture during the 2016 Mw 7.8 Kaikōura earthquake, New Zealand. *Science, 356*(6334), eaam7194.

Hatem, A. E., Dolan, J. F., Zinke, R. W., Van Dissen, R. J., McGuire, C. M., & Rhodes, E. J. (2019). A 2000 Yr Paleoearthquake Record along the Conway Segment of the Hope Fault: Implications for Patterns of Earthquake Occurrence in Northern South Island and Southern North Island, New Zealand. *Bulletin of the Seismological Society of America, 109*(6), 2216-2239.

Hill, M., & Ashraf, S. (2017). Digital surface models from Clarence to Kekerengu using semi-global matching and structure from motion photogrammetry and their use in geomorphic interpretation, GNS Science Report; 2017/17 , GNS Science, Lower Hutt, New Zealand

Howarth, J. D., Cochran, U. A., Langridge, R. M., Clark, K., Fitzsimons, S. J., Berryman, K., . . . Strong, D. T. (2018). Past large earthquakes on the Alpine Fault: paleoseismological progress and future directions. *New Zealand journal of geology and geophysics, 61*(3), 309-328.

Howell, A., Nissen, E., Stahl, T., Clark, K., Kearse, J., Van Dissen, R., . . . Jones, K. (2019). 3D surface displacements during the 2016 MW 7.8 Kaikōura earthquake (New Zealand) from photogrammetry-derived point clouds. *Journal of Geophysical Research: Solid Earth*.

Jackson, J. (1997). Glossary of Geology, American Geological Institute, Alexandria, 769 pp. *DM Lamb et al./Precambrian Research xxx (2007) xxx–xxx, 11*, 999-1012.

Kaiser, A., N. Balfour, B. Fry, C. Holden, N. Litchfield, M. Gerstenberger, E. D'Anastasio, N. Horspool, G. McVerry, J. Ristau et al (2017). The 2016 Kaikōura, New Zealand, Earthquake: Preliminary Seismological Report, Seismol. Res. Lett. 88, 727-739.

Kearse, J. (2018). Surface Fault Rupture and Slip Distribution of the Jordan-Kekerengu-Needles Fault Network during the 2016 Mw 7.8 Kaikōura Earthquake, New Zealand.

Kearse, J., Little, T. A., Van Dissen, R. J., Barnes, P. M., Langridge, R., Mountjoy, J., . . . Benson, A. (2018). Onshore to offshore ground-surface and seabed rupture of the Jordan–Kekerengu–Needles fault network during the 2016 M w 7.8 Kaikōura earthquake, New Zealand. *Bulletin of the Seismological Society of America, 108*(3B), 1573-1595.

Khajavi, N., Langridge, R. M., Quigley, M. C., Smart, C., Rezanejad, A., & Martín-González, F. (2016). Late Holocene rupture behavior and earthquake chronology on the Hope fault, New Zealand. *Bulletin, 128*(11-12), 1736-1761.

Kotô, B. (1893). On the cause of the great earthquake in central Japan, 1891. *J. Sci. Coll. Imp. Univ., 5*, 295-353.

Langridge, Almond, P., & Duncan, R. (2013). Timing of late Holocene paleoearthquakes on the Hurunui segment of the Hope fault: Implications for plate boundary strain release through South Island, New Zealand. *GSA Bulletin, 125*(5-6), 756-775.

Langridge, Campbell, J., Hill, N., Pere, V., Pope, J., Pettinga, J., . . . Berryman, K. (2003). Paleoseismology and slip rate of the Conway Segment of the Hope Faultat Greenburn Stream, South Island, New Zealand. *Annals of Geophysics*.

Langridge, Nicol, A., Clark, K., Pettinga, J., Barrell, D., Stirling, M., . . . Morris, P. (2020). *Paleoseismicity of the 2016 M_w 7.8 Kaikōura Earthquake Faults: Was this event the norm or 'one out of the park'?*

Langridge, R. M., Rowland, J., Villamor, P., Mountjoy, J., Townsend, D. B., Nissen, E., . . . Canva, A. (2018). Coseismic Rupture and Preliminary Slip Estimates for the Papatea Fault and Its Role in the 2016 Mw 7.8 Kaikōura, New Zealand, EarthquakeCoseismic Rupture and Preliminary Slip Estimates for the Papatea Fault. *Bulletin of the Seismological Society of America, 108*(3B), 1596-1622.

Lienkaemper, J. J., & Ramsey, C. B. (2009). OxCal: Versatile tool for developing paleoearthquake chronologies—A primer. *Seismological Research Letters, 80*(3), 431-434.

Lin, A., Guo, J., & Fu, B. (2004). Coseismic moletrack structures produced by the 2001 Ms 8.1 Central Kunlun earthquake, China. *Journal of structural geology, 26*(8), 1511-1519.

Little, Van Dissen, R., Kearse, J., Norton, K., Benson, A., & Wang, N. (2018). Kekerengu fault, New Zealand: Timing and size of Late Holocene surface ruptures. *Bulletin of the Seismological Society of America, 108*(3B), 1556-1572.

Little, Van Dissen, R., Schermer, E., & Carne, R. (2009). Late Holocene surface ruptures on the southern Wairarapa fault, New Zealand: Link between earthquakes and the uplifting of beach ridges on a rocky coast. *Lithosphere, 1*(1), 4-28.

Little, T., & Jones, A. (1998). Seven million years of strike-slip and related off-fault deformation, northeastern Marlborough fault system, South Island, New Zealand. *Tectonics, 17*(2), 285-302.

Mandl, G. (1988). *Mechanics of tectonic faulting*: Elsevier Amsterdam.

Mohr, O. (1906). *Abhandlungen aus dem gebiete der technischen mechanik*.

Naylor, M., Mandl, G. t., & Supesteijn, C. (1986). Fault geometries in basement-induced wrench faulting under different initial stress states. *Journal of structural geology, 8*(7), 737-752.

Quigley, M., Van Dissen, R., Villamor, P., Litchfield, N., Barrell, D., Furlong, K., . . . Noble, D. (2010). Surface rupture of the Greendale Fault during the Darfield (Canterbury) earthquake, New Zealand. *Bulletin of the New Zealand Society for Earthquake Engineering, 43*(4), 236-242.

Ramsey, C. B. (2008). Deposition models for chronological records. *Quaternary Science Reviews, 27*(1-2), 42-60.

Richard, P., & Cobbold, P. (1990). Experimental insights into partitioning fault motions in continental convergent wrench zones.

Riedel, W. (1929). Zur mechanik geologischer brucherscheinungen: Centralblatt für Minerologie. *Geologie und Paleontologie, 1929*, 354.

Schopfer, M. P., & Steyrer, H. P. (2001). Experimental modeling of strike-slip faults and the self-similar behavior. *MEMOIRS-GEOLOGICAL SOCIETY OF AMERICA*, 21-28.

Schreurs, G. (1994). Experiments on strike-slip faulting and block rotation. *Geology, 22*(6), 567-570.

Schreurs, G. (2003). Fault development and interaction in distributed strike-slip shear zones: an experimental approach. *Geological Society, London, Special Publications, 210*(1), 35-52.

Shirahama, Y., Yoshimi, M., Awata, Y., Maruyama, T., Azuma, T., Miyashita, Y., . . . Ochi, T. (2016). Characteristics of the surface ruptures associated with the 2016 Kumamoto earthquake sequence, central Kyushu, Japan. *Earth, Planets and Space, 68*(1), 1-12.

Tchalenko, J. (1970). Similarities between shear zones of different magnitudes. *Geological Society of America Bulletin, 81*(6), 1625-1640.

Van der Kaars, W. (1991). Palynology of eastern Indonesian marine piston-cores: a Late Quaternary vegetational and climatic record for Australasia. *Palaeogeography, Palaeoclimatology, Palaeoecology, 85*(3-4), 239-302.

Van Dissen, R., & Yeats, R. S. (1991). Hope fault, Jordan thrust, and uplift of the seaward Kaikōura Range, New Zealand. *Geology, 19*(4), 393-396.

Wells, A., Yetton, M. D., Duncan, R. P., & Stewart, G. H. (1999). Prehistoric dates of the most recent Alpine fault earthquakes, New Zealand. *Geology, 27*(11), 995-998.

Withjack, M. O., Schlische, R. W., & Henza, A. A. (2007). Scaled experimental models of extension: dry sand vs. wet clay.

Zekkos, D., Manousakis, J., Athanasopoulos-Zekkos, A., Clark, M., Knoper, L., Massey, C., . . . Rathje, E. (2018). *Structure-from-Motion based 3D mapping of landslides & fault rupture sites during 2016 Kaikōura earthquake reconnaissance.* Paper presented at the Proc. 11th US National Conference on Earthquake Engineering, Integrating Science, Engineering & Policy.

Appendix A – 2016 stratigraphy and samples

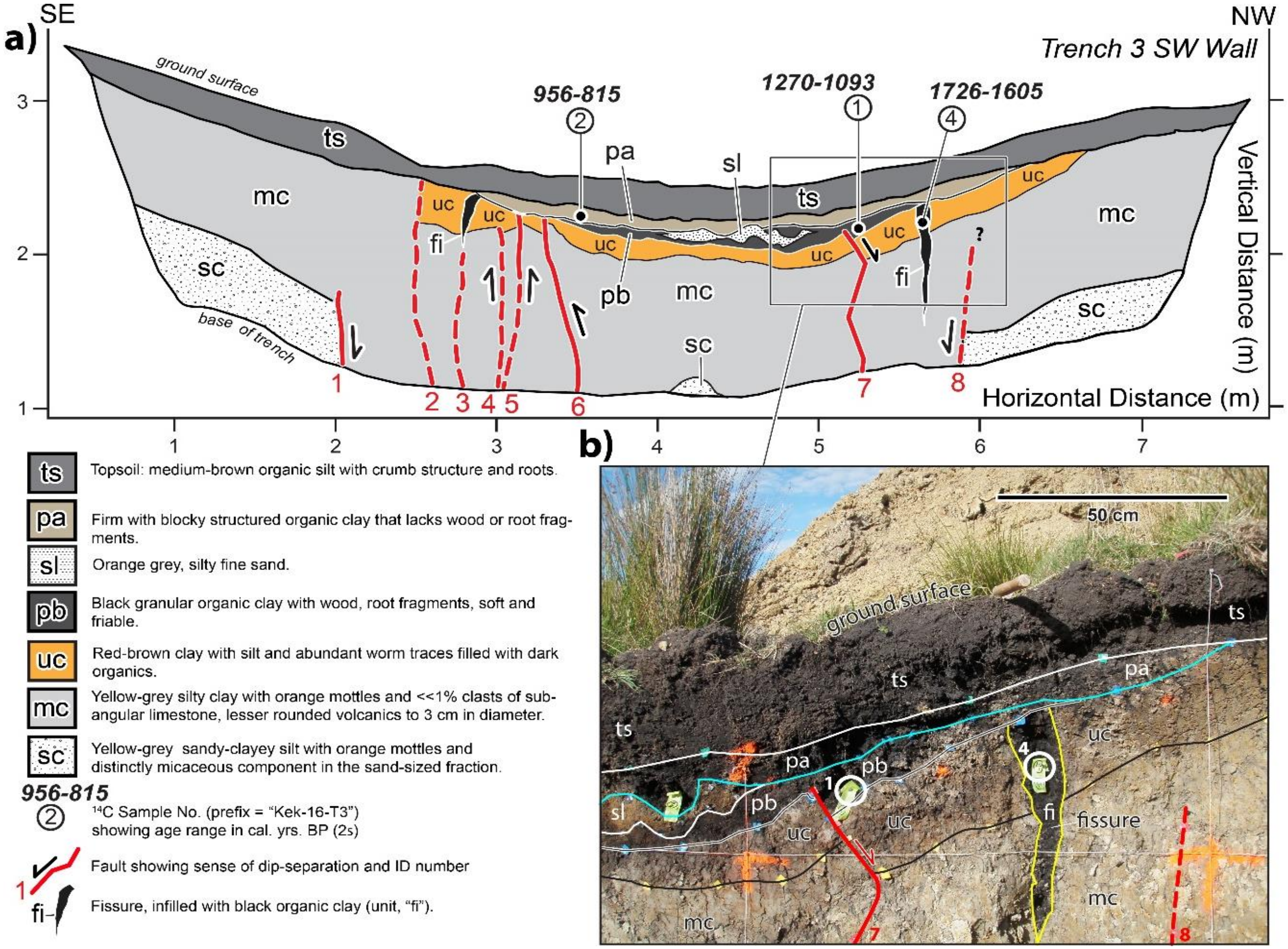

Appendix A.2.1: *Pre-earthquake trench log of the SW wall of Trench 3 from Little et al. (2018). This trench was not re-excavated after the earthquake, but samples 1 and 4 were used in the updated revised model to constrain a paleoearthquake, E4.*

Appendix A.2.2: *Table of samples from Trench 1 and Trench 3 prior to the 2016 earthquake, including radiocarbon ages and sample type. All these sample ages were used in my updated, preferred age model.*

Field Sample Number^	Rafter Lab. No.	$\Delta^{14}C^{\#}$ (‰)	Radiocarbon Age$^{\#}$ (yrs. B.P.)	Calibrated Age* (2σ) (yrs. B.P.) Modes					Probability for each 2σ range (%)					unit	Sample Type
<u>Trench 1 (SW)</u>				1	2	3	4	5	1	2	3	4	5		
Kek-16-T1-**1**	NZA 61005	-25.0 ±0.2	176±20	273-204	192-169	153-133	120-57	28-0	39.5	4.2	10.7	27.1	13.5	mp	Charcoal fragments
Kek-16-T1-**2**	NZA 61009	-24.2 ±0.2	419±20	498-442	364-331				71.2	23.6				mp	Charcoal fragments
Kek-16-T1-**3**	NZA 61010	-24.7 ±0.2	914±20	800-729					94.7					lp	Piece of charcoal
Kek-16-T1-**4**	NZA 61011	-25.5 ±0.2	789±20	721-660					95.3					up	2 charcoal fragments
Kek-16-T1-**5**	NZA 61217	-25.7 ±0.2	1794±23	1716-1592					95.3					uc	Charcoal fragments
Kek-16-T1-**9**	NZA 61012	-25.4 ±0.2	528±20	538-502					95.1					lp	Piece of charcoal
Kek-16-T1-**12**	NZA 61218	-26.1 ±0.2	1844±23	1819-1765	1753-1699	1650-1621			27.0	16.4	7.6			uc	Charcoal fragments
<u>Trench 3 (SW)</u>															
Kek-16-T3-**1**	NZA 61015	-26.0 ±0.2	1305±20	1270-1169	1145-1093				79.9	15.2				pb	Wood fragments
Kek-16-T3-**2**	NZA 61006	-24.7 ±0.2	1044±20	956-902	865-815				70.4	24.6				pa	Piece of charcoal
Kek-16-T3-**4**	NZA 61007	-27.7 ±0.2	1802±21	1726-1605					94.9					u-c	Piece of charcoal

^Final bold number is the one circled and plotted on the trench logs in Figure 2.3, Appendix A.2.1

$^{\#}$Conventional Radiocarbon Age and $\Delta^{14}C$ are reported as defined by Stuiver and Polach (1977).

*Calibrated with SHCal13 (Hogg et al., 2013). Calibrated ages are reported with respect to AD 1950.

Appendix B – 2018 stratigraphy, samples and age modelling

Appendix B.2.3: *Detailed stratigraphic unit descriptions used to describe units identified in the 2018 trench logs, including those that were originally documented in the pre-earthquakes trench(es).*

Unit	**Description**
psp	*Spoil from the 2016 excavations, spread over the ground surface after backfilling. Chaotic melange of silty clays, with streaks of orange layers. Includes ts and peat units. Blocks up to 1 m in diameter. Fibrous, with reeds.*
tbf	Chaotic, faulted, trench backfill from the 2016 excavations
fp	Soft, dark grey organic clay with abundant fibres. Granular with scaly fabric. Very fibrous.
ts	Medium brown, crumbly organic silt, with some roots. Merges gradationally with underlying units
up	Firm, massive, dark brown organic rich silt up to fine grained peat (non-fibrous). Contains 1-2% limestone chips up to 1cm diameter
mp	Firm, massive, very dark brown to black peat (non-fibrous). Contains charcoal concentrated at base.
lp	Deformed lens of organic rich silt to peat with cm-dm thick beds. Locally contains charcoal
ff	Soft, light brown organic clay speckled with granule size clasts of charcoal and (rusty brown) siltstone. Angular to sub-angular clasts, giving a speckled appearance. Peaty in places.
uc	Deformed lens of light grey to brown clayey silt. Contains rare charcoal flecks (<1-2%).
g	Firm medium grey clay, containing mm thick laminae of organics and scattered roots. Deformed sedimentary layering is sub vertical

ml	Massive clayey silt with grey/orange mottles, and 5% angular limestone chips
m	Firm, massive grey silty clay, with pervasive orange vertical mottles
Ms	Similar to unit m, but greyer and with greater silt content. Organics and root casts.
O	Firm, olive coloured clay with disseminated subangular to angular limestone clasts.
Fff	Grey, silty clay with disseminated charcoal to 0.5cm diameter. May contain some of unit uc.
Cff	Soft grey silty clay with orange mottles, and 10% clasts (peat, pebble sized).
Ffb	Blocky black peat with clay rich clasts/blobs of unit ml or m. Also limestone clasts

Appendix B.2.4: *Table of samples taken after the earthquake (2018), from Trenches 1 and 4, and the paleofissure site ~100 m southwest of these trenches (labelled in Figure 2.2). Table includes sample number, radiocarbon age, calibrated age (2σ), and sample content i.e., charcoal, wood. Samples coloured green were used in the preferred age model, samples coloured blue are pooled samples (see Appendix B.2.5 and section 2.2.3 of this thesis), red and white coloured samples were not included in the age model, and orange coloured samples were used in the alternative age model only (from the paleofissure site).*

Field Sample Number^	Rafter Lab. No.	$\Delta^{14}C^{\#}$ (‰)	Radiocarbon Age$^{\#}$ (yrs. B.P.)	Calibrated Age* (2σ) (yrs. B.P.) Modes				Probability for each 2σ range (%)				unit	Sample Type
Trench 1 (SW)				1	2	3	4	1	2	3	4		
Kek-18-S1-**03**	NZA 67128	-25.0 ±0.2	618±24	632-596	567-533			48.6	51.4			fp	single charcoal fragment
Kek-18-S1-**06**	NZA 67364	-27.4 ±0.2	Modern									fp	Plant material
Kek-18-S1-**07**	NZA 67127	-24.7 ±0.2	2178±23	2300-2244	2178-2168	2161-2042	2030-2018	15.9	1.5	81	1.7	uc	Wood
Kek-18-N1-**01**	NZA 67365	-26.7 ±0.2	Modern									bp	Plant material
Kek-18-N1-**02**	NZA 67129	-25.7 ±0.2	2005±23	1997-1945	1943-1870	1850-1839		30.1	66.9	3		ml	Charcoal fragments
Kek-18-N1-**03**	NZA 67125	-25.4 ±0.2	1808±23	1734-1605	1599-1594			99.1	0.9			uc	Charcoal fragments
Trench 1 (NE)													
Kek-18-S1-**20**	NZA 67363	-24.3 ±0.2	1664±23	1570-1429				100				uc	Wood
Kek-18-S1-**21**	NZA 67126		949±22	905-851	844-825	824-745		38.6	5.5	55.9		ff	Charcoal fragments
Kek-18-S1-**22**	NZA 67362	-24.4 ±0.2	454±23	511-451	351-340			95.9	4.1			ff	Charcoal fragments
Kek-18-S1-**23**	NZA 67300	-27.2 ±0.2	1529±20	1408-1316				100				uc	soil
Trench 4 (SW)													
Kek-18-T4-**01**	NZA 67358	-24.7 ±0.2	1857±24	1824-1702				100				ffb	Charcoal fragments
Kek-18-T4-**06**	NZA 67301	-27.8 ±0.2	Modern									pt	Plant material
Kek-18-T4-**07**	NZA 67359	-24.2 ±0.2	1784±24	1710-1587				100				ml	Charcoal fragments
Kek-18-T4-**08**	NZA 67360	-24.9 ±0.2	1799±24	1723-1593				100				ml	Charcoal fragments
Kek-18-T4-**09**	NZA 67361	-26.1 ±0.2	937±23	904-861	841-829	819-735		24.3	1.9	73.8		pt	Wood
*Calibrated with SHCal13 (Hogg et al., 2013). Calibrated ages are reported with respect to AD 1950.													
Benmore Paleofissure Site													
Kek18-PF-**01**	NZA 65131	-25.1 ±0.2	2220±20	2300-2240	2180-2148			43.3	24.9				Charcoal fragments
Kek18-PF-**02**	NZA 65132	-25.0 ±0.2	2200±20	2296-2260	2174-2171	2158-2141	2132-2096	24.3	1.5	14.5	27.8		Charcoal fragments
Kek18-PF-**03**	NZA 65133	-24.9 ±0.2	2196±20	2295-2264	2157-2140	2133-2094		20	14.8	33.2			Charcoal fragments

Appendix B.2.5: *Orthomosaic of the SW wall of Trench 4, constructed using structure from motion images. Fissures can be seen in the centre of the trench that correlate to those on Figure 2.9. On the left of the image, an oblique thrust fault is labelled which displaces the topsoil (ts) over itself, forming a bulged moletrack at the ground surface.*

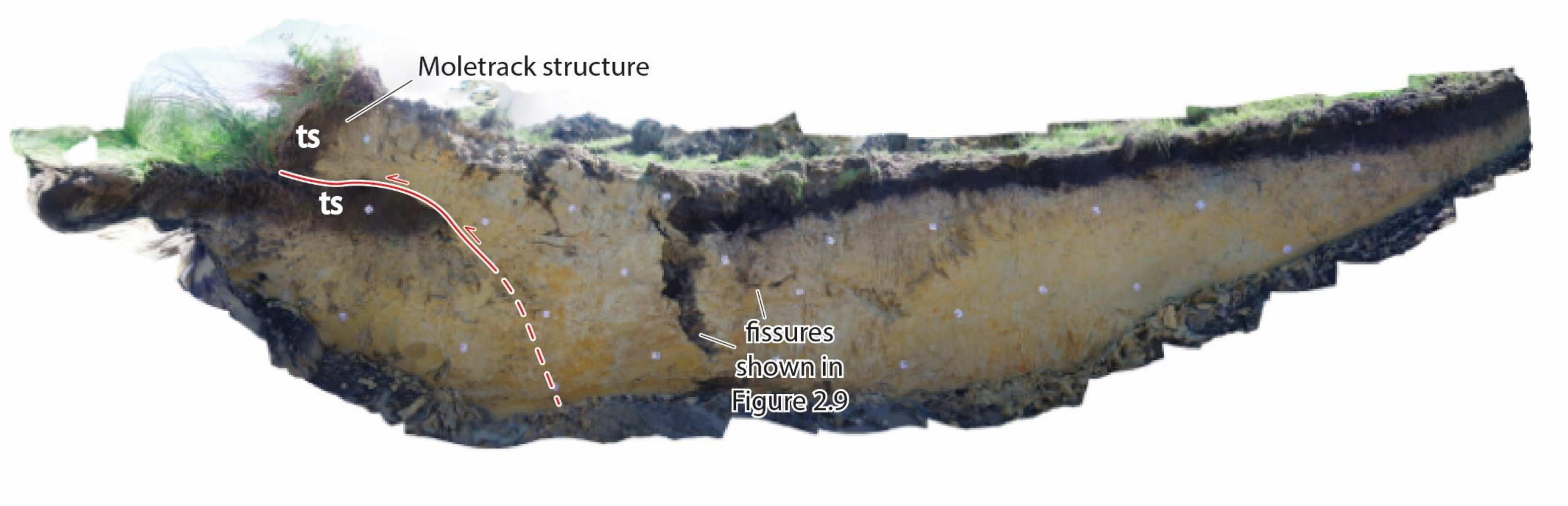

***Appendix B.2.6**: Section of the preferred age model showing the age distributions of samples that were plotted as a "phase" in the age model. Sample numbers are given in brackets. Sequence is referred to as a "virtual trench" in the text.*

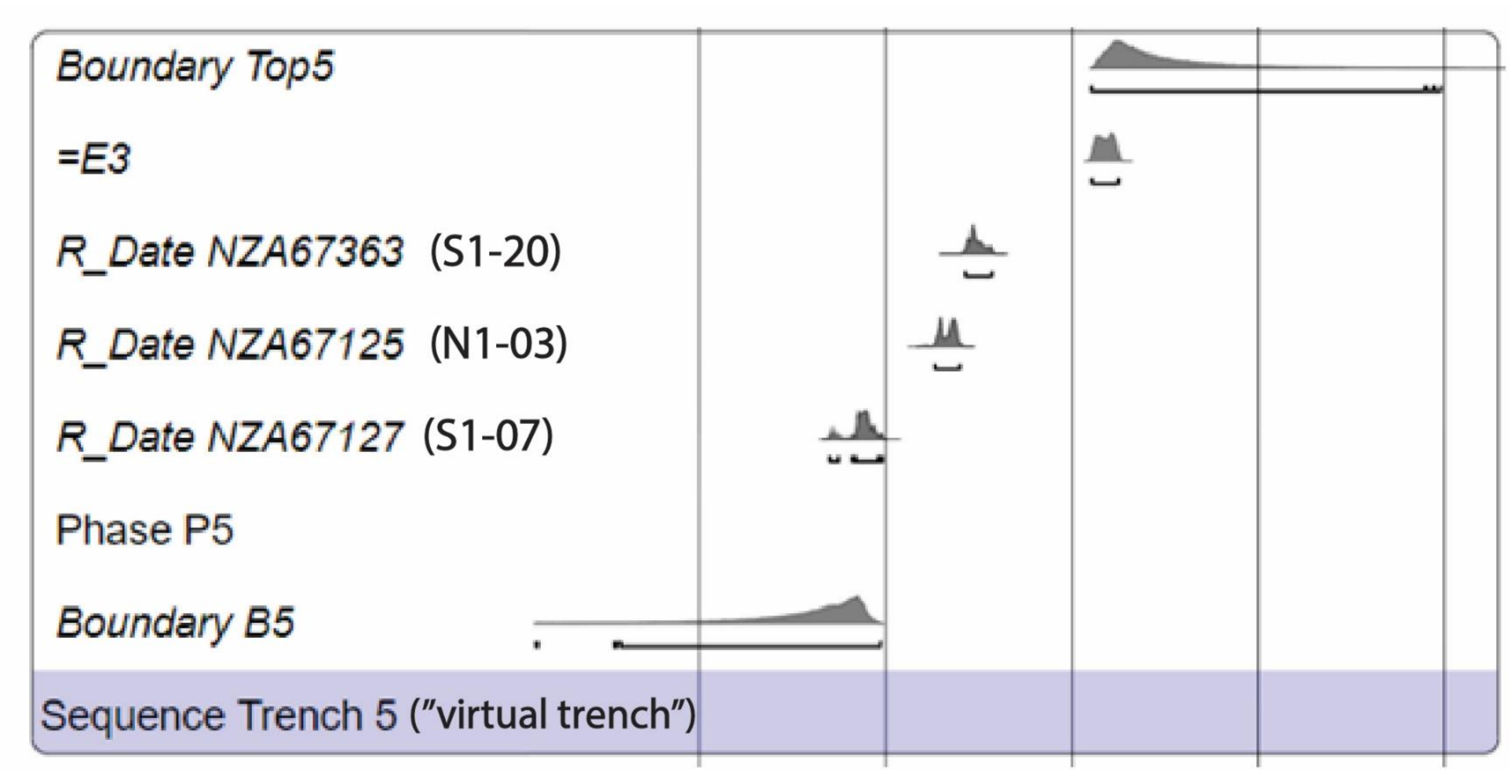

Appendix B.2.7: Full code as used in the preferred age model in OxCal 4.2.3. Annotations show the trench sequences, individual samples, and calculations for interval between paleoearthquakes and recurrence interval.

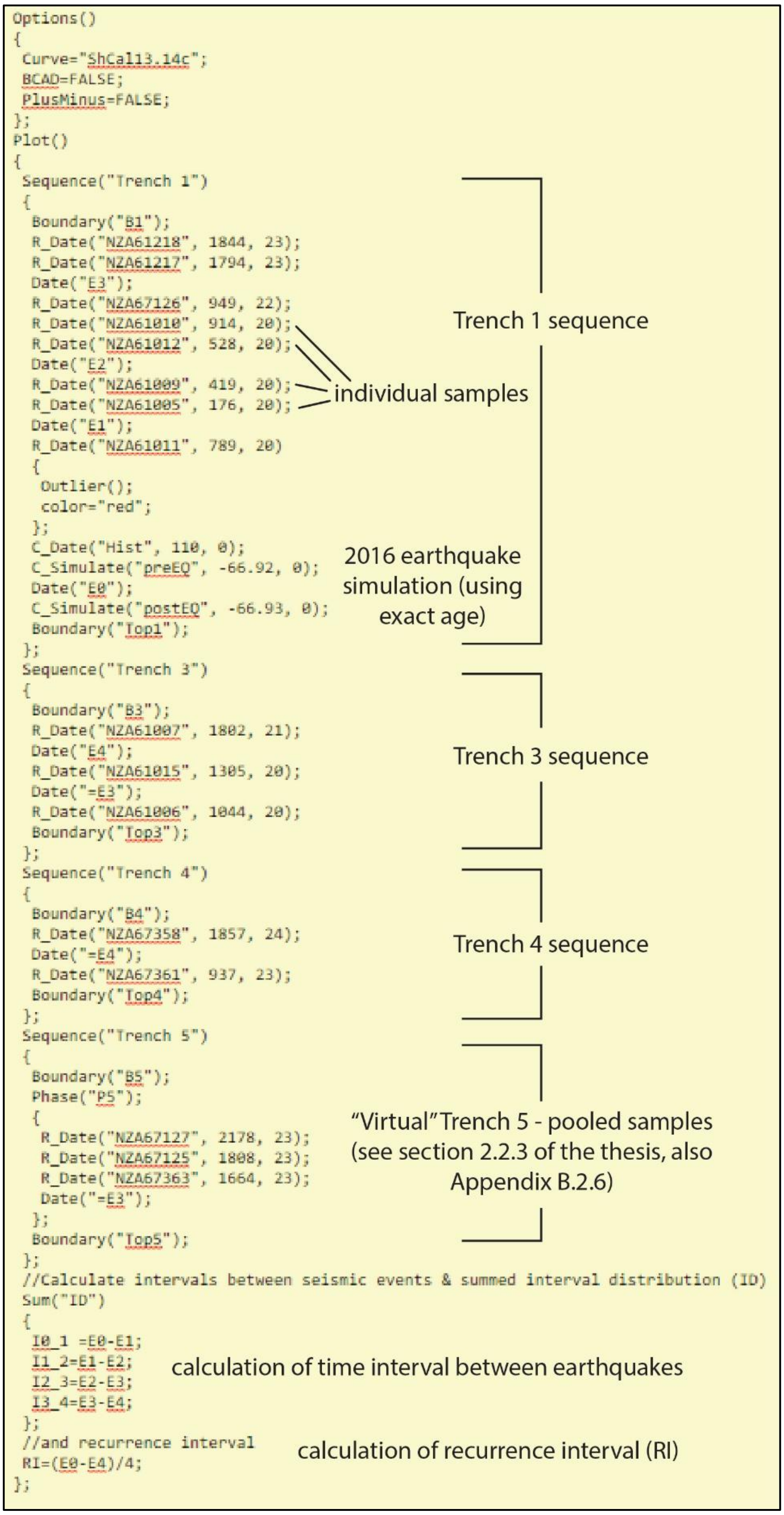

```
Options()
{
 Curve="ShCal13.14c";
 BCAD=FALSE;
 PlusMinus=FALSE;
};
Plot()
{
 Sequence("Trench 1")
 {
  Boundary("B1");
  R_Date("NZA61218", 1844, 23);
  R_Date("NZA61217", 1794, 23);
  Date("E3");
  R_Date("NZA67126", 949, 22);
  R_Date("NZA61010", 914, 20);
  R_Date("NZA61012", 528, 20);
  Date("E2");
  R_Date("NZA61009", 419, 20);
  R_Date("NZA61005", 176, 20);
  Date("E1");
  R_Date("NZA61011", 789, 20)
  {
   Outlier();
   color="red";
  };
  C_Date("Hist", 110, 0);
  C_Simulate("preEQ", -66.92, 0);
  Date("E0");
  C_Simulate("postEQ", -66.93, 0);
  Boundary("Top1");
 };
 Sequence("Trench 3")
 {
  Boundary("B3");
  R_Date("NZA61007", 1802, 21);
  Date("E4");
  R_Date("NZA61015", 1305, 20);
  Date("=E3");
  R_Date("NZA61006", 1044, 20);
  Boundary("Top3");
 };
 Sequence("Trench 4")
 {
  Boundary("B4");
  R_Date("NZA67358", 1857, 24);
  Date("=E4");
  R_Date("NZA67361", 937, 23);
  Boundary("Top4");
 };
 Sequence("Trench 5")
 {
  Boundary("B5");
  Phase("P5");
  {
   R_Date("NZA67127", 2178, 23);
   R_Date("NZA67125", 1808, 23);
   R_Date("NZA67363", 1664, 23);
   Date("=E3");
  };
  Boundary("Top5");
 };
 //Calculate intervals between seismic events & summed interval distribution (ID)
 Sum("ID")
 {
  I0_1 =E0-E1;
  I1_2=E1-E2;
  I2_3=E2-E3;
  I3_4=E3-E4;
 };
 //and recurrence interval
 RI=(E0-E4)/4;
};
```

Appendix C – Datasets used in moletrack analysis

Appendix C.3.1: *Table describing in more detail the various surface geomorphic classes used in Figure 3.2.*

Unit	**Description**
QG	*Quaternary marine gravels that have been displaced along the Heavers Creek Fault*
HEG	*Areas which have been modified by humans such that the expression of geomorphology is impacted – incl. roads, dams*
HWB	*Water bodies that have been man-made – i.e., dammed ponds or lakes*
WBF	*Water bodies formed through natural processes (generally sag ponds forming on releasing bends)*
SC	*Stream channels*
FA	*Alluvial fans deposited alongside streams; an older and younger fan were identified*
DN	*Modern day beach dunes*
BR	*Older beach deposits that have been uplifted or exposed*
HTP	*Areas of relatively high, flat land, including paddocks. Generally found between gullies and landslide areas*
HTM	*Areas of hillslope with moderate slope and generic features*
HTR	*Ridges of hillslopes*
HTG	*Areas of hillslope that are relatively steep, and have formed patterns of ridges and gullies across the surface*
HTI	*Areas of terrain which are defined by either the underlying geology, causing an anomaly on the surface; or fault related features created by movement in earthquakes*
LS	*Areas prone to landsliding, either currently or in the past, with steep slopes*

Appendix C.3.2: *Series of map segments (numbered 1-8 in the following figures) showing exampes of mapped fracture types within the Napoleon segment. All tiles are oriented with North p the page. Black lines are R faults, red-brown lines are rotated R faults, yellow lines are R' faults, and blue lines are T fractures (see Table 3.1 in text for descriptions). Red line in each tile represents the local fault strike.*

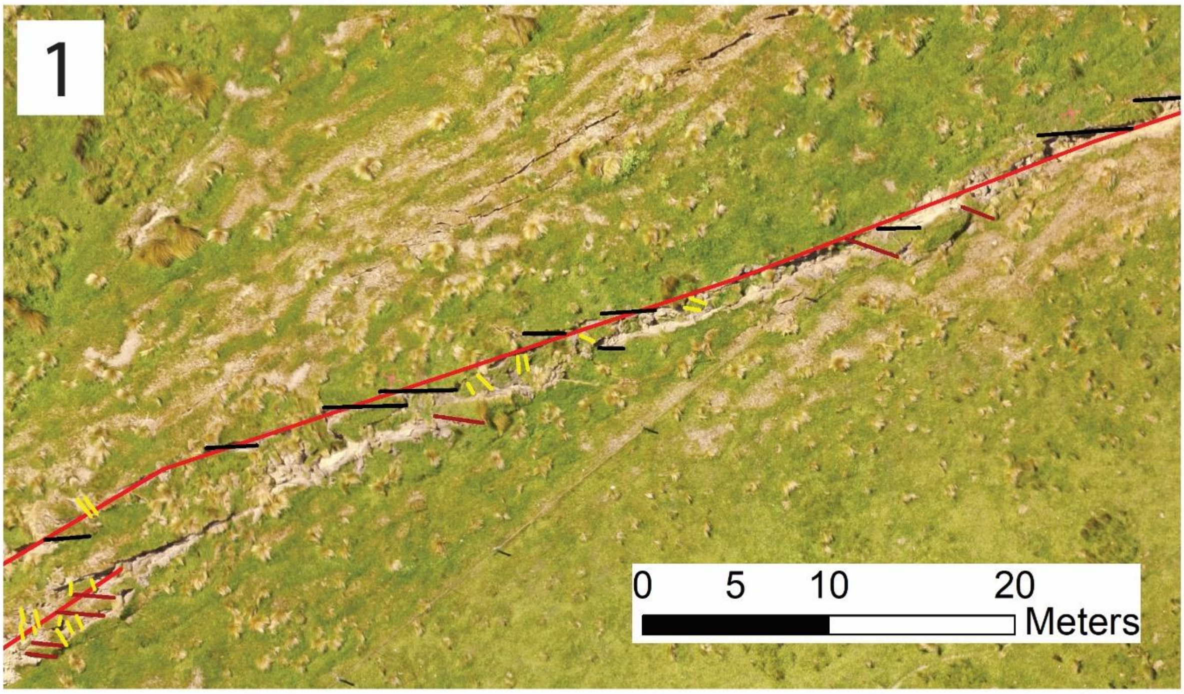

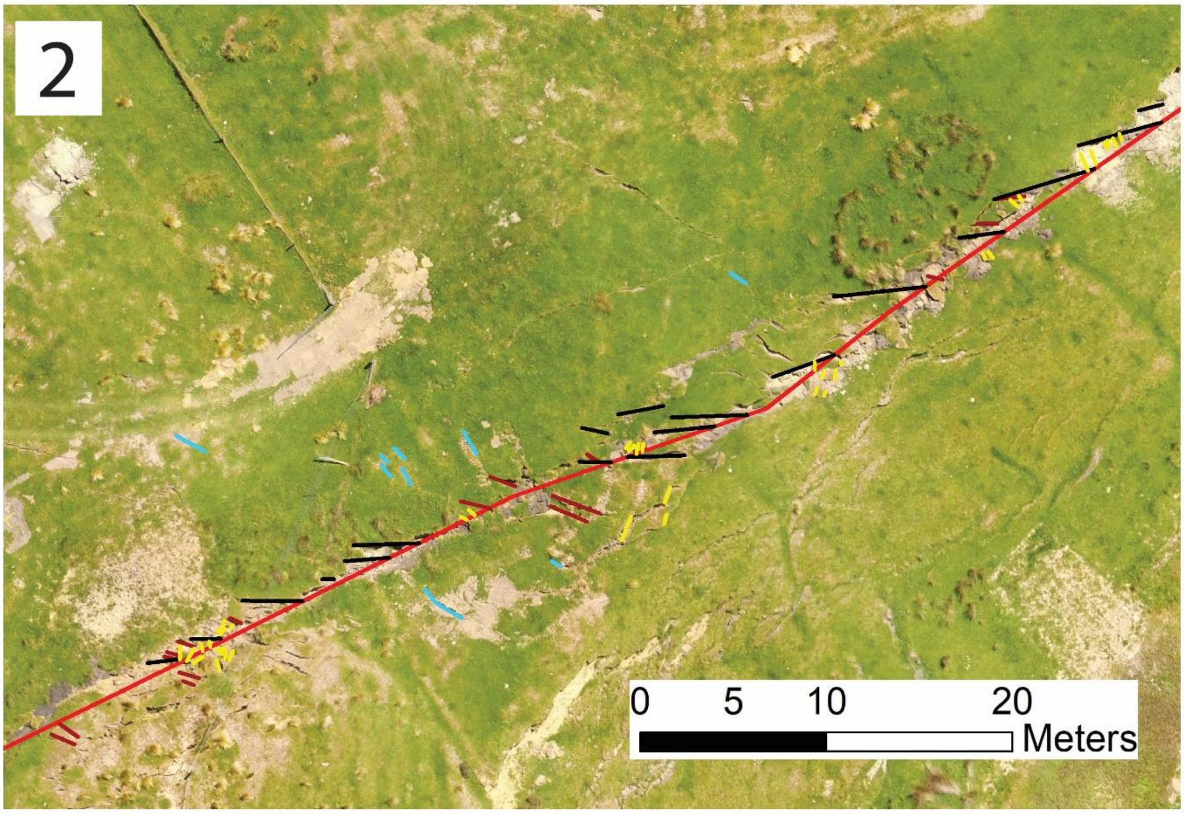

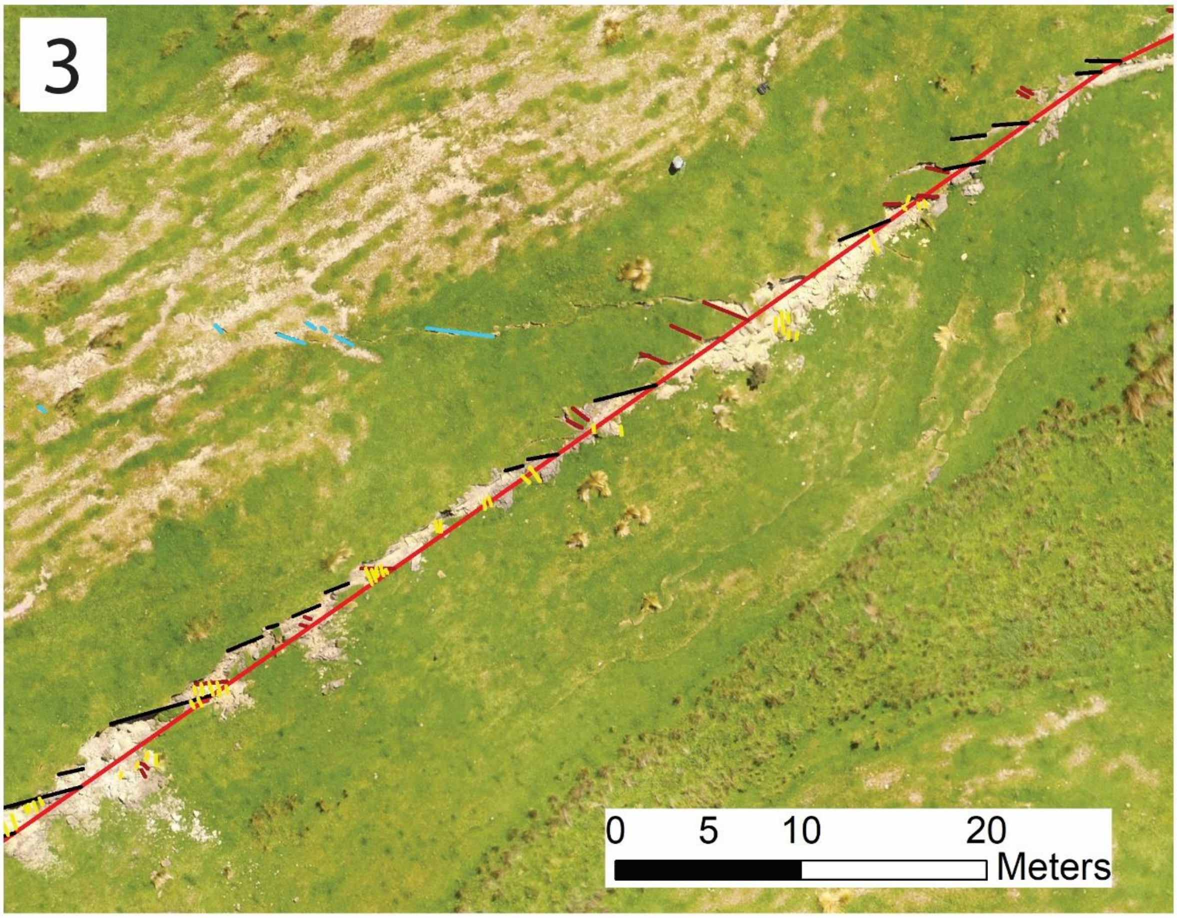
3
0
5
10
20
Meters

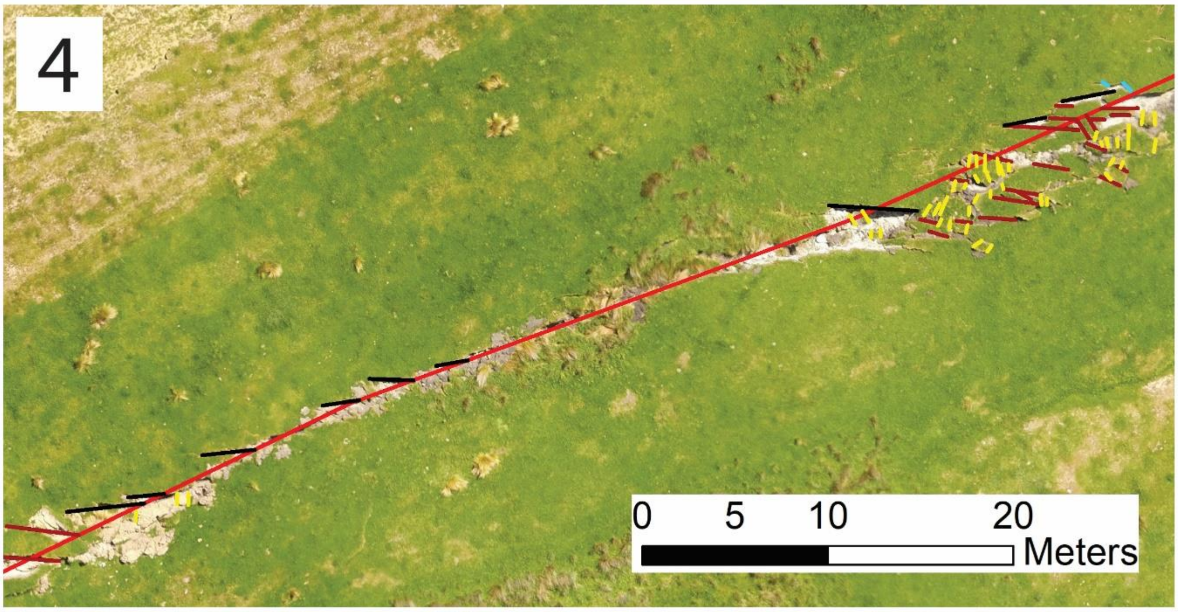
4
0
5
10
20
Meters

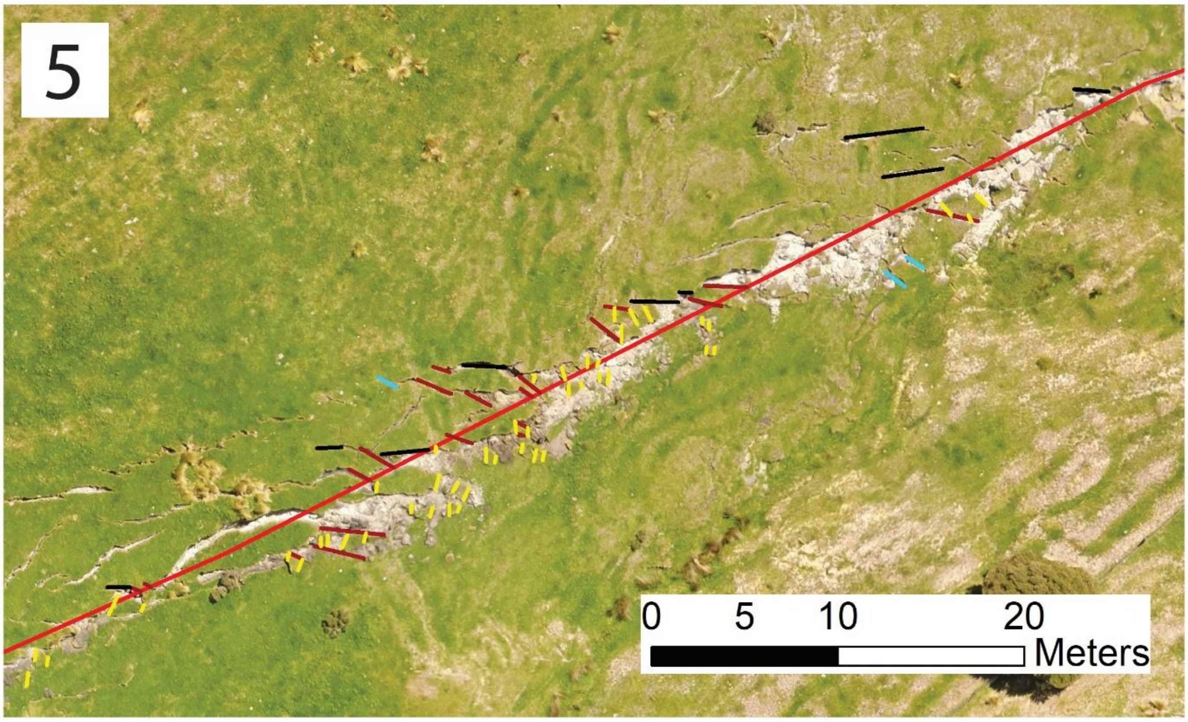
5
0
5
10
20
Meters

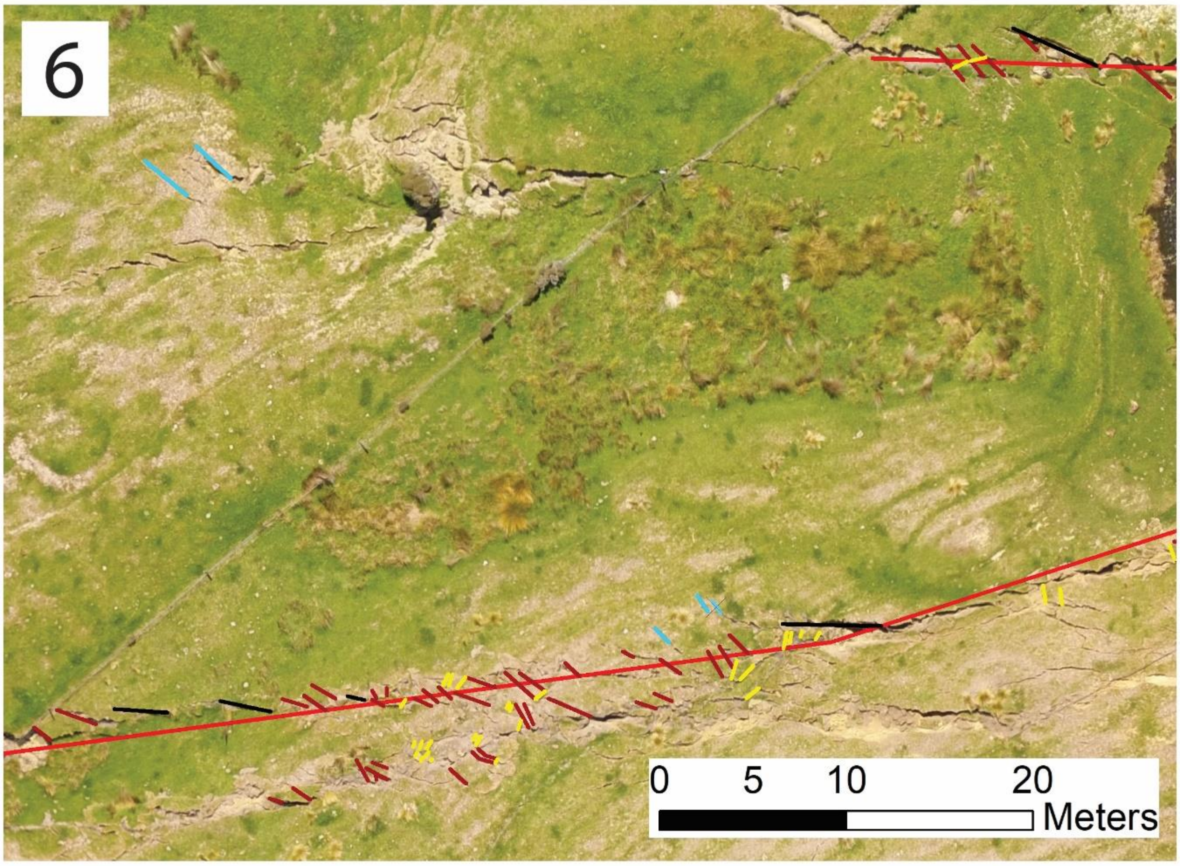
6
0
5
10
20
Meters

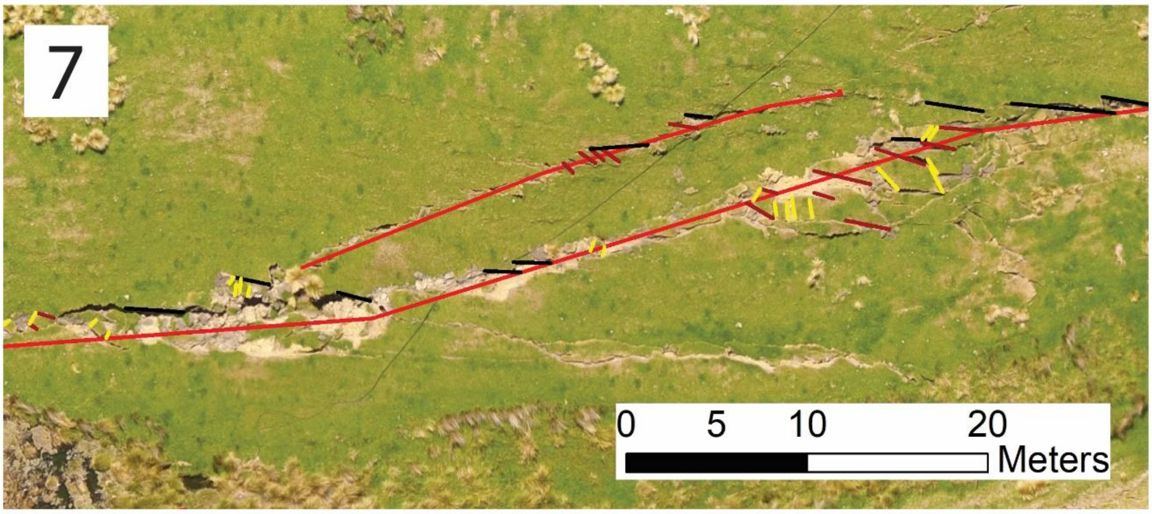
7
0
5
10
20
Meters

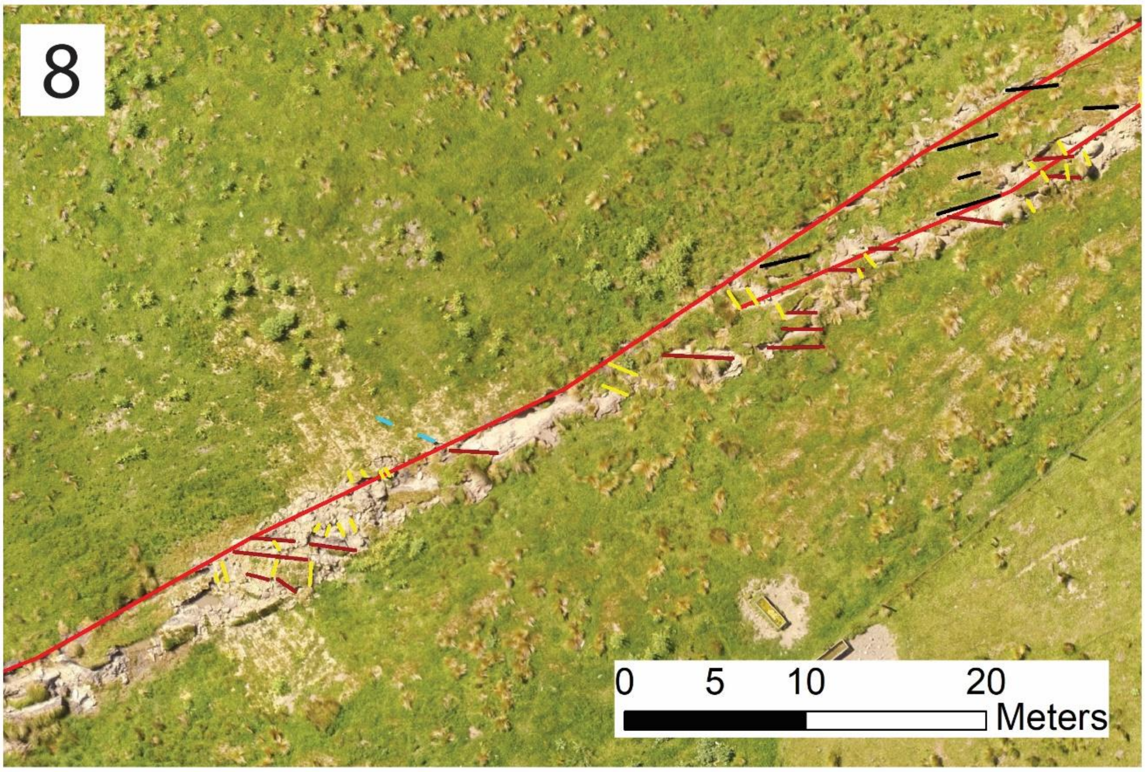
8
0
5
10
20
Meters

Appendix C.3.3: *Tabulated data of the strike of each fracture type relative to local fault strike. Minimum, maximum and average values are given for each type at the end of their respective data series. For ease of reading table is broken into three columns per page.*

R faults	R rotated	R' rotated	T fractures	R faults	R rotated	R' rotated	R rotated	R' rotated	R' rotated
19	26	128	68	22	52	86	48	105	139
31	39	119	55	18	38	106	49	113	99
21	38	133	80	20	34	101	41	114	101
29	40	79	71	14	55	98	43	99	118
24	40	153	70	17	61	105	39	97	146
14	31	103	71	31	45	102	21	106	125
26	23	97	53	17	46	101	41	115	131
19	36	83	43	17	55	121	29	91	153
21	31	82	55	18	50	112	35	120	79
19	33	92	51	14	52	119	27	117	138
18	23	99	47	20	37	104	41	138	77
28	29	98	36	16	52	79	45	137	71
29	24	71	33	14	51	88	27	123	131
20	22	85	47	15	37	101	28	118	125
19	23	81	43	21	36	98	49	121	128
14	37	80	41	23	40	74	47	116	138
32	40	86	32	19	52	107	40	128	136
19	42	109	38	19	52	109	60	153	120
19	30	115	49	21	48	101	29	153	99
20	48	114	48	26	34	117	61	149	79
25	33	112	52	24	29	108	27	155	77
30	30	93	60	25	30	70		108	103
21	35	100	64	20	58	88	avr = 41°	112	121
27	22	107	77	20	51	77	min = 21°	92	146
28	29	151	57	18	35	74	max = 68°	112	
26	24	104	55	18	57	111		146	avr = 114°
24	38	90	60	24	59	155		142	min = 66°
22	29	115	72	20	56	123		139	max = 155°
29	24	89	56	26	63	155		82	
24	41	86	75	18	67	116		132	
20	29	91	83	20	64	115		154	
19	65	81	72	17	38	151		106	

R faults	R rotated	R' rotated	T fractures	R faults	R rotated	R' rotated	R' rotated
29	57	92	64	16	26	152	154
31	55	113	72	16	23	130	151
24	33	92		20	34	107	110
22	30	145	avr = 57°	22	33	104	117
27	48	146	min = 32°	30	28	100	150
20	39	80	max = 83°	16	32	150	129
25	33	74			44	116	140
26	40	154		avr = 22°	51	113	137
17	40	98		min = 14°	41	122	129
20	43	98		max = 32°	33	140	115
27	43	102			53	138	117
20	42	98			45	142	142
22	47	149			55	149	149
20	61	143			54	124	117
23	50	66			45	114	146
24	43	153			65	151	146
24	22	152			34	153	142
27	42	151			39	128	111
24	40	78			43	135	114
25	52	90			51	121	150
28	57	102			28	120	117
30	53	106			45	123	89
26	62	71			53	128	89
27	26	141			68	95	122
28	36	77			65	86	66
15	30	70			43	132	130
15	38	150			49	129	121
17	32	149			43	125	71
24	24	100			47	132	74
24	21	85			50	119	69
20	30	90			32	104	134
23	58	77			31	103	143

Appendix C.3.4: *Tabulated measurements of both inner and total rupture zone width, and excess raft area (both Napoleon and Tirohanga fault segments). Minimum, maximum and average values are given at the end of each respective data series.*

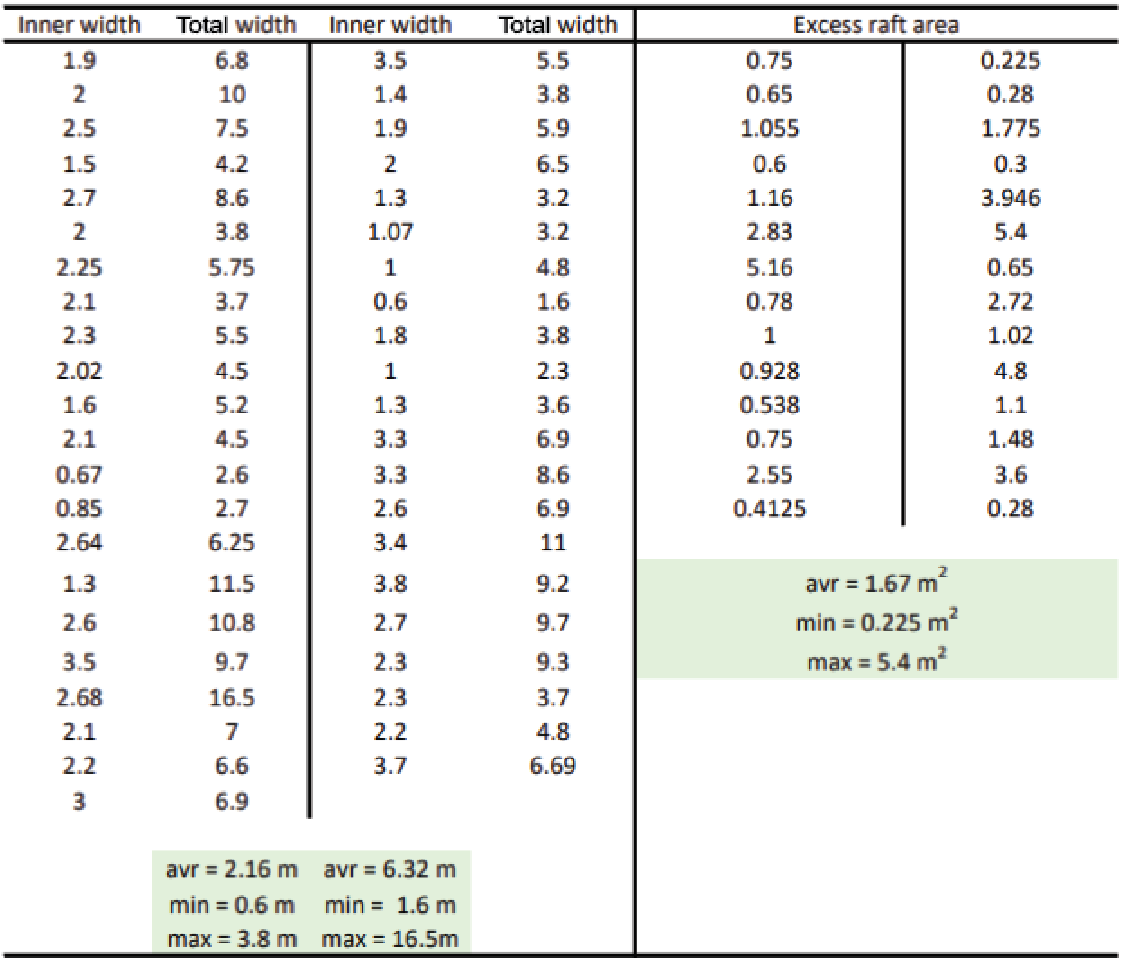

Inner width	Total width	Inner width	Total width	Excess raft area	
1.9	6.8	3.5	5.5	0.75	0.225
2	10	1.4	3.8	0.65	0.28
2.5	7.5	1.9	5.9	1.055	1.775
1.5	4.2	2	6.5	0.6	0.3
2.7	8.6	1.3	3.2	1.16	3.946
2	3.8	1.07	3.2	2.83	5.4
2.25	5.75	1	4.8	5.16	0.65
2.1	3.7	0.6	1.6	0.78	2.72
2.3	5.5	1.8	3.8	1	1.02
2.02	4.5	1	2.3	0.928	4.8
1.6	5.2	1.3	3.6	0.538	1.1
2.1	4.5	3.3	6.9	0.75	1.48
0.67	2.6	3.3	8.6	2.55	3.6
0.85	2.7	2.6	6.9	0.4125	0.28
2.64	6.25	3.4	11		
1.3	11.5	3.8	9.2	avr = 1.67 m^2	
2.6	10.8	2.7	9.7	min = 0.225 m^2	
3.5	9.7	2.3	9.3	max = 5.4 m^2	
2.68	16.5	2.3	3.7		
2.1	7	2.2	4.8		
2.2	6.6	3.7	6.69		
3	6.9				
	avr = 2.16 m	avr = 6.32 m			
	min = 0.6 m	min = 1.6 m			
	max = 3.8 m	max = 16.5m			

Appendix D – Appendices Trench Site Data

Appendix D.4.1: *Original measurement of the rupture zone width and displacement vector at the trench site, taken from Kearse et al. (2018).*

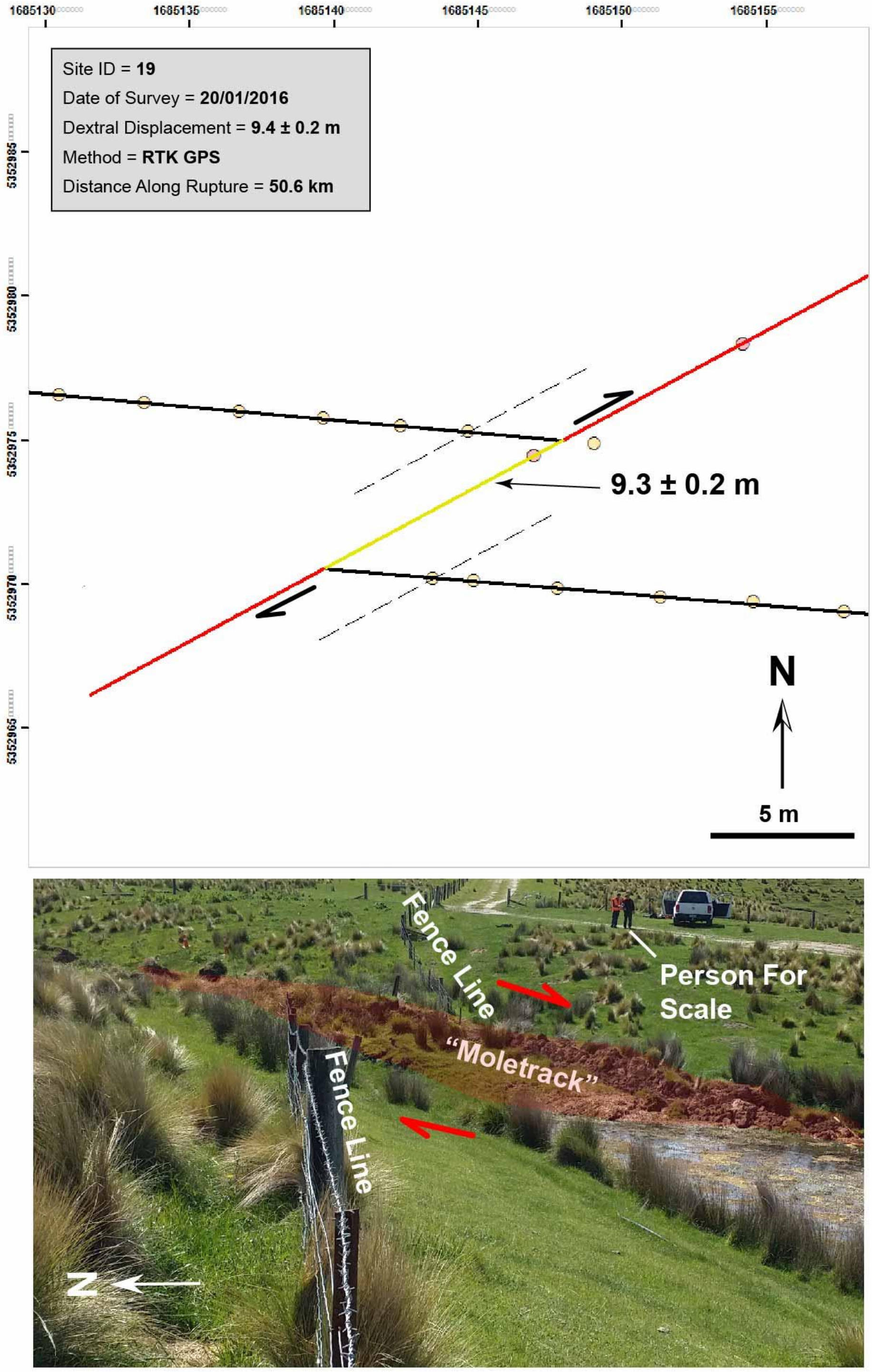

Appendix D.4.2: *Pre-and post-earthquake comparison of trench walls using photographs from the 2016 and 2018 excavations. a) shows where the sections of trench wall shown in the photographs are located in aerial view, denoted by blue and yellow lines (also shown in b, c and d.*

a) Aerial view of trench site, showing locations of annotated photographs in b), c), and d)

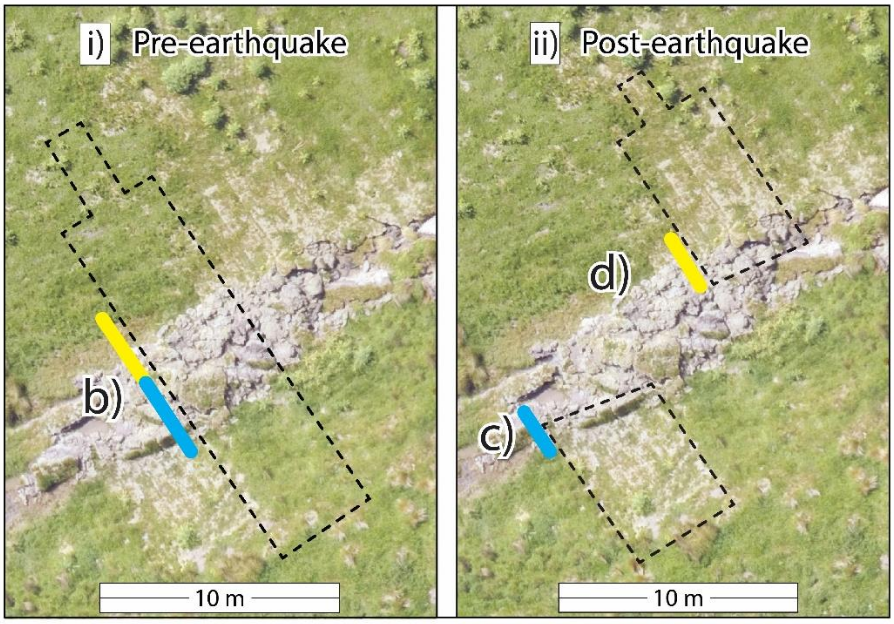

b) Pre-earthquake

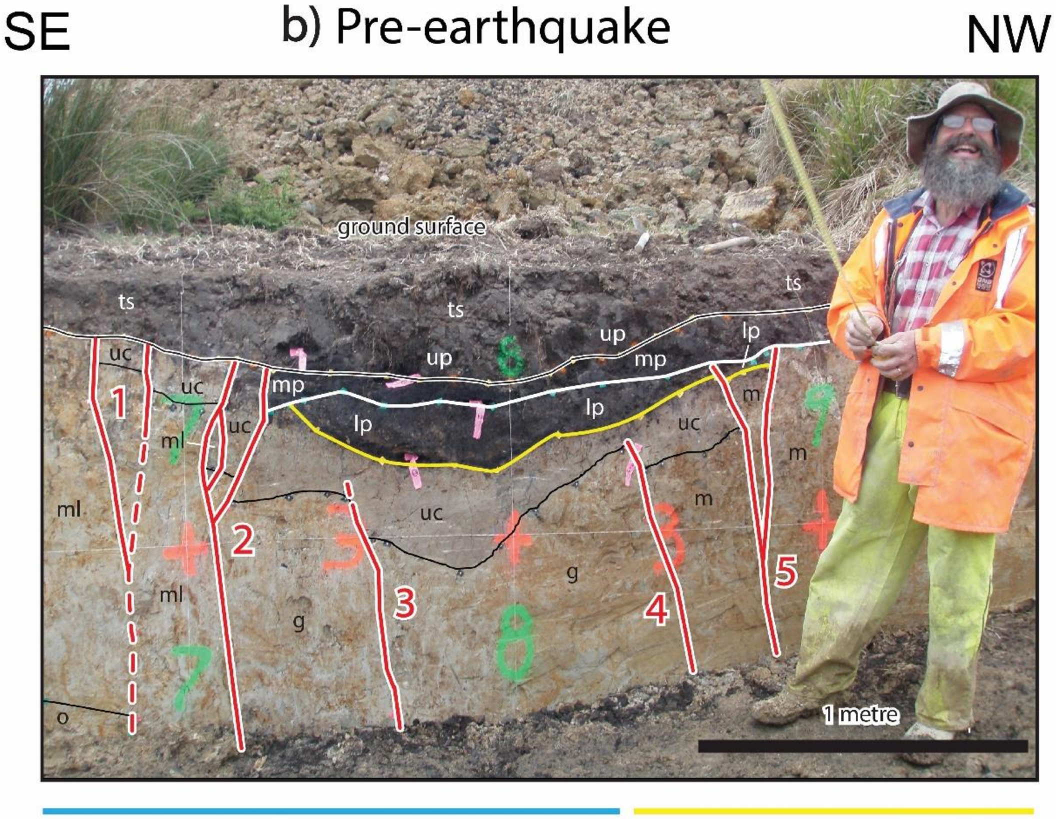

c) Post-earthquake, SE half

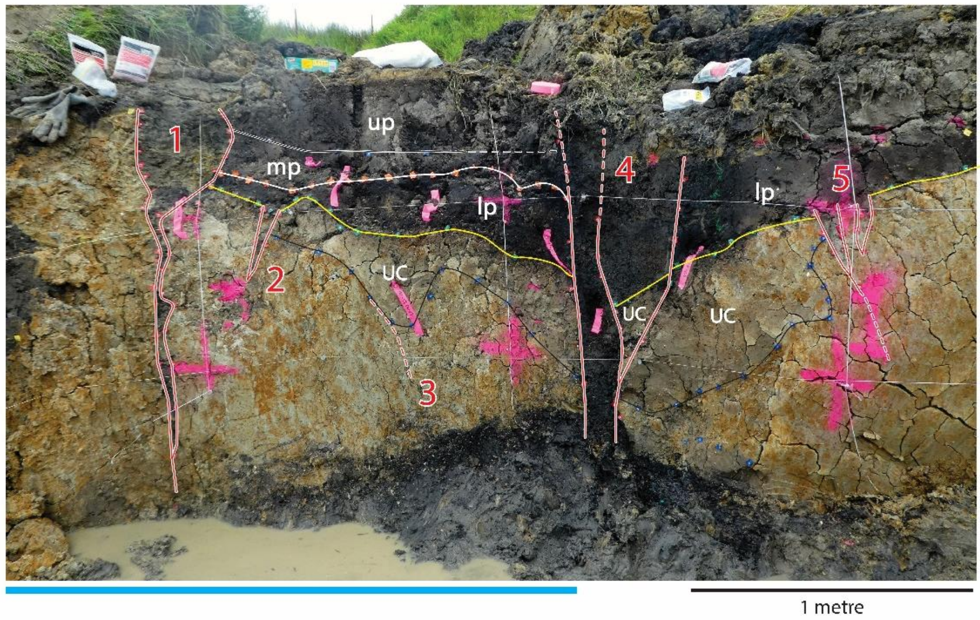

d) Post-earthquake, NW half